UNIVERSIDADE FEDERAL DE SANTA CATARINA
CAMPUS UNIVERSITÁRIO DE FLORIANÓPOLIS
PROGRAMA DE PÓS-GRADUAÇÃO EM ENGENHARIA MECÂNICA

TESE DE DOUTORADO

JURANDIR MARCOS SÁ DE SOUSA

ADDITIVE MANUFACTURING OF AISI 410L STAINLESS STEEL BY THE LASER DIRECTED ENERGY DEPOSITION: PARAMETRIZATION AND EFFECT OF HEAT-TREATMENT ON MECHANICAL, TRIBOLOGICAL AND CORROSION PERFORMANCE

FLORIANÓPOLIS
2025

Jurandir Marcos Sá de Sousa

ADDITIVE MANUFACTURING OF AISI 410L STAINLESS STEEL BY THE LASER DIRECTED ENERGY DEPOSITION: PARAMETRIZATION AND EFFECT OF HEAT-TREATMENT ON MECHANICAL, TRIBOLOGICAL AND CORROSION PERFORMANCE

Tese submetida ao Programa de Pós-Graduação em Engenharia Mecânica da Universidade Federal de Santa Catarina para a obtenção do título de Doutor em Engenharia Mecânica.

Orientador: Prof. Dr. Eng. Milton Pereira

Florianópolis

2025

Ficha catalográfica gerada por meio de sistema automatizado gerenciado pela BU/UFSC.
Dados inseridos pelo próprio autor.

Sousa, Jurandir Marcos Sá de
Additive Manufacturing of AISI 410L Stainless Steel by the Laser Directed Energy Deposition: Parametrization and Effect of Heat-Treatment on Mechanical, Tribological and Corrosion Performance / Jurandir Marcos Sá de Sousa ; orientador, Milton Pereira, 2025.
172 p.

Tese (doutorado) - Universidade Federal de Santa Catarina, Centro Tecnológico, Programa de Pós-Graduação em Engenharia Mecânica, Florianópolis, 2025.

Inclui referências.

1. Engenharia Mecânica. 2. Additive Manufacturing by Laser Directed Energy Deposition. 3. Mechanical Properties. 4. Tribological Performance. 5. Corrosion Resistance. I. Pereira, Milton. II. Universidade Federal de Santa Catarina. Programa de Pós-Graduação em Engenharia Mecânica. III. Título.

Jurandir Marcos Sá de Sousa

ADDITIVE MANUFACTURING OF AISI 410L STAINLESS STEEL BY THE LASER DIRECTED ENERGY DEPOSITION: PARAMETRIZATION AND EFFECT OF HEAT-TREATMENT ON MECHANICAL, TRIBOLOGICAL AND CORROSION PERFORMANCE

O presente trabalho em nível de Doutorado foi aprovado, em 01 de agosto de 2025, pela banca examinadora composta pelos seguintes membros:

Prof. Milton Sérgio Fernandes de Lima, PhD.
Instituto Tecnológico de Aeronáutica

Profa. Ana Sofia Clímaco Monteiro de Oliveira, PhD.
Universidade Federal do Paraná

Prof. Rodrigo Perito Cardoso, PhD.
Universidade Federal de Santa Catarina

Prof. Carlos Enrique Niño Bohórquez, Dr. Eng.
Universidade Federal de Santa Catarina

Certificamos que esta é a versão original e final do trabalho de conclusão que foi julgado adequado para obtenção do título de Doutor em Engenharia Mecânica atribuído pelo Programa de Pós-Graduação em Engenharia Mecânica.



Documento assinado digitalmente
Henrique Simas
Data: 17/09/2025 16:01:07-0300
CPF: ***.194.639-**
Verifique as assinaturas em https://v.ufsc.br

Coordenação do Programa de Pós-Graduação



Documento assinado digitalmente
Milton Pereira
Data: 17/09/2025 15:47:45-0300
CPF: ***.484.489-**
Verifique as assinaturas em https://v.ufsc.br

Prof. Milton Pereira, Dr. Eng.
Orientador

Florianópolis, Agosto de 2025

"Aos meus queridos e amados Pais Vanusa Francisca de Sá e José Tomé de Sousa, por serem os meus heróis, os meus primeiros professores e os meus maiores exemplos de vida".

AGRADECIMENTOS

A Deus e a Nossa Senhora de Nazaré, pela vida, saúde, paz, força e coragem para lutar.

Aos meus amados e queridos pais Vanusa Sá e José de Sousa. Vocês são os meus heróis, os meus primeiros professores e os meus maiores exemplos de vida. Aos meus amados e queridos irmãos Vladimir e Jeremias pelo apoio incondicional. Vocês são os meus eternos melhores amigos. As suas companheiras de vida e minhas amigas Gaby e Juliana, e ao meu futuro sobrinho Luan. A todos os meus demais familiares pela torcida, orações e incentivo.

Ao meu Orientador Prof. Dr. Eng. Milton Pereira. O senhor me falou algo que eu nunca esquecerei: "o doutorado é mais do que receber um certificado ao final. É o processo, o tempo que você dedica, o que você aprende e o que você entrega a sociedade com ele". Obrigado pela orientação, confiança e paciência ao longo destes anos.

Ao Prof. Dr. Eng. Milton Lima por aceitar ser o Relator deste trabalho. Ao Prof. Dr. Eng. Rodrigo Perito e ao Prof. Dr. Eng. Carlos Niño por aceitarem contribuir como membros internos do POSMEC. A Profa. Dra. Enga. Ana Sofia D'Oliveira por aceitar atuar como membro externo. Eu sei que as suas agendas são muito complicadas. Muito obrigado.

Ao corpo docente e técnico do POSMEC e da UFSC como um todo. Gostaria de agradecer ao apoio técnico e estrutural do LMP. O LABMAT e LINDEN também contribuíam para a realização deste. A CAPES e CNPQ, que incentivam a pesquisa Brasileira. Ao apoio técnico e estrutural do ISI-Joinville e ao Projeto "Manufatura Digital - Petrobras".

Durante a minha jornada do Mestrado, eu tive duas casas, que foram a minha pensão lá na Trindade e o LMP-UFSC. No Doutorado, por sua vez, eu tive três casas, que foram o meu apê lá no Costa e Silva, o ISI-Joinville e o LMP-UFSC. Eu nunca as esquecerei, especialmente as duas últimas, pois elas me forneceram suporte técnico-científico para chegar até aqui.

Aos amigos do LMP-UFSC: Santi, Gutjahr, Manoel, Bordin, Carol, Gabi, Sarah, Adriano, Mineiro, João Barba, Volpato, Erick, Claudinho, Panziera, Calil, Gabriel Pilon, Knoblauch, Chico, Delgado. Vários outros nomes caberiam aqui. Vocês surgiram na minha vida a partir de 2017 e me apoiaram, cada um em sua forma. Obrigado pessoal!

A minha jornada profissional começou em 2010, no SENAI-Parauapebas. Foi lá, no curso de mecânica industrial e no período seguinte de menor aprendiz, que eu decidi cursar Engenharia Mecânica. Hoje, é uma alegria trabalhar numa instituição pertencente a rede SENAI. Aos Amigos do ISI-LASER, ISI-MANUFATURA e LATECME, que formam o ISI-Joinville. Ao longo destes anos, eu convivi com muita gente. Muito obrigado a cada um! Eu vou me conter a citar alguns nomes, daqueles que me acompanharam de perto ao longo desta

jornada: Su Fenrich, Gutjahr, Chico, Santi, Henrique Santos, Henrique Oliveira, Anselmo, Prass, Ju Cruz, Camila, Bianca, Marcos Bento, Nanda, Val Luz, Vera, Thamiris, Ana Duarte, Gabi, Belle. Destes, vários outros amigos surgiram, na forma de ex-colegas de trabalho, familiares de amigos e afins. Gostaria de agradecer em especial a Ana Maciel, Bruna Hartmann, Ana Correa, Vall Gomes, Bibow, Bea, Dani, Thiago, Michelle, Lilian, Leandro, Alex, Ana Harada, Carol Pilon, Ana Menezes e ao meu sobrinho de coração Estêvão (Homem-Aranha).

Aos amigos do Pará e da UFPA, pelos anos juntos: Vanêssa, Misley, Vinicius, Karina, Edinaldo, Dru, Dany, Amanda, Lorena, Henri, Pablo e Taci. Aos membros do "Gamlerinha". Aos Professores Paulo Machado, Douglas, Wassim, Jessé e Pedro Paulo.

Gostaria de agradecer aos meus Livros, Filmes, Séries e Músicas. Vocês sempre estiveram comigo, me distraindo, ensinando, alegrando e emocionando. Vocês foram a minha terapia, me ajudando na comemoração de momentos alegres e felizes e me apoiando na travessia de horas difíceis e tristes. Café, muito obrigado. Você é um grande parceiro.

O doutorado é uma jornada intensa, composta por múltiplas horas dedicadas a disciplinas, pesquisa, leitura, experimentos, análises, escrita, revisões, reescrita. É um trabalho muitas vezes lento, solitário e pesado, mas muito nobre e recompensador.

Gostaria de descrever brevemente o maior aprendizado que eu tive durante o doutorado: não é possível concluí-lo sozinho! Diversas pessoas me ajudaram ao longo do caminho. Foram muitas coisas e etapas envolvidas. Sem as pessoas certas para me apoiar, eu teria ficado estagnado em algum ponto do caminho. É a célebre frase: "o que importa é a jornada." Eu a complemento com "e as pessoas que te acompanham nela." O resto é acessório.

Em dedicatória a todas estas pessoas, eu deixo o trecho de uma música espetacular, e a frase que eu tenho tentado levar para a minha vida:

"*Close your eyes, and just hear me sing, one last long goodbye, one last song before you spread your wings. There is so much left to say, and before this moment slips away, what a wonderful life, for as long as you have been at my side, and I want you to know, I loved you so. Then the cold night calls, and the tears fall like rain, it is so hard letting go, of the one thing I will never replace, and soon you will be gone, but these words, they will live on. What a wonderful life my friend* (*Wonderful Life - Alter Bridge*)."

"Não é que tenhamos que viver constantemente em função de ganhar o céu e evitar o inferno, mas que cada ato nosso seja, sem demagogia, o céu para o outro e nada mais. Isso é viver realmente e consequentemente (*Guilherme de Sá*)." Agradeço profundamente a todos aqueles que foram um céu para mim, e espero que eu também possa ter sido um céu para vocês.

“Entre a engenhosidade e a habilidade analítica, existe uma diferença muito maior, de fato, do que aquela entre a fantasia e a imaginação, mas de um caráter análogo. Na realidade, se descobrirá que os engenhosos são sempre fantasiosos, e os verdadeiramente imaginativos nunca deixam de ser analíticos”
Os Assassinatos da Rua Morgue - Edgar Allan Poe.

“O homem só é grande de joelhos,
mesmo o trigo se curva com o vento.”
Atheos - Guilherme de Sá.

“Quantas vezes eu quis, tão longe buscar o que nunca percebi,
por tantos lugares passei, mas afinal, você sempre esteve aqui.
Mesmo fraco, em pedaços, eu prefiro te dizer, obrigado por estar aqui,
ao teu lado, me refaço, eu prefiro ter você, obrigado por estar aqui.”
Obrigado por Estar Aqui - Rosa de Saron.

ABSTRACT

Owing to their properties, martensitic stainless steels (MSS) are applied in cutlery, mining, railways, and the oil & gas industry. Casting, wrought, and rolling processes are used to manufacture these components. However, additive manufacturing (AM) techniques are emerging, offering the possibility of manufacturing customized geometries, on-demand, exploring alloys of poor machinability/weldability, near-net shaping parts, and reducing logistical issues. Among the AM processes, laser directed energy deposition (AM L-DED) stands out, which brings advantages, combined with the laser light features, enabling the manufacture of components with high density and refined microstructure. However, MSSs have complex processability conferred by the brittle martensitic nature. L-DED fast thermal cycles are a troublesome factor. Cracks, chemical composition modification, brittle phase precipitation, and properties depletion can be generated. In this context, the MSS processing by AM L-DED is still poorly explored in the literature. However, with an adequate route of L-DED parametrization, manufacturing, and post heat-treatment (PHT), it may be possible to find conditions that allow obtaining AM L-DED MSS components free from defects, with mechanical properties, tribological performance, and corrosion resistance compatible with this steel grade when processed by conventional techniques. Moreover, low C-content MSS can be a useful substitute since they provide a property set comparable to higher C-content MSS and are easier to process. In this context, the present doctoral thesis aims to investigate a full processing route of the low C-content (0.01 wt.%) AISI 410L MSS by AM L-DED. To achieve this, parameter windows of the process, and a post heat-treatment route were searched to ensure the obtention of multilayer parts with aspects aligned and/or superior to the high C-content AISI 410 (0.15 wt.%), obtained from traditional wrought and hot-rolled processes. First, a design of experiments (DoE) was employed, based on stages of single beads, single layers, and multilayer cubes, to identify the main L-DED parameter windows (spot size, powder feedrate, laser power, travel speed, hatch spacing, and layer height), aiming to meet the established acceptance criteria in two L-DED parameterizations, named production (PRO) and resolution (RES). The first is intended for greater deposition rates and manufacturing bulkier parts, while the second is dedicated to lower deposition rates, more complex, and thinner components. Results from these stages were analyzed in terms of defects absence, geometry, density, microstructure, hardness, mechanical strength, Charpy impact toughness, dry-sliding linearly reciprocating ball-on-flat tribological test, and electrochemical corrosion by the potentiodynamic polarization method. Four PHT routes were applied to a set of samples manufactured with the optimized parameters from PRO DoE. The PHT route that showed the most significant influence on the microstructure and mechanical properties of hardness, tensile strength, and Charpy impact of the as-built (AB) condition was employed to heat-treat half of the samples. Thus, the performance of samples manufactured with two L-DED parameters (PRO and RES), and two states (AB and PHT), was benchmarked to the reference material (as-received substrate, SUB-AR). The results suggest the robustness of both optimized L-DED parameters, as the samples were free of deleterious defects and exhibited high density. The microstructure was formed by a ferritic matrix with martensite laths concentrated at the grain boundaries, due to the laser fast cooling, and the low C-content of AISI 410L. The more refined microstructure of the RES parameter provided higher hardness, mechanical strength, tribological performance, and corrosion resistance. PHT proved essential only when higher toughness is required.

Keywords: Martensitic stainless steels. Low C-content AISI 410L. Additive manufacturing. Laser directed energy deposition. Thermal history.

RESUMO

Devido às suas propriedades, os aços inoxidáveis martensíticos (AIM) são aplicados nas indústrias de cutelaria, mineração, ferroviária e óleo & gás. Processos de fundição, conformação e laminação são usados para fabricar estes componentes. No entanto, a manufatura aditiva (MA) vem permitindo fabricar geometrias customizadas, sob demanda, explorar ligas de difícil usinabilidade/soldabilidade, fabricar peças quase acabadas e reduzir problemas logísticos. Entre os processos de MA, a deposição de energia direcionada a laser (DED-L) traz estas vantagens aliadas às características da radiação laser, permitindo a fabricação de componentes de alta densidade e microestrutura refinada. No entanto, estes aços possuem processabilidade complexa devido à natureza frágil da martensita. Os ciclos térmicos rápidos do DED-L são um agravante. Pode ocorrer nucleação de trincas, modificação na composição química, precipitação de fases frágeis, e perda de desempenho. Nesse contexto, os AIM ainda são pouco processados por MA DED-L. Entretanto, realizando uma parametrização adequada, e tomando os cuidados durante a fabricação e pós-tratamento térmico (TT), é factível a obtenção de componentes de AIM por MA DED-L livres de defeitos, com propriedades mecânicas, performance tribológica e resistência à corrosão compatíveis as técnicas convencionais. Os AIM de baixo teor de C podem ser uma alternativa, pois fornecem um conjunto de propriedades comparáveis aos de alto teor de C e possuem processabilidade mais simples. Nesse contexto, a presente tese de doutorado investiga uma rota completa de processamento do AIM de baixo teor de C (0,01 % em peso) AISI 410L por MA DED-L. Foram experimentadas janelas de parâmetros e rotas de tratamento térmico para garantir peças multicamadas com propriedades compatíveis ao AISI 410 de maior teor de C (0,15 % em peso) obtido a partir de processos tradicionais de conformação e laminação a quente. Foi empregado um planejamento de experimentos, baseado em etapas de cordões simples, camadas simples e cubos multicamadas, para identificar as principais janelas de parâmetros DED-L (diâmetro de feixe, taxa de alimentação de pó, potência do laser, velocidade de varredura, sobreposição entre cordões, e sobreposição entre camadas), visando atender aos critérios de aceitação estabelecidos em duas parametrizações, identificadas como produção (PRO) e resolução (RES). A primeira é destinada a taxas de deposição maiores e peças mais simples e volumosas, enquanto a segunda é dedicada a taxas de deposição menores e componentes de geometrias mais complexas. Os resultados foram analisados em termos de ausência de defeitos, geometria, densidade, microestrutura, dureza, resistência mecânica, tenacidade ao impacto Charpy, ensaio tribológico linear reciprocante de esfera sobre plano com deslizamento em meio seco e corrosão eletroquímica por polarização potenciodinâmica. Foram avaliadas quatro rotas de TT em um conjunto de amostras MA DED-L fabricadas com os parâmetros otimizados de PRO. O tratamento térmico que exerceu maior influência na microestrutura, dureza, resistência à tração e tenacidade ao impacto Charpy da condição como fabricada (CF), foi usado para tratar termicamente metade das amostras. Assim, o desempenho das amostras fabricadas com as duas parametrizações (PRO e RES) e dois estados (CF e TT) foi comparado ao material de referência (substrato como-recebido, SUB-CR). Os resultados sugerem a robustez de ambos os parâmetros DED-L otimizados, pois as amostras ficaram livres de defeitos e exibiram alta densidade. A microestrutura foi formada por matriz ferrítica com martensita na forma de ripas concentradas nos contornos de grão, devido ao resfriamento rápido imposto pelo processamento a laser e ao baixo teor de C do AISI 410L. A microestrutura mais refinada do parâmetro de RES lhe proporcionou maior dureza, performance mecânica, tribológica e à corrosão. O tratamento térmico se mostrou essencial apenas quando é requerida maior tenacidade.

Palavras-chave: Aços inoxidáveis martensíticos. Baixo teor de C. Manufatura aditiva. Deposição de energia direcionada a laser. Histórico térmico.

RESUMO EXPANDIDO

Introdução:

A indústria de fabricação e reparo de componentes metálicos sempre apresenta desafios, trazendo à luz a necessidade de novos materiais e processos, que atendam aos critérios de aceitação de importantes setores econômicos, em termos de propriedades mecânicas, performance tribológica e resistência à corrosão. Os aços inoxidáveis martensíticos são ligas a base de Fe-Cr-C intensamente utilizadas nas indústrias agrícola, ferramentaria, ferroviária, mineração e óleo e gás, devido à sua elevada dureza, resistência mecânica, tribológica e à corrosão em temperaturas moderadas de operação (~20-450 °C). As técnicas de manufatura aditiva metálica vêm sendo incorporadas a estes setores, possibilitando a fabricação de geometrias customizadas, sob demanda, processabilidade de materiais de difícil soldabilidade/usinabilidade. A deposição de energia direcionada a laser se destaca por agregar estas possibilidades, além de ser aplicável a processos de fabricação, revestimento e reparo. Dessa forma, processar componentes de AIM por DED-L pode gerar melhorias nas características do material e processo, representando uma alternativa interessante. Entretanto, existem desafios quanto à processabilidade complexa do AIM e ao histórico térmico do DED-L. Do ponto de vista do material, uma das principais preocupações é a natureza frágil da martensita, que pode reduzir a ductilidade e tenacidade. Pelo lado do processo, os ciclos rápidos de aquecimento/resfriamento podem resultar em alteração de composição química localizada, tensões residuais, segregação e anisotropia. Os AIM de menores teores de C oferecem um conjunto de propriedades compatível, além de uma processabilidade mais simples em comparação com os AIM mais ricos em C. Neste contexto, o presente trabalho se propõe a investigar a processabilidade do AIM AISI 410L (0,01 % de C em peso) por MA DED-L. Em vista dos desafios apresentados e da literatura escassa, será executado um estudo completo de parametrização DED-L, varrendo todas as etapas do planejamento de experimentos. Como a indústria moderna se baseia na fabricação modular, duas parametrizações são almejadas, uma visando maior produção (PRO, maior taxa de deposição) e uma para maior resolução (RES, menor taxa de deposição). Além da otimização, serão estudadas rotas de tratamento térmico compostas por etapas de recozimento, têmpera e revenimento. Com os parâmetros e a rota de TT definidos, amostras MA DED-L multicamadas serão obtidas, preparadas e avaliadas quanto a microestrutura, propriedades mecânicas (dureza, resistência à tração e tenacidade ao impacto Charpy), performance tribológica (ensaio de deslizamento reciprocante de esfera sobre plano em meio seco) e resistência à corrosão (polarização potenciodinâmica em solução salina de NaCl 3,5 % em peso). A ideia é comparar a diferença de performance entre os parâmetros no estado como fabricado (PRO-CF e RES-CF), como TT (PRO-TT e RES-TT) e um material comercial referência (AIM AISI 410 com 0,15 % de C em peso). Como novidade científica, esta Tese contribuirá agregando conhecimento sobre os mecanismos atuantes na formação de microestrutura do AISI 410L processado por DED-L, a influência dos diferentes parâmetros (PRO and RES) e estado do material (CF e TT) sobre as respostas mecânicas, com foco na tenacidade por impacto Charpy, sobre a performance tribológica, abordando as condições de contato no tribossistema formado e sobre a resistência à corrosão, entendendo quais são os mecanismos atuantes sobre as diferentes condições. Como contribuição tecnológica, o usuário poderá escolher quais as condições de processamento e/ou pós-tratamento térmico empregar, em função dos requisitos da sua aplicação final.

Objetivos:

O objetivo principal deste trabalho é determinar uma rota de fabricação para o AIM AISI 410L a partir do processo de manufatura aditiva por deposição de energia direcionada a laser, visando obter componentes livres de defeitos e com características apropriadas de densidade, geometria,

microestrutura, propriedades mecânicas, desempenho tribológico e resistência à corrosão. De forma específica: I - definir parâmetros MA DED-L otimizados para produzir componentes multicamadas de AIM AISI 410L; II - estabelecer as relações entre os diferentes parâmetros (PRO e RES) e as respostas de densidade, geometria, microestrutura, propriedades mecânicas, desempenho tribológico e resistência à corrosão; III - entender a influência dos diferentes aspectos da microestrutura MA DED-L sobre as propriedades mecânicas, desempenho tribológico e resistência à corrosão; IV - definir uma rota de TT para proporcionar alívio de tensões, homogeneizar a microestrutura e melhorar as propriedades mecânicas, desempenho tribológico e resistência à corrosão em relação à condição CF; V - estabelecer as ligações entre o histórico térmico MA DED-L e o TT e as respostas de microestrutura e propriedades do AIM AISI 410L de baixo teor de carbono quando comparadas a um AIM comercial de maior teor de carbono.

Materiais e métodos:

Esta seção da tese foi dividida em procedimentos experimentais e materiais necessários. Na primeira, foi realizado um estudo para otimizar os principais parâmetros DED-L para processar o pó de AISI 410L AIM de 53-150 μm (diâmetro do feixe laser, taxa de alimentação de pó, potência do feixe laser, velocidade de varredura, sobreposição entre cordões e sobreposição entre camadas). Para isto, foram executadas etapas de deposição no sistema DED-L RPMI 535, usinagem e análises quantitativas de propriedades geométricas em cordões simples, camadas simples e blocos multicamadas. Em cada etapa, reduziu-se o número de parâmetros variáveis, até chegar a uma combinação ideal, baseada nos critérios de aceitação impostos. Os cordões simples foram analisados apenas nas superfícies, empregando estereoscópio ótico (EO). Os dados gerados serviram para limitar as janelas de parâmetros. As camadas simples foram avaliadas na seção transversal com o auxílio do EO e do software Image J. Os dados foram avaliados em funções de parâmetros definidos de regressão e desejabilidade, implementados no software Python®. Ao final, uma verificação experimental foi realizada. Na etapa de blocos multicamadas, foram investigados diferentes níveis de sobreposição entre camadas. Estas foram analisadas em termos de densidade em balança de Arquimedes e quantificação de porosidades por microscopia ótica (MO). Com todos os parâmetros DED-L selecionados, foram fabricadas amostras multicamadas destinadas à análise de microestrutura por MO, microscópio eletrônico de varredura e espectroscópio de energia dispersiva (MEV-EDS), difratômetro de raios-X (DRX) e dureza Vickers. Com os dois parâmetros DED-L otimizados (PRO e RES), foram fabricadas amostras destinadas aos ensaios de tração e impacto Charpy, nas orientações horizontal e vertical em relação ao substrato. Estas foram usinadas e ensaiadas de acordo com os padrões das normas ASTM. Também foram fabricadas amostras multicamadas destinadas ao ensaio tribológico de deslizamento reciprocante de esfera sobre plano em meio seco, e ao ensaio de corrosão eletroquímica por polarização potenciodinâmica, ambos seguindo normas ASTM vigentes. Os resultados mecânicos foram avaliados em termos de limite de escoamento, tensão de resistência máxima, alongamento, energia absorvida ao impacto Charpy e aspectos das fraturas por MEV. Do ensaio tribológico, analisou-se o coeficiente de atrito, coeficiente de desgaste e os mecanismos atuantes nas superfícies por MEV. No ensaio de corrosão, analisou-se o potencial de corrosão, corrente de corrosão, resistência à polarização e mecanismos atuantes via MEV. Nas etapas de microestrutura, dureza e resistência mecânica, foi fabricado um conjunto de amostras multicamadas destinadas a um estudo de TT, no qual três rotas foram caracterizadas. A melhor rota definida nesta etapa foi aplicada às amostras das demais caracterizações, tendo o seu desempenho comparado às condições CF. Com as mesmas especificações das amostras DED-L, foram usinadas amostras de um substrato comercial como recebido (SUB-CR, AISI 410 com maior teor de C em relação ao AISI 410L), que foram submetidas às mesmas caracterizações das amostras DED-L e serviram como referência.

Resultados e discussões:

Em relação ao planejamento de experimentos, a etapa de cordões simples delimitou os parâmetros de taxa de alimentação de pó, potência do laser e velocidade de varredura para PRO e RES. Foram identificadas janelas processáveis mais largas para as maiores taxas de alimentação, aliadas a menores velocidades de varredura e potências intermediárias. Nas camadas simples, as superfícies não revelaram defeitos. A avaliação geométrica das seções transversais quanto à altura média de pico, diluição, ondulação relativa, inclinação e eficiência de deposição permitiu, através de funções de regressão e desejabilidade, encontrar um conjunto de parâmetros DED-L que entregassem camadas simples dentro dos critérios de aceitação. Sobreposições laterais intermediárias geraram melhores resultados. A microestrutura das camadas simples foi formada por matriz ferrítica com martensita na forma de ripas refinadas, devido ao resfriamento rápido imposto pelo processamento a laser e à migração de carbono do substrato. A dureza exibiu média compatível com a literatura, com um pico na transição diluição/zona afetada pelo calor, devido à martensita mais refinada, estabelecida pela extração de calor por condução para o substrato. Nas multicamadas, encontrou-se densidade de 99,9 % para os parâmetros PRO e RES. Os únicos defeitos foram porosidades arredondadas, advindas do aprisionamento de bolhas de gás. Para ambos os parâmetros, não se observaram variações de composição química. A microestrutura mostrou matriz ferrítica com martensita refinada na forma de ripas concentradas nos contornos de grãos. Este aspecto foi atribuído ao baixo teor de carbono do AISI 410L e ao resfriamento rápido imposto pelo processamento a laser. A condição RES-CF gerou grãos mais refinados com uma maior área de contornos com martensita, o que lhe conferiu dureza superior à PRO-CF. Comportamento similar foi observado para as amostras fabricadas na orientação horizontal em relação ao substrato quando comparadas às amostras fabricadas na vertical. Nas primeiras, a maior área de contato camada/substrato facilitou a extração de calor por condução para o substrato, resultando em uma microestrutura mais refinada. A difratometria de raios-X revelou picos comuns em ambas as condições, com maior intensidade da fase martensita de estrutura tetragonal de corpo centrado (TCC) para a RES-CF. O TT de austenitização mais têmpera (AT) homogeneizou a microestrutura, dissolvendo a martensita na forma de ripas para martensita na forma de pacotes em meio à matriz ferrítica. A dureza se manteve similar à da condição CF. Diferentes rotas de austenitização mais têmpera e revenimento (ATR) foram investigadas, e apenas a realizada na temperatura mais elevada (600 °C, ATR600) proveu crescimento de grãos efetivo, o que reduziu a dureza significativamente. O DRX revelou as mesmas fases, porém, com resquícios de martensita TCC para a RES-AQT600. O substrato como recebido exibiu microestrutura homogênea formada por grãos grosseiros de ferrita e martensita revenida. Além disso, foram identificados carbetos de Cr ($Cr_{23}C_6$) e cementita. A dureza deste foi significativamente inferior à de todas as condições DED-L. Avaliando os resultados mecânicos, para as amostras CF, no ensaio de tração, o limite de escoamento (LE) e tensão de resistência máxima (TRM) foram favorecidos pela microestrutura mais refinada provida pelos parâmetros de RES e orientação de fabricação horizontal (Hor). Entretanto, o alongamento (AL) e a energia absorvida (EA) no ensaio de impacto Charpy foram inferiores nas amostras de PRO e na orientação Vertical (Ver). As condições AT e ATR nas menores temperaturas (300 e 450 °C, ATR300 e ATR450) elevaram o limite de escoamento e a tensão de resistência máxima, enquanto o AL e a EA se mantiveram similares às condições CF. Isto se deve à microestrutura ainda refinada, heterogênea e tensionada, sob influência do histórico térmico do L-DED e da etapa de têmpera. Apenas a condição ATR600 proveu revenimento efetivo da martensita, distribuindo os grãos homogeneamente na matriz ferrítica. Como resultado, o limite de escoamento e o TRM foram reduzidos, ao passo que o alongamento e a energia absorvida aumentaram significativamente. As amostras TT fabricadas com os parâmetros de RES e na orientação Hor demonstraram maior LE e tensão de resistência máxima, e menor alongamento e energia absorvida, o que pode ser

atribuído ao histórico térmico destas. O SUB-CR exibiu limite de escoamento similar e maiores níveis de TRM, AL e EA em comparação às condições como fabricada, em função da sua microestrutura mais próxima à condição PRO-ATR600. As análises de fraturas por MEV demonstraram aspecto frágil com planos de clivagem e fratura intergranular nas condições CF, AT, ATR300 e ATR450. Alvéolos característicos de fraturas dúcteis foram observados apenas nas amostras ATR600. Os resultados do ensaio tribológico reciprocante de esfera sobre plano em meio seco revelaram melhor performance da condição RES-CF. Nesta, além da maior dureza, a maior quantidade de martensita concentrada nos contornos de grãos propiciou ancoramento às tribocamadas óxidas. Estas últimas também ficaram mais compactas em relação às demais condições, o que estabilizou o Coeficiente de Atrito (CA) e reduziu a intensidade da adesão e abrasão, resultando em menor coeficiente de desgaste (k). O TT prejudicou a resistência ao desgaste, devido à redução da dureza e de áreas de ancoramento para as tribocamadas, que exibiram aspecto menos compacto. Além de não fornecerem lubrificação, estas últimas foram removidas durante o ensaio na forma de interfaces adesivas. Além disso, a quantidade superior de debris livres nas superfícies intensificou a abrasão, o que elevou o k. O SUB-AR exibiu tribocamadas menos compactas recobrindo boa parte das superfícies. Estas se ancoraram de forma mais efetiva em comparação às amostras TT, o que se deve aos carbetos de $Cr_{23}C_6$. A menor dureza e a menor parcela de tribocamadas compactas justificam a performance inferior destas em relação às condições DED-L CF. Avaliando os resultados de corrosão eletroquímica em solução salina de 3,5 % de cloreto de sódio (NaCl), a condição RES-CF exibiu potencial de corrosão (E_{corr}) mais positivo, menor corrente de corrosão (I_{corr}) e maior resistência de polarização (R_p). A melhor performance da RES-CF foi atribuída à sua microestrutura mais refinada, que entregou uma maior energia de superfície e suporte para a camada passiva de óxido de Cr (Cr_2O_3). Apesar da maior quantidade de martensita nos contornos de grãos, que é uma fase mais suscetível à corrosão, a maior captura de C de solução sólida da matriz de Fe reduziu a corrosão nas regiões ferríticas e a sensitização na RES-CF. Efeito contrário foi encontrado na condição PRO-CF, de modo que a microestrutura mais grosseira e com porosidades maiores desta facilitaram a formação de pites. Além disso, assumindo a presença de carbetos de Cr na PRO-CF, o material pode ter sofrido sensitização. O tratamento térmico tornou a microestrutura mais grosseira e menos adequada para suportar a camada passiva. Assim, a corrosão foi mais intensa nestas quando comparadas às amostras CF. Entretanto, todas as condições DED-L superaram o SUB-CR. Devido à martensita uniformemente distribuída, o SUB-CR foi atingido pelo mecanismo de corrosão uniforme. Além disso, os carbetos de Cr geraram sensitização acentuada.

Considerações finais:

Esta tese investigou o AIM de baixo teor de C AISI 410L processado por DED-L em diferentes parametrizações (PRO e RES) e condições (CF e TT). Empregando parâmetros otimizados e a rota de TT definida, foram fabricadas amostras multicamadas para análises de microestrutura, resistência mecânica, tribológica e à corrosão. Os resultados indicaram melhor performance para a condição RES-CF, em termos de refino de grãos, dureza, LE, TRM, CA, E_{corr}, I_{corr} e R_p. Os parâmetros de PRO e a aplicação do tratamento térmico foram vantajosos em termos de AL e EA ao impacto Charpy. Todas as condições DED-L exibiram desempenho igual ou superior ao SUB-CR em praticamente todas as propriedades avaliadas.

Palavras-chave: Aços inoxidáveis martensíticos. Baixo teor de C. Manufatura aditiva. Deposição de energia direcionada a laser. Histórico térmico.

LIST OF ABREVIATIONS AND ACRONYMS

A	Deposited Area
AB	As-Built
AE	Absorbed Energy
AIM	Aços Inoxidáveis Martensíticos
AISI	American Iron and Steel Institute
AL	Alongamento
AM	Additive Manufacturing
AR	Aeration Ratio
ASTM	American Society for Testing and Materials
AT	Austenitização e Têmpera
ATR	Austenitização, Têmpera e Revenimento
B	Molten Area
BCC	Body-Centered Cubic
BCT	Body-Centered Tetragonal
BFE	Basic Flowability Energy
BPP	Beam Parameter Product
CA	Coeficiente de Atrito
CAD	Computer-Aided Design
CAM	Computer-Aided Manufacturing
CE	Counter Electrode
CF	Como Fabricado
COF	Friction Coefficient
DED-L	Deposição de Energia Direcionada a Laser
DIC	Digital Image Correlation
DoE	Design of Experiments
DRX	Difratômetro de Raios-X
EA	Energia Absorvida
EBSD	Electron Backscatter Diffraction
ECA	Equivalent Circular Area
EDS	Espectroscopia de Energia Dispersiva
EL	Elongation
EO	Estereoscópio Ótico
F	Powder Feedrate
FCC	Face-Centered Cubic
FEG	Field Emission Gun
FRI	Flow Rate Index
G	Thermal Gradient
GDP	Gross Domestic Product
HAZ	Heat-Affected Zone
HIP	Hot Isostatic Pressing
HS	Hatch Spacing
ISO	International Organization for Standardization

L-DED	Laser Directed Energy Deposition
LE	Limite de Escoamento
LH	Layer Height
L-PBF	Laser Powder Bed Fusion
MA	Manufatura Aditiva
MEV	Microscópio Eletrônico de Varredura
MG	Multilayer Geometry
MO	Microscópio Ótico
MSS	Martensitic Stainless Steel
OCP	Open Circuit Potential
O&G	Oil and Gas
OES	Optical Emission Spectroscopy
OM	Optical Microscope
OS	Optical Stereoscope
P	Laser Power
PCD	Passive Current Density
PH	Precipitation Hardening
PHT	Post Heat-Treatment
PRO	Production
R	Solidification Ratio
RES	Resolution
S	Travel Speed
SB	Single Bead
SCE	Saturated Calomel Electrode
SE	Specific Energy
SEM	Scanning Electron Microscope
SI	Stability Index
SL	Single Layer
SS	Stainless Steel
SUB-AR	Substrate As-Received
SUB-CR	Substrato Como Recebido
S+VFR	Stability and Variation Flow Rate
TCC	Tetragonal de Corpo Centrado
TEM	Transmission Electron Microscope
TRM	Tensão de Resistência Máxima
TT	Tratamento Térmico
TTT	Time-Temperature-Transformation
UTS	Ultimate Tensile Strength
YS	Yield Strength
WE	Work Electrode
XRD	X-Ray Diffractometer

LIST OF SYMBOLS

A_1	Lower transformation temperature	I_p	Passive corrosion current
A_3	upper transformation temperature	D_{SB}	Single bead dilution
k	Wear coefficient	D_{SL}	Single layer dilution
E_{corr}	Corrosion potential	η_{SB}	Single bead efficiency
I_{corr}	Corrosion current	η_{SL}	Single layer efficiency
R_p	Polarization resistance	h	Height
M_s	Martensitic start temperature	α	Ferrite
T_0	Initial temperature	δ	Delta ferrite
Q1, Q3	Quartile 1 and 3	γ	Austenite
G_M	Free chemical energy of the martensite	σ	Sigma phase
G_γ	Free chemical energy of the austenite	E_{break}	Breakdown potential
E_b^c	Non-chemical energy barrier	I_{break}	Breakdown current
ΔT_c	Critical undercooling	ʎ	Wavelength
E_b	Total barrier energy	M^2	Laser beam quality
ΔW_{def}	Plastic deformation variation	TEM_{00}	Theoretical mode
w	Width	H_2S	Hydrogen sulfide
χ	Chi phase	F_L	Frictional load
Ø	Spot size	N_L	Normal load
Θ	Wettability angle	SiO_2	Silicon-oxide
ρ	Powder density	Si_3N_4	Silicon-nitride
$\bar{h}$	Average peak height	E_{break}	Breakdown potential
Δh	Defect sensitivity	I_{break}	Breakdown current
$\Delta h'$	Waviness	P_1, P_2, P_3	Peaks 1, 2, and 3
$h_{Equiv.A}$	Height equivalent area	V_1, V_2, V_3	Valleys 1, 2, and 3
Θ	Slope	Q	Volume loss
C_G	Carrier gas	l	Wear track length
S_G	Shielding gas	k	Wear coefficient
F_{laser}	Laser beam focus distance	A	Wear track area
D_{laser}	Laser beam defocusing distance	SD	Sliding distance
$Ø_{laser}$	Incident laser beam diameter	D_n	Powder diameter (number)
A_{laser}	Incident laser beam area	D_v	Powder diameter (volume)
E_p	Electrode polarization	F_{powder}	Powder focus distance
I_{cc}	Critical corrosion current	$Ø_{powder}$	Powder focus diameter
Fe^{2+}	Fe-ion	e^-	Electron
OH^-	Hydroxide	E_{app}	Applied potential
D	Dilution	F	Powder feedrate
A	Deposited area	B	Molten area
S	Travel speed	$\bar{V}$	Average of last 3 SL valleys

CONTENTS

1 INTRODUCTION 21
1.1 CONTEXTUALIZATION 21
1.2 MOTIVATION 24
1.3 OBJECTIVES 25
1.3.1 General objective 25
1.3.2 Specific objectives 25
1.4 THESIS STRUCTURE 26
2 SCIENTIFIC BACKGROUND 27
2.1 STAINLESS STEEL CONCEPTS 27
2.2 MARTENSITIC STAINLESS STEEL (MSS) 27
2.2.1 Definition 27
2.2.2 Alloying elements in MSS 28
2.2.3 Phase diagrams 29
2.2.3.1 Binary Fe-Cr system phase diagram 29
2.2.3.2 Ternary Fe-Cr-C system phase diagram 31
2.3 MARTENSITIC STAINLESS STEEL PROCESSING 32
2.3.1 MSS microstructure phases 32
2.3.2 Martensitic transformation and post heat-treatment applied to MSS 32
2.4 METAL ADDITIVE MANUFACTURING 37
2.4.1 Contextualization 37
2.4.2 AM L-DED process 37
2.4.2.1 AM L-DED overview 37
2.4.2.2 AM L-DED setup 38
2.4.2.3 AM L-DED parameters 39
2.4.2.4 General features of AM L-DED parts 41
2.4.2.5 Production vs. resolution 43
2.4.2.6 AM L-DED design of experiments 44
2.5 TRIBOLOGICAL PERFORMANCE 46
2.5.1 Tribology concepts 46
2.5.2 Wear mechanisms 46
2.5.3 Wear prevention 49
2.5.4 Tribological tests 49
2.6 CORROSION RESISTANCE 50
2.6.1 Corrosion concepts 50
2.6.2 Corrosion mechanisms 51
2.6.3 Corrosion assessment techniques 53

2.6.4 Corrosion prevention 54
2.7 MARTENSITIC STAINLESS STEEL MANUFACTURED BY AM L-DED 55
2.7.1 Microstructure 55
2.7.2 Mechanical performance 60
2.7.2.1 Hardness 61
2.7.2.2 Tensile strength 62
2.7.2.3 Impact toughness 65
2.7.3 Tribological performance 66
2.7.4 Corrosion resistance 68
2.7.5 Post heat treatment applied to MSS processed via AM L-DED 69
2.7.5.1 PHT effects on the microstructure 69
2.7.5.2 PHT effects on the hardness 71
2.7.5.3 PHT effects on the tensile strength 72
2.7.5.4 PHT effects on the impact toughness 73
2.7.5.5 PHT effects on the tribological performance 74
2.7.5.6 PHT effects on corrosion resistance 75
3 SCIENTIFIC CONTRIBUTION 77
4 EXPERIMENTAL PROCEDURES 79
4.1 STAGE 1: EXPLORATORY 79
4.2 STAGE 2: MODELING 83
4.3 STAGE 3: OPTIMIZATION 85
4.4 STAGE 4: MULTILAYER GEOMETRY CUBES 85
4.5 CHARACTERIZATION TESTS 86
4.5.1 Microstructure assessment 86
4.5.2 Mechanical behavior 87
4.5.3 Tribological performance 90
4.5.4 Corrosion resistance 91
5 MATERIALS AND EQUIPMENT 92
5.1 SUBSTRATES 92
5.2 AISI 410L MSS POWDER 93
5.3 L-DED SYSTEM 95
5.4 CHARACTERIZATIONS 97
6 RESULTS AND DISCUSSION 100
6.1 SINGLE BEADS (SB) 100
6.1.1 Operational process window 100
6.1.2 Stable set of parameters 101
6.2 SINGLE LAYERS (SL) 105
6.2.1 Geometry evaluation 105

6.2.2 Modeling and experimental verification 106
6.2.3 Single layer microstructure and hardness characterization 108
6.3 MULTILAYER GEOMETRY (MG) 110
6.3.1 Density analysis 110
6.3.2 Chemical composition of as-built samples by Spark-OES 111
6.4 MICROSTRUCTURE AND HARDNESS CHARACTERIZATION 112
6.4.1 Effects of the L-DED parameters 112
6.4.2 Effects of the building orientation 116
6.4.3 Effects of the post heat-treatment 117
6.5 MECHANICAL PROPERTIES 121
6.5.1 Effects of the as-built condition and building orientation on tensile strength and impact toughness 121
6.5.2 Effects of the post heat-treatment and building orientation on tensile strength and impact toughness 125
6.6 TRIBOLOGICAL PERFORMANCE 130
6.6.1 Effects of L-DED parameters and PHT on tribological performance 130
6.6.2 Wear track analysis 133
6.7 CORROSION RESISTANCE 139
6.7.1 Effects of L-DED parameters on corrosion resistance 139
6.7.2 Effects of PHT on corrosion resistance 144
7 RESEARCH ACCOMPLISHMENTS 148
7.1 CONCLUSIONS 148
7.2 RECOMMENDATIONS FOR FUTURE WORK 151
7.3 LIST OF PUBLICATIONS 152
REFERENCES 154

1 INTRODUCTION

This section presents the general work context, highlighting its fundamental aspects and indicating the motivations and justifications for its accomplishment.

1.1 CONTEXTUALIZATION

Stainless steels (SS) are a steel class with notorious industrial applicability. Martensitic stainless steels (MSS) are found within this family, which possess high hardness, mechanical strength, resistance to wear, and corrosion at milder temperatures (~20-450 °C). MSSs are applied in power transmission system gears, aircraft landing gear, bearings, magnetic separators, turbine blades, petrochemical equipment, punches and dies, cutlery, plastic molds, high-pressure pipes, heat exchanges, exhaust systems, pumps, and valve parts [1]–[5]. Due to their easier processability and comparable properties to Carbon-richer MSS, low C-content MSS have been employed in several sectors, such as oil and gas, tooling, and railway [6], [7]. Currently, casting, wrought, and rolling, followed by finishing machining processes, produce many of these parts [8]. However, some challenges are still faced in the industry, such as obtaining customized geometries, the need to keep spare parts stock, and production stoppages for the deteriorated components replacement [2], [9]. In this sense, it is necessary to search for materials and manufacturing processes that contribute to mitigating these drawbacks.

The MSS property set, as previously highlighted, makes these materials an attractive option. As for the manufacturing process, Additive Manufacturing (AM) techniques can be an interesting alternative for these cases. In AM processes, components are built from a digital three-dimensional (3D) model, usually layer by layer, unlike other conventional subtractive and forming manufacturing techniques. AM provides the manufacture of single and/or complex geometries, eliminating punches and dies; manufacturing on-demand and in loco, mitigating the need to keep a spare parts stock, minimizing logistical issues; lead time reduction in maintenance stoppages; obtaining near net shaping components, reducing the post-machining efforts. In summary, these advantages can be translated into cost reduction [10], [11].

Laser technology is being integrated as a power source for metallic AM processes, available in two technologies: Laser Powder Bed Fusion (L-PBF) and Laser Directed Energy Deposition (L-DED). The first is a process in which thermal energy selectively melts regions

of a powder bed, forming the part structure [12]. It is suitable for more precise dimensions and surface finishing [8]. The latter, in turn, defined as a process in which focused thermal energy is used to melt materials as they are being deposited [13], has similar proposals to the L-PBF process, however, with higher productivity, translated by greater deposition rates and larger dimension tolerances in the built parts. L-DED is also available for repair processes [14].

L-DED brings advantages, meeting all the AM features, as mentioned above, added to aspects such as the possibility of obtaining a refined microstructure, low level of distortions, excellent heat input control, the possibility of processing a wide alloy range (in the powder or wire state), and work with functional gradient materials (employing different metallic powders) [15]. However, L-DED experiences high levels of thermal gradient (G) and solidification ratio (R), and multiple thermal cycles (heating-cooling). As a result, problems may occur concerning residual stresses [11], defects (porosities, cracks), anisotropy [11], [16], modifications in chemical composition, microstructure, wear performance, and corrosion resistance [8], [17], [18]. Furthermore, this is still a significant cost technology owing to the need for offline model evaluation, design modifications, scanning strategies development, raw material, pre, and post-processing operations [9], [19], [20].

In this context, considering the intrinsic MSS properties and the interest in this alloy by industry, allied with AM technology benefits, and L-DED technique features, the possibility of manufacturing MSS parts using the AM L-DED process turns up as an interesting alternative. Nonetheless, there are some challenges. Regarding the MSSs, despite their attractive property set, this SS grade is complex to process by techniques with fast thermal cycles, as is the L-DED case, which can compromise the microstructure, mechanical properties, wear performance, and corrosion resistance of the final component. Concerning the L-DED process, to reach the level of maturity to the point of being applied on an industrial scale, this process must be fully mastered by users. Then it is necessary to find process optimization tools that allow the manufacture of defect-free components, with adequate geometry, and properties [8], [21], [22].

To overcome these drawbacks, different approaches can be adopted. Generally, a design of experiments (DoE) of the AM L-DED process comprises three steps: single beads (SB, it is possible to vary all L-DED parameters at random to identify adequate bead section), single layers (SL, suitable hatch spacing is investigated to avoid lack or excess of overlap between SBs) and multilayer geometry (MG cubes, overlap between SLs is evaluated, aiming to mitigate lack of fusion, porosity, and to balance energy input layer after layer to ensure deposition uniformity from the first to the last layer) [5], [23].

In the AM L-DED context, it is necessary to assess application requirements, focusing on optimizing manufacturing. Thus, solutions need to be sought, aiming at higher production or resolution. Production (PRO) parameters refer to those dedicated to the manufacturing of larger and/or ordinary parts and, usually, less geometric precision (e.g., thick walls and massive parts). In this sense, higher deposition rates are needed, which can be translated into parameters of higher laser spot size, powder feedrate, and energy density. Parameters aiming at better resolution (RES) are required for the manufacturing of components with smaller dimensions and thinner geometries. Here, it is necessary to use narrower spot sizes, lower deposition rates, and energy density [24]–[26].

To mitigate defects and ensure build integrity, a few techniques are proposed. The most commonly used is the search for AM L-DED optimized parameters [5] through DoE approaches. Mathematical models aimed at predicting the deposited layer features are also found [27]. Along with manufacturing, there are other laser processes, that can affect the quality of the final component, such as laser remelting (e.g. surface finish enhancement [28], lack of fusion mitigation [29], surface properties improvement [30]–[33]), and laser power modulation techniques (e.g. porosity control [34], grains refinement [35], residual stress relief [36]).

Besides, in the AM L-DED chain, after component manufacturing, it is essential to carry out post-treatments. General post-treatments required for AM L-DED parts include powder removal (part assessment and verification), substrate removal (to release the part for all post-processes), machining (to match surface finishing, tolerances adjustment), and heat-treatments (stress relief PHT to provide residual stress relief, and properties improvement) [5], [16]. Hot Isostatic Pressing (HIP) can also be applied to reduce porosity [21].

In this work, the need to perform post-treatments is driven by two factors, which are the intrinsic features of AM L-DED parts and the metallurgical nature of MSS. This SS grade requires applying post heat-treatment (PHT) routes to correct the brittle nature of the martensite, ensuring the microstructure homogenization, and improving mechanical, tribological, and corrosion resistance. Regarding PHT, typically MSS undergoes austenitization, followed by quenching and tempering routes. Stress relief is performed below the austenitization temperature to decrease the stress concentration [37]. In austenitization, the material is heated above the critical temperature, allowing the phases to dissolve in the austenite (γ). With this, it is possible to eliminate the thermal history of previous processes. In quenching, the material is

cooled rapidly (in water, oil, or a salt bath) to obtain a martensitic microstructure. Tempering was performed after quenching, aiming to relieve residual stresses and correct the excessive hardness and brittleness of martensite [38]–[40].

1.2 MOTIVATION

The industry still faces challenges related to the costs of parts manufacturing and maintenance, due to the deterioration or failure of these components in operation. Some studies present surveys in this sense, correlating mechanical and tribological issues with financial and environmental losses [41]. The action of corrosion mechanisms also generates enormous direct (e.g., application, operation, and maintenance) and indirect (e.g., production stoppages, reduced efficiency and life span, environmental, and safety issues) costs. It is estimated that corrosion losses exceed 3% of the world´s Gross Domestic Product (GDP) [42]–[44].

As described in item 1.1, for components that require high hardness, elevated mechanical, tribological, and corrosion resistance at milder temperatures, MSSs are an interesting option. AM has been revolutionizing the industry, and the L-DED process employed as an AM tool has shown successful results. Besides the possibilities conferred by this material and manufacturing technique, this work is also motivated by the processing challenges related to the brittle MSS nature and the complex L-DED thermal history. The main concerns are the incomplete martensitic transformation, in which the two-phase microstructure (ferrite with martensite) deteriorates the mechanical, tribological, and corrosion properties; cracks nucleation due to the residual stresses and martensite's brittle nature; sensitization and poor impact toughness associated with martensite and formation of second-phase constituents at grain boundaries [3], [45], [46]. Concerning PHT routes applied to MSS, as expected, there seems to be no literature consensus regarding the tempering step, so the temperatures and times evaluated are quite dissimilar. For a given tempering condition, variations in microstructure, mechanical, tribological, and corrosion performance can occur [47]–[49].

In this context, to achieve the requirements imposed by industry (defect absence, geometry, microstructure, mechanical properties, tribological, and corrosion resistance), it is necessary to fulfill some steps: selection of L-DED parameters and conditions (pre-processing); monitoring and controlling during processing; performing heat-treatments (post-processing). Besides, it is important to remark on whether the AM system singularities and the specific part features are better suited to production or resolution AM L-DED conditions.

Systematic research in the databases (SCOPUS®, WEB OF SCIENCE®, ENGINEERING VILLAGE®, WILEY®, and GOOGLE SCHOLAR) was employed. For the AISI 410L MSS feedstock, 3 keywords were selected: ("410 Stainless Steel"), ("4?? Stainless Steel"), and ("Martensitic Stainless Steel"). For the L-DED process, 12 terms were selected: ("Laser Directed Energy Deposition"), ("Additive Manufacturing" AND "Laser"), ("Laser Metal Deposition"), ("Direct Metal Deposition"), ("Laser Engineering Net Shaping"), ("Laser Additive Manufacturing"), ("Direct Laser Deposition"), ("Direct Laser Fabrication"), ("Direct Metal Laser Deposition"), ("Shape Deposition Manufacturing"), ("Laser-based Additive Manufacturing"), and ("Laser Solid Forming"). These were arranged in queries combining process and material, such as ("Laser Directed Energy Deposition" AND "410 Stainless Steel"), ("Laser Directed Energy Deposition" AND "4?? Stainless Steel"), ("Laser Directed Energy Deposition" AND "Martensitic Stainless Steel").

1.3 OBJECTIVES

This section describes the main objective and specific developments from it. These will guide the theoretical and experimental work steps.

1.3.1 General objective

Determine a manufacturing route for AISI 410L MSS by laser directed energy deposition (L-DED) process, to produce additively manufactured (AM) components free from deleterious defects, with high density, precise geometry, homogeneous microstructure, and high levels of mechanical strength, toughness, tribological performance, and corrosion resistance.

1.3.2 Specific objectives

- ✓ Define an experimental route for appropriate AM L-DED parameters selection to produce AISI 410L MSS multilayer parts.
- ✓ Understand the connections between the different AM L-DED evaluated parameters (production and resolution) and the responses of density, geometry, microstructure, mechanical properties, tribological performance, and corrosion resistance.

- ✓ Investigate the influence of different aspects of AM L-DED microstructure on mechanical properties, tribological performance, and corrosion resistance.
- ✓ Finding an appropriate PHT route to provide stress relief, homogenize the microstructure, and improve the mechanical properties, tribological performance, and corrosion resistance regarding the as-built condition.
- ✓ Understand how the AM L-DED thermal history and the applied post heat-treatment affect the low carbon-content AISI 410L microstructure, and property responses when compared to a high C-content commercially supplied material.

1.4 THESIS STRUCTURE

This document is divided into seven chapters, each further subdivided into sections according to the topics covered.

I. The first chapter (Introduction) introduced the work, presenting the context, motivation, and general and specific objectives.
II. The second chapter (Scientific Background) discusses topics on MSS, metal AM, and L-DED. Microstructure, mechanical strength, tribological performance, and corrosion resistance of laser-processed MSS, both in the AB and PHT states, are also presented. A discussion of the literature was conducted to understand the state of the art.
III. The third chapter (Scientific Contribution) presents the work's scientific contributions, highlighting its unique aspects regarding the literature found during the systematic review.
IV. The fourth chapter (Experimental Procedures) presents the experimental procedures carried out from the DoE stages to the characterizations and performance tests performed.
V. The fifth chapter (Materials and Equipment) presents all the required materials and equipment, as well as essential information about them.
VI. The sixth chapter (Results and Discussion) presents and discusses all the results obtained. This chapter is divided into seven subsections, with the first three presenting the DoE outcomes, while the last four focus on microstructure and hardness, mechanical strength, toughness, tribological performance, and corrosion resistance. The results from the evaluated L-DED conditions were benchmarked to the reference material and the literature.
VII. The seventh chapter (Research Accomplishments) presents the conclusions, recommendations for future work, and the list of publications.

2 SCIENTIFIC BACKGROUND

This section describes the scientific background necessary to provide a full comprehension of the work steps and results presented in the following chapters.

2.1 STAINLESS STEEL CONCEPTS

Stainless steels (SS) make up one of the most important engineering materials classes, being used in several industries, including power generation, oil and gas, agriculture, medical, mining, tools, cutlery, and railway. SS are high alloy steels belonging to the Fe-Cr, Fe-Cr-C, and Fe-Cr-Ni systems, with a minimum 10.5 wt.% chromium (Cr) content. Cr establishes a passive oxide layer that protects the metal against corrosion. For higher Cr and carbon (C) contents, carbide precipitation can occur, which can cause sensitization, decreasing corrosion resistance. However, wear performance is benefited due to hardness increase and the formation of barriers against the wear mechanisms, and a network for lubricating tribolayers [50]–[52].

SS are categorized according to the predominant microstructure phase: austenitic, ferritic, martensitic, and duplex. The American Iron and Steel Institute (AISI) uses nomenclatures to identify these (e.g., 3XX, 4XX). Magnetic properties are also commonly used to classify these. Austenitic SS is non-magnetic. Ferritic and martensitic, in turn, are ferromagnetic. Duplex SS is relatively magnetic due to its ferrite content. Owing to this work's purpose, more details will be presented only about martensitic stainless steels (MSS).

2.2 MARTENSITIC STAINLESS STEEL (MSS)

This section brings fundamental concepts of MSS, encompassing definition, alloying elements, and phase diagrams.

2.2.1 Definition

Martensitic stainless steels (MSS) are alloys based on the ternary Fe-Cr-C system. They have a Cr-content between 11.5 and 18 wt.%, C between 0.1 and 1.2 wt.%, and low contents of nickel (Ni) and manganese (Mn) [2], [21]. These SS undergo an allotropic

transformation and form martensite from austenite (γ). This steel grade has a body-centered tetragonal crystal martensitic structure (BCT). In lower C-content MSS, the C-content may be less than 0.01 wt.%. Thus, the microstructure moves away from a fully martensitic appearance to a biphasic formation of ferrite and martensite. Cr-carbides may precipitate, depending on the C and Cr-content, the processing conditions, and the post heat-treatments performed. Cr-carbides formation is facilitated in MSS richer in these elements, and, in cases of slower cooling, which drives the diffusion mechanism [46], [53].

2.2.2 Alloying elements in MSS

The main alloying elements added to SS are C and Cr for ferritic and MSS, and Ni for austenitic and duplex. Mn and silicon (Si) are intentionally added to all SS grades. Other elements include molybdenum (Mo), niobium (Nb), titanium (Ti), aluminum (Al), copper (Cu), and tungsten (W) (Table 2.1).

Table 2.1 (start) - Main effects of some alloying elements on SS features.

Element	Main Effects
Chromium (Cr)	- It forms a stoichiometric oxide (Cr_2O_3) on the SS surface, which acts as a passive layer against corrosion, even at high temperatures. - Promotes the formation and stabilization of the ferrite. - With other elements (e.g., C and nitrogen N), it can form precipitates, which impair corrosion but improve mechanical and tribological performance. - It helps the precipitation of the intermetallic compounds, most of which are brittle (e.g., sigma σ, chi χ, and Laves phases). - For high Cr-contents (≈45 wt.%), the σ-phase starts to precipitate from the δ-ferrite around 820 °C. Below 600 °C, δ segregation occurs in α crystals, being responsible for the effect called embrittlement at 475 °C in SS. - Improves solid solution strength.
Nickel (Ni)	- The primary function of promote γ formation. - Influences the precipitation of carbides and intermetallic compounds. - Increases solid solution strength, toughness, and corrosion resistance.
Manganese (Mn)	- Mn combines with S and O, forming sulfides (MnS) and oxides (MnO), decreasing the low melting point elements content in the Fe-matrix, responsible for hot cracks nucleation. - It contributes to the γ formation and stabilization, avoiding martensitic transformation. However, at high temperatures, it can stabilize α. - Increases the N solubility in γ. - It improves resistance to abrasion, corrosion, and high work temperatures.
Silicon (Si)	- Present in virtually all SS, its primary function is to promote deoxidation (by combining with O to form oxides) during melting. - Improves self-fluxing properties. - It forms silicates and intermetallic compounds, which embrittle the material.

Table 2.1 (end) - Main effects of some alloying elements on SS features.

Element	Main Effects
Carbon (C)	- Available in all steels. It is recommended to keep the C-content <0.1 wt.% An exception is the MSS, in which C plays a fundamental role in the martensitic transformation. - Promotes the γ formation. - It combines with other elements (e.g., Cr, Mo, Nb) to form carbides. These increase hardness and wear resistance; however, they reduce the solid solution strength, by depleting these elements from Fe-matrix.
Other elements	- Molybdenum (Mo) can form carbides. It provides the α and improves corrosion resistance. Influence the σ, χ, and Laves phases precipitation. - Nitrogen (N) is a γ promoter and facilitates Cr-nitrides precipitation. Sulphur (S) and phosphorus (P) improve machinability. However, they worsen corrosion resistance and weldability and cause hot cracks. - Ti, Nb, and W bind to C, forming carbides, avoiding Cr-carbides precipitation, which reduces corrosion resistance. Improve wear performance.

Source: [38], [50], [54], [55].

Alloying elements added to SS affect the balance and stability of γ and α. The martensite, in turn, is a product of the fast cooling of γ. Austenitic SS has high levels of Ni and other γ-stabilizing elements, the predominant phase at room temperature. Ferritic SS contains α as the predominant phase. MSS are austenitic SS at high temperatures, but the γ phase is unstable and transforms to martensite during cooling. In this sense, the balance of γ and α phases in the microstructure significantly influences mechanical properties, corrosion, and wear resistance. For a better comprehension of the elements' effects on the phases formed in the SS, it is important to know the phase diagrams [38], [50], [54], [55].

2.2.3 Phase diagrams

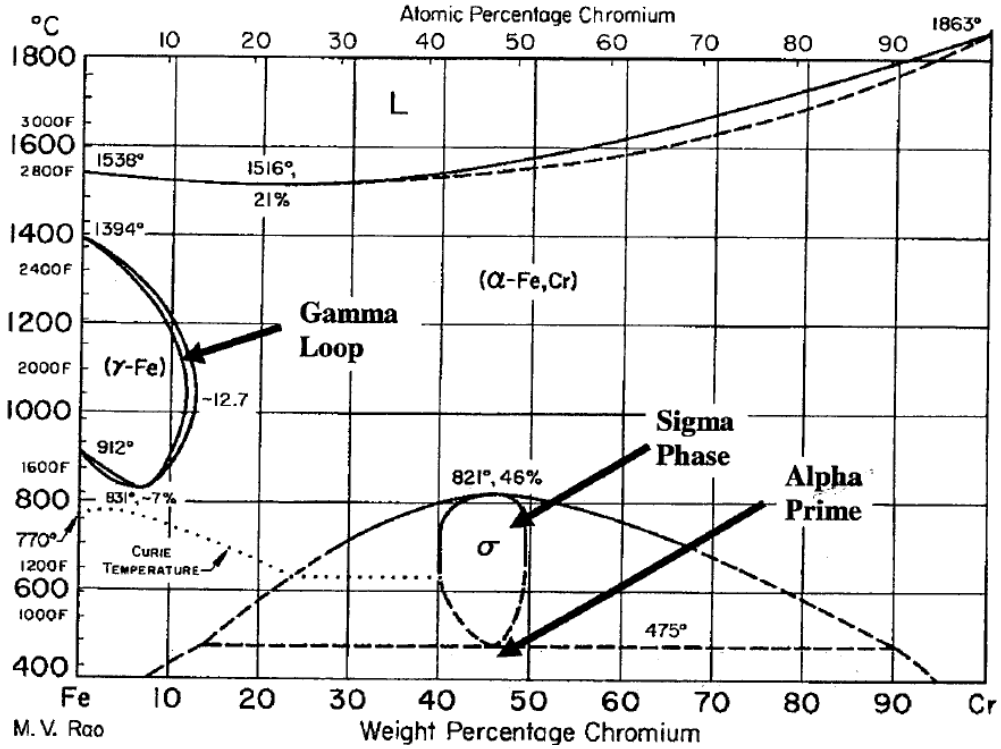
Phase diagrams provide indications of the microstructure developed. However, processes with fast heating/cooling/solidification cycles result in non-equilibrium conditions, which are then only approximately described by these diagrams [50], [54].

2.2.3.1 Binary Fe-Cr system phase diagram

The Fe-Cr system diagram (Figure 2.1) is the starting point for describing the phase stability in SS. For low Cr-contents (0-12.0 wt.%), there is an austenitic field (γ-loop) in the

temperature range between 912 and 1394 °C. Alloys with Cr content >12.7 wt.% will be fully ferritic (α) at high temperatures. These will not experience γ-α transformation, so grain refining and hardening associated with transformation will not occur. This is because Cr is a strong α-promoter, restricting the γ formation. Alloys with Cr content <12 wt.% will be fully austenitic inside the γ-loop. If cooled slowly, this portion of γ transforms back into α, so that the SS will present a fully α structure at the end of solidification. If subjected to fast cooling, this γ can transform into martensite. At lower temperatures, under equilibrium conditions, the so-called sigma phase (σ) can be precipitated. At high Cr-contents, around 820 °C, this phase begins to precipitate from the δ-ferrite grain boundaries. It has a stoichiometric ratio (Fe, Cr) of approximately 45 wt.% Cr, being an intermetallic compound with a BCT structure and slow precipitation kinetics. Its precipitation depletes Cr from the Fe-matrix to the σ-phase, decreasing corrosion and increasing mechanical and tribological performance. PHT austenitization at 1000 °C can dissolve this phase. Below 600 °C, the Fe-Cr diagram displays a horizontal line within the σ+α field at 475 °C, wherein high-hardness Cr-rich precipitates are formed inside the ferritic matrix, weakening the material. In the binary Cr-Ni system, the Ni-content expands the γ-loop to higher Cr-contents and lower temperatures. This Ni effect is important to developing low-C MSS since the ferrite precipitation is reduced. The γ crystals precipitated on cooling or PHT are transformed during further cooling into α and, if fast cooled, martensite [50], [54].

Figure 2.1 - Fe-Cr equilibrium phase diagram.

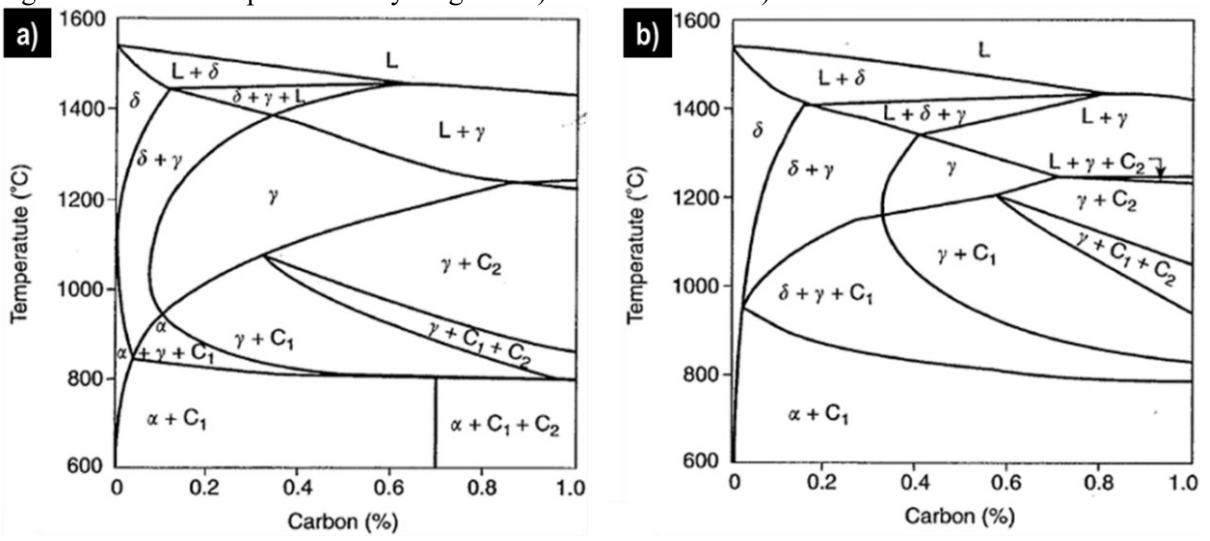


Source: [50].

2.2.3.2 Ternary Fe-Cr-C system phase diagram

The addition of C to the Fe-Cr system changes the equilibrium phases. The C-content expands the γ-loop, stabilizing γ at higher temperatures. This mechanism is fundamental in the MSS, since, aiming to form martensite during cooling, the steel must be γ at elevated temperatures. Due to the complexity of the ternary diagrams, it is common to use pseudobinary diagrams, in which one of the elements is kept constant. In Figure 2.2a diagram (Fe-Cr-C system for 13 wt.% Cr), due to the C addition, carbide precipitation occurs. For ferritic and martensitic SS with low Cr-content, and with C<0.1 wt.%, ternary alloys fully transform into δ at high temperatures. If cooled fast enough, they may remain as δ at the end of solidification. This is the basis of low Cr ferritic steels. For C>0.1 wt.% contents, γ will be established at high temperatures, and a mixture of γ and δ will form just below the start liquidus temperature. On cooling, the structure becomes fully γ at temperatures below 1200 °C. If the cooling rate is sufficiently fast, this γ will turn into martensite. This is the basis of low Cr MSS (e.g., 410). In cases of very low C-contents (e.g., C<0.05 wt.%), a biphasic γ+δ will be present at high temperatures, generating, at room temperature, a microstructure composed of α and martensite from fast cooling. For higher Cr-contents, the δ-loop is expanded, while the γ-loop is narrowed, as represented in the diagram with 17 wt.% Cr constant section (Figure 2.2b). This behavior is conferred by the Cr δ-promoting effect. As a result, δ formed at high temperatures will be stable, and higher C-content will be required to form γ at high temperatures [50].

Figure 2.2 - Fe-Cr-C pseudobinary diagram: a) 13 wt.% Cr and b) 17 wt.% Cr.



Source: Adapted from [50].

2.3 MARTENSITIC STAINLESS STEEL PROCESSING

This section will describe some fundamental concepts about MSS, from processing to microstructure and resulting properties.

2.3.1 MSS microstructure phases

Conceptually, the MSS microstructure is fully martensitic. However, it may consist of different phase combinations, including γ, retained-γ, δ-ferrite, α-ferrite, and carbides. It is also possible to observe the sigma (σ) phase [8], [50]:

- Austenite (γ) and retained-γ: γ is a Fe-γ solid solution that provides toughness and corrosion resistance. When heated over the austenitic transformation temperature (A_3), the metal enters an austenitic condition. In the MSS, depending on the chemical composition (e.g., austenitizing elements) and cooling conditions (e.g., speed, M_s temperature), a portion of the γ may remain retained at the end of solidification [38], [56].
- Ferrite (α and δ): α-ferrite is a product of secondary precipitation from γ-loop below 911 °C. It is a Fe-α allotropic state phase, containing C in solid-solution. It exhibits low hardness and tensile strength, and elevated ductility [38]. The primary ferrite formed from the molten metal is called δ-ferrite. Under equilibrium conditions, δ transforms into γ upon reaching γ-loop and, subsequently, secondary solid-state γ-α transformation takes place. However, in non-equilibrium conditions and with fast cooling, an amount of δ can be retained in the material at room temperature [39], [40], [57].
- Carbides: The rejected C can combine with Fe and Cr, forming Fe and Cr-carbides (e.g., Fe_2C and $M_{23}C_6$). These can improve hardness, mechanical, and tribological performance. On the other hand, they may reduce ductility and corrosion resistance [48], [58].

2.3.2 Martensitic transformation and post heat-treatment applied to MSS

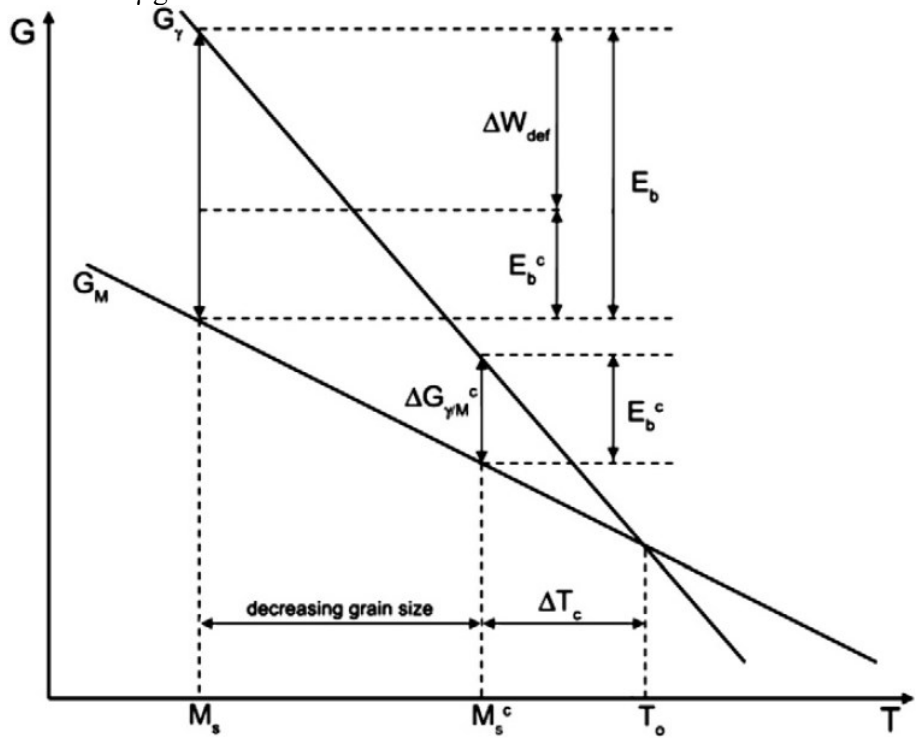
The predominant phase transformation in the bulk and heat-affected zone (HAZ) of MSS is the γ-martensite type. High cooling rates increase the M_s and the amount of retained-γ. During γ cooling, martensite transformation only starts when M_s is reached. In a refined grains structure, M_s reduction can be explained by the martensitic transformation theory, which establishes that the energy barrier imposed on the martensite formation is composed of the energy needed to trigger a shear deformation parallel to the habit plane (coherent plane between

γ and martensite) and a uniaxial expansion, normal to the habit plane. The γ must then be deformed. In this sense, the energy barrier required for the martensitic transformation corresponds to the strain energy required to achieve the necessary shear deformation [54], [59].

The M_s reduction can be due to the primary γ grains refinement [49], [60]. In a coarse-grained γ structure, the γ resistance and hence M_s are dependent on the material's chemical composition. However, in a refined structure, the extra barrier energy imposed by the material's resistance requires a greater driving force, which translates into M_s decrease. Solid solution strengthening affects martensite transformation, including the transmission of slips across grain boundaries, a region with higher resistance. Despite this phase close to γ grain boundaries, martensite only nucleates in contours with sufficient energy. The relationship between γ grain size and M_s can also be checked for the probability of finding nucleation sites for the martensitic grain formation [17], [59], [61].

Other factors that affect M_s, such as chemical composition, residual stress, and γ homogenization, are influences on the proportion of retained γ-content. As for composition, M_s decreases with a higher number of alloying elements. As for residual stress, an inverse relationship between this and M_s is reported. The precipitate concentration increases M_s by the high C-content within γ, and nuclei sites generation [38], [62]. Figure 2.3 illustrates the free energy variation of γ and martensite with temperature. At initial temperature T_0, the free chemical energy of martensite (G_M) and γ (G_γ) are equal and both phases are in thermodynamic equilibrium. Due to the non-chemical energy barriers (E_b^c), martensite nucleation is started only in a critical undercooling (ΔT_c), in which the absolute difference between the free energies of the martensite and γ ($\Delta G_{\gamma/M}^c$) is equal to the total barrier energy (E_b). In this sense, ΔT_c is dependent on the material's chemical composition and M_s. Two types of plastic deformation must occur during martensitic transformation: shear stress in the habit plane of martensite, and the deformation imposed by the volume expansion associated with the γ-martensite transformation. One of the E_b components (Figure 2.3) will result from plastic deformation variation (ΔW_{def}), which is associated with the material's resistance. In this sense, grain refinement will cause an increase in plastic deformation variation (ΔW_{def}) and, consequently, in E_b [61].

Figure 2.3 - Illustrative representation of the Gibbs free energy changes in martensitic transformation and the contribution of γ grain refinement.



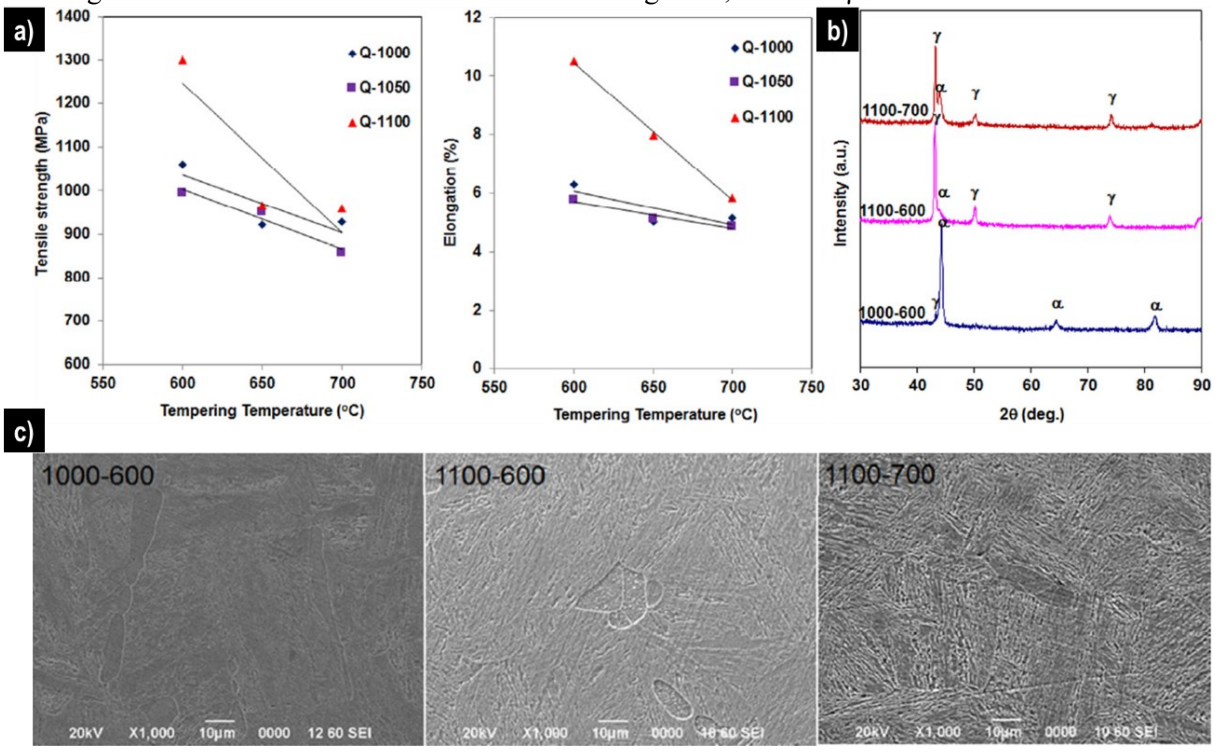
Source: [59].

Post heat-treatments (PHT) are indispensable for MSS, due to the martensite brittleness. The main objectives of these are to temper the martensite and provide residual stress relief. In the PHT route, austenitization re-austenizes the entire structure, dissolves the carbides and alloying elements [40]. After austenitization, in the quenching, γ is transformed into α, rejecting C from the solid solution. In combination with α, it forms perlite. However, when such a high cooling speed is applied, C rejection may not occur. In these cases, there is the establishment of a solid solution supersaturated with C, which constitutes martensite. The high hardness of martensite can be attributed to the distortion of the original body-centered cubic (BCC) structure caused by C supersaturating, establishing a new BCT [38]. Tempering accompanies the quenching. In this, martensite heating reverts the BCT structure to the original BCC, providing residual stress relief, ductility, and toughness improvement [40], [63]. Selecting tempering conditions is a challenge in MSS, due to the carbide precipitation embrittlement trend between 375-575 °C and the segregation of low melting point elements at the parent-γ grain boundaries, which reduces mechanical, tribological, and corrosion resistance [48], [64].

In the literature, a convergence between austenitization and quenching PHT is noted, with sharper variations in the tempering step. An example is the work of Mabruri *et al.* [40],

who analyzed the effects of the PHT on the microstructure and mechanical performance of wrought 410-3Ni3Mo MSS. Three sample sets were evaluated: austenitization at 1000, 1050, and 1100 °C for 60 min, followed by oil quenching. Tempering at 600, 650, and 700 °C for 60 min, followed by air cooling. In the results, the highest capability of plastic deformation and strain hardening was experienced by the sample quenched at 1100 °C and tempered at 600 °C (higher yield strength YS, and elongation), which was provided by the dissolved carbides as a function of the greater temperature. Tempering at lower temperatures generated more refined martensite, while temperature increase resulted in coarser grains. Figure 2.4 illustrates the mechanical behavior and microstructure characteristics.

Figure 2.4 - Wrought state 410-3Ni3Mo: a) YS and elongation; b) X-ray diffraction (XRD) diffractogram, illustrating the γ and α peaks; c) Scanning electron microscope (SEM) microstructure, showing the variation in martensite content and refining level, retained-γ and δ-ferrite contents.



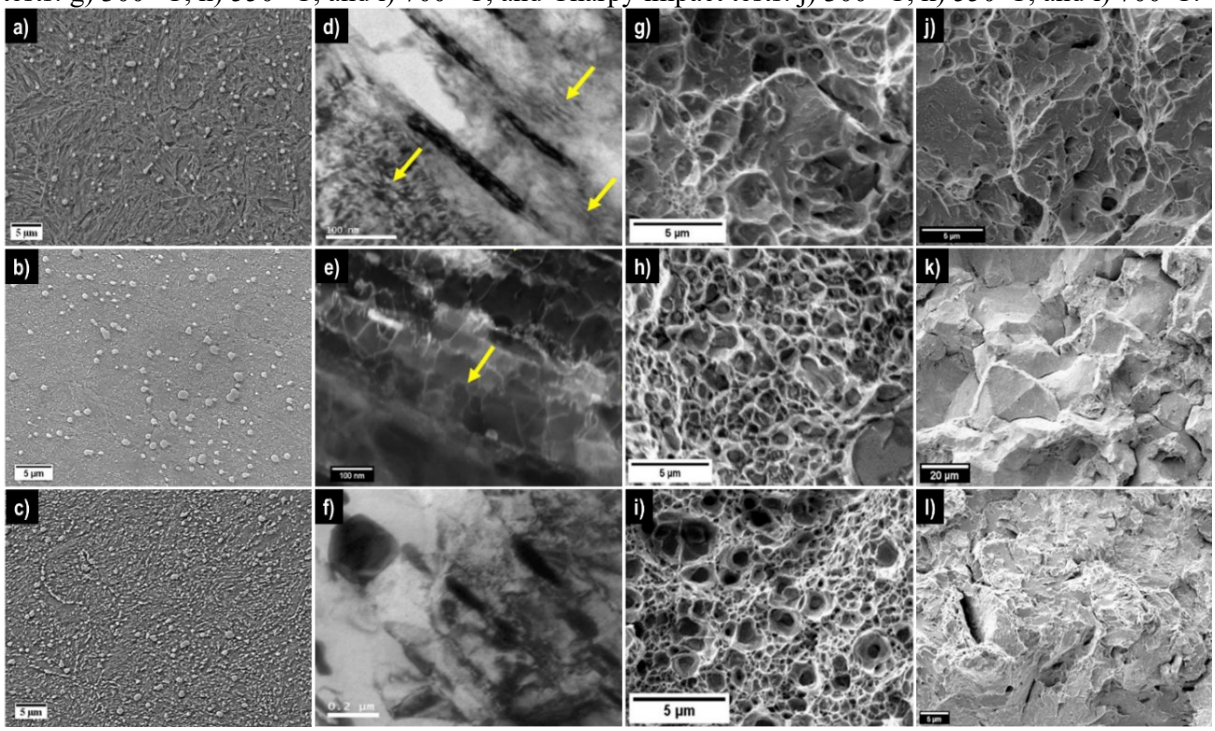
Source: Adapted from [40].

A limitation of MSS is their poor impact toughness, owing to the brittle nature of martensite. One approach to surpass this issue is performing PHT. Mabruri *et al.* [65] evaluated the austenitization (950-1100 °C for 60 min, oil quenching) for a fixed tempering (600 °C for 60 min, air cooling), applied to the wrought 410-1Mo MSS. Charpy impact toughness exhibited an enhancement until 1050 °C, followed by a drop at 1100 °C. Lower temperature behavior was

attributed to the retained-γ content. Higher temperature impact toughness drop was conferred to the brittleness of the high C-content martensite, and the parent-γ grain coarsening. Moreira *et al.* analyzed AISI 410 MSS samples (as-received) collected from piston rods of spillway floodgates. Tensile results exceeded the ASTM A276 standard [66]. However, Charpy impact absorbed energy (AE) was only 6 J. SEM fractography revealed an intergranular mode with cleavage, which propagated cracks in the parent-γ grain boundaries [3].

Bonagani *et al.* [63] studied the influence of tempering temperature on a 13 wt.% Cr MSS (as-received). Austenitization at 1020 °C for 30 min followed by oil quenching transforms γ into lath martensite. Tempering was carried out for 2.5h at 300, 550, and 700 °C, followed by air cooling (Figure 2.5). Temperature increase elevated the volume and size of carbides (Figure 2.6a-c) and reduced the dislocation density (Figure 2.6d-f), decreasing the hardness, YS, and ultimate tensile strength (UTS). However, elongation and Charpy AE were higher. SEM fractures of quenched condition exhibited a brittle aspect owing to the untempered martensitic microstructure, while the lower tempering temperatures (300 and 550 °C) showed the ductile-brittle mix with cleavage. Tempering at 700 °C resulted in a fully ductile fracture (Figure 2.6g-i and Figure 2.6j-l), due to carbide coarsening and martensite-ferrite reversion.

Figure 2.5 - SEM microstructure showing higher content of carbides with increasing tempering temperature: a) 300 °C, b) 550 °C, and c) 700 °C. Transmission electron microscope (TEM) microstructure illustrating density dislocation reduction with temperature increase: d) 300 °C, e) 550 °C, and f) 700 °C. SEM indicating ductile-brittle, entirely brittle, and entirely ductile aspect in the tensile tests: g) 300 °C, h) 550 °C, and i) 700 °C, and Charpy impact tests: j) 300 °C, k) 550°C, and l) 700°C.



Source: Adapted from [63].

2.4 METAL ADDITIVE MANUFACTURING

This section will provide some aspects regarding metal AM, emphasizing the AM L-DED process.

2.4.1 Contextualization

In additive manufacturing (AM) processes, the component is built from a 3D model, layer by layer. The literature highlights the advantages of manufacturing complex/custom geometries, near-net shaping, lead-time reduction, and on-demand production. Due to the high costs associated with these technologies, such as equipment and feedstock, developments in the area are still restricted to frontier industrial sectors, such as aerospace, high-performance automobile, and O&G [5], [16], [23], [67]. However, this scenario has been changing, with the research expansion and the recognition of AM's possibilities. There are different AM processes. The nomenclature statement used in this work follows ISO/ASTM 52900, which subdivides them into seven categories, according to the energy source and feedstock [12]: material extrusion, material jetting, sheet lamination, vat photopolymerization, binder jetting, powder bed fusion, and directed energy deposition. Directed energy deposition (DED) is defined as a process in which focused thermal energy (e.g., electron beam, plasma arc, laser) is used to melt materials (e.g., powder, wire) as they are being deposited [13]. In the present work, laser directed energy deposition (L-DED) with powder as feedstock was used.

2.4.2 AM L-DED process

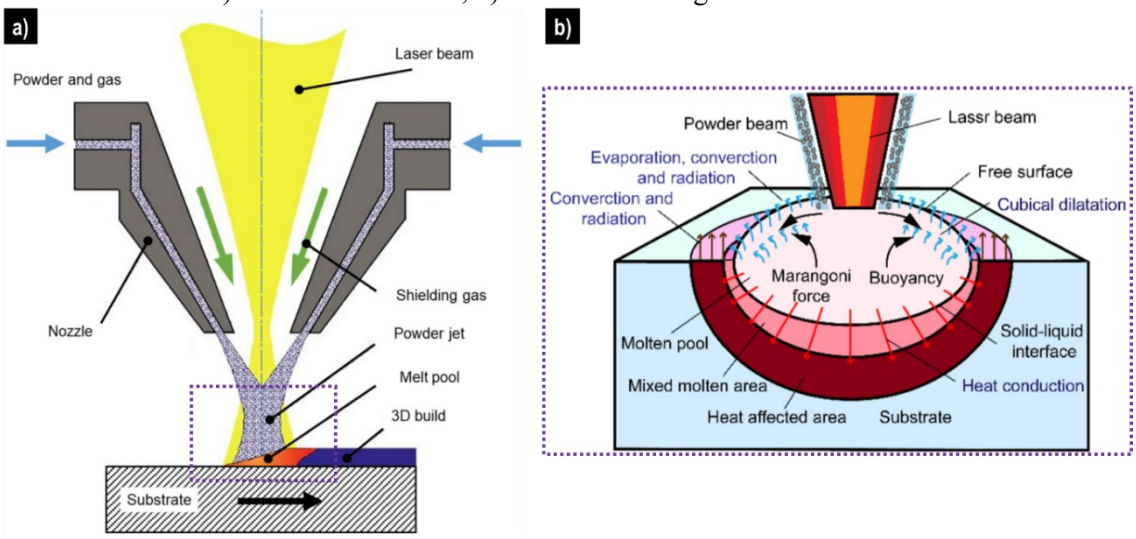
This section describes some fundamental aspects of L-DED technology. The references list provides more information, with special emphasis on review papers.

2.4.2.1 AM L-DED overview

In the metallic AM context, laser beam employment as an energy source has been highlighted, mainly in the L-PBF and L-DED techniques. Laser radiation has some features (e.g., highly coherent, collimated, and monochromatic), which make it a useful tool [68]. In the

L-DED (see Figure 2.6), the inherent characteristics of accurate heat-input control, formation of strength metallurgical bond, and narrow HAZ, low insertion of distortions, possibility to process a wide alloys range of alloys, including graded materials, and metal-matrix composites, are some of its advantages. This technique encompasses attractive AM features. However, L-DED is a non-equilibrium thermodynamic process, which exhibits a high thermal gradient, elevated cooling speeds, and very fast heating/cooling/solidification thermal cycles. The large number of variables, which include physical, thermodynamic, and metallurgical mechanisms, increases the process complexity, making it rather difficult to model/control [16]. L-DED encompasses aspects such as laser variables, powder beam dynamics, heat transfer, molten pool kinematics, and solidification [11].

Figure 2.6 - L-DED: a) illustrative scheme, b) characteristic regions of interaction and formation.



Source: Adapted from [69], [70].

As Figure 2.6b) illustrates, molten pool behavior is a synergy of several phenomena, such as heat sinking mechanisms (e.g., substrate contact conduction, surrounding atmosphere irradiation, and convection to the process gases); Buoyancy forces (upward motion from the density differences originated by the thermal gradients); Marangoni convective currents (from surface gradient tension from middle to the boundaries of the molten pool) [11], [16].

2.4.2.2 AM L-DED setup

To manufacture a L-DED part, some conditions must be set. The setup is composed of the L-DED system, build platform, laser source, substrate, and feedstock. The L-DED process has several parameters, whether inherent to the hardware and/or set by the user, which need to

be monitored and controlled [71]. One can highlight the optical system (e.g., stand-off distance, laser beam defocusing adjustment [72], [73]), powder nozzle design (e.g., coaxial or lateral [74]), laser source characteristics, build atmosphere condition (e.g., build platform surrounding, carrier and shielding gas flow [14], [75]), substrate (e.g., chemical composition, laser power absorptivity capability [76]), feedstock (e.g., powder particle size, morphology, rheology [77]), and build strategies (e.g., build positioning and orientation, scanning, slicing [78]).

Concerning the L-DED system, the market offers several options in terms of build volume, feedstock type, hardware (e.g., optics, nozzles, laser source, atmosphere control), and software (e.g., Computer-Aided Design/Manufacturing CAD/CAM system, process control, and monitoring). Generally, these systems are built for the intended applications. Hybrid AM machines are also being developed, which perform the manufacturing and subsequent machining and finishing steps necessary in the same equipment [5].

For AM, it is interesting that the substrate material is as close as possible to the feedstock, mainly when operating with high energy inputs and in the first layers, which facilitates metallurgical bond and avoids the deleterious effects imposed on the microstructure and properties owing to the mixture with elements dragged from dissimilar substrates. It is necessary to pay attention to reflectivity, absorption, and heat sink capability [77].

Regarding feedstock, L-DED uses wire or powder. When working with metallic powder, it is necessary to consider chemical composition, morphology, particle size distribution, and rheology. The current technique predominantly used in AM metallic powder manufacturing is the atomization process, carried out in water, gas, or plasma medium. This sequence indicates an increase in powder quality and also in production cost [71], [79].

2.4.2.3 AM L-DED parameters

Concerning input L-DED parameters, stand out the spot size (Ø, mm) laser power (P, W), travel speed (S, mm/min), powder feedrate (F, g/min), hatch spacing (HS, mm), layer height (LH, mm), and process gases (carrier C_G and shielding S_G, l/min). There is also laser wavelength (ʎ, nm), laser beam focus distance (F_{laser}, mm), laser beam defocusing distance (D_{laser}, mm), incident laser beam diameter ($Ø_{laser}$, mm), incident laser beam area (A_{laser}, mm^2),

powder focus distance (F_{powder}, mm), powder focus diameter ($Ø_{powder}$, mm). Some of the main parameters are detailed as follows:

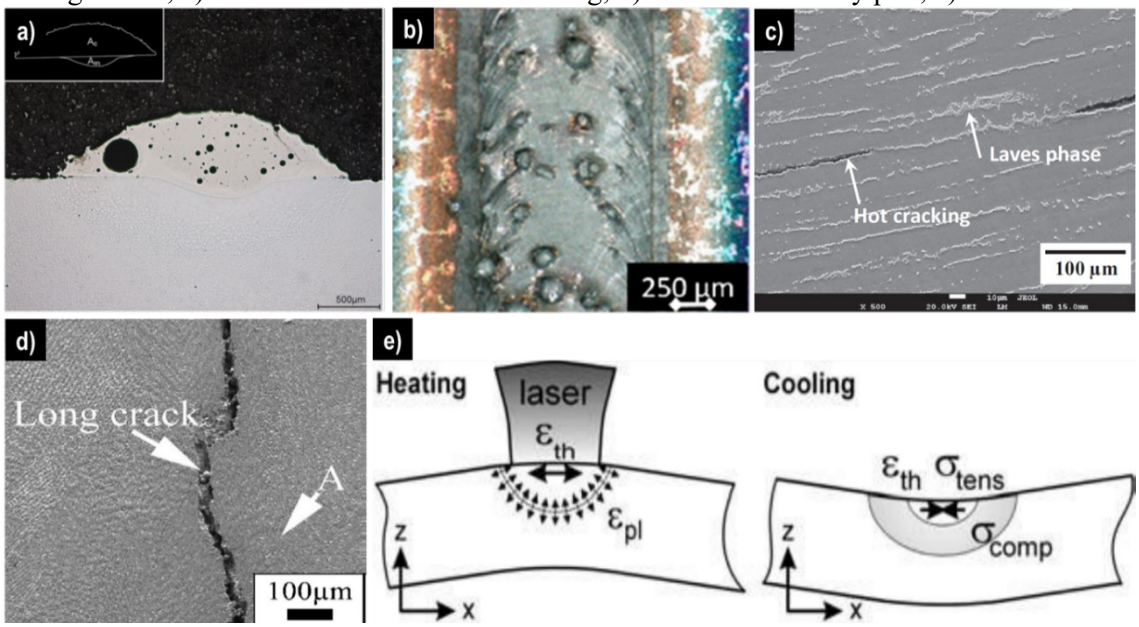
- Spot size (Ø): Spot size at the focus is the interaction region between the laser and powder beams. The incident laser beam diameter ($Ø_{laser}$), on the other hand, prescribes the diameter incident beam on the substrate. Ø increase distributes the laser beam energy over a greater contact area with the substrate, enlarging the molten pool. Ø reduction, in turn, promotes a more concentrated energy distribution, increasing the molten pool penetration [80].
- Laser Power (P); Travel Speed (S); Powder feedrate (F): P increase elevates the energy density; S elevation reduces the energy density and the powder amount per unit length; F increment promotes higher powder amount per unit length. It is important to remember the influence of the laser light wavelength (ʎ), as this affects the material energy absorption. To ensure energy efficiency, it is interesting that the laser wavelength (ʎ) is compatible with the spectrum absorbed by the material. Energy absorption also depends on the physical properties, geometry, and surface finish. Laser beam quality is another key point. M-square (M^2 factor) informs the beam deviation from the ideal Gaussian shape. Obtained by the relationship between the Beam Parameter Product (BPP) of the laser beam and the BPP of a perfect Gaussian (Theoretical mode: TEM_{00}) with the same ʎ [68], [81], [82].
- Hatch spacing (HS) is the lateral distance between adjacent single beads (SB) while depositing a single layer (SL). This must be high enough to avoid defects between SBs and at the interface with the substrate [27], [29], [83].
- Layer height (LH) is the remelting depth of the previous SL. Similar to the HS, it must be sufficiently high to ensure a strong metallurgical bond between SLs and to mitigate defects. On the other hand, it must not be too high, to the point of remelting a deep thickness of the previous SL. It is important to pay attention to the layer height programmed in the CAD/CAM and the actual experimental layer height. These must be compatible to avoid the propagation of geometrical error in several layers deposition [84], [85].
- Process gases: L-DED with powder as feedstock uses two gas flows, one for the powder particles carrier and the other for the molten pool shielding. There are also L-DED systems that have enclosed chambers, with a protective atmosphere throughout their volume. Process gases are essential to ensure a constant powder particle carrier, as well as shield the build platform from atmospheric impurity elements (e.g., oxygen O, and hydrogen H), minimizing the formation of oxides and inclusions. The control of these flows also influences process aspects such as efficiency, porosity, and heat sinking [75], [86].

- Deposition strategies: The manufacturing orientation on the substrate (vertical, horizontal, 45°) is important from the points of view of thermal history (heat-sink, residual stresses), defects, productivity (material and time consumption), and anisotropy. Scanning strategies can improve heat distribution, microstructure homogenization, and reduce residual stresses [21]. There are also limiting complex features (e.g., overhang, islands, wall intersections) and their consequences, whether by hardware (e.g., kinematics, accessibility), software (e.g., codes), physical phenomena (e.g., thermal, gravity). ASTM F3413 addresses these issues for DED processes [87]. It is also essential to highlight the design for AM. The adoption of theory, techniques, and tools, such as cellular, monolithic, support structures, materials, orientation, and complexity, is encompassed within this area [5], [25].

2.4.2.4 General features of AM L-DED parts

The substrate or previously deposited layer governs the solidification structure close to the molten pool boundary, while the middle region is commanded by competitive growth, generating the directional dendritic structure and different solidification front orientations [10], [67]. Solidification mode can be planar, cellular, columnar, or equiaxed dendritic, a characteristic that is governed by the chemical composition and the relation between temperature gradient (G) and solidification ratio (R) [23], [88]. Hardness varies along with the built thickness, due to microstructure change. It is common to verify higher hardness close to the substrate and the surface when compared to the middle layers. This variation is attributed to the more efficient heat sink of the boundary regions (conduction to the substrate and convection to the atmosphere), while the middle is slowly cooled, which provides the formation of refined and harder grains in these regions [15], [16]. Mechanical, tribological, and corrosion performance are dependent on the entire manufacturing set, encompassing microstructure, thermal history, and build strategy. Post-treatment routes can improve the AM L-DED part properties [89]–[91]. Owing to the intrinsic characteristics, some defects can arise in these, such as segregation, porosities, lack of fusion, cracks, delaminations, unmelted particles, and effects of residual stress (Figure 2.7).

Figure 2.7 - Defects in AM L-DED: a) porosities in a Fe-alloy single bead; b) unmelted particles in a 316L single bead; c) hot cracks in Inconel 718 coating; d) Cracks in Ni-alloy part; e) residual stress.



Source: Adapted from [37], [92]–[95].

Chemical composition change: during the fast heating/cooling L-DED cycles, solutes are redistributed, leading to element segregation at the grain boundaries and/or new compound formation, altering the local composition. Besides, due to the different melting points of the elements, some of them may be volatilized with the molten pool temperature levels, thus modifying the alloy's chemical composition [10], [16].

Porosities and lack of fusion: porosities may result from incomplete melting or insufficient energy input to fully melt the feedstock. They can also form due to gas entrapment during fast solidification. Besides, powder particles with inherent porosity may transfer this defect into the molten pool. Moisture evaporation is another potential porosity source. Lack of fusion, on the other hand, can occur when penetration between the deposited layer and either the substrate or a previously deposited layer is insufficient [16], [27], [29].

Unmelted particles: AM parts have accentuated roughness owing to two main reasons. The first is the stair-step effect provided by the peaks and valleys between the single beads of the layers. The second is the incomplete powder particles melting. The latter can be attributed to the insufficient energy density to melt the total amount of particles; high energy density, in turn, increases molten pool turbulence and drags particles to their boundaries through the Marangoni phenomena; very high travel speeds (S) can cause the rebound effect; powders with large dimensions and/or uneven morphology are difficult to melt; L-DED systems with displacement between the powder beam and laser beam may exhibit low powder catchment

efficiency. The process stability with powder feeding always results in efficiency below 100%, as not all the powder is directed to the molten pool. Besides, a portion of the powder particles reaches the partially solidified molten pool and does not encounter enough energy to fully melt it. Unmelted powder particles in the previous layer can generate porosity and delamination induced by a weak metallurgical bond, and also act as nucleation sites for grain growth [23].

Cracks and delamination: cooling crack nucleates along the grain boundaries due to the inversion of the thermal cycle of compressive-tensile stress. Hot cracks occur in alloys with dissimilar melting point elements, which provide an imbalance between the solidified portions and the remaining liquid. Thus, when the remaining liquid solidifies, the inversion of the compressive-tensile stress cycle nucleates cracks along their length. Delamination is the rupture between two layers, triggered by residual stress [88], [96]. In the martensite transformation crack can nucleates due to the associated volumetric expansion [97]–[99].

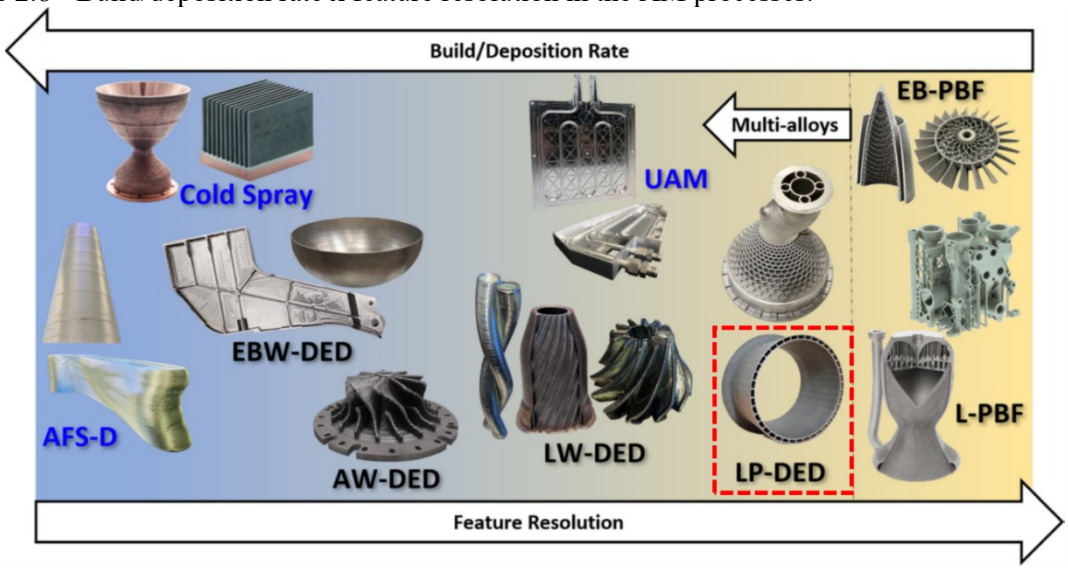
Residual stress: loss of geometric tolerances, and delaminations. The literature indicates three origins for these. The first is the spatial temperature gradient owing to the localized heating/cooling cycle. The second is the expansion/compression phenomenon imposed on the material by the fast heating/cooling cycle. The last one is the uneven deformations, associated with a non-uniform balance of forces [88], [100].

2.4.2.5 Production vs. resolution

Each AM process has a minimum limit of design feature complexity (e.g., hatching, wall thickness, internal channels). The L-PBF technique can easily build geometries with dimensions <0.1 mm, while in the L-DED process, it can be complex to achieve wall thicknesses <1.0 mm [101]. However, with the same technique, it is possible to work in conditions looking for higher production (PRO) or higher resolution (RES). These are then dependent on feedstock, hardware, and process parameters [26]. There is a correlation between deposition rate and resolution, which is conferred to the molten pool size [102]. Figure 2.8 graph summarizes this inverse relationship between deposition rate and resolution. Figure 2.9 illustrates the same preform manufactured under different parameter settings. When higher RES parameters are applied, the preform exhibits greater geometric accuracy. However, this comes at the expense of increased time and cost compared to manufacturing the same preform with

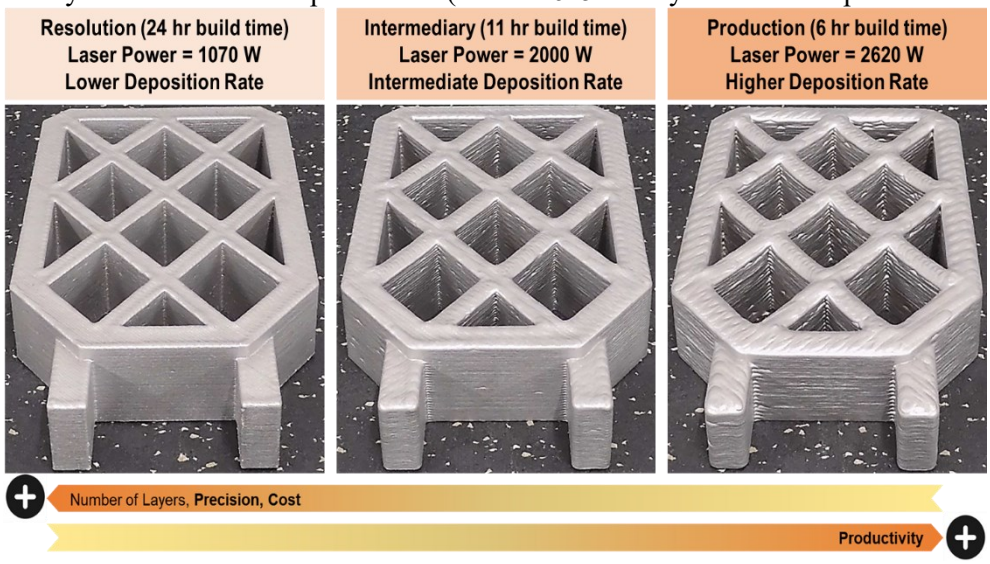
higher PRO parameters. Therefore, selecting the appropriate parameter involves a trade-off between precision and efficiency [26].

Figure 2.8 - Build/deposition rate x feature resolution in the AM processes.



Source: Adapted from [5].

Figure 2.9 - Difference between production and resolution parameters: same part manufactured in the same L-DED system with different parameters (Inconel 625® alloy - no further specifications).



Source: Adapted from RPM Innovations Inc. (Courtesy of RPM Innovations Inc.) [https://www.rpm-innovations.com/laser-deposition-services.html].

2.4.2.6 AM L-DED design of experiments

The key steps of the AM L-DED design of experiments are single beads (SB), single layers (SL), and multilayer geometry cubes (MG). From the cross-section of a single bead (SB),

one may assess height (h), width (w), dilution (D), wettability angle (Θ), and efficiency (η). This work will focus on the analysis of D, Θ, and η [10], [16]:

- Dilution (D): the portion of substrate that has been mixed with the feedstock. Literature reports an increase in this proportionality to the P elevation, allied with F and S reduction.
- Wettability angle (Θ): estimated as the tangent angle between the SB surface and substrate or between h and w. Higher values according to the increase in S and P, and lower F.
- Efficiency (η): the ratio of the total amount of feedstock effectively caught and melted to the portion delivered. P and F are the most significant parameters.

D must be as low as possible, aiming to ensure metallurgical bond and the absence of lack of fusion defects [14], [103]. Θ indicates the flatness degree between the substrate and SB surface and should be high enough to avoid lack of fusion between SBs [104]–[106]. η affects the economic process viability. The cost of metallic powder acquisition is one of the factors that most increases the overall process cost [5], [92], [103]. SB integrity is also impacted by L-DED system features (e.g., stand-off distance [72], laser and powder beam defocusing [73]); powder nozzle (e.g., coaxial or lateral [74]); laser source characteristics, build atmosphere (e.g., carrier and shielding gas flow, O_2-content [14], [107]); substrate (e.g., chemical composition [77], [105]), and feedstock (e.g., particle size distribution, morphology, rheology [76]). Gutjahr studied the AISI 316L powder degradation during the L-DED process. It presents a summary of the main L-DED parameter effects [71].

Single layers (SL) are constituted by lateral SBs deposited and partially overlapped. At this stage, Hatch Spacing (HS) is added as a variable. On the SL cross-section, one can access deposited (A) and molten (B) areas, dilution (D), height (h), and width (w):

- Average peak height (h) and width (w): h and w correspond to the distance between the substrate surface and the top of the SL, and the distance from one end to another of molten pool boundaries, respectively [84], [85].
- Dilution (D): it follows the same trends described in the SB stage (item 6.1).
- Waviness ($\Delta h'$): expresses the h variation of peaks and valleys along with the component SBs of the SL. Of the L-DED parameters, HS and S exert the most significant influence. SL $\Delta h'$ should be as low as possible since it can generate problems in the multilayer stage (e.g., lack of fusion, standoff distance fluctuations, and distortions) [108], [109].

- Slope (Θ): describes the SL slope degree along with the deposited SBs. Lower HS values, combined with lower S, generally form a more sloped SL. SL Θ should be as low as possible. High SL Θ can generate a lack of fusion in the first SBs of the SL, and excessive remelting of the last ones, owing to the stand-off distance fluctuation [109].
- Efficiency (η): the reheating and the greater heat input imposed by the multiple SBs deposition provide an effective melting of the caught particles. Increasing P improved η_{SL} while elevating F and S worsened it. P and F were the most significant parameters [14], [92], [110].

At the multilayer geometry cubes (MG) stage, Layer Height (LH, %) was added as a variable, meaning the vertical overlapping. Low LH% generates lack of fusion, delamination, and porosities. High LH% promotes excess remelting of the previous SL, which affects geometry, microstructure, material properties, and productivity [5], [23]. The ideal LH% should allow the height increment of the real experimental layer to be equal to the value set in the CAD/CAM software of the L-DED system, maintaining the correct standoff distance. Likewise, it is required to verify the defects' absence and perform a porosity quantification [86].

2.5 TRIBOLOGICAL PERFORMANCE

MSS are also recommended for their tribological performance. This section discusses some fundamental points focused on this work's objectives.

2.5.1 Tribology concepts

Tribology is a science dedicated to finding solutions to mitigate or reduce the harmful action of wear mechanisms. This science is based on analyses of friction, wear, and lubrication. High operating temperatures, humidity, mechanical stress, and contamination in industry create severe tribosystems. In this context, tribology seeks alternatives to extend the components' lifespan, reducing costs and logistical issues [111]–[113].

2.5.2 Wear mechanisms

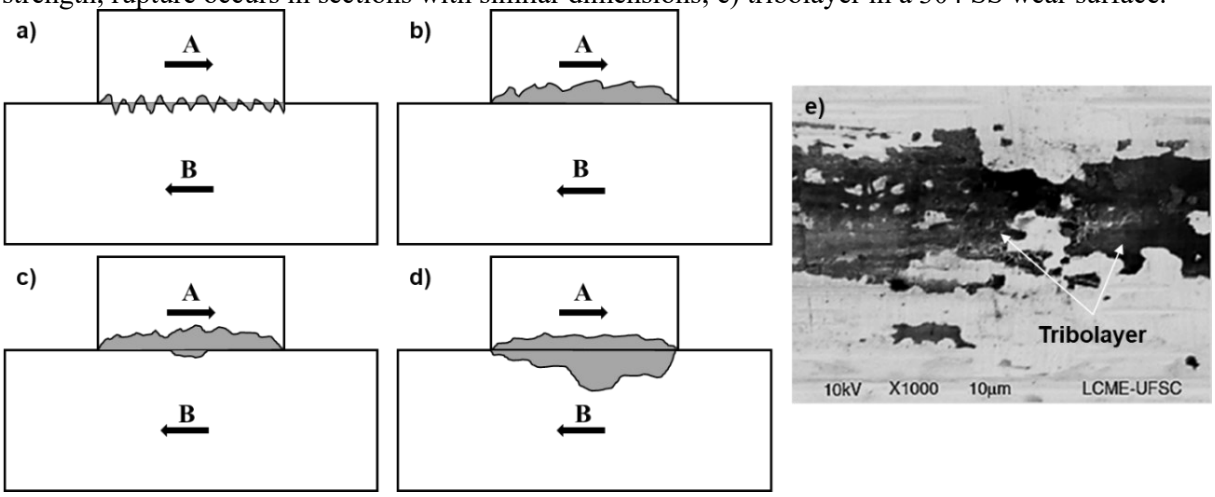
Wear can occur due to different mechanisms, such as abrasive, adhesive, corrosive, erosive, cavitation, fatigue, and tribochemical. When two surfaces are in contact under a load, the difficulty of moving one surface relative to the other corresponds to friction. Friction is proportional to the applied normal load, independent of the apparent contact area and the sliding

speed. Equation 2.1, the relationship between the frictional load (F_L) and the normal load (N_L), is known as the friction coefficient (COF). This is influenced by the properties of the materials in contact, sliding speed, and medium characteristics. In a tribosystem, after some cycles, COF tends to reach a steady state, where COF stabilizes [111], [114].

$$COF = F_L - N_L \tag{2.1}$$

Besides friction, this work also highlights two main wear mechanisms: adhesion and abrasion. The first results from the contact between specific points on the surfaces of solid parts lead to material transfer between them or from one to the other at the adhesive interface. Adhesion is influenced by the physical and chemical properties of the materials in contact, the applied load, and the surface characteristics. Figure 2.10 illustrates the types of adhesive interfaces: a) when the resistance of the interface is lower than that of the contacting materials (A and B), rupture occurs at the interface; b) and c) the more resistant material loses a smaller portion of material due to adhesion; d) in materials with similar strength, rupture tends to occur in sections with analogous dimensions [51].

Figure 2.10 - Adhesion: a) interface with lower resistance regarding the materials; b) and c) when one of the materials has higher strength, rupture occurs in the weaker material; d) in materials with similar strength, rupture occurs in sections with similar dimensions; e) tribolayer in a 304 SS wear surface.



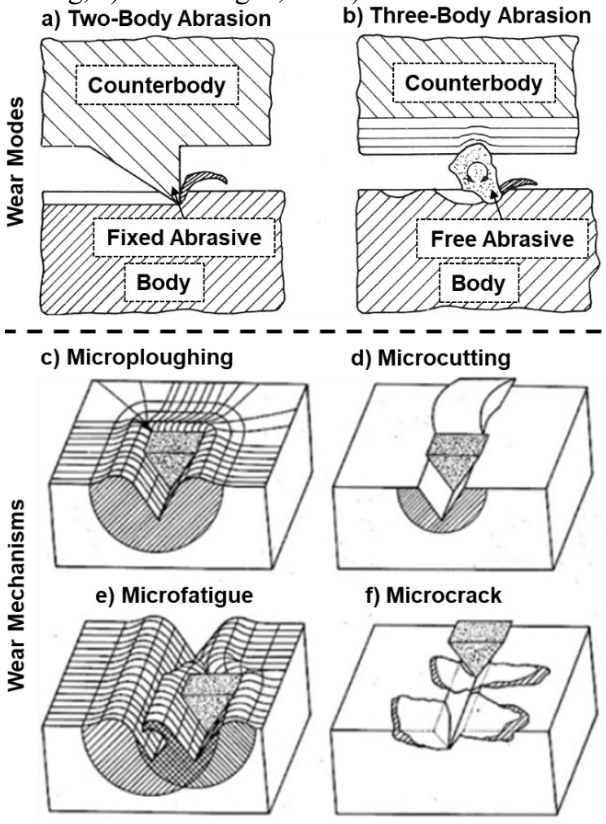
Source: Adapted from [115].

Within the adhesive mechanism, it is important to highlight the tribolayers (Figure 2.10e). These are layers formed by the accumulation and compaction of debris over anchoring areas (microstructural phases or surface defects) at the interfaces of two surfaces in relative motion. Their formation is facilitated at higher temperatures. Tribolayers can be more or less

compact. The compact tribolayer provides effective lubrication in COF reduction and offers a barrier against wear mechanisms. Once consolidated, tribolayers can persist for long periods of component operation or be destroyed, generating more debris [115]–[117].

Abrasion results from the interaction between hard particles against surfaces in relative motion. This can lead to plastic deformation and material removal. Wear mode can occur by sliding due to greater surface hardness, or by hard particles adhered to one of the surfaces (two-body, Figure 2.11a); or of the rolling type due to the free hard particles at the interface (three-body, Figure 2.11b). Wear can also be classified based on the surface aspect into four types: microploughing (Figure 2.11c), where the deformed material accumulates in front of the abrasive particle and flows to the edges of the plough; microcutting (Figure 2.11d), in which the abrasive particles cut the surface, removing material and leaving a clean scratch appearance; microfatigue (Figure 2.11e), where the material is subjected to cyclic deformation until it reaches the fatigue limit, leading to material removal; and in microcracking (Figure 2.11f), in which fragments are detached from the surfaces. The number of factors influencing abrasive wear is extensive, encompassing the load to which the component is subjected, abrasive features (hardness, geometry, and size), and the properties of the materials in contact [51], [111].

Figure 2.11 - Abrasion wear modes: a) and b) two and three body; abrasion wear mechanisms: c) microploughing, d) microcutting, e) microfatigue, and f) microcrack.



Source: Adapted from [51].

2.5.3 Wear prevention

Protecting components subjected to wear can be achieved by adopting measures that reduce friction and wear while maximizing lubrication. The use of wear-resistant materials, such as some SS and superalloys, and the application of post-treatments like heat-treatment [6], remelting [31], and thermochemical treatments (boronizing, nitriding [114], [118]); thin-films (chemical vapor deposition and plasma vapor deposition [119], [120]) are important. Cladding techniques (welding, hardfacing, plasma transferred arc, tungsten inert gas [7], [121], [122], thermal spraying [31], [123], and L-DED [18], [124], [125]) can also be employed.

2.5.4 Tribological tests

Tribological tests can be either phenomenological (general wear setups) or operational (specific setups, such as in-situ tests). Tribometers are devices that simulate actual application conditions on an accelerated scale. Some of these tests are standardized:

- Wear tests for sliding and rolling: evaluate wear conditions between two bodies, where a specific mechanism is not characterized. Examples include block-on-ring [126], cylinder-on-cylinder, pin or ball-on-disk [127], and linearly reciprocating ball-on-flat [128].
- Abrasive wear tests: evaluate three-body wear conditions. The formation of ploughings and scratches is common in these configurations. Examples include pin-on-sandpaper, microabrasion calotest, and dry sand/rubber wheel apparatus [129].

These tests can be performed in either dry or wet environments, at milder or elevated temperatures. This study evaluates the tribological performance of AISI 410L manufactured by AM L-DED in terms of friction, adhesion, and sliding abrasion. Therefore, the linearly reciprocating ball-on-flat test [128] was chosen, aiming to replicate an oscillatory sliding effort, which is generally more severe than the rotational ball-on-disk test [127], owing to the difficulty placed on the debris' compaction due to the abrupt and ongoing change in the applied effort, which increases friction and wear coefficient. Severe contact was intended by selecting a short track length, a high normal load, and a sliding speed that would stress the tribosystem [130].

2.6 CORROSION RESISTANCE

Stainless steels, including the MSS grade, are also industrially recognized for their corrosion resistance. This section briefly describes general aspects of this science.

2.6.1 Corrosion concepts

All chemical elements tend to return to their thermodynamic condition of greater stability, with lower free energy, which is the mineral state. Corrosion occurs when chemical and electrochemical reactions with other atmospheric elements generate deterioration and material removal [43], [131]. The main corrosion mechanisms are atmospheric, galvanic, high temperature, and fatigue. Atmospheric corrosion is most commonly found in marine environments and is caused by water (H_2O), O_2, carbon dioxide (CO_2), hydrogen sulfide (H_2S), chlorides (Cl^-), microorganisms, and salts [132].

Electrochemical corrosion is established by two electrochemical reactions, one partial anodic (metal oxidation) and one partial cathodic (reduction of H_2O, H_2, or O_2). The process starts in a stress riser region of the anode (e.g., defect). From this, a Fe-ion (Fe^{2+}) leaves the metallic surface and goes towards the electrolyte, thus losing electrons, that is, oxidizing. This anodic reaction is expressed by Equation 2.2. Simultaneously, the electrons resulting from the Fe^{2+} dislocation are sent from the anode to the cathode through the electrically conductive steel. At the same time, a reaction takes place at the cathode in which electrons are accepted by the electrolyte, and O_2 absorption (Equation 2.3). When corrosion starts in the O_2 presence, the formation of rust occurs, which is the Fe in its lowest energy state (Fe_2O_3) [42], [132].

$$Fe \rightarrow Fe^{2+} + 2e^- \tag{2.2}$$

$$2H_2O + O_2 + 4e^- \rightarrow 4OH^- \tag{2.3}$$

Electrochemical corrosion can be started by: metals with impurities (one is cathodically protected by the other due to the potential difference); equal metals with different solution concentrations (the metal immersed in a less concentrated solution is dissolved from this electrode and deposited on the electrode immersed in a more concentrated solution); similar metals exposed to different temperatures (when these are in electrical contact, the metal dissolves at the lower temperature anode, and is deposited at the higher temperature cathode). When a metal is immersed in a solution containing self-ions, it can lose an electron (corrosion) to form metal ions, or these metal ions can gain electrons (reduction) and enter the solid metal.

When a current is applied, the difference between the applied potential (E_{app}) and the corrosion potential (E_{corr}) corresponds to the electrode polarization (E_p, Equation 2.4). When a cathode current is applied to the electrode, electrons accumulate in the metal because of the low transfer charge. To avoid charge accumulation on the electrode, the sum of the anode currents must equal the sum of the cathode currents. During polarization, the anodic and cathodic curves intersect at a point where the current is maximized, and the E_{corr} is measured. The current value measured in E_{corr}, called the corrosion current (I_{corr}) is used to calculate the corrosion rate [43].

$$E_p = E_{app} - E_{corr} \tag{2.4}$$

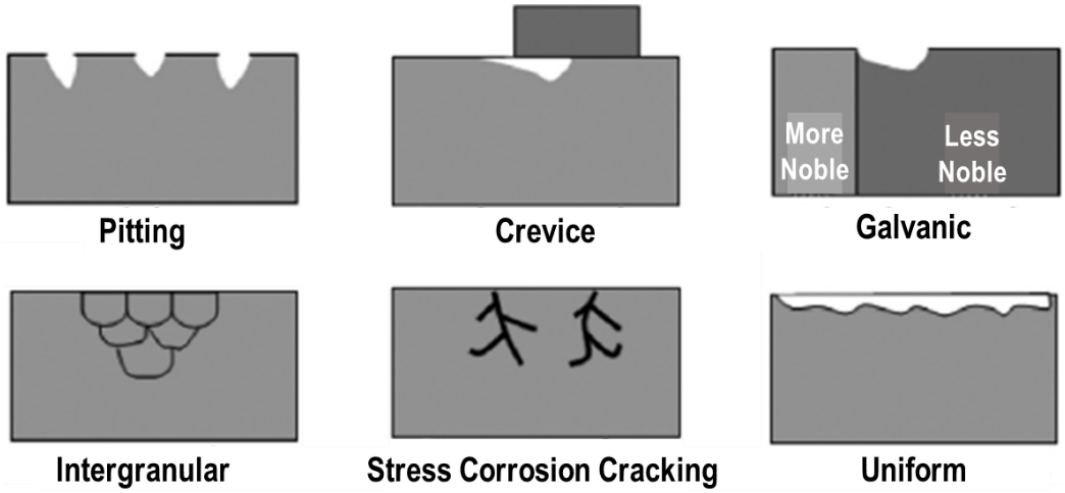
2.6.2 Corrosion mechanisms

Literature categorizes corrosion mechanisms into different nomenclatures, which are illustrated in Figure 2.12:

- *Pitting Corrosion*: a localized etching occurs on the material surface, nucleated over a defect (porosities, cracks, regions with deficient chemical composition) or by breaks in the Cr_2O_3 passive layer. Its intensity is related to the ions (e.g., Cl^-) concentration, environment pH, temperature, structural characteristics, and chemical composition [133], [134].
- *Crevice Corrosion*: its nucleation is dependent on a crevice's existence. The same influencing factors highlighted for the pitting are valid here [135].
- *Galvanic Corrosion (Bimetallic)*: occurs when different metals are placed in the same electrolyte. When an electric current flows between the two, the less noble one (anode) is corroded at a higher rate when compared to a condition with these same metals separated. It is common to employ less noble sacrificial anodes (e.g., zinc, Zn), which are consumed by anodic dissolution and protect the more positive metal against corrosion [43].
- *Intergranular Corrosion*: grain boundaries are susceptible to corrosion when enriched or depleted in elements regarding the matrix, due to the formation of compounds [136].
- *Stress Corrosion Cracking*: is a time-dependent chemical-mechanical anodic crack nucleation process that occurs in metals immersed in a corrosive environment (e.g., H_2O, Cl^-, O_2, H_2S), and with the simultaneous applied stress greater than the material yield strength (YS) [42], [137].

- *Uniform Corrosion*: causes deleterious effects in a generalized form, without identifying preferred cathodic and anodic sites. It can be measured electrochemically or by weight loss. It is governed by humidity, temperature, electrolyte pH, and ions (e.g., Cl^-) [138].

Figure 2.12 - Illustration of corrosion mechanisms.



Source: Adapted from [139].

It is also important to highlight the concern with hydrogen (H). This element can be involved with other elements during corrosion, in defects (e.g., porosities and voids) in the form of gaseous molecules with a large size, which reduce the atomic surface energy for a tensile effort, nucleating cracks [42], [43].

Different aspects contribute to the nucleation and expansion of corrosion mechanisms:

- Surface finish: elevated roughness leads to the accumulation of impurities and forms valleys, which concentrate corrosion products [137], [140].
- Porosities: these can be interconnected or closed. The first type is more damaging as it allows a free pathway between the corrosive environment and the exposed surface. Closed porosities, in turn, facilitate the corrosive material accumulation [141], [142].
- Humidity: in the presence of corrosive agents (e.g., Cl^-), higher humidity may be desired, as it provides dissolution, reducing the solution's E_{corr}. It is recommended that this be as low as possible, as H_2 and O_2 increase corrosion susceptibility [143].
- Microstructure: the existence of inclusions in the microstructure is a critical point, as these act as nucleators and propagators of corrosive mechanisms. Austenite (γ) is the phase with higher corrosion resistance, given its chemical composition and lower level of residual stresses [144]. After γ, ferrite is more corrosion-resistant due to its BCC structure with low-C solubility and consequently greater difficulty in forming precipitates. Martensite,

on the other hand, is more susceptible to corrosion due to its C-rich, uneven BCT structure, which is prone to precipitate formation, generating pits, and sensitization [145].

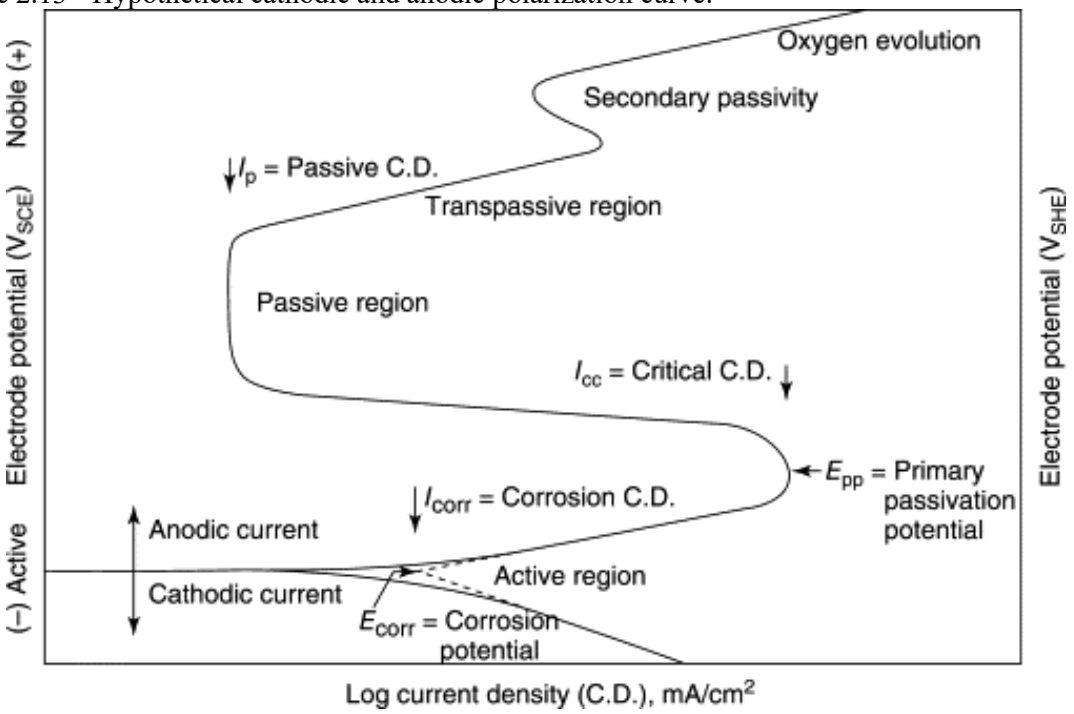
Regarding PHT influence, in the austenitization, the entire structure is annealed, providing dissolution of grain boundaries and precipitates. The fully martensitic microstructure in the quenching stage reduces the corrosion performance. If tempering is performed improperly, it can generate precipitates that decrease the Fe-matrix corrosion performance by corrosion-resistant elements depletion, such as Cr, owing to the sensitization [3], [146]–[148].

2.6.3 Corrosion assessment techniques

There are different methods to investigate corrosion resistance, such as corrosive solution immersion [149], salt spray atmosphere [150], and electrochemical tests (potentiodynamic polarization) [151]. In the latter, when metallic materials are placed in an electrolyte, there is a change in the start potential of the electrodes. The electrode potentials approach each other. This technique sweeps the potential continuously, recording the current.

Figure 2.13 illustrates the theoretical curve of applied potential versus current density on a logarithmic scale (LOG). In this, regions are defined from a more active to a nobler potential (anodic), passing through the active, passive, and transpassive stages. The immunity region is the range in which the material does not undergo oxidation, given the applied potential, while the active region describes where the current increases with potential elevation. However, from a certain potential, the current reduces to a constant density region (primary passive potential, E_{pp}). To reach the passive region, one must exceed the critical corrosion current (I_{cc}). Next, there is the passive region itself. Depending on the applied potential, the current increases again, and the region above this is called the transpassivation region. In this, the passive layer is deteriorated or removed. Corrosion start is defined by the potential at which the anodic and cathodic currents cancel each other out. The more positive the corrosion potential (E_{corr}) and the lower the current corrosion (I_{corr}), the greater the corrosion resistance. The passive region is the potential range in which the passive corrosion current (I_p) is maintained [42], [151].

Figure 2.13 - Hypothetical cathodic and anodic polarization curve.



Source: Adapted from [151].

2.6.4 Corrosion prevention

There are two main ways to combat corrosion, the use of special materials or mitigating deleterious environmental conditions. Regarding the latter, the atmosphere can be modified (e.g., deoxidizing elements, such as S) or the modification of operating conditions (e.g., temperature, humidity). As for special materials, alloys enriched in anti-corrosive elements, or coatings (e.g., hardfacing, thermal spray, and laser cladding) [131], [143], [152].

The SS possesses a Cr-oxide passive layer (Cr_2O_3, formed by exposing the high Cr-content SS to an O_2-rich atmosphere), which provides a potential change of the electrode towards lower activity, whether it be more cathodic or anodic, which separates the SS surface from the corrosive atmosphere. This passive layer is formed by the Fe^{2+} oxidation at the SS-oxide interface, while O dissolved in water is ionized at the oxide-electrolyte interface to O anions. Passive layer maintenance results from the migration of O ions within the electrolyte-oxide interface to react with the metallic ions inside the oxide and Fe^{2+} that migrate from the oxide-Fe interface to the oxide-electrolyte interface and thus react with the oxides. At the same time, the electrons generated in the anodic reaction at the SS-oxide interface are transported to the cathodic reaction at the oxide-electrolyte interface [153].

2.7 MARTENSITIC STAINLESS STEEL MANUFACTURED BY AM L-DED

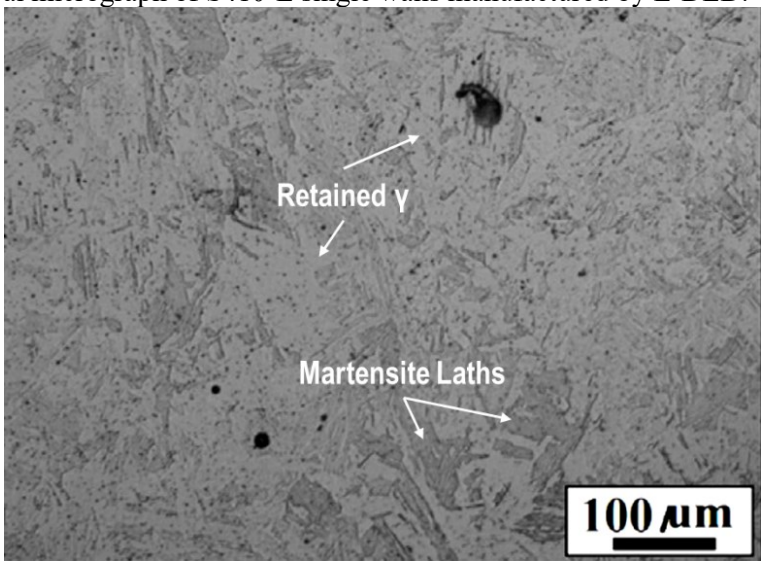
This section provides a state-of-the-art review regarding the processing of 410L MSS by AM L-DED, aiming to present a context about the microstructure, mechanical properties, tribological performance, corrosion resistance, and the effects of PHT on these aspects.

2.7.1 Microstructure

Additive manufacturing by laser directed energy deposition generated a heterogeneous microstructure. Near the layer's boundaries, microstructure tends to present an elongated morphology, with cellular growth due to the directional solidification front. When moving towards upper layer regions, the solidification mode changes to equiaxial. This behavior refers to the relationship between the temperature gradient (G) and solidification ratio (R). G*R product determines the cooling rate and grain size, while the G/R relation prescribes the solidification mode. With G/R increase, the solidification front changes from planar to cellular, columnar, and equiaxial dendritic, respectively. Thus, in the first layers, close to the substrate, G and R are higher, characterized by planar and epitaxial growth. In the upper layers, reheating and cooling of the previous layers revert this relationship and switch the solidification mode to cellular, columnar, and equiaxed dendritic. G and R also fluctuate according to the geometry, material properties, and process conditions [15], [88]. MSS chemical composition provides the martensitic transformation during and after solidification [62], [154].

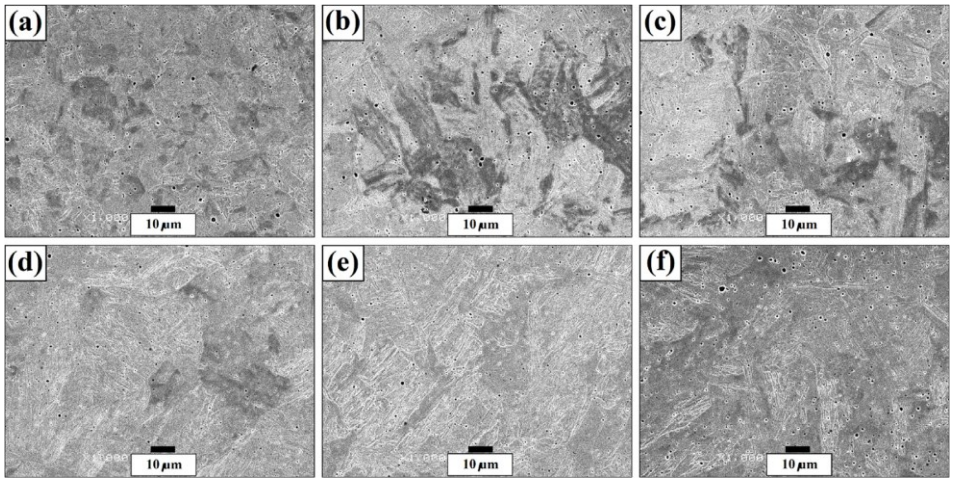
Khodabakhshi *et al.* [8] evaluated the properties of S410-L MSS single walls built by AM L-DED. In the optical microscope (Figure 2.14), the authors observed martensite laths (darker regions) and retained-γ (light regions). The scanning electron microscope (Figure 2.15) showed martensite blades and micro-twinings. Khodabakhshi *et al.* [155] investigated the AM L-DED crystallographic texture of the S410-L MSS single walls' microstructure. SEM revealed equiaxed grains for commercial S410-L MSS (hot-rolled). S410-L AM L-DED, in turn, exhibited a fully lath martensitic microstructure. Martensite laths became coarser with the layers number increase, due to the peak temperature increment and the reheating/cooling cycles. Electron Backscatter Diffraction (EBSD) maps (Figure 2.16) showed that the mean grain size, misorientation angle, and *J-index* were much higher in the AM L-DED S410-L compared to the commercial S410-L MSS, attesting to the L-DED microstructure heterogeneity.

Figure 2.14 - Optical micrograph of S410-L single walls manufactured by L-DED.



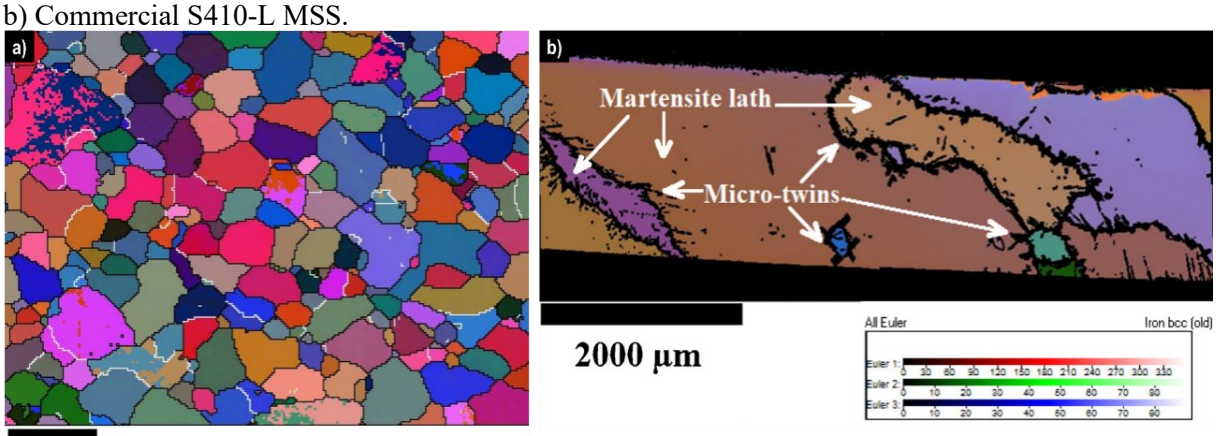
Source: Adapted from [8].

Figure 2.15 - SEM micrographs of S410-L single walls manufactured by AM L-DED: a-d: martensite blades, e-f: micro-twins between martensitic structure.



Source: [8].

Figure 2.16 - EBSD grain structure maps and some microstructural details: a) AM L-DED S410-L MSS, b) Commercial S410-L MSS.



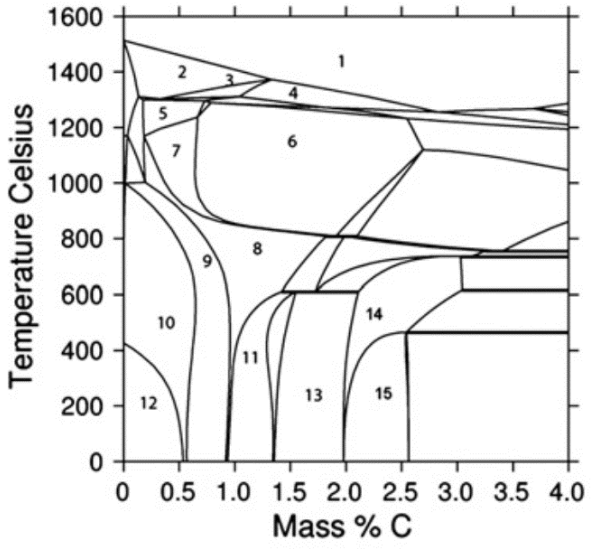
Source: Adapted from [155].

Farshidianfar *et al.* [85] analyzed S410-L MSS single walls manufactured by L-DED under two conditions (1 - controlled, in which the travel speed was adapted to provide 3 different fixed cooling rates; 2 - uncontrolled, in which the travel speed was varied by 3 fixed levels and the cooling rate was a consequence). The higher cooling rate parameters generated a homogeneous microstructure while reducing the height of the single walls. The size and morphology of the martensite laths and micro-twins in condition 2 were more heterogeneous, due to the sudden cooling rate variation between layers. Condition 1, in turn, exhibited greater homogeneity, owing to the less intense thermal history fluctuation. As the martensitic is a solid-state transformation, S410-L MSS is only influenced by the G*R relation, which rules the cooling rate. Thus, the higher the cooling rate, the higher the level of refining and consequently the volume fraction of martensite laths and micro-twins.

Fenech, Grech, and Betts [156] evaluated temperature variation and WC powder particles dissolution in AISI 410 MSS laser cladding combined with microstructure analysis by ThermoCalc® prediction and experimental approach. The results showed coarse epitaxial grains from the substrate for the AISI 410 MSS without WC coating. EBSD revealed that the Fe-matrix is martensite, while the secondary is M_7C_3 carbide. Martensite can be explained by the isothermal diagram (Figure 2.17), in which, under ordinary cooling conditions, upon reaching the γ-loop (No. 6), with further cooling, a BCC structure must be noted (No. 7, 8), however, undercooling imposed by the laser suppresses this transformation, establishing an uneven fully martensitic structure. The C-content rejected in this kinetics reduces the solidus temperature, allowing secondary carbides precipitation (No. 13, 14, 15).

In another study, Fenech *et al.* [97] evaluated the AISI 410 MSS+Cr_3C_2 deposited by L-DED over the AISI 420 MSS substrate. In the theoretical isotherm curves, the authors pointed out that Cr_3C_2, beyond 2% addition, stabilizes γ owing to the C introduction, switching the α to γ. The as-built AISI 410 MSS microstructure exhibited an epitaxial growth close to the substrate, followed by competitive growth near the upper layers. The Cr_3C_2 addition provided grain refining and carbide precipitation at grain boundaries. In the XRD, as-built AISI 410 SS showed α as the primary phase. Martensite was detected in 2% Cr_3C_2 cladding, and the Cr_3C_2 increased by 5% and 10%, generating a biphasic martensite-γ and fully γ, respectively.

Figure 2.17 - Isothermal phase diagram (ThermoCalc®) according to C-content (wt.%) variation keeping Fe, Cr, and W contents constant.



1 Liquid
2 liquid + BCC
3 Liquid + BCC + FCC
4 Liquid + FCC
5 BCC + FCC + M_6C
6 FCC + $M_{23}C_6$ + M_6C
7 BCC + FCC + $M_{23}C_6$ + M_6C
8 BCC + $M_{23}C_6$ + M_6C
9 BCC + Laves + $M_{23}C_6$ + M6C
10 BCC + Laves + $M_{23}C_6$
11 BCC + $M_{23}C_6$ + M_6C + M_7C_3
12 BCC + BCC2 + Laves + $M_{23}C_6$
13 BCC + M_6C + M_7C_3 + MC
14 BCC + M_7C_3 + MC
15 BCC + M_3C_2 + M_7C_3 + MC

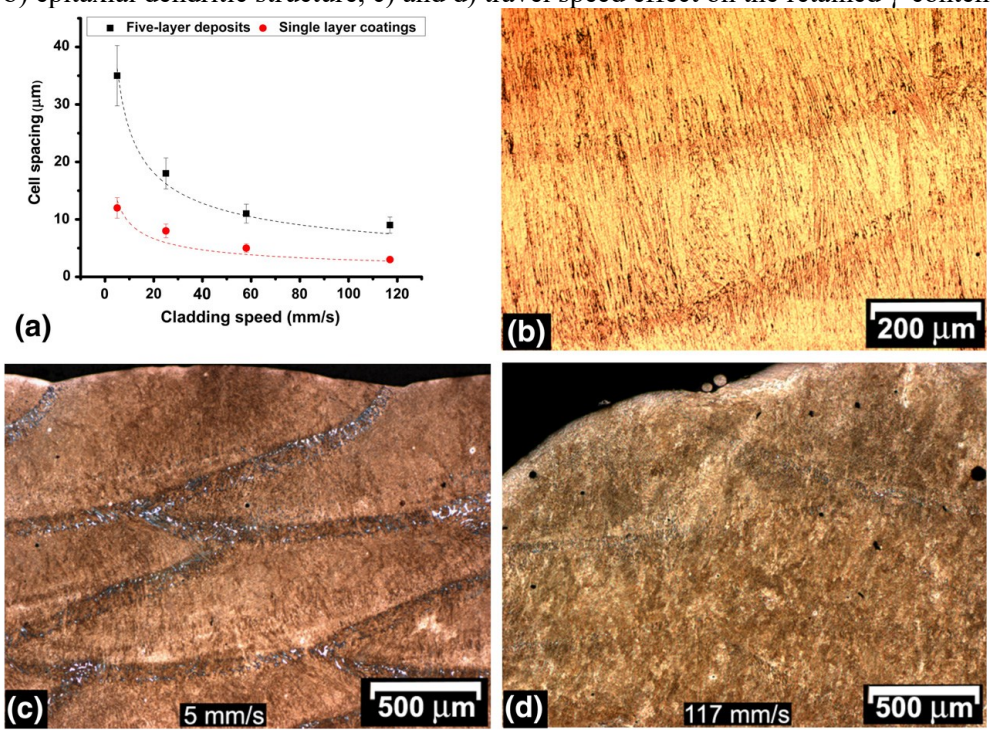
Source: [156].

Hemmati *et al.* [17] evaluated the effect of the travel speed on the microstructure of AISI 431 MSS deposited by laser cladding. The authors investigated coatings with 1 and 5 layers, with travel speeds of 5, 25, 58, and 117 mm/s. The authors observed a reduction in dendritic cell spacing of 3 μm (1 layer) and 9 μm (5 layers), respectively (Figure 2.18a), owing to the heat accumulation provided by the increase in the number of layers. An example of dendritic epitaxial growth from the upper region is seen in Figure 2.18b. Figure 2.18c-d demonstrated that elevating travel speed generated coatings with higher retained-γ content. Similar interactions were described by Colaço *et al.* [61] and Chen *et al.* [157] in the microstructure study of AISI 420 MSS laser cladding. However, contrary behavior was reported by Krishna and Bandyopadhyay [158] in the evaluation of AISI 410 MSS treated by L-DED, where the higher cooling speeds elevated M_s and reduced the retained-γ content.

Uematsu *et al.* [159] analyzed the 420 MSS single walls manufactured by L-DED, with and without cooling dwell-time to room temperature at half the perform height. The reference material (annealed, quenchend+tempering) exhibited a mix of ferrite and martensite plus dispersed carbides. L-DED microstructure, in turn, was predominantly martensitic.

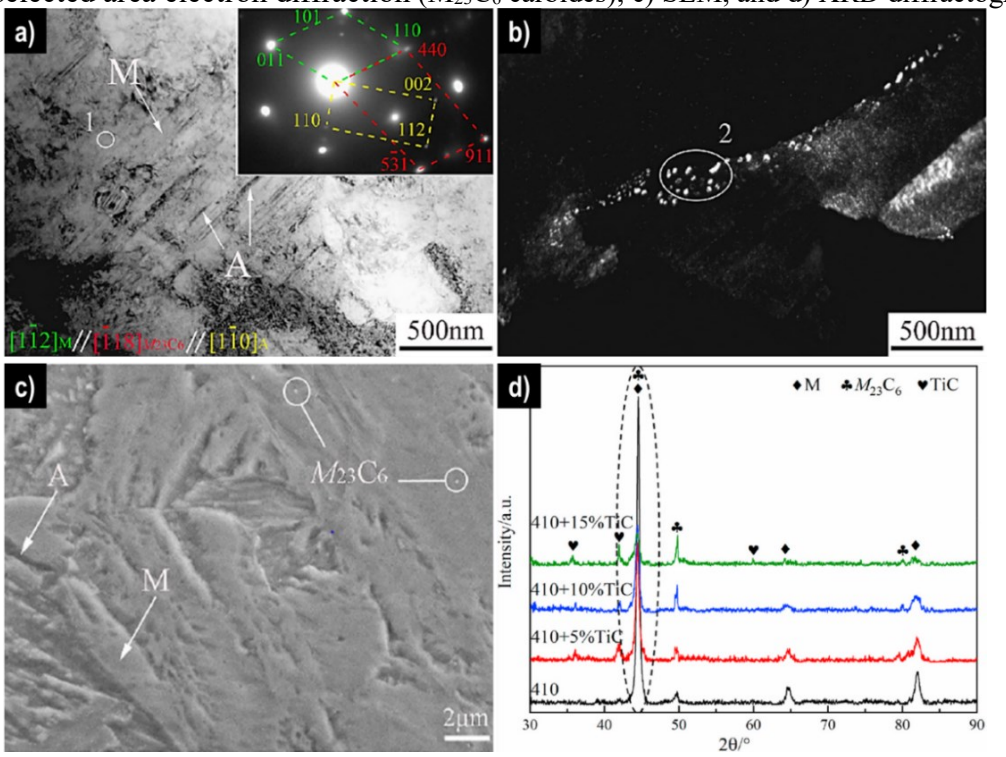
Zhu *et al.* [18] evaluated AISI 410 MSS coatings with Ti-carbides (TiC) deposited by laser cladding. Transmission electron microscope (TEM) analysis of the coating microstructure without TiC showed martensite lath (M), uneven retained-γ bands (A) (Figure 2.19a, bright field, and selected area electron diffraction), and $M_{23}C_6$ carbides (2) (Figure 2.19b, dark field). These features corroborated the SEM aspects (Figure 2.19c) and XRD (Figure 2.19d).

Figure 2.18 - Laser cladding of AISI 431 MSS: a) travel speed effect on the cell spacing of 1 and 5-layer coatings, b) epitaxial dendritic structure, c) and d) travel speed effect on the retained γ-content.



Source: [17].

Figure 2.19 - AISI 410 MSS coatings microstructure: a) TEM bright field (martensite M, austenite A); b) TEM selected area electron diffraction ($M_{23}C_6$ carbides); c) SEM, and d) XRD diffractogram.



Source: Adapted from [18].

Lai *et al.* [46] analyzed 410L MSS coatings deposited by laser cladding for rail protection. Coatings with 1 and 2 layers were studied, with the application of preheating at 350 °C, and pre- and post-heating at 350 °C. Regardless of the number of layers and the heat-treatment, large dendritic ferrite grains dominated the top and overlayer regions. Martensite was evident only in the first layer and in the HAZ of all coatings. The condition with pre- and post-heating was efficient in reducing and tempering the martensite volume, due to the lower cooling rate. The low C-content in the regions far from the substrate and the constrained elements homogenization provided by fast solidification influenced the ferrite formation. This behavior was attested by a previous work by Lai *et al.* [160], which evaluated the effects of preheating and dilution with the C-rich hypereutectoid substrate on the 410L MSS coatings with 1 and 2 layers. The martensite was predominantly and evenly distributed in the first layer, while in the second, elongated ferrite grains extended along the entire layer thickness and the overlap regions. The first layer acts as a barrier against dilution with the C-rich substrate. Reheating imposed by the second layer promotes a redistribution of C atoms so that the ferritic grains of the first layer merge with those of the second layer. In other works by the group focused on the analysis of these pre- and post-heating treatments on wear resistance, contact fatigue, and mechanical performance of 410L MSS, Roy *et al.* [98], [161] found an analogous microstructure, with martensite being only at the interface as a function of dilution with C-rich substrate. In another study, Lai *et al.* [96] investigated the applicability of 410L MSS in rail repair by laser cladding. Besides martensite and ferrite, the authors detected retained-γ, whose presence was attributed to the segregation of C and Mn at the grain boundaries.

As noted, several factors influence the final microstructure characteristics of MSS when processed by L-DED. Under process parameters, thermal history (e.g., dimensions, distance from the substrate, thermal management handling), the chemical composition of feedstock and substrate (e.g., contents of γ or α stabilizer elements), microstructures with a greater predominance of one phase, different levels of grains refining, different kinds of precipitates, as well as the possibility of embrittlement mechanisms occurrence.

2.7.2 Mechanical performance

AM L-DED mechanical behavior is dependent on the entire manufacturing set, encompassing thermal history, density, microstructure, build patterns, and orientation.

2.7.2.1 Hardness

AM L-DED generated hardness variation along with the built thickness, due to microstructure (e.g., grain size, morphology), and different thermal histories. The first layer benefits from greater heat-sink through the conduction mechanism to the substrate, while the upper layers exchange less heat by this mechanism, having more convection and radiation with the atmosphere. The middle, on the other hand, is subjected to the reheating cycles of the subsequent layers, remaining for a longer period at high temperatures. As a result, usually, higher hardness is observed in the lower and upper regions [15], [16], [90].

Khodabakhshi *et al.* [8] reported that the fully martensitic S410-L MSS transformation provided by L-DED generated a significant hardness increase. The hardness profile varied according to the indentation position, being higher in martensite laths and lower in retained-γ films. A 290 HV average was obtained for S410-L single walls manufactured by AM L-DED, 25% higher when compared to the as-rolled state. This performance was attested in another paper by Khodabakhshi *et al.* [155], in which the hardness of S410-L MSS in the as-built state (~290 HV, lath martensitic microstructure surrounded by micro-twins) was significantly higher than that of commercial state S410-L MSS (~233 HV).

In the S410-L MSS single walls, Farshidianfar *et al.* [85] claimed that for both conditions (1 - controlled; 2 - uncontrolled), the hardness increased with the travel speed elevation, and the consequent cooling rate. The condition 1 hardness profiles were more homogeneous, due to their more refined martensite laths and micro-twins. In condition 2, the hardness decreased according to the elevation of the number of layers.

Krishna and Bandyopadhyay [158] evaluated the hardness of AISI 410 MSS treated by L-DED. The authors observed that the hardness variation as a function of the L-DED parameters showed a similar trend to the retained-γ content, and the samples treated with higher P and S showed greater hardness (350 HV in the melting zone) due to the lower amount of retained-γ. Hardness reduced from 300-200 HV in HAZ owing to the complete steel austenitization, while the substrate exhibited only 120 HV.

In the laser cladding AISI 410 MSS+Cr_3C_2, Fenech *et al.* [97] observed a hardness increase for 2% Cr_3C_2, followed by a reduction provided by the Cr_3C_2 increment. This

performance was conferred to the strengthening generated by γ-martensite transformation. Meanwhile, C-content increases with higher Cr_3C_2 levels, lowering M_s, stabilizing the γ.

Hemmati *et al.* [17] observed greater homogeneity of laser cladding AISI 431 MSS, composed of 1 layer in assessing hardness. Whereas the 5-layer coatings did not show changes according to S modification, the 1-layer coatings exhibited a decrease in hardness proportional to the deposition rate increment. This variation can be given to the different phases formed during cooling. According to the time-temperature-transformation (TTT) diagram, AISI 431 is highly hardenable, so phases other than martensite can only be formed at low cooling rates. In this paper's concern, achieving these cooling levels is virtually impossible. In this sense, hardness fluctuation may be an indication of different amounts of martensite and retained-γ.

Uematsu *et al.* obtained a 532 HV hardness for the reference material and 573 HV for the 420 MSS manufactured by L-DED. However, the hardness profile along the single wall exhibited a softer region in the middle of the preform. This behavior is due to the tempering provided by the slow cooling cycle at room temperature [159]. In the laser cladding AISI 410 MSS coatings without TiC, Zhu *et al.* achieved a 462 HV, so it exhibited insignificant variation along the profile performed in the layer, thus attesting to the microstructure homogeneity along the coating thickness [18].

In the work by Lai *et al.*, hardness profile fluctuation was insignificant for the 410L MSS coating submitted to pre- and post-heating treatment at 350 °C, which was attributed to the microstructure tempering. In the preheating condition, a hardness peak was observed in the HAZ, which was attributed to the dilution with C-rich hypereutectoid substrate [46]. Similar trends were described in other works by the group [160], [161].

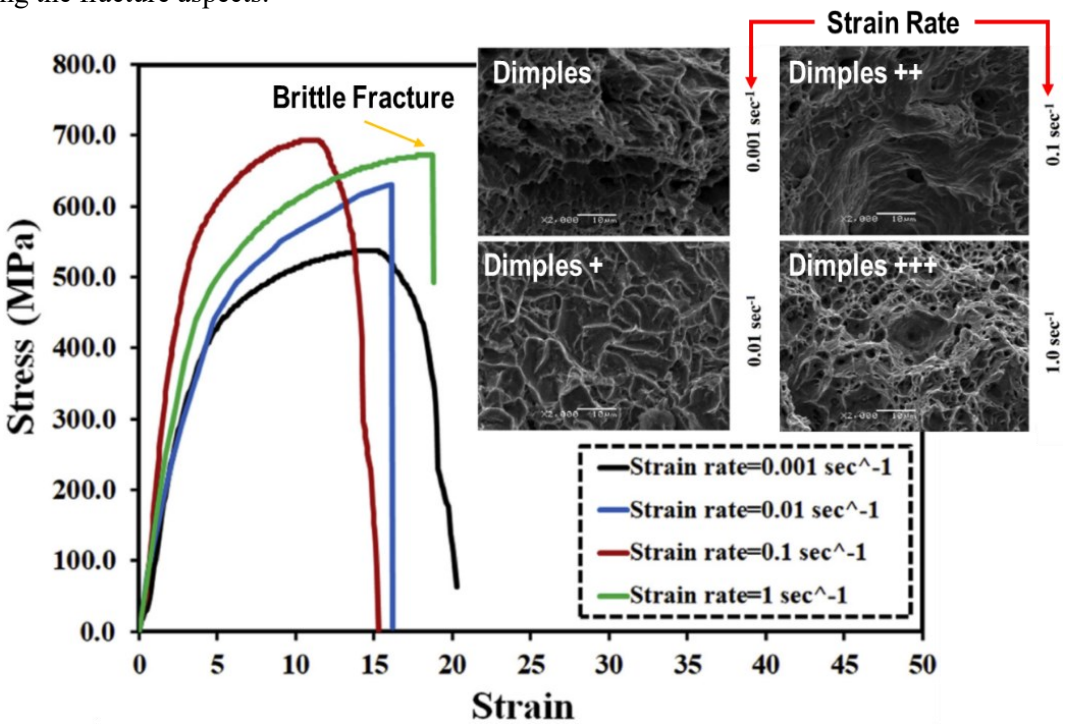
As noted, hardness is a function of different microstructure characteristics. In general, microstructures fully martensitic, with refined grains, and with strengthening phases precipitation (e.g., carbides) showed greater hardness. These aspects also affect other mechanical properties of built components.

2.7.2.2 Tensile strength

Khodabakhshi *et al.* [8] analyzed the tensile strength (ASTM E8M, specimen 2) of S410-L MSS processed by AM L-DED, varying the strain rate. A direct dependence of this on the UTS was observed, with the maximum value (696 MPa) being 30% higher than the others. This behavior can be attributed to the activation of phase transformations under high-straining

rates through the micro-twining mechanism. In the digital image correlation (DIC) analysis, S410-L did not exhibit necking until the fracture. This result can be explained by the superplasticity theory, which claims that the refined equiaxed grain structural morphology can present a large amount of even and uneven strains through the grain slip mechanism. However, martensitic transformation imposed by the micro-twinning during the L-DED makes the microstructure sensitive to sudden fracture after any tensile flow instability, a phenomenon observed in Figure 2.20. In the fractures, a quasi-ductile appearance was observed, owing to the presence of martensite, retained-γ, and micro-twins in the microstructure. Elevation in strain rate enhances the fracture toughness (area under the stress-strain curve), while the size of the dimples increases proportionally.

Figure 2.20 - Stress-strain tensile flow curves of S410-L manufactured via AM L-DED and SEM images showing the fracture aspects.



Source: Adapted from [8].

In another work, Khodabakhshi *et al.* [155] evaluated the effects of AM L-DED crystallographic texture on the S410-L MSS single walls' tensile behavior. The plastic deformation associated with lath martensite formation and micro-twinning mechanism increased the UTS by 125% concerning S410-L in the commercial state. However, elongation (EL) was reduced by half owing to the poor martensite ductility.

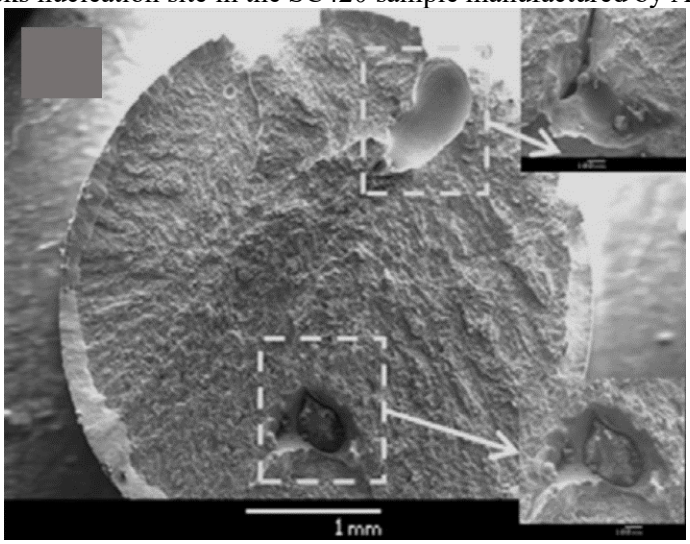
Huang *et al.* [162] evaluated the tensile behavior of 410L MSS from a rectangular sample manufactured by L-DED. The authors found YS=330 MPa, UTS=545 MPa, and EL=18%. SEM fracture analysis showed an entirely ductile aspect, with dimples and microvoids. This performance was conferred to the biphasic microstructure composed of large and elongated ferrite grains and a small amount of martensite at the grain boundaries.

Roy *et al.* [98] analyzed the tensile strength of samples taken from 410L MSS laser cladding coatings applied to rails. Samples were evaluated under longitudinal and transversal orientations concerning deposition, with pre-heating at 350 °C, and with pre- and post-heating at 350 °C. Outlining results, longitudinal orientation with only pre-heating showed lower EL, greater YS, and UTS. Post-heating applied to the transversal orientation increased EL and UTS, while YS was similar. In the longitudinal orientation, the post-heating increased the EL by 2 times. Comparing the longitudinal and transversal orientations, the difference in YS and UTS was only 5 and 10%, respectively. The EL, in turn, was greater in the longitudinal orientation, representing a 33% difference in the pre-heated samples and 18% in the post-heated ones. Despite this fluctuation, the absolute values were very low, in the order of 2-6%, which was conferred to the martensite brittleness. Post-heating improved this performance by the formation of a refined microstructure with tempered martensite, and the SEM fractures exhibited smaller dimples regarding pre-heated condition.

Ravi *et al.* [21] evaluated the tensile strength of SC420 MSS specimens (ASTM E8M) manufactured in vertical and horizontal orientations. In the vertical orientation, each layer required 30 s to be deposited in front to 200 s from the horizontal. The vertical sample retained a greater heat-input, being annealed, which gave it 13% EL. The commercial wrought and annealed material showed 15% EL, and in the tempered condition, only 8%. In the horizontal orientation, the longer layer deposition time provided a greater heat-sink by conduction to the substrate, and the EL obtained was only 2-4%, well below the commercial state. Figure 2.21 SEM fractures showed unmelted particles that remained entrapped within the tensile samples, which acted as stress risers and crack nucleation sites.

As noted, tensile strength depends on the entire manufacturing set, from parameters, strategies, and thermal history, through the resulting microstructure characteristics (e.g., predominant phase, strengthening phases), as well as the presence of defects (e.g., cracks, porosities, unmelted particles) that can act as stress risers and crack nucleation sites.

Figure 2.21 - SEM brittle fracture appearance due to the presence of an unmelted particle that acted as a stress raiser and cracks nucleation site in the SC420 sample manufactured by AM L-DED.



Source: Adapted from [21].

2.7.2.3 Impact toughness

Owing to the limited number of references related to the impact toughness of MSS processed by L-DED, in this section, some insights taken from the L-PBF process will be provided. L-PBF is characterized by higher G/R ratios, given the lower energy density levels normally encountered. As a result, there are more refined microstructures, lower residual stresses, and varied mechanical properties concerning the L-DED process [37].

Oh *et al.* [163] evaluated the Charpy impact toughness (ASTM E23) of a 630 (0.05 wt.% C) MSS manufactured by L-DED. In the as-built state, the Charpy impact absorbed energy (AE) of 138 J was attributed to a biphasic microstructure, with tempered martensite laths and retained-γ bands, which increased the AE capability.

Deev *et al.* [164] analyzed Charpy impact toughness at room temperature of AISI 410 MSS samples manufactured by L-PBF. In the as-built, AE was only 5-6 J. This poor performance was attributed to the residual stress. EBSD confirmed the presence of these residual stresses, due to the untempered martensite. After dilatometry analysis, the authors concluded that the two-phase transformations that take place (α-γ around 696 °C, and later martensite formed between 450-190 °C) justify the high level of residual stresses. SEM fracture analysis showed a fully brittle cleavage appearance.

Seede *et al.* [165] analyzed the Charpy impact toughness of an AF9628 (0.2 wt.% C) MSS manufactured by L-PBF. The AE was 28 J, which was attributed to the microstructure with tempered martensite, obtained along with the multilayer's deposition. SEM fractures exhibited small shear lips and microvoids, characteristic of ductile fracture.

Tian, Chadha, and Aranas [166] investigated the Charpy impact toughness of 420 MSS manufactured by L-PBF and obtained an AE of only 11 J. This poor performance was attributed to the fully martensitic and highly tensile stressed microstructure, arising from the intrinsic L-PBF fast solidification.

Impact toughness is a property that is still poorly explored both in L-DED literature and in laser processing in general. Similar to the records observed for tensile strength, impact toughness is dependent on the entire manufacturing history. Attention is called to the greater sensitivity described concerning the presence of stress risers and crack nucleation sites (e.g., strengthening phases, porosities, cracks, and unmelted particles).

2.7.3 Tribological performance

L-DED thermal history influences the material's geometry, microstructure, and mechanical properties. Tribological performance is dependent on all these aspects. This section presents outcomes from studies found, focusing on 410L MSS processed by L-DED. Owing to the limited number of works, the scope was also extended to the laser cladding configuration.

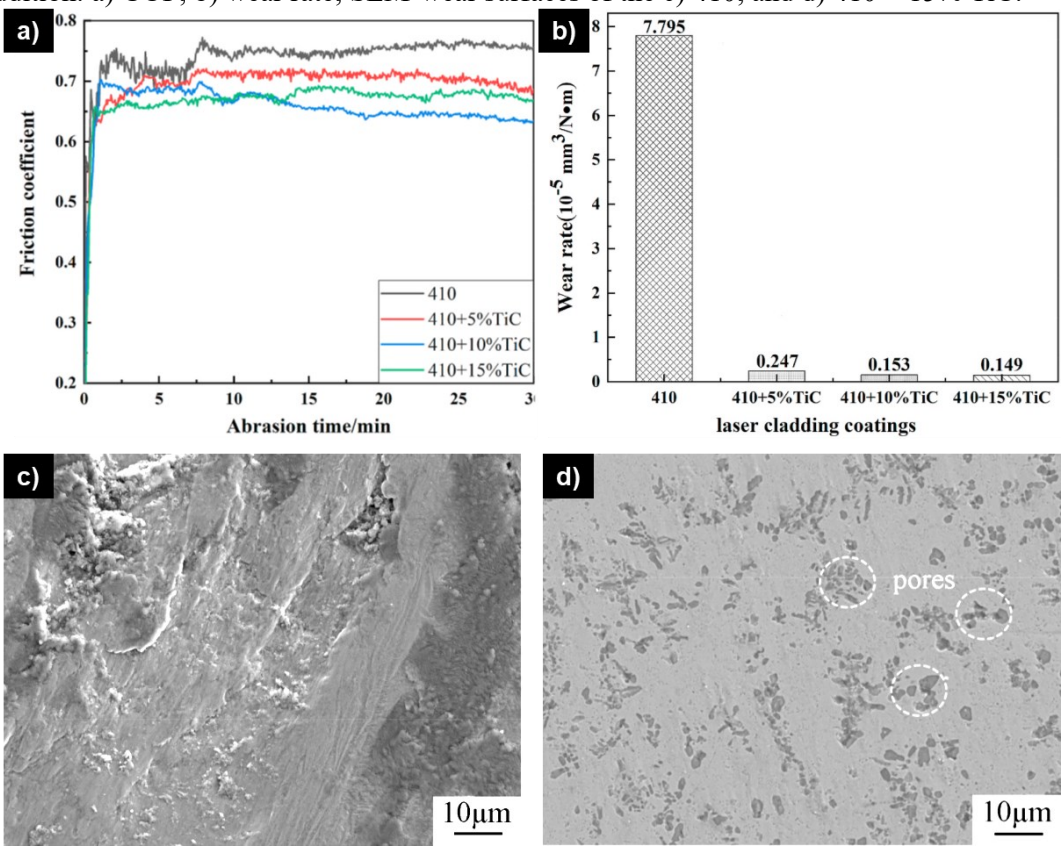
Meura *et al.* [167] performed the ball-on-plane microabrasion test by introducing an abrasive silicon-oxide (SiO_2) solution into the interface between the Ø25.4 mm AISI 52100 ball counterboby and the AISI 410L 5-layer coating (0.02 wt.%C) deposited by L-DED, aiming at its application in the coating of ball valve plugs. L-DED as-built condition exhibited a lower wear coefficient than the current ball plug material. Scratches and SiO_2 inclusions identified by SEM on the wear surfaces of the L-DED condition were less severe than in the ball plug. Refined microstructure and similar hardness justified better L-DED performance.

Roy *et al.* [161] conducted a roller-on-disc test to assess the rolling contact fatigue of 410L coatings (0.01 wt.%C) applied to a hypereutectoid rail substrate (0.93 wt.%C). The roller was the counterbody of hardened S1214 steel. The hardness was 475 HV in the 410L as-deposited condition. The same substrate was coated with a 420 MSS and Stellite 6. 410L exhibited a higher wear rate compared to these, which was attributed to its significantly lower hardness and the formation of retained-γ bands, due to fast cooling and insufficient C-content

to form martensite. Thus, the microstructure was primarily composed of austenite and ductile ferrite. SEM-wear surfaces showed severe plastic deformation, with multiple ploughings.

Zhu *et al.* [18] analyzed 410 MSS coatings (0.11 wt.%C) deposited by laser cladding with and without the TiC addition and subjected them to the ball-on-disk test with a Ø5 mm Si_3N_4 counterbody. Results showed that the COF and wear rate (Figure 2.22a-b) were significantly reduced as the volume of TiC in the Fe-matrix increased. These responses were primarily attributed to the substantial hardness enhancement provided by TiC, due to grain refinement, precipitation strengthening by nano-sized TiC, and second-phase strengthening due to the presence of unmelted TiC. In the SEM wear surfaces (Figure 2.22c-d), 410 MSS showed plastic deformation and adhesive wear. Conditions with TiC, on the other hand, exhibited only mild abrasive and adhesive wear, which was attributed to the higher hardness of the surfaces, making it more difficult for the counterbody to penetrate and displace the material. Additionally, TiC facilitated the anchoring of lubricant-effect tribolayers.

Figure 2.22 - Tribological performance of 410 coatings deposited by laser cladding with and without TiC addition: a) COF; b) wear rate; SEM-wear surfaces of the c) 410, and d) 410 + 15% TiC.



Source: Adapted from [18].

Jeyaprakash *et al.* [168] analyzed the 420 MSS coatings (0.15 wt.%C) and a Ni-based alloy Colmonoy 5 deposited on a 410 (0.15 wt.%C) substrate. The authors conducted the ball-on-disk test with a carbide ball counterbody. COF and wear rate were lower in the 420 coatings compared to the 410 substrate, due to the higher hardness of the former. In the SEM wear surfaces, 410 showed cuttings and ploughings. 420 exhibited shallow ploughings.

2.7.4 Corrosion resistance

Owing to the fast solidification of the AM L-DED process, the microstructure is heterogeneous and anisotropic, which can be deleterious to corrosion. Residual stress can generate defects (e.g., cracks). If the substrate is different from the feedstock, it can affect corrosion [148]. To keep the SS's corrosion resistance, a passive layer must be formed and maintained. Thick passive layers with greater Cr-oxide concentrations and elevated densities offer superior corrosion resistance, since the passive layer is more resistant against breaking and pits. Besides, repassivation is facilitated due to the lower amount of defects [143], [169]–[171]. Below are some insights from specific papers. Due to the lack of literature focused on the material and process investigated in this work, an attempt was made to identify trends that occurred in materials with some level of proximity and processed by L-DED or L-PBF, with corrosion investigation by potentiodynamic polarization.

Fang *et al.* [91] analyzed corrosion resistance by potentiodynamic polarization in 3.5% NaCl solution at room temperature of the Fe-Cr-Ni-Mn-Mo-Nb-Si MSS alloy processed by L-DED in the as-built state and of a reference material (FV520B MSS, as-received). The corrosion potential (E_{corr}) of L-DED was 001 V, while that of the reference material was -0.283 V. The corrosion current (I_{corr}) was also significantly lower in L-DED. Thus, L-DED performance was superior to the reference material. This result was attributed to the microstructure, which did not show segregation at the grain boundaries and Cr-depleted regions.

Wang *et al.* [172] compared the corrosion resistance by potentiodynamic polarization in 3.5% NaCl solution at room temperature of 18Ni300 Maraging MSS manufactured by L-DED, and L-PBF. L-DED I_{corr} was lower concerning L-PBF. Besides, L-PBF breakdown potential (E_{break}) surpassed that of L-DED, indicating better stability of the L-DED passive layer. L-PBF E_{corr} was also less positive concerning L-DED, so its tendency to corrode is greater. This result was attributed to the best L-DED chemical composition homogeneity, due to the lower number of L-DED thermal cycles, and a slower cooling speed regarding L-PBF.

Kochta *et al.* [173] evaluated the corrosion resistance by potentiodynamic polarization in 3.5% and 0.035% NaCl solutions at room temperature of the Fe85Cr4Mo8V2C1 MSS alloy manufactured by L-PBF, and in the wrought state. The E_{corr} difference between the L-PBF and wrought was minimal, due to the chemical composition similarity. However, the more refined microstructure and even distribution of the L-PBF phases delayed the corrosive activity.

Yazdanpanah *et al.* [174] investigated the influence of different types of porosities (rounded and irregular) on corrosion resistance by potentiodynamic polarization in 3.5% NaCl solution at room temperature of 316L SS manufactured by L-PBF. Samples with higher density exhibited greater E_{break} and lower breakdown current (I_{break}). In the samples with irregular porosities, E_{break} reduction and I_{break} increase were observed. The I_{break} variation between the groups with the same porosity type was attributed to the amount and dimensions of these. Corroded surface SEM analysis attested that samples with irregular porosities are more susceptible to pitting, crevice, and stress corrosion cracking mechanisms.

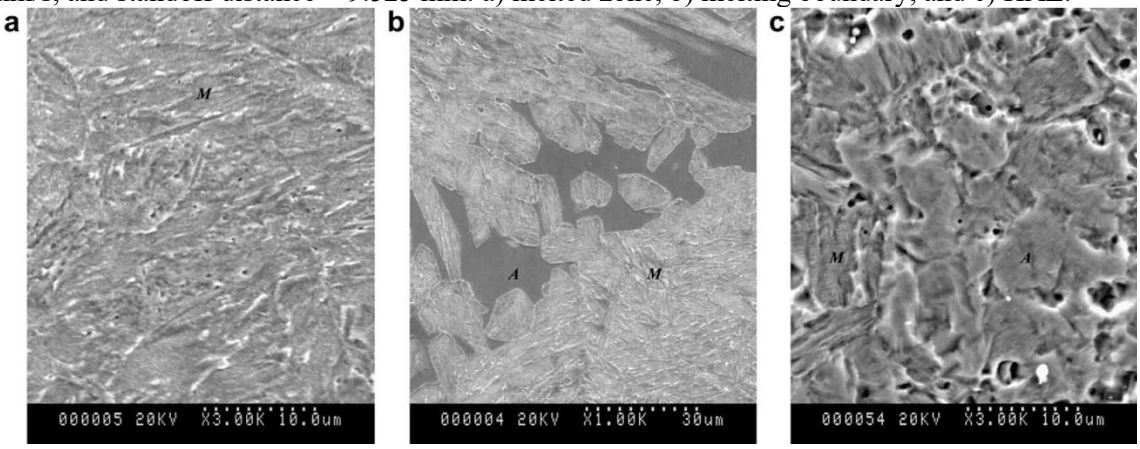
2.7.5 Post heat treatment applied to MSS processed via AM L-DED

Post heat-treatment routes can be applied to AM-LDED parts to mitigate defects and improve the microstructure and material properties. The PHT route for MSS is composed of austenitization, quenching, and tempering, with less literature convergence in this last step.

2.7.5.1 PHT effects on the microstructure

Krishna and Bandyopadhyay [61] evaluated the effects of L-DED surface remelting of AISI 410 MSS. The authors observed three well-defined microstructure regions, as shown in Figure 2.23 a) melted zone composed of martensite formed along fast cooling from enriched γ; b) partially melted zone with retained-γ; and c) HAZ, in which only solid-state transformation occurred, followed by martensitic transformation from γ during fast cooling, with a large amount of retained-γ [158]. In an earlier work developed by Colaço *et al.*, the effects of L-DED surface melting on the quenching of DIN X42Cr13 MSS were evaluated. The authors highlighted that the L-DED surface melting generates supersaturation of chemical elements and refined grains, which reduces the M_S, stabilizing the retained-γ [61].

Figure 2.23 - SEM microstructures of different regions of the L-DED treated surface at P = 500 W, S = 5 mm/s, and standoff distance = 9.525 mm: a) melted zone, b) melting boundary, and c) HAZ.



Source: [158].

Gonçalves *et al.* [2] evaluated the PHT effects on laser welded AISI40 MSS. When comparing the austenitization (1100 °C for 180 s followed by water quenching) with the tempering (300, 400, 500, and 700 °C for 12 hr then air cooling), the authors detected that the microstructure of both conditions was constituted by columnar grains surrounded by martensite laths. As the quenching condition has a martensitic structure, the thermodynamic driving force for γ transformation (on heating) and again to martensite (on cooling) is lower when compared to the tempering condition, because of the time required for the solute diffusion from the ferrite. From 500 °C tempering, coarse ferrite grains were observed, indicating over-aging.

Fenech *et al.* [97] evaluated laser cladding AISI 410 MSS+Cr_3C_2 under PHT routes composed of heating at 650-1020 °C for 15-20 min, then nitrogen (N) quenching and tempering at 200-575 °C, then air cooling. PHT routes generated grain refining owing to the allotropic transformation and eliminated retained-γ. The 2% Cr_3C_2 addition formed a martensite lath structure. Cr_3C_2 increment to 5% and 10% resulted in refined carbides precipitation. In the XRD evaluation, PHT does not show an appreciable influence on AISI 410 MSS diffractograms. With Cr_3C_2 addition, tempering at 200 °C results in a martensite structure with $M_{23}C_6$ carbides, while tempering at 575 °C provides a martensite-α reversion. Laser fast cooling does not provide enough time for carbide development. Thus, the re-austenitization and re-tempering promoted by the PHT provided the time required for this transformation kinetics.

Oh *et al.* [163] evaluated the effect of austenitization PHT (heating at 1040 °C for 1 hr then N quenching, A) and austenitization+precipitation hardening (heating at 480 °C for 4 hr then air cooling, A+PH) on the performance of a 630 (0.05 wt.% C) MSS manufactured by L-DED. All conditions exhibited γ (FCC) and martensite or α-ferrite (BCC) in the microstructure. In the as-built condition, martensite, retained-γ, and δ were observed. In condition A, δ was

eliminated, and coarse martensite was observed, with remaining grain boundaries, indicating that the recrystallization was incomplete. PHT A increased the martensite volume fraction. However, it reduced retained-γ concerning as-built. A+PH condition, on the other hand, exhibited a higher volume fraction of more refined martensite grains, and kept a higher retained-γ content regarding condition A, due to coarse carbide precipitation at the grain boundaries, which can be attributed to the presence of reverse-γ provided by the long aging period.

Seede *et al.* [165] analyzed the effects of three PHT routes (PHT1=stress relief at 600 °C for 2 hr then air cooling, followed by normalization at 1010 °C for 2 hr then air cooling, followed by austenitization at 1010 °C for 1.5 hr then water quenching, and tempering at 200 °C for 4 hr then air cooling; PHT2=same PHT1, however, without normalization step; PHT3= normalization at 1010 °C for 2 hr then air cooling, followed by heating at 680 °C for 4 hr then air cooling, followed by austenitization at 1010 °C for 1.5 hr then water quenching, and tempering at 200 °C for 4 hr then air cooling) over the performance of an AF9628 (>0.2 wt.% C) MSS manufactured by L-PBF. The authors observed coarse martensite laths for the as-built state, while refined martensite laths were demonstrated by all PHT conditions, without significant aspect differences between them. Likewise, the dendritic epitaxial growth of the as-built state generated larger parent-γ grain boundaries, which enhanced anisotropy.

Tian, Chadha, and Aranas [166] studied the 420 MSS manufactured by L-PBF and subjected it to a PHT of austenitization at 1043 °C for 1 hr, then N quenching, followed by double tempering at 182 °C for 3 hr then air cooling. PHT microstructure showed tempered coarse martensite laths, with refined Cr-carbides. EBSD analysis exhibited that the preferential built direction growth of the as-built state gave place to polygonal grains of random texture.

As observed, the PHT application to MSS processed by laser is essential to provide residual stress relief, martensite tempering, microstructure homogenization, and strengthening phases' precipitation. It is worth remembering that the brittle nature of martensite requires PHT performance for any manufacturing process.

2.7.5.2 PHT effects on the hardness

In the work of Gonçalves *et al.* [2], when the tempering temperature is 300-400 °C, there was an overall hardness increase in the substrate, melting zone, and HAZ, due to the

carbide precipitation. At 500 °C tempering, a hardness decrease between substrate and HAZ was observed, behavior conferred to the marked coarsening and spheroidization of carbides.

In the laser cladding of AISI 410 MSS+Cr_3C_2, Fenech *et al.* [97] noted that retained-γ was eliminated by PHT and allowed martensite formation during subsequent cooling. Tempering at 200 °C decreased the hardness of the 0% and 2% Cr_3C_2, while a hardness elevation was found in the 5% and 10% Cr_3C_2. Tempering at 575 °C, in turn, significantly reduced the hardness, owing to the martensite-γ reversion and precipitation of coarse carbides.

In assessing the hardness of 630 (0.05 wt.% C) MSS samples manufactured by L-DED, Oh *et al.* [163] found 403 HV for the A+PH condition, 388 HV for A, and only 264 HV for the as-built state. This performance contrast was conferred to the higher volume fraction and refinement of the A+PH condition martensite, while the coarser martensite of condition A and the higher retained-γ content of the as-built condition provided lower hardness.

Seede *et al.* [165] noticed a hardness increase in AF9628 (0.23 wt.% C) MSS manufactured by L-PBF, between as-built (482 HV) and PHT (502 HV) conditions. This performance was conferred to the highest volume fraction of refined martensite laths. Besides, the standard deviation of the as-built condition was also pronounced, owing to the uneven microstructure generated by localized quenching as a function of the L-PBF fast thermal cycles.

As observed, the PHT route application can significantly affect the hardness performance. This is provided by the martensite tempering, carbides precipitation, and homogenization of the chemical composition and properties along the Fe-matrix.

2.7.5.3 PHT effects on the tensile strength

Deev *et al.* [164], when applying a PHT of austenitization at 1100 °C for 1 hr, then oil quenching, followed by tempering at 700 °C for 1 hr, then air cooling, observed an EL improvement from 3 to 9% in the 410L MSS samples manufactured by L-PBF. The UTS remained virtually the same at 450 MPa, while the YS dropped from 375 to 350 MPa. This result was conferred to residual stress relief and martensite tempering.

Oh *et al.* [163] analyzed the performance of 630 MSS (0.05 wt.% C) manufactured by L-PBF according to ASTM E8, and obtained an improvement of YS and UTS, in contrast with EL reduction observed for both PHT routes. YS=419 MPa, UTS=1183 MPa, and EL=21% were found in the as-built state. Post heat-treatment A resulted in YS=546 MPa, UTS=1364 MPa, and EL=13%. Post heat-treatment A+PH generated YS=1005 MPa, UTS=1434 MPa, and EL=20%. The higher volume fraction of martensite justified the improvement of YS and UTS

of PHT routes. However, the presence of this phase impaired their EL resistance. The improvement observed for A+PH was attributed to the residual stress relief and reverse-γ films at the grain boundaries. SEM fractures exhibited dimples in the as-built and A+PH, while condition A showed brittle cleavage and intergranular fracture.

Seede *et al.* [165], when analyzing the tensile strength of AF9628 (0.23 wt.% C) MSS manufactured by L-PBF, obtained higher YS and UTS in all PHT conditions regarding the as-built. This result was attributed to martensite lath refinement, which increased the mechanical strength. However, EL was impaired due to the martensite brittleness and associated volumetric expansion, which stressed the microstructure.

Tian, Chadha, and Aranas [166] investigated the tensile strength of 420 MSS manufactured by L-PBF and noted an increase in YS (1057-1380 MPa) and UTS (1745-1960 MPa) PHT concerning the as-built. This was attributed to the refined carbides precipitation and the retained-γ elimination. However, the EL dropped by 22-16%, owing to the carbides' brittleness. SEM fractures attest to this result by revealing more dimples in the as-built.

As noted, tensile strength can be improved by PHT. However, a trade-off relation exists between YS, UTS properties, and EL. This is because mechanisms that improve YS and UTS (e.g., martensite, grain refining, retained-γ elimination) worsen elongation.

2.7.5.4 PHT effects on the impact toughness

With the PHT application, Deev *et al.* [164] obtained an increase in AE for samples of AISI 410 MSS in the Charpy impact test, from 5-17 J (U-notch in the build direction) and 6-32 J (U-notch normal to the build direction). This improvement was attributed to residual stress relief. Besides, the greatest data fluctuation detected for samples with U-notches in the normal build direction was due to their higher anisotropy originating from the L-PBF fast cooling.

Oh *et al.* [163], when comparing the PHT conditions over the 630 MSS (0.05 wt.% C) obtained by L-PBF, detected AE reduction, with the as-built exhibiting 138 J, while A dropped to 65 J, and A+PH to 27 J. This result was attributed to the different volumes of martensite, which increased with the PHTs, elevating the brittleness and the residual stress. The formation of reverse-γ films at A+PH was not enough to improve the Charpy impact toughness.

Seede *et al.* [165], when analyzing the Charpy impact toughness of AF9628 MSS (0.23 wt.% C) manufactured by L-PBF, observed a reduction of 28-24 J between the as-built and

PHT3, which was the PHT route with the highest AE. This difference was attributed to the ductility reduction provided by refining the martensite laths and the parent-γ grain boundaries.

Tian, Chadha, and Aranas [166] investigated the Charpy impact toughness of 420 MSS manufactured by L-PBF, and reported a significant AE increase of 11-35 J. This performance improvement was attributed to martensite tempering and residual stress relief.

As noted, the relationship between PHT and impact toughness is more complex regarding tensile strength. The martensite tempering and residual stress relief achieved by PHT benefit the Charpy impact toughness. However, microstructure refining, retained-γ mitigation, and carbide precipitation worsened this property.

2.7.5.5 PHT effects on the tribological performance

As previously highlighted, tribological behavior is a systemic response. With the PHT application to AISI 410L MSS processed by L-DED, recrystallization, grain coarsening, residual stress relief, and martensite tempering are expected. Thus, contact conditions are modified, which is reflected in the COF, wear coefficient, and aspects of the wear surfaces.

Meura *et al.* [167] verified that the two PHT routes (austenitization at 1050 °C for 60 min, then water quenching; and austenitization plus quenching and tempering at 350 °C for 60 min, then air cooling) applied to 410L L-DED 5-layer coatings increased hardness and wear coefficient regarding the L-DED as-built and the reference ball plug material. In the SEM wear surfaces, scratches and SiO_2 indentations were observed in the PHT, indicating a more severe contact condition between the harder surface and the counterbody.

Roy *et al.* [161] evaluated the 410L coatings (0.01 wt.%C) after the substrate pre-heating and substrate plus coating post-heating at 350 °C for 60 min, then slow-cooling at room temperature. This strategy increased the hardness, as it formed tempered martensite bands within the ferritic matrix. As a result, the wear rate was reduced, and the martensite protected the surface against counterbody. Sem wear surfaces exhibited microcuttings and microcracks.

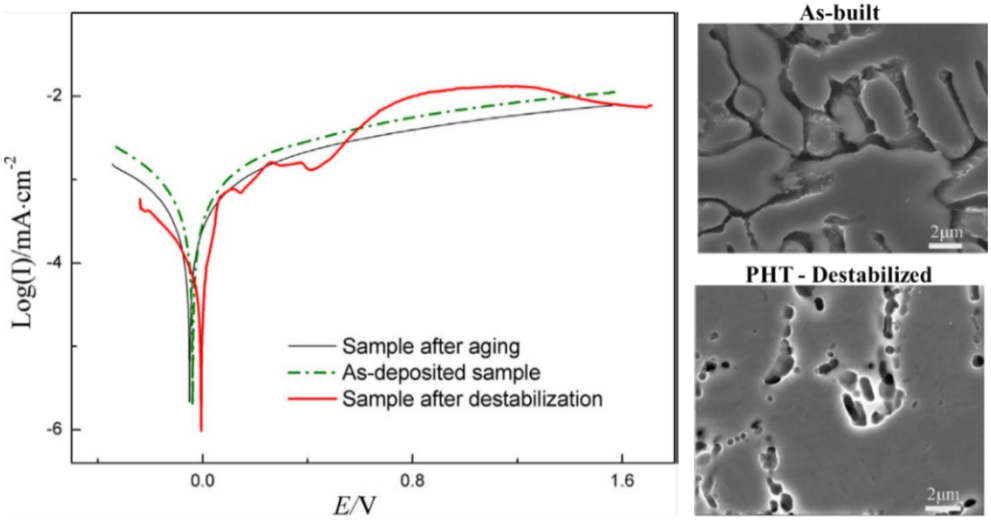
Nayebi *et al.* [6] applied L-DED surface melting at different scanning speeds on an AISI 410S steel sheet (0.01 wt.%C). In the ball-on-disk test with an AISI 52100 counterbody, the authors found a lower wear rate after treatment at intermediate scanning speeds, as these conditions generated high hardness and microstructure homogenization. In the SEM wear surfaces, these conditions exhibited only adhesion, with wide bands of oxide tribolayers supported by the microstructure, which mitigated the action of abrasion scratches.

2.7.5.6 PHT effects on corrosion resistance

The MSS corrosion resistance is sensitive to the carbide volume dissolved in the Fe-matrix after the austenitization stage for quenching and depends on carbide precipitation during tempering. Typically, austenitization temperature increases tend to improve corrosion resistance as they increase carbide dissolution [175]. Below are some insights from papers investigating the effects of PHT routes on corrosion resistance by potentiodynamic polarization. It was necessary to detect possible trends in other SS grades, processed by L-DED and L-PBF.

Fang *et al.* [176] investigated corrosion resistance by potentiodynamic polarization in 3.5% NaCl solution at room temperature of Fe-Cr-Ni-B MSS manufactured by L-DED, in the as-built, and under two PHT routes (heating at 480 °C for 1 hr then air cooling), and destabilized (heating at 1050 °C for 30 min then air cooling). In Figure 2.24 polarization curve, the E_{corr} was higher in MSS as-built regarding the aged PHT, due to carbide precipitation. The destabilized PHT showed higher E_{corr} and lower I_{corr} owing to the Cr-content increase at the grain boundaries. Figure 2.24 SEM of the corroded surfaces indicated intergranular corrosion in the as-built. Destabilized PHT showed a Fe-matrix still rich in Cr, with fewer pits.

Figure 2.24 - Potentiodynamic polarization curves of Fe-Cr-Ni-B MSS, and SEM of corroded surfaces after tests at 3.5% NaCl solution.

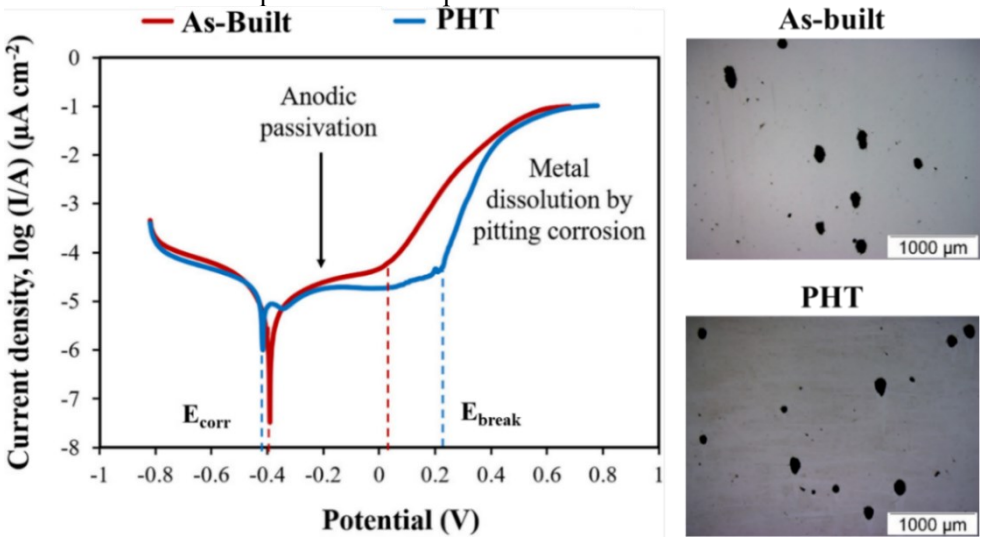


Source: Adapted from [176].

Nath *et al.* [153] evaluated the corrosion resistance by potentiodynamic polarization in 3.5% NaCl solution of 420 MSS under L-PBF as-built, L-PBF as-PHT (heating at 315 °C for 2 hr then air cooling), and reference wrought. Figure 2.25 L-PBF as-PHT generated a higher

I_{corr} than L-PBF as-built and wrought. The corrosion rate was also higher in L-PBF as-PHT. The E_{corr} was more negative in L-PBF as-PHT (-0.42 V) over L-PBF as-built (-0.39 V). Breakdown potential (E_{break}) was higher in L-PBF as-PHT (0.22 V) compared to L-PBF as-built (0.05 V). The OM corrosion mechanism (Figure 2.25) was pits initiated in L-PBF porosities. The superior performance of the wrought was conferred to its higher γ-content when compared to the L-PBF refined martensite, which is a phase with lower corrosion resistance.

Figure 2.25 - Potentiodynamic polarization curves for as-built and PHT L-PBF 420 MSS after test in 3.5% NaCl solution. Corrosion pits initiated in porosities from L-PBF.



Source: Adapted from [153].

In another paper, Nath *et al.* [177] studied the effects of layer thickness and PHT of heating at 315 °C for 2 hr, then air cooling on the corrosion resistance by potentiodynamic polarization in 3.5% NaCl solution of 420 MSS manufactured by L-PBF. No significant changes occur in the E_{corr} after PHT. The higher density and amount of martensite in the thinner layers, regardless of the PHT, increased the corrosion resistance concerning the thicker layer. The higher E_{break} in the lower density sample was corroborated by the greater pit incidence.

Shahriari *et al.* [169] studied the corrosion resistance by cyclic potentiodynamic polarization in 3.5% NaCl solution of a 13 wt.%Cr named MSS CX built by L-PBF and subjected to PHT (austenitization at 900 °C for 1 hr then air quenching, followed by aging at 530 °C for 3 hr then air cooling) compared to that of a 420 MSS as-cast and subjected to PHT (austenitization at 1150 °C for 30 min then air quenching, followed by tempering at 400 °C for 2 hr then air cooling). The higher E_{corr} of MSS CX showed a more effective passivation, which was attributed to the refined L-PBF microstructure. The pitting potential (E_{pit}) was nobler in the L-PBF. The repassivation I_{corr} was also lower in the L-PBF concerning the cast 420 MSS, pointing to the higher corrosion resistance of the former.

3 SCIENTIFIC CONTRIBUTION

As highlighted in the introduction and discussed throughout the scientific background, the material under study in this work (AISI 410L MSS) has an extensive application field, encompassing strategic industrial sectors, both in the manufacture of new components and the repair of worn parts. The interest in this material is justified by its mechanical properties, tribological performance, and corrosion resistance at milder temperatures (~20-450 °C). Regarding the AM L-DED process, this technology brings a set of possibilities, which can provide solutions to problems faced with conventional manufacturing techniques.

Despite the highlighted advantages, the processability limitations of MSS by AM L-DED were also discussed, due to the martensite's brittle nature and the L-DED thermal history. The interaction between these can impose deleterious effects on the microstructure and material properties. In this sense, the present work proposes a full and robust method for finding the optimized parameters and conditions of the AM L-DED process, which ensures the manufacturing of ordinary as-built (AB) multilayer geometries free from defects and with high density. Regarding the post-heat treatment (PHT), which aims to relieve the residual stresses imposed during AM L-DED manufacturing, provide martensite tempering, phase homogenization, and properties enhancement, this Thesis proposes a study to develop a PHT route. The performance of the optimized AB and PHT conditions was characterized in terms of microstructure, mechanical, tribological, and corrosion properties:

- AM L-DED parametrization route: discussions about the interaction mechanisms between the AM L-DED parameters and the analyzed responses in terms of defects absence, geometry stability, and density. It is expected that this will enable processing the material using L-DED, both in AM and cladding operations, employing this experimental sequence, which is interchangeable between L-DED systems.
- Production and resolution parameters: another literature gap is the lack of development of parameters aimed at greater production and resolution. This is an important issue, especially in the actual modular manufacturing industry, in which the same component can have bulkier and ordinary parts (higher production) and smaller, more complex parts (higher resolution). The present work addresses two AM L-DED process routes in parallel. With these, it is expected to find manufacturing conditions more appropriate for higher

production and resolution, respectively, considering the differences in geometry and dimensions.

- Microstructure: understanding the mechanisms involved in the formation of the microstructure of a low C-content MSS processed by AM L-DED, whose thermal history is different from conventional processes. The discussion is presented in two as-built conditions (production and resolution), where the deposition rate levels differ. The effects of the different PHT routes studied on the microstructure of the analyzed AM L-DED samples are discussed, with a focus on the tempering, a stage expected to play a critical role in residual stress relief and homogenizing the L-DED heterogeneous microstructure.
- Mechanical properties: understanding how the different AM L-DED parameters and PHT routes affected the mechanical performance in terms of hardness, tensile strength, and Charpy impact toughness. Charpy impact is a critical point. The discussion on the trade-off relationship between properties helps to select the appropriate AM L-DED conditions, as the various L-DED parameters are expected to affect the extent of microstructural refinement, whereas heat treatment alters the heterogeneous growth behavior and the magnitude of residual stresses.
- Tribological performance: understanding the effects of different AM L-DED conditions and PHT on the tribosystem responses evaluated in terms of friction and wear coefficients, simulating common applications of this MSS grade. Besides hardness, the various microstructural characteristics are expected to influence the formation of tribolayers and the active wear mechanisms.
- Corrosion resistance: as an intrinsic SS property, and given the application environments of MSS, understanding how AM L-DED and PHT conditions affect the corrosion resistance of a component is fundamental. Different microstructure aspects resulting from these conditions may affect corrosion potential, corrosion current, polarization resistance, and passive layer features, which can completely change the material's performance against corrosion.
- With all these mapped characteristics, the user will be able to choose which properties to prioritize for the final application and thus select the best possible combination of processing and post-processing.

4 EXPERIMENTAL PROCEDURES

This section describes the general method and experimental procedures, from the exploratory stage to the post-processing route, encompassing all the steps of AM L-DED design of experiments (DoE). Additional tests performed are also presented. Figure 4.1 flowchart illustrates the experimental procedures performed:

- Exploratory stage (Single Beads, SB): operational process windows and a stable set of parameters were established.
- Modeling and Optimization stages (Single Layers, SL): hatch spacing (HS) values were defined and experimentally tested in the modeling stage. In the optimization, multiple responses of the regressions were evaluated through the desirability function.
- Multilayer stage cubes (Multilayer Geometry, MG): this step aims to identify the best layer height (LH), in terms of defects absence, density, and the number of layers required.
- Additional tests (SL and MG): one of the SLs from the experimental verification step was subjected to characterizations. With all the AM L-DED parameters defined, MG samples were manufactured to evaluate their geometry, microstructure, hardness, mechanical, tribological, and corrosion performances. Besides, a PHT route study was conducted, and its results were compared to those of the AB state, SUB-AR, and AM L-DED literature.

4.1 STAGE 1: EXPLORATORY

Looking at Figure 4.1 flowchart, this stage aims to find appropriate processing windows of laser power (P), travel speed (S), and powder feedrate (F) parameters that result in continuous single beads (SB) and meet the acceptance criteria. As the parameter combinations are virtually infinite, it is necessary to design experiments based on user reality and keep some parameters fixed. In this work, at first, only the spot size was fixed: Ø2.54 mm (PRO) and Ø1.78 mm (RES). Operational process windows were investigated by searching for the hardware thresholds. Thus, 2 F levels were selected, and “n” levels of P and S were varied until reaching a condition where continuous SBs were no longer formed. The SBs were deposited at 25 mm in length on the substrate, spaced at 10 mm, and with a 5 min dwell time. Only the SB surfaces were qualitatively evaluated in this step through optical stereoscope (OS) images. From the processing windows that formed SB, two parameter matrices were established.

Figure 4.1 (start) - General method flowchart: Exploratory (SL), Modeling and Optimization (SL), Multilayer, Additional Tests.

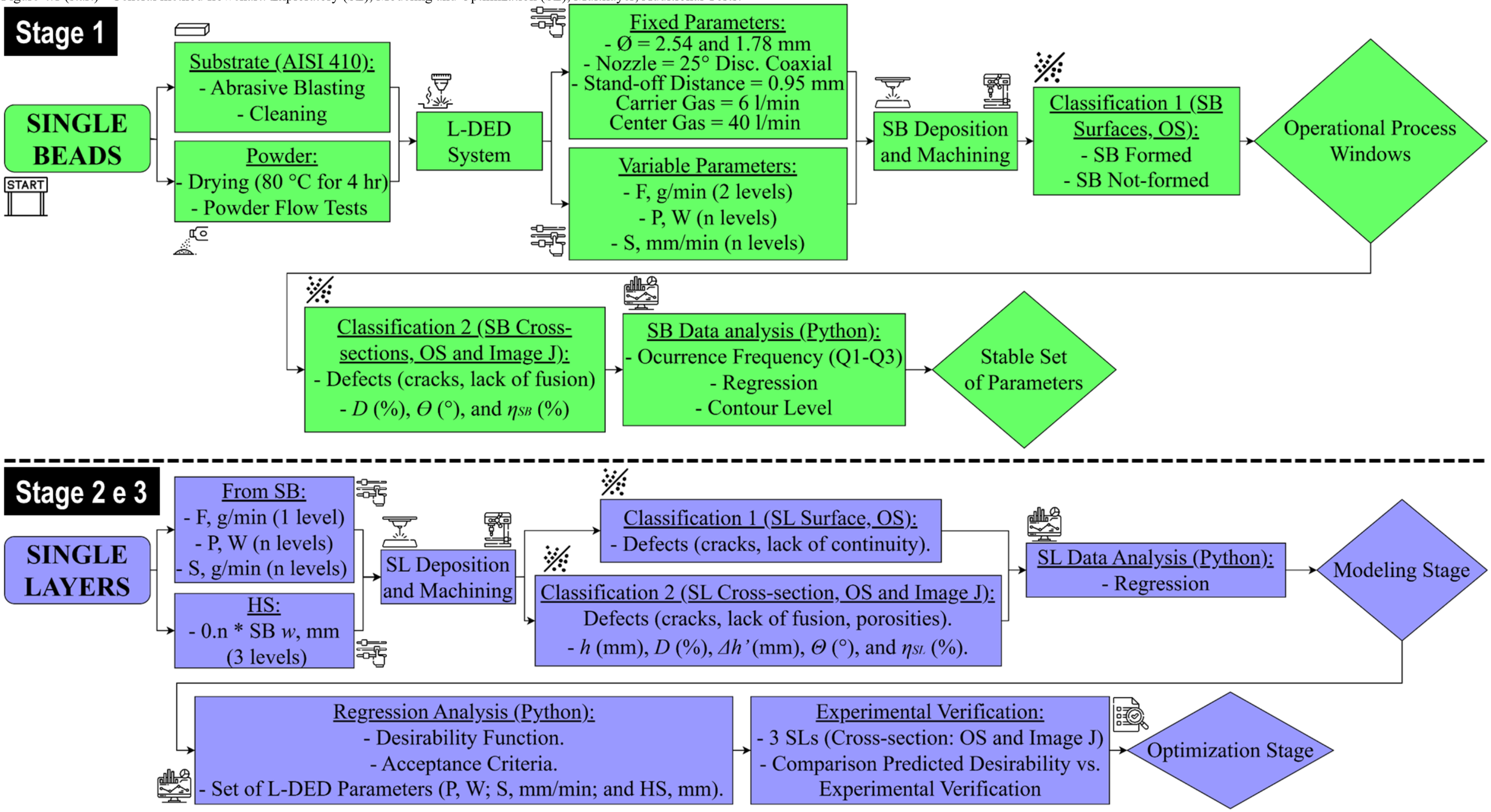
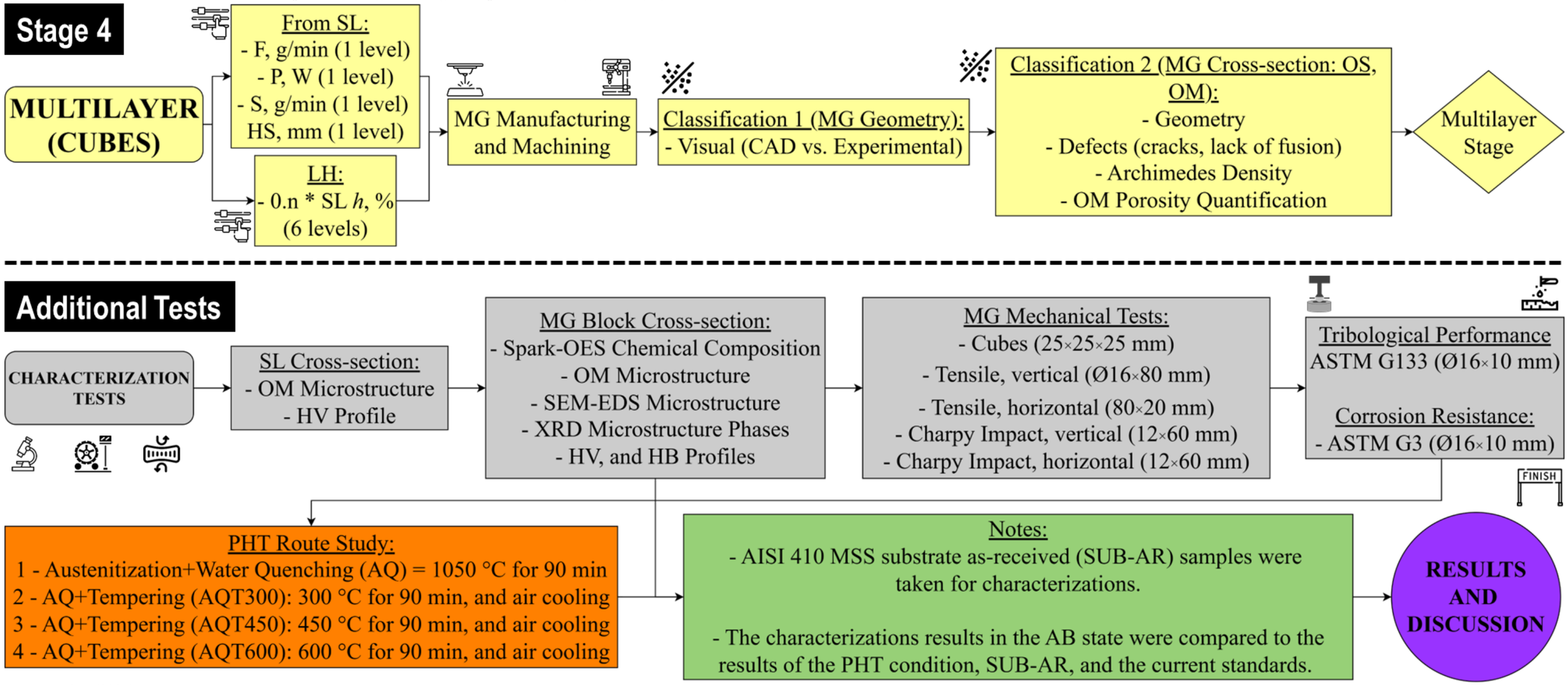


Figure 4.1 (end) - General method flowchart: Exploratory (SL), Modeling and Optimization (SL), Multilayer, Additional Tests.



Source: Author (2025).

For the stable set of parameters, SBs from the operational process windows were cut in cross-section, prepared for metallographic analysis (sanding #80-1200 *Mesh*, polishing in 0.3 µm diamond solid-solution suspension, chemically etched by Ralph's reagent [178]), and analyzed by OS. The surfaces and cross-sections of the SB were visually examined to attest to the defect's absence (e.g., cracks). Then, SB cross-sections had their dilution (D - Equation 4.1 [82]), wettability angle (Θ - Equation 4.2 [80]), and efficiency (η_{SB} - Equation 4.3 [80]) measured by ImageJ® software. To define the acceptance criteria, the frequency of occurrences statistical tool was applied, where quartile 1 (Q1) and quartile 3 (Q3) were taken as the lower and upper limits, respectively. Experimental data were evaluated through regression and contour levels, until finding a stable set of parameters that allowed for meeting the acceptance criteria simultaneously.

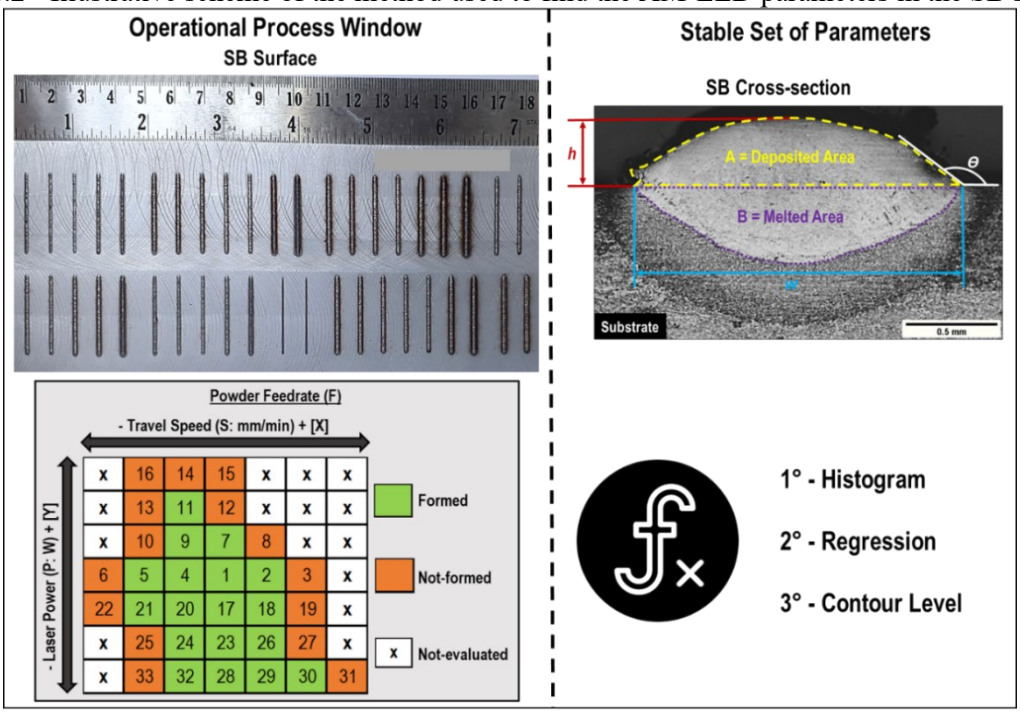
Figure 4.2 illustrates these procedures, and a cross-section of an SB, where A=deposited area, B=molten area, h=SB height, w=SB width, S=travel speed, and ρ=powder density.

$$D = \frac{B}{A+B} * 100\ (\%) \tag{4.1}$$

$$\theta = 180 - 2 * \arctan\left(2 * h/w\right)\ [\%] \tag{4.2}$$

$$\eta_{SB} = \frac{A*S*\rho}{F} * 100\ [\%] \tag{4.3}$$

Figure 4.2 - Illustrative scheme of the method used to find the AM-LED parameters in the SB stage.



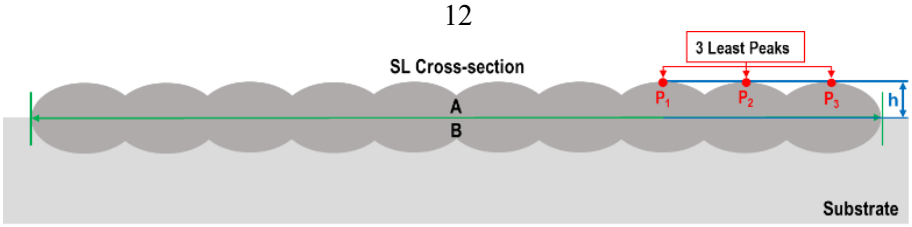
Source: Author (2025).

4.2 STAGE 2: MODELING

From the optimized parameter windows (P, S, and F) of stage 1, a new full-factorial DoE is carried out, using the hatch spacing (HS) as a variable to find an ideal lateral overlap between SB for obtaining single layers (SL). The HS represents a percentage of the average width (w) of the SBs from the optimized. SLs were programmed with 10 SBs (25 mm in length). In the SL deposition, to mitigate excessive heat-input, before depositing a second SL on a substrate, it had its temperature measured by a thermal camera. If the temperature was >50 °C, it was cooled using an Ar-jet. After depositing, the SLs were then cut into cross-section, prepared for metallographic analysis, subjected to OS image capture, and evaluated for defects' absence (e.g., cracks and lack of fusion). The approved SLs were quantitatively analyzed:

- Average peak height ($\bar{h}$): average distance between the substrate surface and the last 3 SL peaks (P_1-P_3) (Figure 4.3, Equation 4.4).

Figure 4.3 - Illustration of SL average peak height ($\bar{h}$) measurement.

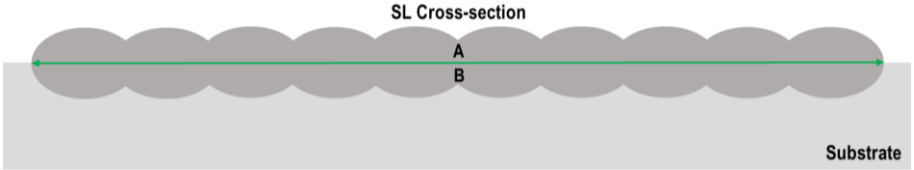


Source: Author (2025).

$$\overline{h_P} = (P_1 + P_2 + P_3)/3\ [mm] \tag{4.4}$$

- Dilution (D): the relationship between melted area (B) and the sum of deposited area (A) and melted area (B) (Figure 4.4, Equation 4.1). This considers the effect of multiple overlapping single beads, where part of the energy is directed to the substrate and part to the previously deposited single bead, which alters the dilution.

Figure 4.4 - Illustration of SL dilution (D) measurement.

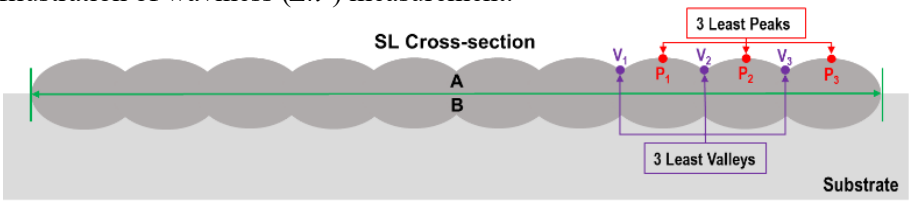


Source: Author (2025).

- Waviness ($\Delta h'$): difference of $\bar{h}$ and the average ($\bar{V}$) of the last 3 SL valleys (V_1-V_3, Equation 4.5) is defect sensitivity (Δh, Equation 4.6). Relation of A with w is the height

equivalent area ($h_{Equiv.A}$, Equation 4.7). Finally, the relation of Δh and $h_{Equiv.A}$ was the waviness ($\Delta h'$, Figure 4.5, Equation 4.8). Optimizing this parameter is important to avoid lack of fusion between the valleys in the multi-layer stage.

Figure 4.5 - Illustration of waviness ($\Delta h'$) measurement.



Source: Author (2025).

$$\bar{V} = (V_1 + V_2 + V_3)/3\ [mm] \tag{4.5}$$

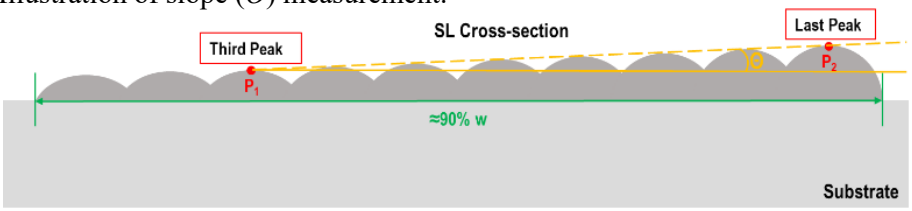
$$\Delta h = \bar{h} - \bar{V} \tag{4.6}$$

$$h_{Equiv.A} = w/A\ [mm] \tag{4.7}$$

$$\Delta h' = \frac{\Delta h}{h_{Equiv.A}}\ [\%] \tag{4.8}$$

- Slope (Θ): estimated through a straight row tangent to the SL surface. The 3rd (P_1) and last peaks (P_2) are set as references (Figure 4.6, Equation 4.9). Optimizing this parameter is critical to avoid deviations in the Z-axis focus position during multilayer manufacturing.

Figure 4.6 - Illustration of slope (Θ) measurement.



Source: Author (2025).

$$\Theta = tan^{-1}\frac{(P_1 - P_2)}{0.9 * w}\ [°] \tag{4.9}$$

- Efficiency (η_{SL}): relation between A and the number of SB, whose result is multiplied by the product between S and ρ. The entire relation result is divided by F (Equation 4.10).

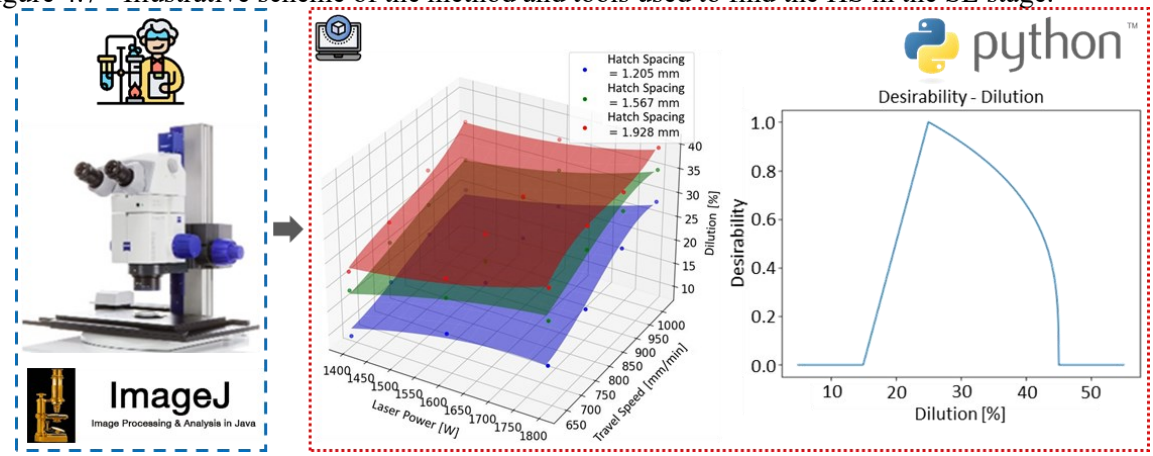
$$\eta_{SL} = (((\frac{A}{10}) * S * \rho))/F\ ) * 100\ [\%] \tag{4.10}$$

The experimental data are then analyzed mathematically in an empirical-statistical model through an algorithm based on a 3rd order polynomial multiple regression using the Minimum Square Errors method developed in the Python® software. This was based on the literature [80], being developed with implementations in Ferreira's work [179].

4.3 STAGE 3: OPTIMIZATION

The multiple responses of the regression function from stage 2 are simultaneously evaluated through the desirability function implemented in the algorithm. This function attaches a score to each of the regression responses so that the mean value of all these individual scores gives the global desirability for each property, aiming for one of the objectives: maximization, minimization, or target. From the response models of stage 2, it is determined the L-DED process parameters set (P, S, F, and HS) that provide the highest global desirability. These parameters are then verified experimentally through the deposition of SL in triplicate. The average results of the measured properties are compared to the model prediction (Figure 4.7).

Figure 4.7 - Illustrative scheme of the method and tools used to find the HS in the SL stage.



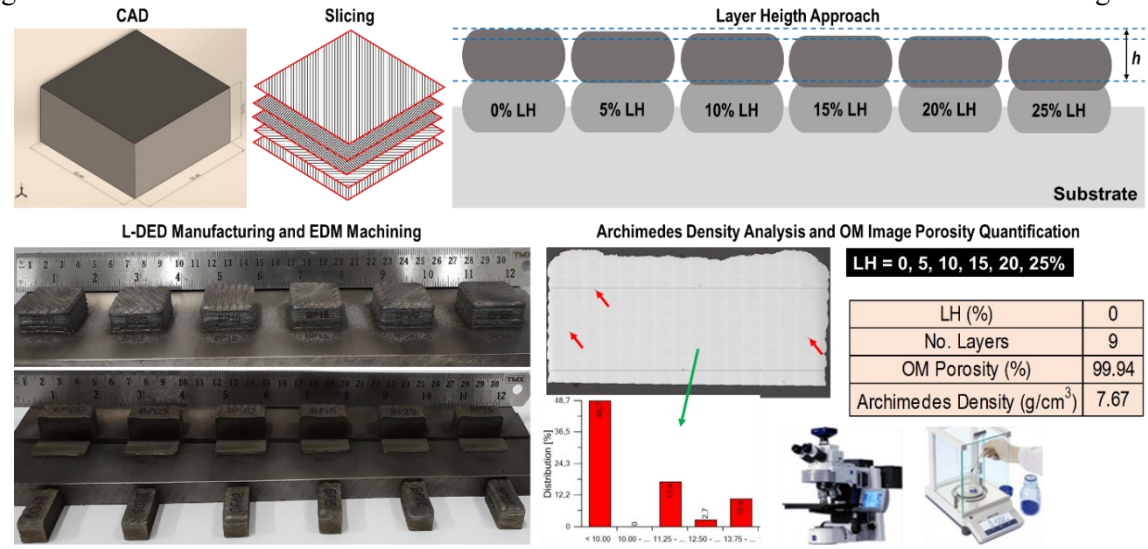
Source: Author (2025).

4.4 STAGE 4: MULTILAYER GEOMETRY CUBES

The last stage consists of performing an experimental procedure to obtain an ideal layer height (LH) to manufacture defect-free and high-density multilayer geometry cubes (MG). It was manufactured an ordinary MG (e.g., cube), using optimized parameters (P, S, F, and HS). Different levels of LH are varied. Range from 0% (non-layer height) to 25% (0.75 x SL *h*), with 5% increments, was analyzed. After the substrate, powder, and L-DED system preparation, from a CAD model (25×25×25 mm), cubes were manufactured. As a slicing strategy, a "start to end-end to start" trajectory was used between SBs, and a 45° hatching angle between SLs. To mitigate excessive heat-input between cubes, 60 min dwell time was allowed. This step was carried out in an inert, Ar-rich environment (O_2<10 ppm), aiming to reduce the oxidation along

the SLs deposition, which can insert defects, such as delamination, porosities, and lack of fusion. This was necessary due to the higher heat-input and the multiple heating/cooling cycles imposed in AM L-DED multilayer manufacturing [75]. Once built, the cubes were W-EDM cut in the cross-section, prepared metallographically, and visually evaluated for the defects' absence. Then, Archimedes' density analysis (allows a comparison to the nominal material density), and OM porosity quantification (allows quantification and verification of the porosities morphology) were performed. LH, which provides the absence of defects, the highest density, and a lower number of layers required, is then selected (Figure 4.8). Thus, at the end of the 4th method stage, the user has the AM L-DED parameters (P, S, F, HS, and LH) defined for the manufacturing of ordinary multilayer geometries.

Figure 4.8 - Illustrative scheme of the method and tools used to find the LH in the MG cube stage.



Source: Author (2025).

4.5 CHARACTERIZATION TESTS

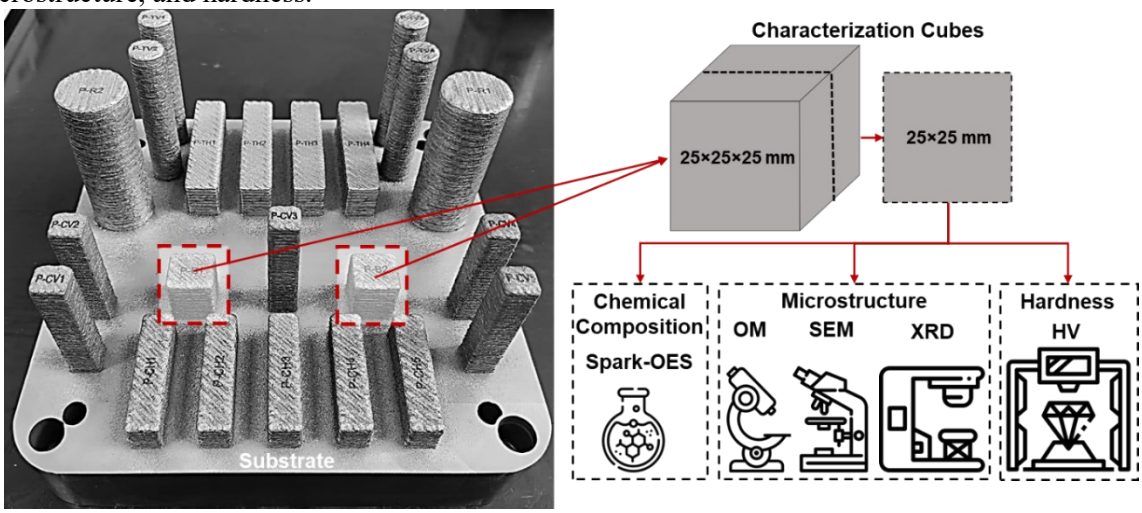
With all the AM L-DED parameters defined, the MG sample manufacturing planning was carried out.

4.5.1 Microstructure assessment

One of the SLs from the experimental verification step was prepared for metallographic analysis and subjected to OM and Vickers HV hardness characterization. Figure 4.9 shows 2 cubes built for Spark-OES chemical composition (3 equidistant-spaced analyzing points were performed on the surface). OM microstructure, SEM-EDS microstructure, and

chemical composition were evaluated. With the samples in a polished state, X-ray diffractometer (XRD) microstructure phase detection (Cu Kα radiation at a 2° per minute speed, 0.02° step, 40 kV, and 30 mA) was carried out. With the samples in a polished state, 3 equidistant HV profiles with 10 indentations each (5 N load HV0.5, and 10 s indentation time ASTM E384 [180]) were performed.

Figure 4.9 - AISI 410L MG cube samples manufactured for evaluation of the chemical composition, microstructure, and hardness.



Source: Author (2025).

4.5.2 Mechanical behavior

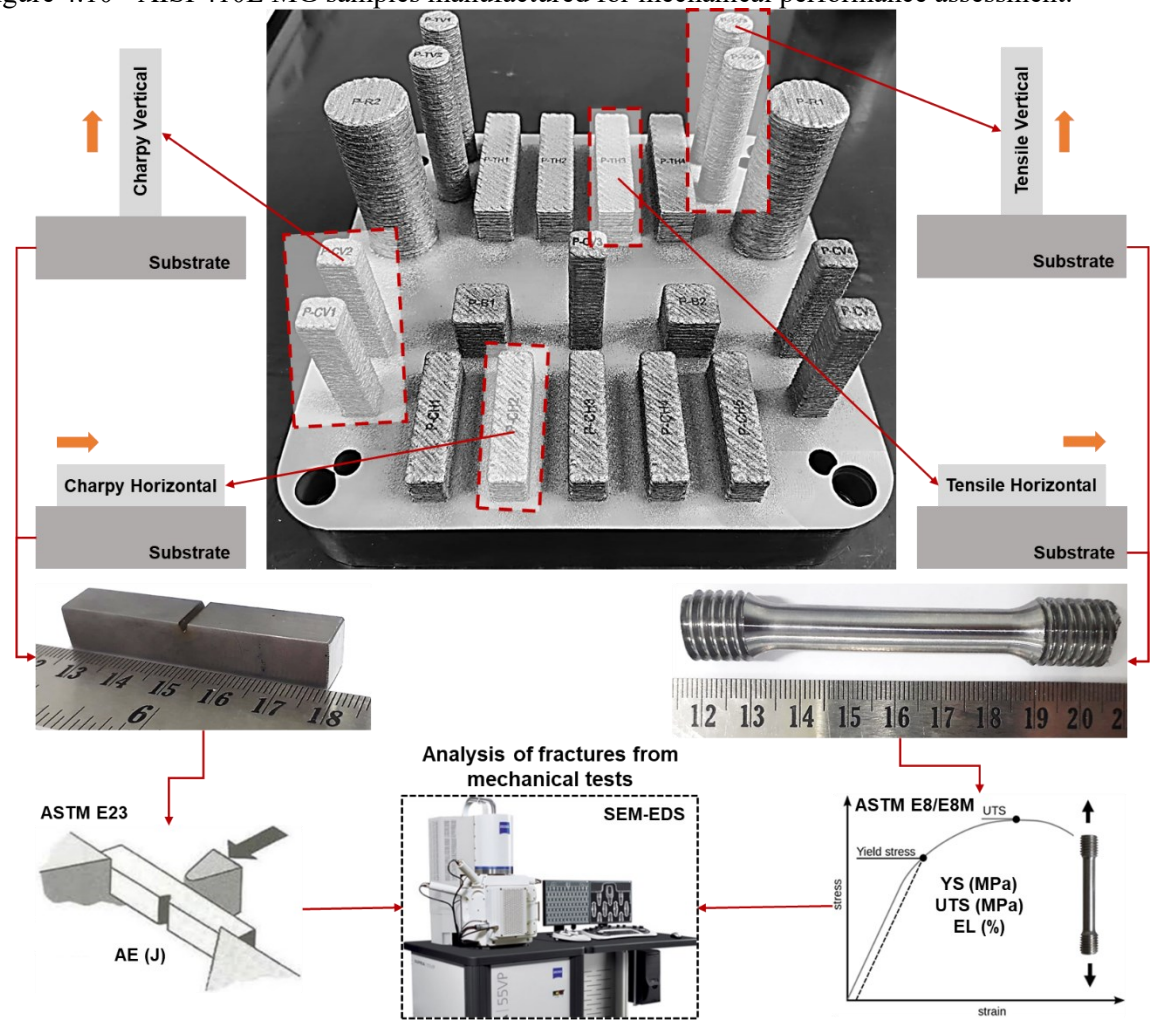
For the mechanical behavior assessment, 8 tensile (using *specimen 2* from ASTM E8/E8M, being 4 horizontal and 4 vertical concerning the substrate) [181]; and 10 Charpy impact samples (using *V-notch* pattern from ASTM E23, being 5 horizontal and 5 vertical concerning the substrate) [182]), as shown in Table 4.1 and Figure 4.10. AISI 316 SS (250×250×50 mm) substrate was used. This step was carried out in an inert, Ar-rich environment (O_2<10 ppm). After manufacturing, samples were machined (W-EDM for removing from substrate, milling and turning for tensile, milling for Charpy, W-EDM for Charpy V-notch). A laser video extensometer was used to measure the deformation. Yield Strength (YS) and Ultimate Tensile Strength (UTS), and elongation (EL) were analyzed. Charpy V-notch was machined on the side of the samples. Mechanical tests were carried out at 20 °C room temperature. One sample of each mechanical test (tensile and Charpy impact) and condition evaluated (L-DED parameter and state) had its fractures investigated by SEM-EDS.

Table 4.1 - Set of samples for characterization tests (dimensions of the AB samples by L-DED).

Set of Samples for Characterization Tests			
Sample	Orientation	Dimensions (mm)	Quantity
Cube	Vertical	25×25×25	2
Tensile	Vertical	Ø16×80	4
Tensile	Horizontal	80×20	4
Charpy	Vertical	12×60	4
Charpy	Horizontal	60×12	4
Tribology	Vertical	Ø30×80	2
Corrosion	Vertical	Ø30×80	2

Source: Author (2025).

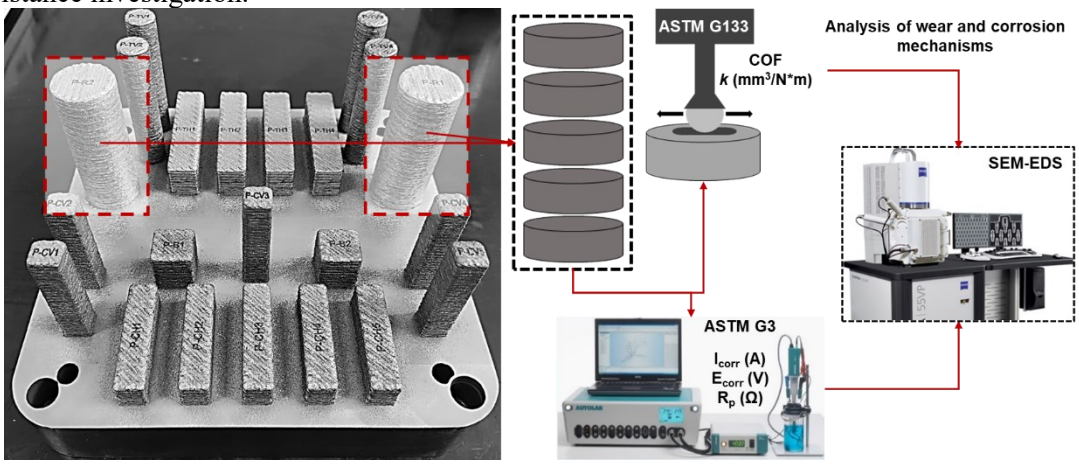
Figure 4.10 - AISI 410L MG samples manufactured for mechanical performance assessment.



Source: Author (2025).

Two cylindrical samples (Ø30×80 mm) for tribological performance by dry-sliding linearly reciprocating ball-on-flat (ASTM G133 [128]), and electrochemical corrosion resistance by potentiodynamic polarization (ASTM G3 [151]) tests were also built. After testing, a representative sample of each condition was analyzed by SEM to investigate the wear and corrosion mechanisms, respectively (Figure 4.11).

Figure 4.11 - AISI 410L MG samples manufactured for tribological performance and corrosion resistance investigation.



Source: Author (2025).

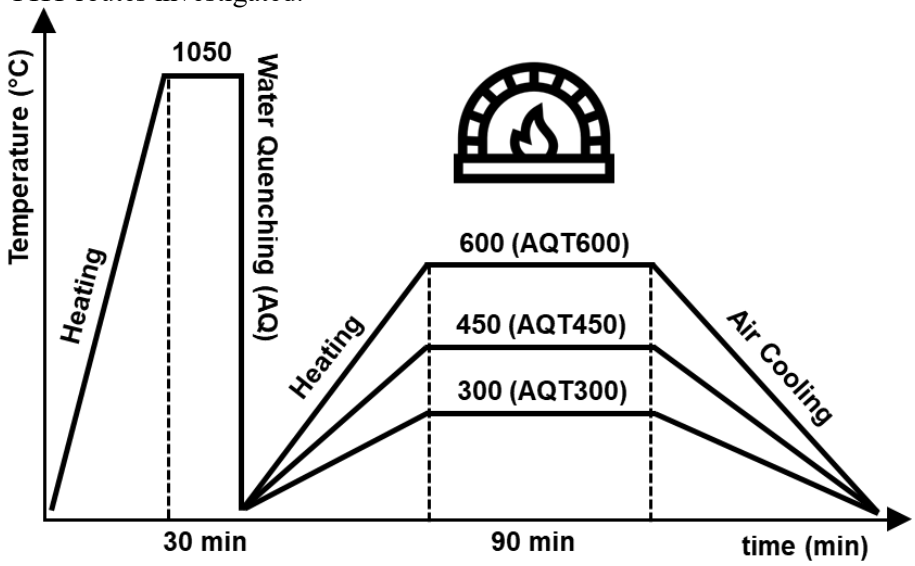
All analyses described were applied to samples in the as-built (AB) state, obtained by AM L-DED, and the reference substrate as-received (SUB-AR). Based on the traditional PHT literature applied to MSS and on the few specific AM information, it was designed to study 4 different PHT routes. In this sense, Table 4.2 and Figure 4.12 sample conditions were evaluated in this work. Temperatures were also planned as a function of the 475 °C embrittlement (item 2.2.3 [54]), aiming to evaluate values below and above this range. To analyze the PHT routes, a set of 28 samples was developed: 12 tensile (vertical), 12 Charpy impact (horizontal), and 4 cubes. Thus, there are 3 samples for each test and 1 cube for each PHT route characterization. The idea was to select the best PHT route based on the microstructure characteristics and mechanical performance. This route was then applied to samples of mechanical strength, tribological performance, and corrosion resistance, whose results were benchmarked with the AM L-DED samples in the AB, SUB-AR, and AM literature.

Table 4.2 - Conditions of evaluated samples.

Samples Conditions	
Nomenclature	Description
AB	As-Built
AQ	Quenching at 1050 °C for 30 min then water cooling
AQT300	Quenching plus Tempering at 300 °C for 90 min then air cooling
AQT450	Quenching plus Tempering at 450 °C for 90 min then air cooling
AQT600	Quenching plus Tempering at 600 °C for 90 min then air cooling
SUB-AR	Substrate As-Received

Source: Author (2025).

Figure 4.12 - PHT routes investigated.



Source: Author (2025).

4.5.3 Tribological performance

All samples intended for the tribological test were W-EDM machined into Ø30×10 mm sections. Following the metallographic preparation up to the polishing step, before tribological tests, all samples had their surface roughness measured five times by a contact profilometer (TAYLOR HOBSON FORM TALSURF 50®). All conditions showed samples with an average roughness R_a lower than 0.08 µm. These were then subjected to the dry-sliding linearly reciprocating ball-on-flat tribological test (CETR UMT-2 Tribometer, Figure 4.11), following the ASTM G133 [128]. Tribological test parameters are presented in Table 4.3. Because AISI 52100 steel (63 HRC=772 HV) is widely used in industry for sliding wear-prone parts such as axes, rollers, punches, and bearings, it was selected as the counterbody [183].

Table 4.3 - Parameters used in the dry-sliding linearly reciprocating ball-on-flat tribological test.

Samples Conditions		
Parameters	Specification	Unit
Counterbody (AISI 52100 ball)	Ø5	mm
Wear track length	10	mm
Normal load N_L	20	N
Sliding Speed	2 (40)	Hz (mm/s)
Sliding Distance	48	m
Relative Humidity	60	%
Temperature	20	°C

Source: Author (2025).

- Friction coefficient (COF): follows Equation 2.4 and is captured by a load cell.
- Volume loss (Q): two-dimensional profile of the wear tracks was measured at 5 points, spaced 2 mm apart, along the 10 mm length of the wear track. Using their entire length (l, mm), the wear tracks' area (A, mm^2) result was converted to volume loss (Equation 4.11).

$$Q = A * l\ [mm] \tag{4.11}$$

- Wear coefficient (k): estimated by Equation 4.12, where the volume loss (Q, mm^3) was divided by the product between normal load (N_L, N), and the total sliding distance (SD, m).

$$k = Q/(N_L * SD)\ [mm^3/N * m] \tag{4.12}$$

- Wear tracks: following the tribological test, a representative sample of each condition was selected and analyzed by SEM-EDS to identify the wear mechanisms.

4.5.4 Corrosion resistance

Three samples from each condition were subjected to the electrochemical corrosion test (ASTM G3 [151]). Each sample was placed in a plastic bag after being metallographically prepared, polished, and kept in this condition for 10 days before the tests to allow for natural passivation. Samples were W-EDM machined to a 10 mm thickness (Figure 4.10). The equipment used is a METROHM potentiostat PGSTAT 302 [184], composed of: sample (WE, work electrode) with a 28.5 mm^2 exposed area, a saturated calomel electrode (SCE, reference electrode), and a platinum electrode (CE, counter electrode). Tests were performed in a 3.5 wt.% NaCl aqueous solution. Cathodic polarization at -773 mV (vs SCE) for 30 min was performed. The Open Circuit Potential (OCP) was monitored for 60 min. Once OCP was concluded, potentiodynamic polarization was carried out employing a 0.10 mV/s scan rate. NOVA 2.1 software was used for data processing. After the test, a sample from each condition was analyzed by SEM-EDS to investigate the corrosion mechanisms.

5 MATERIALS AND EQUIPMENT

Table 5.1 presents information on the equipment and materials that will be employed to characterize the substrate and feedstock powder.

Table 5.1 - Substrate preparation and metallic powder characterization.

Material / Equipment	Specification	Functionality	Illustration
Abrasive Blasting Machine	IEPCO PEENMATIC® 620	Substrates abrasive blasting	50 µm steel grit
Abrasive Material	Steel grit G-12 (0.30 mm)		
Spark Optical Emission Spectroscopy	Spark-OES, OXFORD FOUNDRY-MASTER	MG cube and SUB-AR chemical composition	Detector for stainless steels
Glove Box	MBRAUN UNIlabpro Inert in Ar	Powder storage	<5 ppm of O_2
Furnace	TE-393/2-TECNAL®	Powder drying	80 °C
Precision Scale	MARTE® AD3300	Powder weighing	0.01 g resolution
Optical Microscope (OM)	ZEISS AXIO M2M	Powder cross-section, and SUB-AR	1000x magnification
Field Emission Gun-Scanning Electron Microscope (FEG-SEM)	ZEISS SUPRA 55VP	Powder morphology, and SUB-AR	10E6x of magnification and EDS with BSD and SE
Particle Insight	VISION ANALYTICAL PARTICLE SHAPE 2.55	Powder size distribution	Equivalent circular area diameter in terms of number and volume
Rheometer	FREEMAN TECHNOLOGY FT-4	Powder rheology	Stability and Variation Flow Rate (S+VFR), and Aeration Ratio (AR) tests

Source: Author (2025).

5.1 SUBSTRATES

For the SB and SL deposition, as-received AISI 410 MSS plates without heat-treatment (300×75×16.5 mm) were used as the substrate, provided as wrought, hot-rolled, and milled. For MG manufacturing, AISI 316 SS substrates (250×250×50 mm) were employed, supplied as wrought and milled (Table 5.2).

Table 5.2 - Chemical composition of the substrates.

Chemical Composition										
AISI 410 MSS	Element	Cr	Mn	Mo	Si	Ni	C	P	S	Fe
	wt.%	13.5	1.0	-	1.0	0.7	0.15	0.04	0.03	Bal.
AISI 316 SS	Element	Cr	Mn	Mo	Si	Ni	C	P	S	Fe
	wt.%	16.0	2.0	2.5	0.7	12.0	0.03	0.04	0.01	Bal.

Source: [185].

5.2 AISI 410L MSS POWDER

AISI 410L MSS in the powder particle state (Höganäs S/A supplier) was employed as feedstock. The metallic powder was manufactured by gas atomization, with particle size between 53-150 µm, and the chemical composition given by the manufacturer is shown in Table 5.3. Powder morphology was evaluated by FEG-SEM. Figure 5.1a-b illustrates some particles with different magnifications. In general, the particles exhibited good circularity. However, some satellite particles were observed, which can negatively affect the powder rheology. At random, powder samples were prepared for metallographic evaluation (embedding, sanding, and polishing in 0.3 µm diamond solid-solution suspension) of cross-section by OM. From Figure 5.1c-d, it was perceived some porosities (with dimensions <5 µm) were perceived inside the powder particles. These originate from the powder manufacturing process.

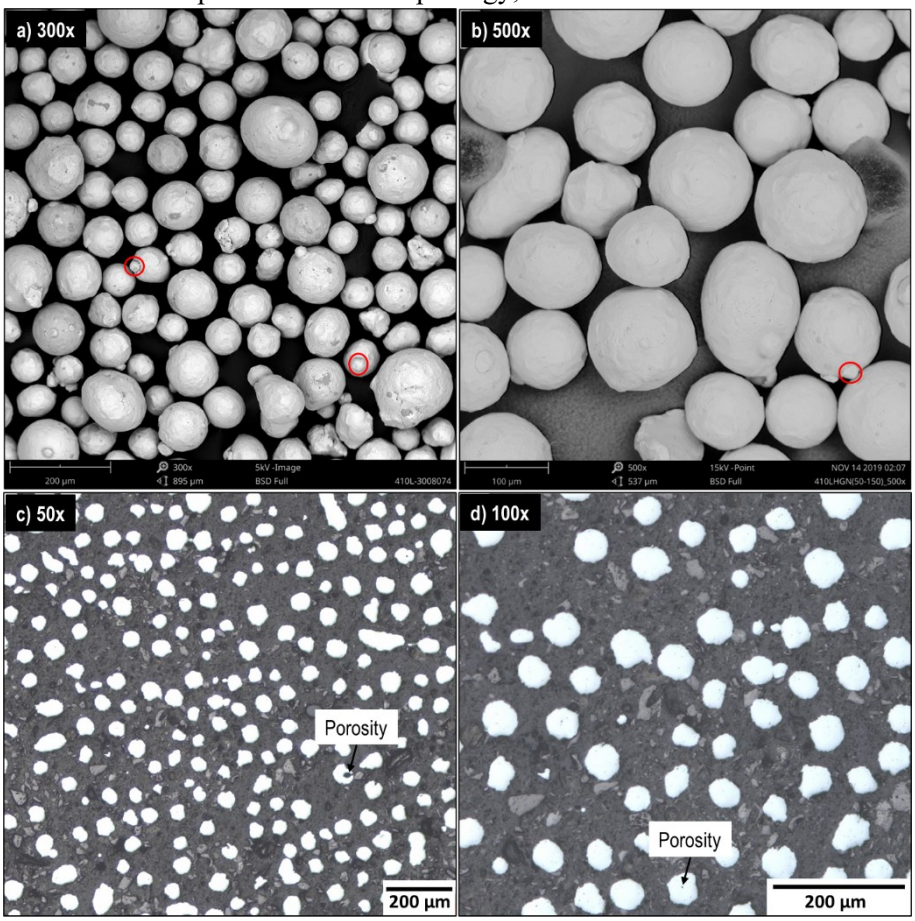
Table 5.3 - Chemical composition of the AISI 410L MSS powder employed as feedstock.

Chemical Composition							
Elements	Cr	Mn	Si	Ni	C	S	Fe
wt.%	12.2	0.6	0.6	0.1	0.02	0.01	Bal.

Source: [186].

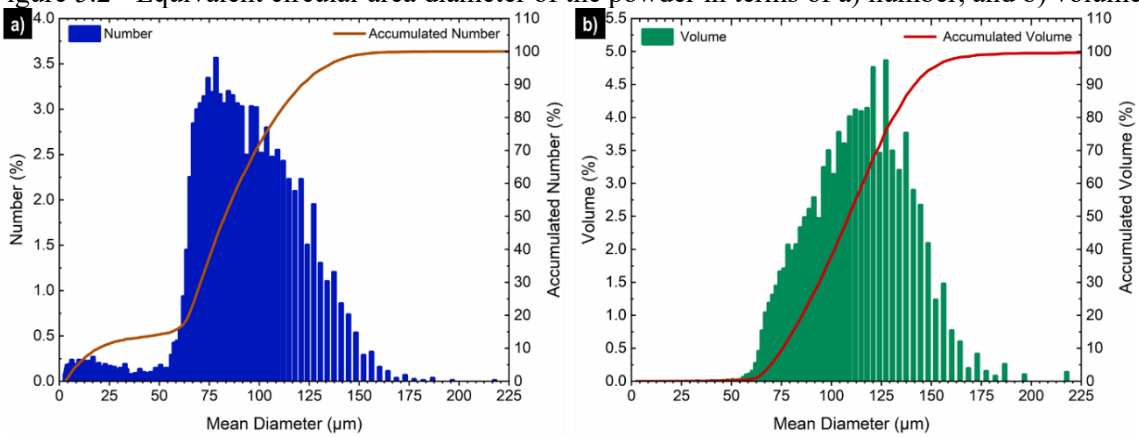
The powder particle distribution was analyzed with a Particle Insight. Sampling was taken following ASTM B215 [187]. Results of the distribution of equivalent circular area diameter (ECA) are provided in Figure 5.2 graph. In terms of number (D_n, Figure 5.2a), a mean D_n50 - 84 µm and a mode D_n90 - 123 µm were observed. In terms of volume (D_v, Figure 5.2b), the mean was D_v50 - 110 µm and the mode D_v90 - 144 µm. This result indicates that the amount of smaller and/or satellite particles in the powder is not significant.

Figure 5.1 - AISI 410L MSS powder: SEM morphology, and OM cross-section.



Source: Author (2025).

Figure 5.2 - Equivalent circular area diameter of the powder in terms of a) number, and b) volume.

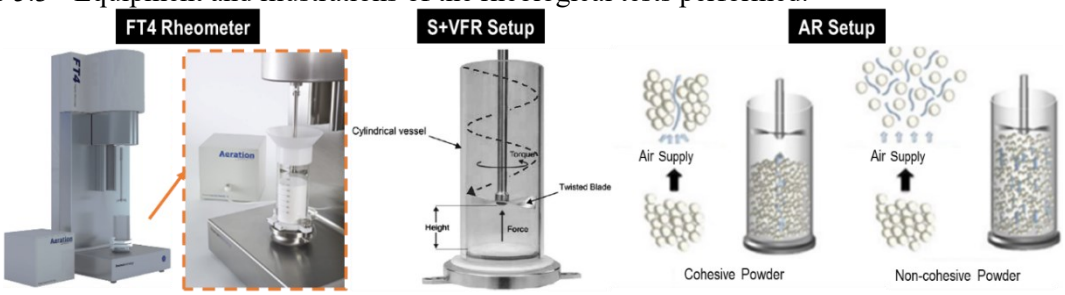


Source: Author (2025).

In the L-DED process, the powder is subjected to aeration efforts during transport through the hoses and compression when conditioned in the powder supplier. In this sense, the tests with Stability and Variation Flow Rate (S+VFR) and Aeration Ratio (AR) were analyzed. In a scientific paper, the manufacturer of the FT4 rheometer (FREEMAN Technology) used in this work presents a comprehensive background on the powder characteristics and indicates the

acceptance criteria [79]. Figure 5.3 illustrates these tests. Table 5.4 brings the results. In the S+VFR test, the powder exhibited a Stability Index (SI) close to 1, which categorizes it as a stable powder. The average Flow Rate Index (FRI) was close to 1, thus the powder is insensitive to the powder mass flow variation. Basic Flowability Energy (BFE) demonstrated a high standard deviation, which was consistent with the presence of satellite particles. Specific Energy (SE) remained constant. Thus, it was not possible to infer that the powder showed a particle cohesion reduction [79]. Aeration (AR) tests investigate how sensitive the powder is under airflow variation. The average AR energy observed (1.54) was lower than the FT4 manufacturer's limit (2). Therefore, the powder was not sensitive to aeration [79].

Figure 5.3 - Equipment and illustrations of the rheological tests performed.



Source: Adapted from [79].

Table 5.4 - Measured values of the rheological properties of the AISI 410L MSS powder.

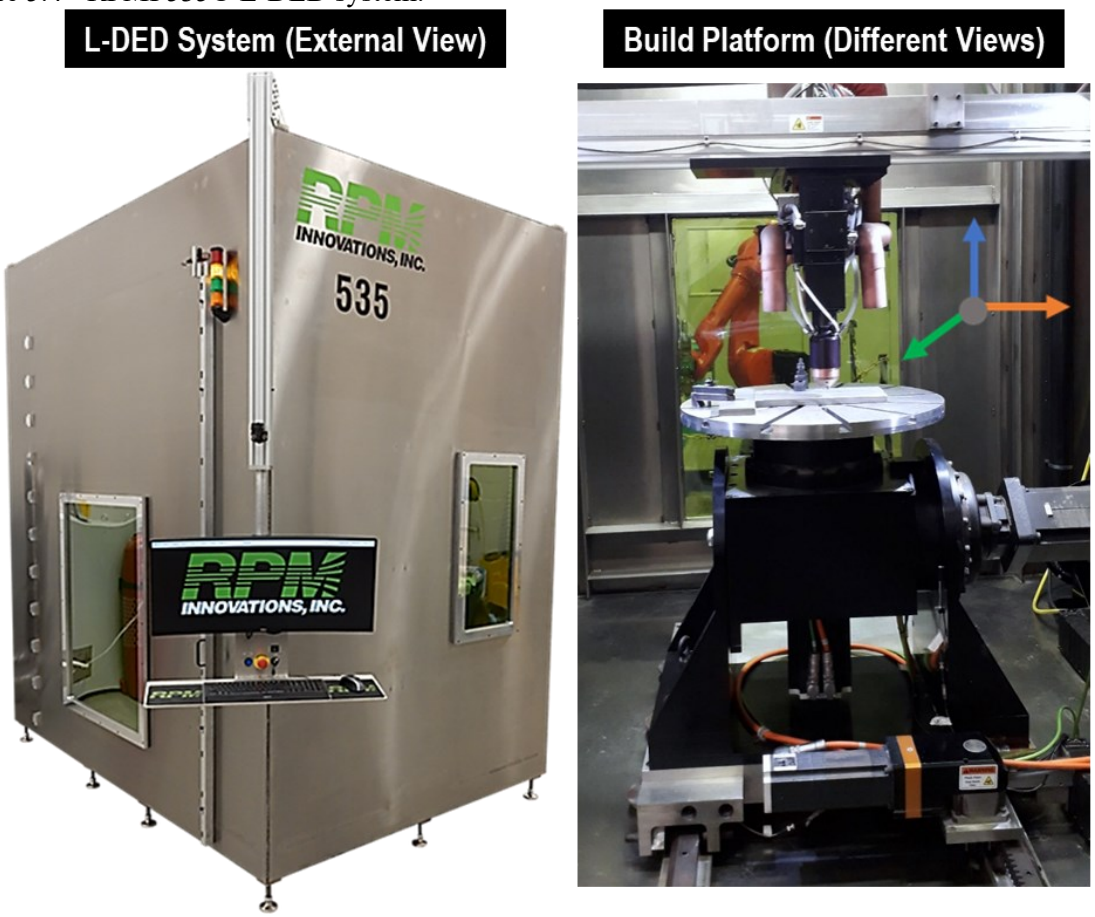
Rheological Properties (AISI 410 MSS Powder)					
Test	S+VFR				Aeration
Property	SI	FRI	BFE (mJ)	SE (mJ/g)	AR
R1	0.97	1.01	458	1.58	1.55
R2	0.95	1.02	447	1.58	1.53
R3	0.99	1.05	474	1.58	1.53
Mean±SD	0.97±0.02	1.03±0.02	460±11	1.58±0.00	1.54±0.00

Source: Author (2025).

5.3 L-DED SYSTEM

L-DED system used was the 5-axis RPMI 535® from RPM Innovations Inc. (Figure 5.4 and Table 5.5). This can operate in an Argon (Ar)-controlled atmosphere, where the oxygen (O_2) level is monitored. This machine is coupled to a continuous 100 µm fiber laser source doped with Ytterbium (Yb) with a laser power of 3300 W (YLS-3000-CT) and 1064 nm ʎ from IPG Photonics®. The Beam Parameter Product (BPP = 10.0) and Beam Quality Parameter (M^2 = 29.7) were measured using the Focus Monitor FM+ beam profilometer from PRIMES GmbH.

Figure 5.4 - RPMI 535® L-DED system.



Source: Author (2025); Adapted from RPM Innovations Inc. [188].

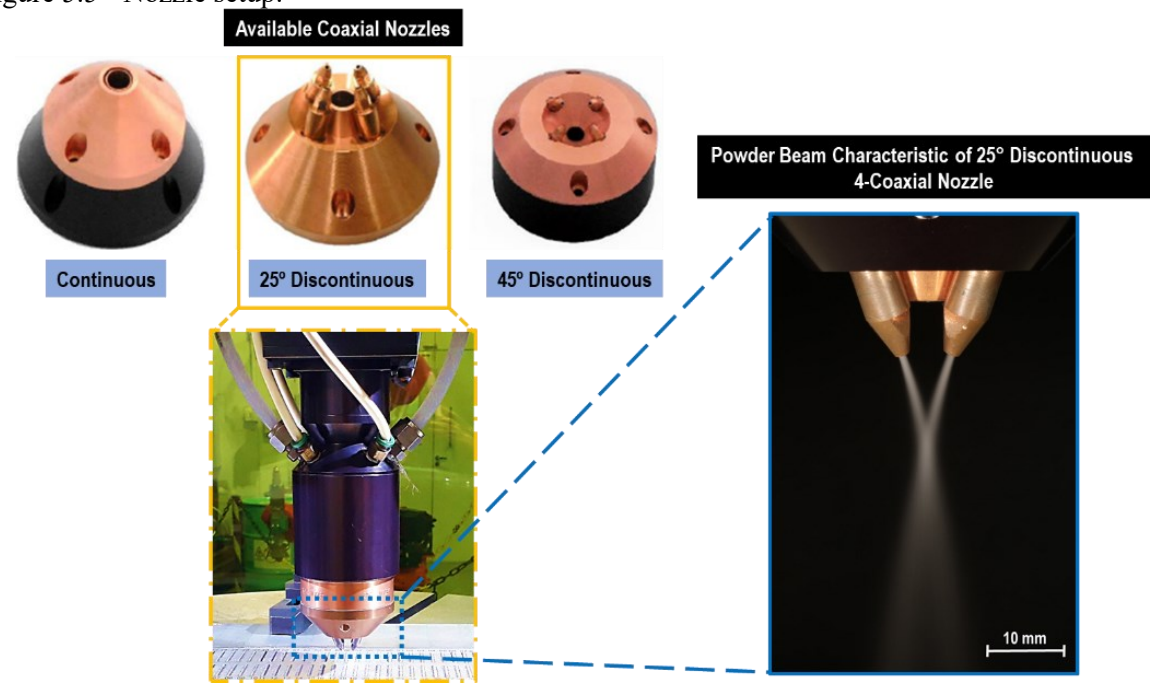
Table 5.5 - RPMI 535® technical specifications.

Feature	Value	Unit
Travel speed (S)	3810	mm/min
Powder feedrate (punctured disc) (F)	20	rpm - % (g/min)
Movement precision	0.025	mm
Maximum building volume	1524 x 914 x 1524	mm
Oxygen (O_2) content level (purged)	< 5	ppm
Load capacity	1000	kg
Axes	5	X, Y, Z, A, C

Source: Adapted from RPM Innovations Inc. [188].

RPMI 535® has a powder supplier system consisting of 2 powder suppliers, individual and independent, with two hoppers each, so that one of them can be refilled during controlled atmosphere manufacturing, without contamination inlet. RPMI 535® possesses 3 powder feed nozzle setups (Figure 5.5): continuous coaxial, and discontinuous coaxial (25° and 45°). The 25° discontinuous 4-coaxial nozzle was the type used in this work. The standoff distance (from the nozzle tip to the substrate) in this setup is 9.95 mm.

Figure 5.5 - Nozzle setup.



Source: Author (2025); Adapted from RPM Innovations Inc. [188].

5.4 CHARACTERIZATIONS

Table 5.6 presents information on the equipment and materials that will be employed in the characterization steps.

Table 5.6 (start) - Materials and equipment used in the characterization steps.

Material / Equipment	Model	Functionality	Specification
Optical Stereoscopy (OS)	ZEISS DISCOVERY V8	SB and SL surfaces	80x magnification
Thermal Camera	IRISYS IRI4030	SL surface temperature	Emissivity set at 0.70 (stainless steel with opaque surface)
Wire Electrical Discharge Machining (W-EDM)	AGIE CHARMILLES CUT 20P	Samples and cross-section machining	0.25 mm diameter brass wire
Spark Optical Emission Spectroscopy	Spark-OES, OXFORD FOUNDRY-MASTER PRO	MG cube and SUB-AR chemical composition	Detector for stainless steels

Table 5.6 (continuation) - Materials and equipment used in the characterization steps.

Material / Equipment	Model	Functionality	Specification
Metallography preparation	Politrix (AROTEC)	Sanding, polishing, and chemical etching	Grinding with 80-1200 *Mesh* sandpapers; polishing with 0.3 μm diamond solid-solution suspension, and chemical etching with Ralph's reagent
Optical Microscope (OM)	ZEISS AXIO M2M	Samples cross-section	1000x magnification
Field Emission Gun-Scanning Electron Microscope (FEG-SEM)	ZEISS SUPRA 55VP	Samples cross-section, mechanical test fractures, tribology, and corrosion surfaces	10E6x magnification and EDS with BSD and SE
X-Ray Diffraction (XRD)	RIGAKU MINIFLEX600	MG cubes and SUB-AR microstructure phases identification	Peak detection (Cu Kα radiation at a 2° per minute speed, 0.02° step, 40 kV, and 30 mA).
Archimedes Scale	METTLER TOLEDO ME204/A	MG cubes density	0.01 g resolution (weighing performed at ambient temperature)
PHT furnace	JUNG LF00612	MG, and mechanical test samples PHT	Heating ramp rate of 10 °C/min
Microhardness Tester (HV)	WILSON 402 MVD	SL, MG cubes, and SUB-AR microhardness	HV0.5 (5 N, 500 gf); three equidistant HV profiles with 10 indentations each were performed.
Tensile Tester	INSTRON 5988	MG and SUB-AR tensile tests	Strain rate of 0.2; 200 N/s and 0.07 mm/s for force and displacement control of the test; performed at room temperature.

Table 5.6 (end) - Materials and equipment used in the characterization steps.

Material / Equipment	Model	Functionality	Specification
Impact Tester	INSTRON SI-1D3	Substrate, and MG Charpy impact tests	Specimen and V-notch machined by wire electrical discharge machining (W-EDM); pendulum capacity of 170 J; performed at room temperature.
Tribometer	CETR UMT-2	MG and SUB-AR tribological test	Dry-sliding linearly reciprocating ball-on-flat tribological test with a Ø6 mm AISI 52100 steel counterbody; performed at room temperature. The friction coefficient was measured during the test using a load cell, while the wear coefficient was evaluated post-test based on the dimensions of the worn tracks.
Potentiostat	METROHM PGSTAT 302	MG and SUB-AR corrosion test	Sample (WE, work electrode) with a 28.5 mm^2 exposed area, a saturated calomel electrode (SCE, reference electrode), and a platinum electrode (CE, counter electrode); tests were performed in a 3.5 wt.% NaCl aqueous solution; the Open Circuit Potential (OCP) was monitored for 60 min; performed at room temperature.

Source: Author (2025).

6 RESULTS AND DISCUSSION

In this chapter, the main results are presented, accompanied by a discussion of the differences observed between conditions and their comparison with literature.

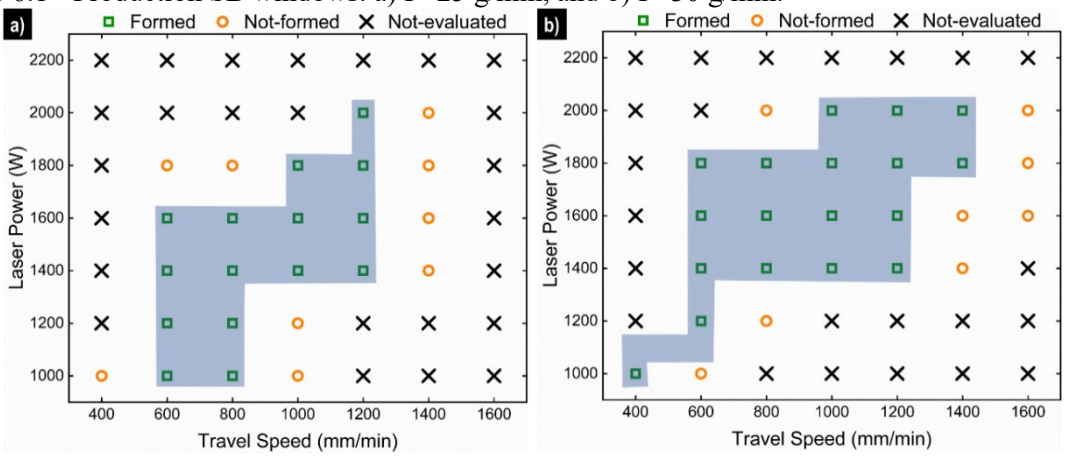
6.1 SINGLE BEADS (SB)

The SBs results are divided into two sections: the first explores hardware operational limits, and the second identifies stable parameter windows to meet acceptance criteria.

6.1.1 Operational process window

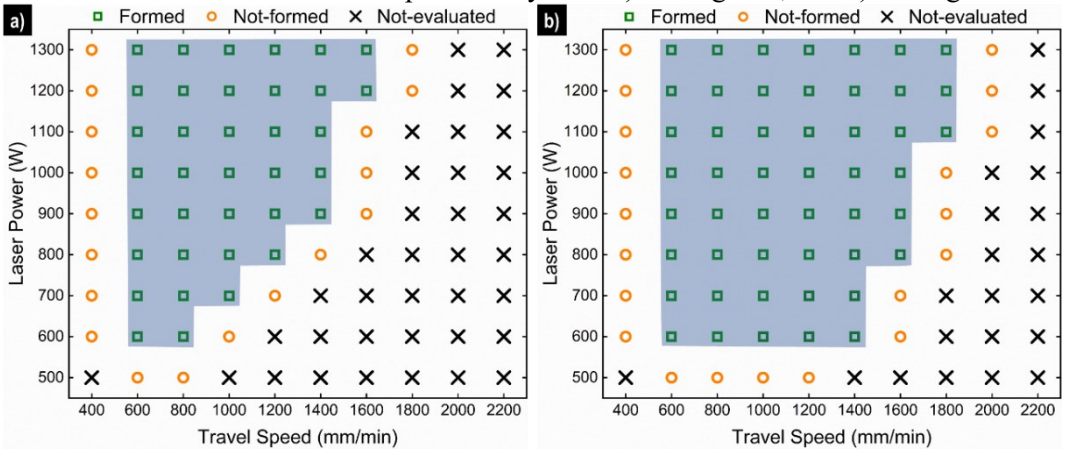
After the SBs' deposition and surface analysis, Figure 6.1 shows the operational process windows obtained for the production parameters, and Figure 6.2 for the resolution.

Figure 6.1 - Production SB windows: a) F=25 g/min, and b) F=30 g/min.



Source: Author (2025).

Figure 6.2 - Resolution windows for the preliminary SBs: a) F=20 g/min, and b) F=25 g/min.



Source: Author (2025).

From Figure 6.1 and Figure 6.2, regarding laser power, its elevation extended the maps to larger travel speeds in all powder feedrate windows. This factor then governed the lower P

limits, which may be related to insufficient energy density (J/mm) to melt the powder amount and a portion of the substrate. The upper P limits evaluated were defined concerning the L-DED system manufacturer's recommendation RPMI 535® for each spot size, to avoid damage to the optical system [188].

Concerning S, with F increasing, there was a displacement of the operational region for higher P ranges. This can be verified by the fluctuation in the powder amount per unit length and the sufficient energy density. Greater powder feedrates expanded the operational maps. This behavior can be linked to the stability provided for the formation of single beads, as well as the variation in the powder amount per unit length, and the energy density required to melt it [189]. This stage thus provided the thresholds of the main L-DED parameters.

6.1.2 Stable set of parameters

In the stable set of parameters, SB cross-sections from the operational process window were prepared for metallographic analysis, and the data obtained were evaluated. To establish the acceptance criteria within the hardware thresholds, an occurrence frequency analysis was performed, and Q1 and Q3 were defined as the lower and upper limits (Table 6.1).

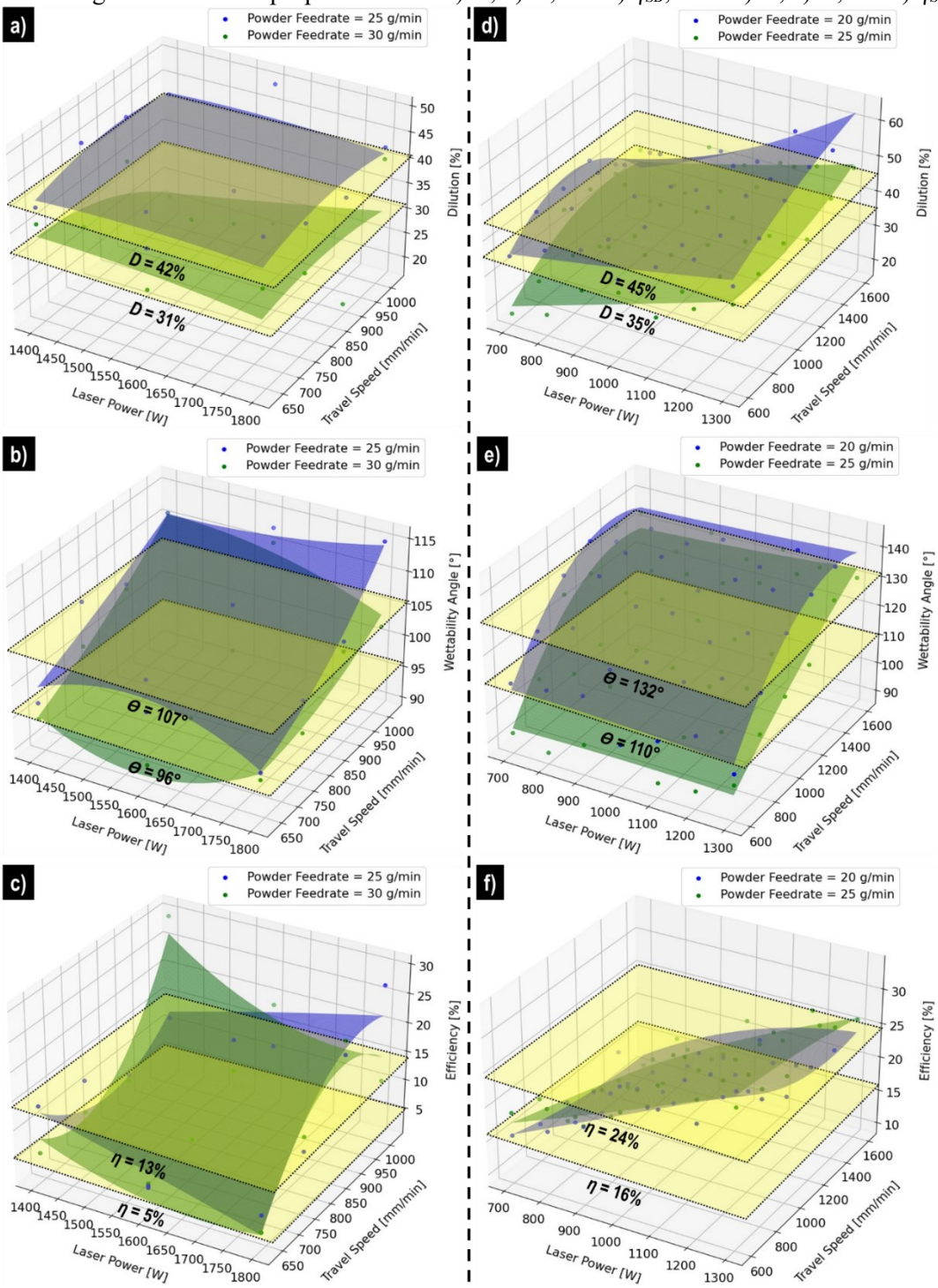
Table 6.1 - Estimated acceptance criteria for the SB properties.

Acceptance Criteria	**Production**		**Resolution**	
	Q1	Q3	Q1	Q3
D (%)	31	42	35	45
Θ (°)	96	107	110	132
η_{SB} (%)	5	13	16	24

Source: Author (2025).

From Table 6.1, regarding dilution, looking at Q1, the probability of lack of fusion occurring is low. Q3 is feasible with AM since D decreases with multilayer deposition. In additive manufacturing, higher D is preferred compared to coatings [76], [103], [105]. Concerning the wettability angle, Q1 is sufficiently high to avoid porosities between single beads, and Q3 is capable of ensuring SBs free from defects at the interface [82]. For efficiency, the ideal scenario is for Q3 to be as high as possible. Regarding Q1, this question ranges from the specific application, materials, hardware features, and operational costs [92]. Figure 6.3 shows the regressions obtained between the L-DED parameters (input) and properties of a) D, b) Θ, and c) η_{SB} (output). This illustrates the flat reference surfaces with acceptance criteria.

Figure 6.3 - Regressions for SB properties: PRO a) D, b) Θ, and c) η_{SB}; RES d) D, e) Θ, and f) η_{SB}.



Source: Author (2025).

From Figure 6.3, greater laser power and S ranges, allied to lower F, resulted in higher dilutions. On the other hand, lower D was seen in the lower P and travel speeds. Lack of fusion was not detected, while the lowest D found was 18% (PRO) and 12% (RES). Laser power increase enhances the heat input on the substrate and the molten pool turbulence. Higher S promotes a lower powder amount per unit length and decreases the heat input on the substrate,

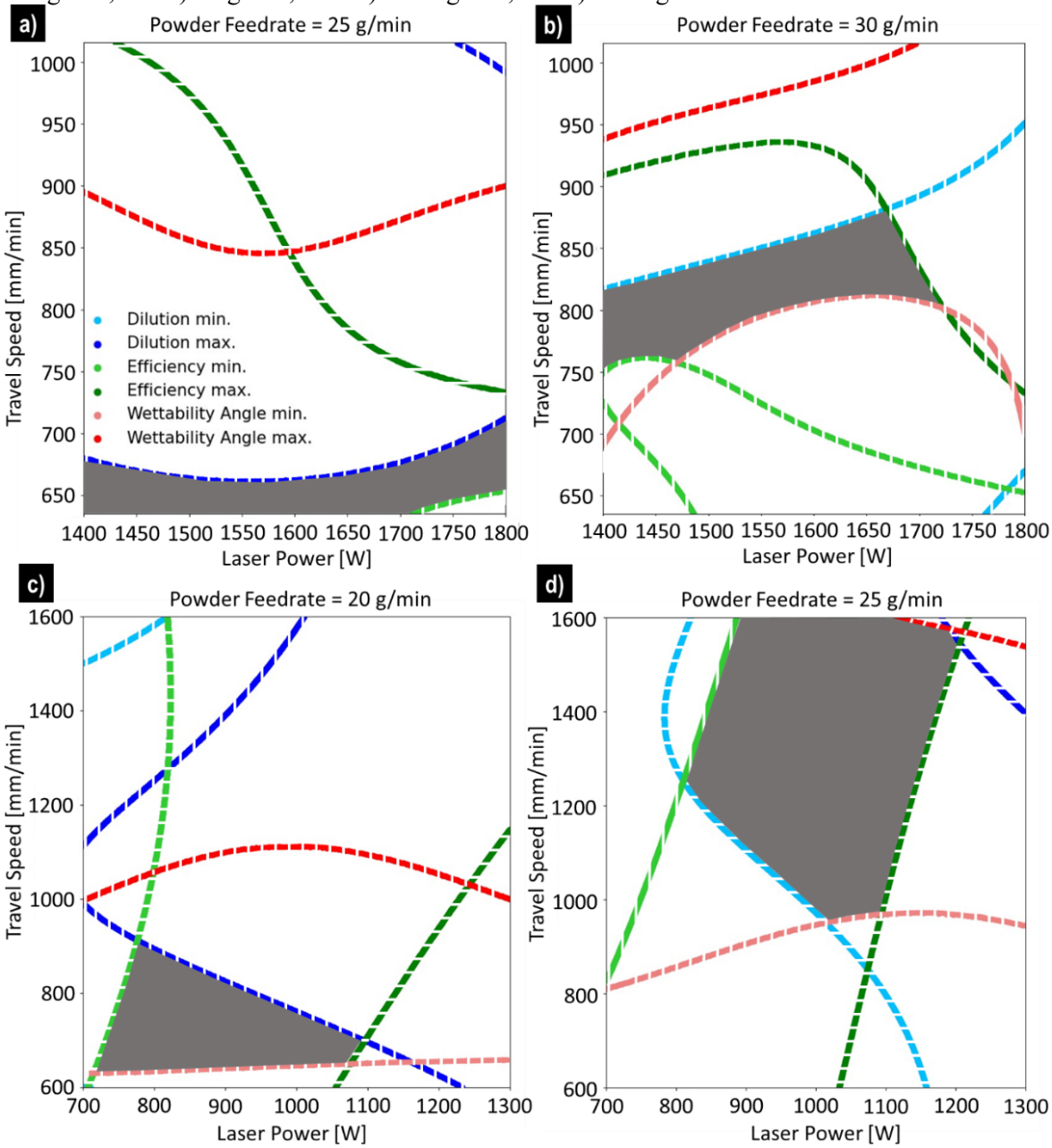
owing to the shorter interaction time between this and the power source. Powder feedrate increment provides a higher absorption of the heat required to melt the greatest amount of powder particles added, which directs a lower heat input to the substrate. For production, *D* was defined by F (30% decrease between 25 g/min and 30 g/min). Concerning resolution, *D* was governed by P (36% increase between 700 W and 1300 W) and F (24% increase between 20 g/min and 25 g/min) [103], [190], [191].

Regarding the wettability angle, for PRO, there was a decrease inversely proportional to travel speed (13% reduction between 635 and 1016 mm/min). For RES, Θ was proportional to S. Θ increases from 90° to 140° (36% increase between 600 and 1800 mm/min). Concerning F, a 10% reduction was noted between 25 g/min and 20 g/min. Production performance can be related to greater efficiency in catching and melting the feedstock. Resolution behavior, in turn, is explained by the decrease in powder amount per unit length and increase in energy input per unit length, which raises the heating and widens the molten pool [80], [191].

Evaluating efficiency for PRO, this was governed by S, followed by P, and F. With travel speed elevation from 635 mm/min (η_{SB}≈7%) to 1016 mm/min (η_{SB}≈18%), η_{SB} increased more than twice. With laser power increment from 1440-1800 W, a 22% increase was noticed. In the RES, η_{SB} was higher concerning PRO. The lower PRO η_{SB} suggests that a greater portion of the energy density is being destined for the substrate melting, increasing dilution and wettability angle. In RES, η_{SB} performance was proportional to P. In the P axis, η_{SB} virtually increased by two times with the elevation from 700 W (η_{SB}≈14%) to 1300 W (η_{SB}≈28%). Travel speed also exerts a significant influence (21% decrease between 600 and 1600 mm/min). Concerning PRO, with S increase, heat input was reduced, decreasing dilution and providing enough energy to melt the feedstock. Regarding RES, with P increasing and F decreasing, the catchment and melting of the powder particles in the molten pool increased. With travel speed reduction, the laser beam/feedstock-substrate interaction time increased, elevating the energy available to melt the powder, and enhancing efficiency [80], [92], [192].

In practice, acceptance criteria must be reached simultaneously; that is, the selected region of powder feedrate, laser power, and travel speed should generate single beads with values of dilution, wettability angle, and efficiency within this range. In this sense, the intersection between the response surfaces and reference planes of the acceptance criteria (Figure 6.3) resulted in the contour levels shown in Figure 6.4.

Figure 6.4 - Stable set of parameters that meet the acceptance criteria imposed simultaneously: PRO a) F=25 g/min, and b) 30 g/min; RES c) F=20 g/min, and d) F=25 g/min.



Source: Author (2025).

From Figure 6.4, a wider stable set of parameters (highlighted in gray) was delivered by F=30 g/min for production, and F=25 g/min for resolution. Furthermore, these parameters fell within intermediate and well-defined ranges of laser power and travel speed. Consequently, operating near these boundaries may lead to single beads falling outside the acceptance criteria. Thus, F=30 g/min was chosen to compose the PRO, and F=25 g/min the RES window in the next design of experiments stage (Single Layers, SL). The P and S matrices were then assembled from the within ranges illustrated in Figure 6.4.

6.2 SINGLE LAYERS (SL)

The single layers are categorized into two sections, one focusing on geometry evaluation and the other on the modeling and experimental verification.

6.2.1 Geometry evaluation

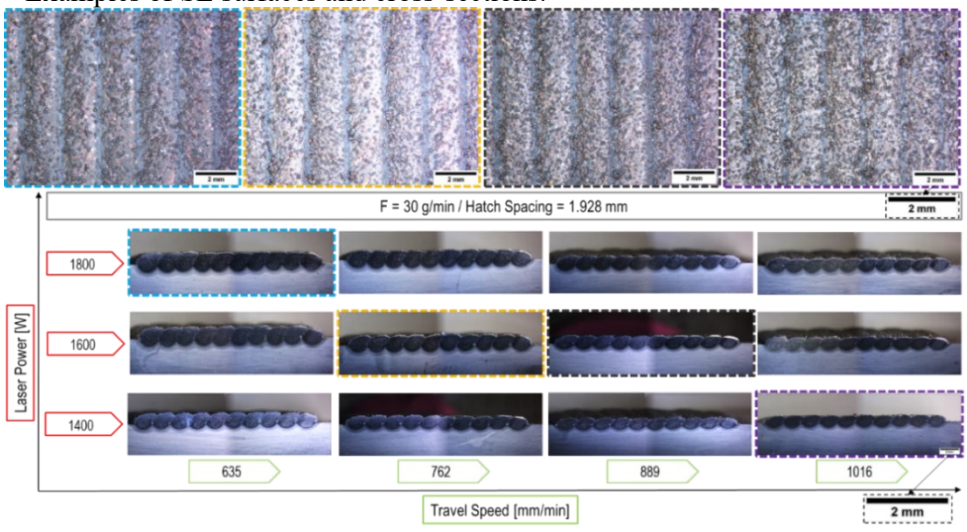
Analysis by optical stereoscope of single layer surfaces and cross-sections (Figure 6.5) did not reveal lack of fusion and cracks. Table 6.2 shows the properties of each hatch spacing. For PRO and RES, average peak height ($\bar{h}$) and slope (Θ) decreased with HS elevation, owing to the stair-step along the deposition of largely spaced single beads. Dilution (D) and waviness ($\Delta h'$) increased according to the HS, due to the greater heat input into the substrate. The $\bar{h}$ was more influenced by S, due to the fluctuation of powder amount per unit length. D increased with P, due to the greater heat input. As expected, efficiency was benefited from P increase and S reduction, due to the greater powder amount per unit length and sufficient energy to melt it.

Table 6.2 - Average values of SLs properties according to the HS.

SL Property / HS (mm)	Production			Resolution		
	1.93	**1.57**	**1.20**	**1.10**	**0.90**	**0.70**
$\bar{h}$ (mm)	1.05	1.22	1.53	0.51	058	0.75
D (%)	32	27	19	43	38	27
$\Delta h'$ (%)	21.50	9.95	6.55	17.70	11.55	6.70
Θ (°)	0.30	0.40	0.90	0.37	0.55	1.50
η_{SL} (%)	39.30	38.50	38.00	15.20	14.60	14.70

Source: Author (2025).

Figure 6.5 - Examples of SL surfaces and cross-sections.



Source: Author (2025).

6.2.2 Modeling and experimental verification

With the single layer properties measured, using a PYTHON® algorithm, the histograms of occurrence frequency showed the Table 6.3 values. Figure 6.6 regression graphs were plotted for production and resolution. Observing curves of $\bar{h}$, this increases with travel speed and hatch spacing reduction, owing to the higher powder amount per unit length and the increased laser energy density onto the previously deposited single beads, which is consistent with the literature [84], [85].

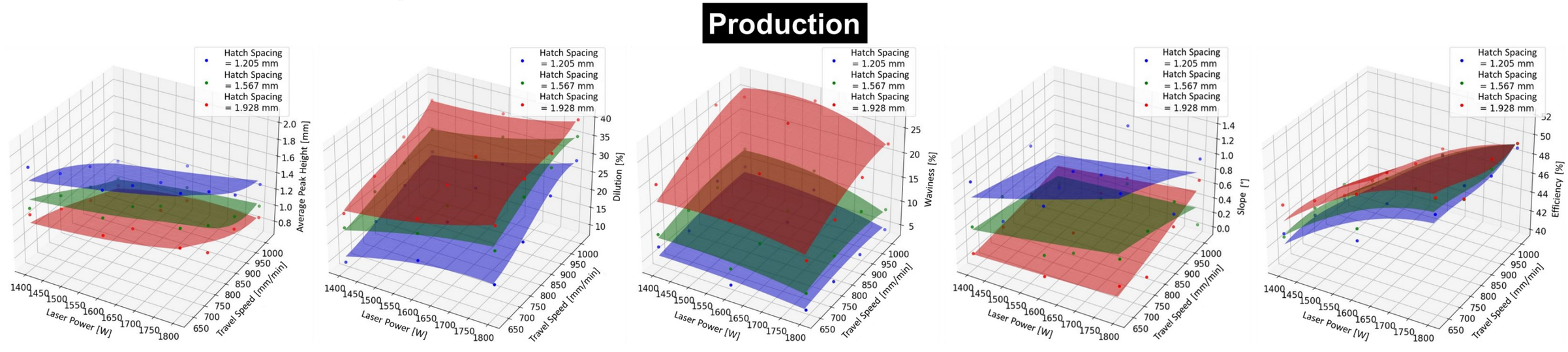
Dilution increased according to S and HS elevation. The larger spaced single beads focused a greater laser beam energy toward the substrate, while the higher S inserted a lower powder amount per unit length. The higher *D* delivered by RES concerning PRO can be attributed to the narrower spot size, lower F, and larger S used in the RES, which provides a lower catchment of powder particles, directing more energy to the substrate, as reported by [92], [103].

The waviness increased with HS elevation. The wider space between SBs directed a lower amount of powder particles and laser energy to fill the valleys. There was no significant difference between the PRO and RES. Regarding slope, lower HS generated higher Θ. At the greatest HS, Θ was higher with S elevation. Higher Θ observed in the RES when compared to the PRO may be related to the lower energy density to melt the valleys, which provided lateral rebound, as described by [108], [109].

The efficiency was dependent on laser power. This phenomenon was observed in both parameters. In general, η_{SL} average values were much higher (above 2x) in the production window, which is justified by the greater energy availability to melt the added powder, as well as the larger particle catchment area provided by the greater spot size, a behavior frequently reported in the literature [92], [103], [193].

To establish the desirability functions, acceptance criteria were defined and are presented in Table 6.4. Only the average peak height was switched between parameters, owing to the relationship of this property with production and resolution intent. Dilution limits were designed to avoid lack of fusion (minimum), low productivity, and excessive heat input (maximum). The maximum waviness and slope, and minimum efficiency were stipulated based on the concepts presented in Ferreira's work [179] and the application of this method by Thiesen [24]. Table 6.5 presents the optimized L-DED parameters and the single layer properties “predicted” by the model. 3 layers of PRO and RES were deposited and evaluated. The “real” values were added to Table 6.5.

Figure 6.6 - Regression functions for the SLs of PRO and RES parameters.



Source: Author (2025).

Table 6.3 - SL properties values obtained in the histogram analysis.

SL Properties Values Obtained in the Histograms					
Parameter / SL Property	$\bar{h}$ (mm)	D (%)	$\Delta h'$ (%)	Θ (°)	η_{SL} (%)
Production	0.8-2.0	10-40	5-30	0.0-1.4	40-55
Resolution	0.3-1.3	15-53	5-30	0.0-2.5	13-23

Source: Author (2025).

Table 6.4 - Acceptance criteria imposed on the desirability function.

Acceptance Criteria Imposed on the Desirability Function						
	Production			Resolution		
SL Property / Type	Minimum	Target	Maximum	Minimum	Target	Maximum
$\bar{h}$ (mm)	0.7	1.0	1.5	0.5	0.7	0.9
D (%)	15	25	45	15	25	45
$\Delta h'$ (%)	0	-	30	0	-	30
Θ (°)	0	-	2	0	-	2
η_{SL} (%)	20	-	100	20	-	100

Source: Author (2025).

Table 6.5 - SL properties (algorithm predicted vs. real experimental verification).

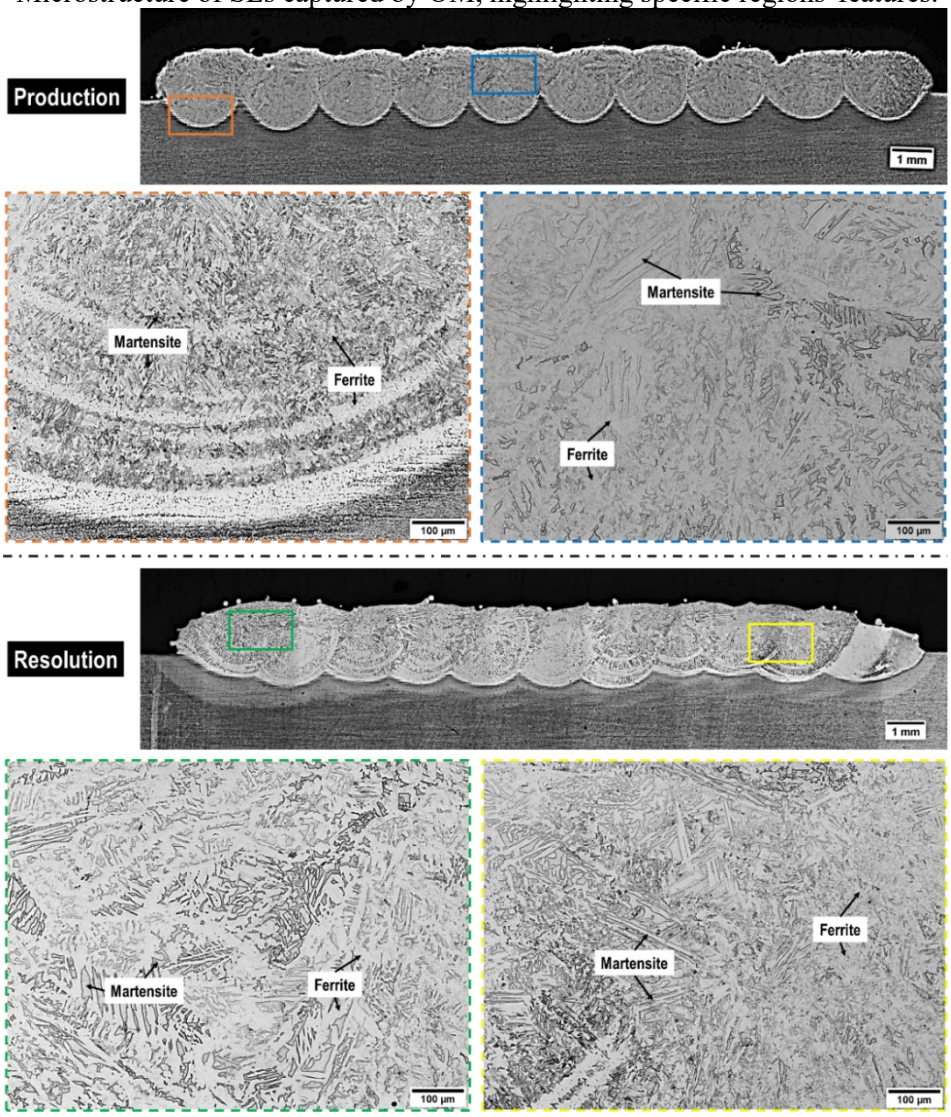
SL Properties (Predicted vs. Real)										
Parameters	Production (F=30 g/min; P=1800 W; S=635 mm/min; HS=1.93 mm).					Resolution (F=25 g/min; P=1300 W; S=800 mm/min; HS=1.03 mm).				
SL Property	$\bar{h}$ (mm)	D (%)	$\Delta h'$ (%)	Θ (°)	η (%)	$\bar{h}$ (mm)	D (%)	$\Delta h'$ (%)	Θ (°)	η (%)
Predicted	1.44	32	15	0.16	43	0.84	35	11	0.42	19
Real	1.35	30	17	0.22	40	0.94	33	13	0.88	23

Source: Author (2025).

6.2.3 Single layer microstructure and hardness characterization

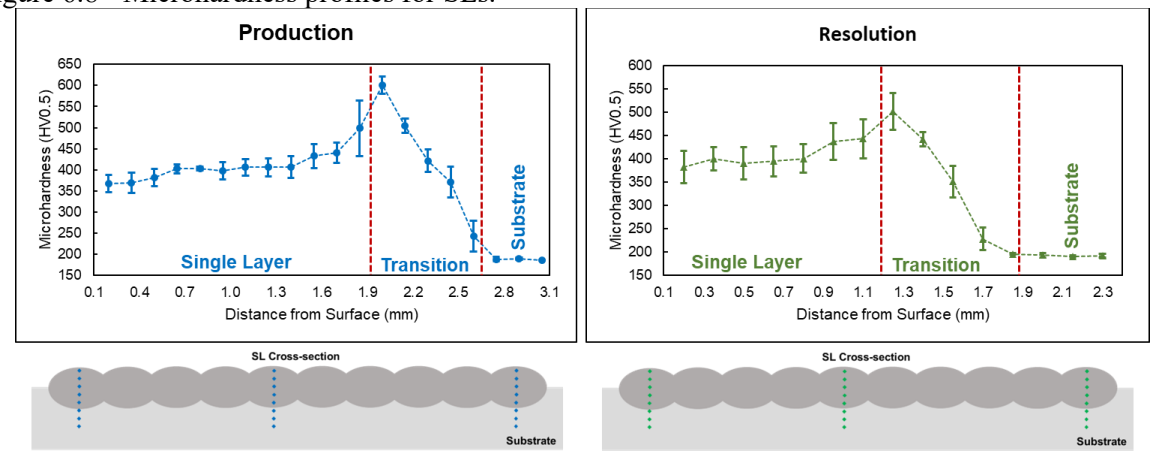
Figure 6.7 shows the optical microscope of the SLs deposited with optimized parameters. Some molten pool boundaries were observed, from where grains grew in different orientations. The microstructure exhibited a ferrite matrix with dispersed refined martensite laths, due to the laser's fast cooling and the dilution with C from the SUB-AR to the layer [18], [53]. Figure 6.8 graphs show the hardness profiles for SLs. The average values were 394±15 and 398±13 HV for PRO and RES, respectively. A transition with higher values (450±25 HV) and harsh fluctuation was observed, comprising dilution and HAZ. Probably, this peak can be attributed to the more refined martensite provided by the dilution with higher C-content from the substrate, as reported by Lai *et al.,* who observed an average hardness of 350–400 HV in the layer as they studied the application of AISI 410L MSS in the coating of railways. Due to the dilution with the C-rich substrate, 450-490 HV is recorded at the transition region [46], [160]. Steady was achieved at 200 HV, attending the annealed SUB-AR meeting.

Figure 6.7 - Microstructure of SLs captured by OM, highlighting specific regions' features.



Source: Author (2025).

Figure 6.8 - Microhardness profiles for SLs.



Source: Author (2025).

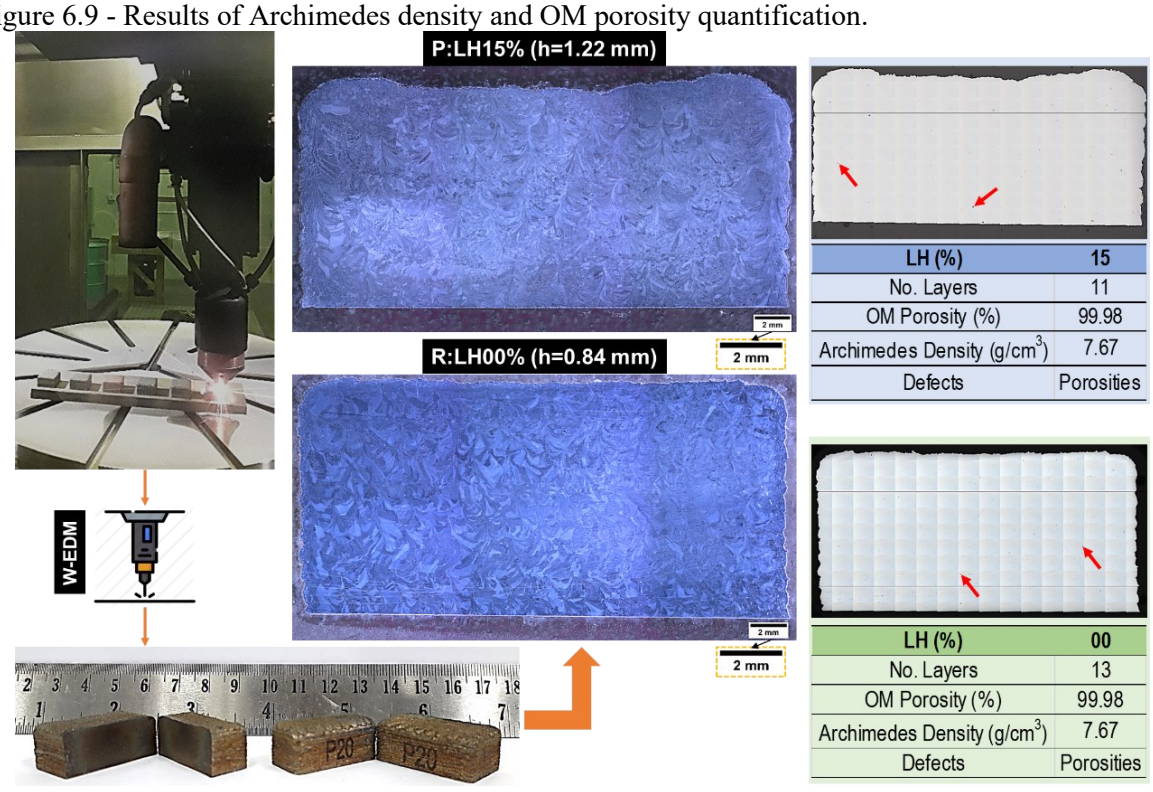
6.3 MULTILAYER GEOMETRY (MG)

Multilayer geometry results are divided into two sections, one presenting the density, and another the chemical composition delivered by the optimized L-DED parameters.

6.3.1 Density analysis

In terms of geometry, the MG cubes obtained did not show significant differences regarding the 3D CAD model. This behavior was noticed in all LH% parameters. Figure 6.9 brings the results of Archimedes' density and OM porosity quantification. for both parameters and all LH% analyzed, the density obtained was close to the reference value for AISI 410L MSS (7.74 g/cm^3). Optical microscope evaluation did not show defects (e.g., lack of fusion, delaminations), but only rounded porosities, probably resulting from gas blisters entrapment, as documented in the literature [75], [92].

Figure 6.9 - Results of Archimedes density and OM porosity quantification.



Source: Author (2025).

In Figure 6.9, for production, from LH15% (h=1.22 mm) onward, no further density increase was observed. In the resolution, no gains were achieved from LH > 0% (h=0.84 mm). Therefore, LH15% and LH0% were selected for the PRO and RES parameters, respectively, eliminating the need for 1 (LH25% = 12 > LH15% = 11) and 5 (LH25% = 18 > LH00% = 13)

additional layers to reach the MG cube dimensions. This difference between parameters may be attributed to the lower layer thickness in the RES parameter [189].

No oxide inclusions were observed (Figure 6.9), which may be attributed to the method taken in powder handling and using an Ar-controlled atmosphere in MG manufacturing. The importance of this method was evidenced in Gutjahr's research, which investigated the degradation of AISI 316L SS powder over 8 L-DED build reuse cycles, concluding that the O_2-content variation was negligible, thus not compromising the microstructure and mechanical properties of tensile strength, and Charpy impact toughness [71], [194].

6.3.2 Chemical composition of as-built samples by Spark-OES

Table 6.6 shows the AISI 410L MSS chemical composition, in the powder state (Höganäs supplier), and the results from the Spark-OES test measured in the MG cube cross-section. The contents of the elements observed were virtually the same. This fact suggests that the L-DED processing conditions utilized had no discernible impact on the chemical composition. The literature shows that there can be significant differences in the powder chemical composition between the inside and outside of the particles. The primary reason is the more intense surface oxidation resulting from atmospheric exposure. Additionally, the bulk chemical composition of the same material may differ from that of the powder [195]. Using a regulated argon-rich atmosphere in the current work protected the material from these interactions. This was demonstrated in Gutjahr's research, which examined AISI 316L through 8 build reuse cycles using L-DED and found no appreciable O_2-content evolution [71], [194].

Table 6.6 - Chemical composition of AISI 410L powder vs MG cube evaluated by Spark-OES.

Chemical Composition			
Elements (wt.%) / Source	Höganäs (powder)	Production	Resolution
Cr	12.85	11.50	11.60
Mn	0.80	0.80	0.80
Si	0.80	0.66	0.60
Ni	0.50	0.10	0.09
C	0.02	0.01	0.01
S	0.02	0.01	0.01
Fe	Bal.	Bal.	Bal.

Source: [186]; Author (2025).

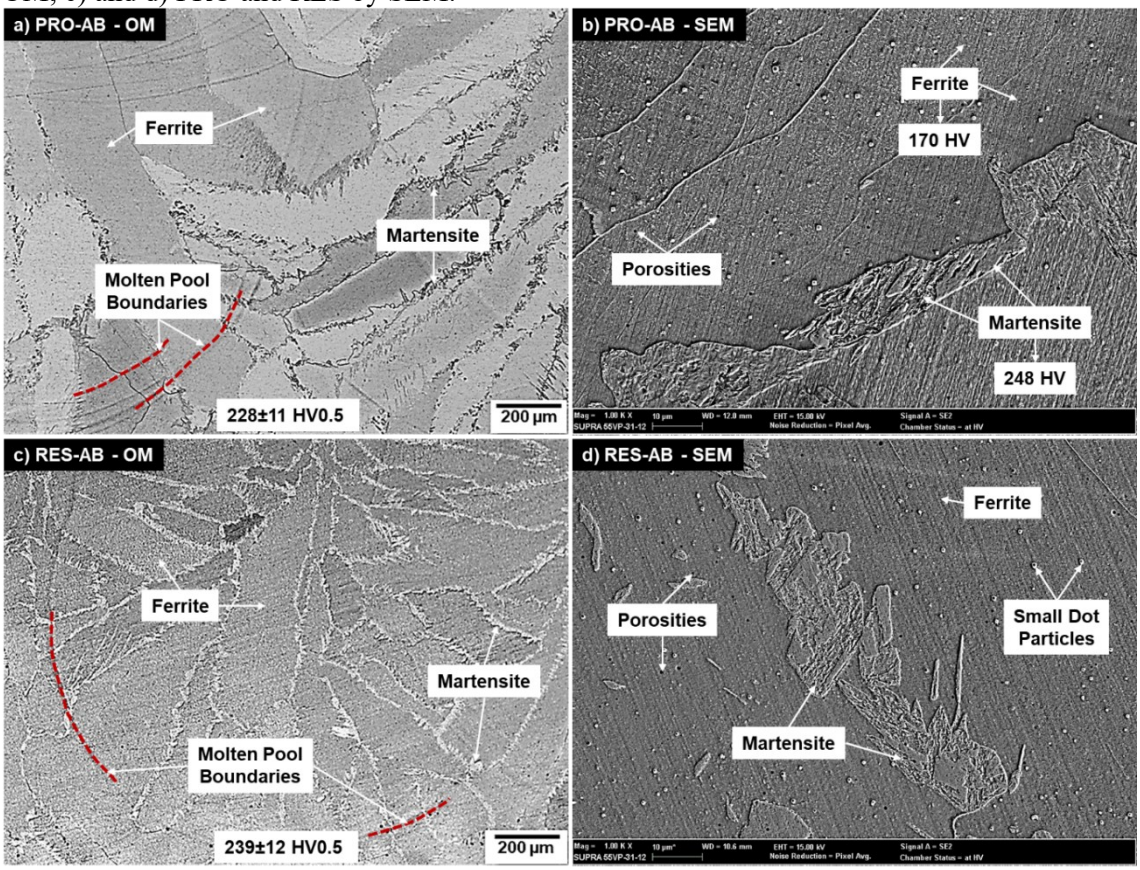
6.4 MICROSTRUCTURE AND HARDNESS CHARACTERIZATION

This section presents the effects of laser directed energy deposition parameters and post heat-treatment on the microstructure and hardness characterization of the multilayer geometries. The MG cubes were used in this stage.

6.4.1 Effects of the L-DED parameters

Figure 6.10 presents the microstructure of production (Figure 6.10a-b) and resolution (Figure 6.10c-d) MG cube samples of AISI 410L in the as-built state captured by optical and scanning electron microscopes. These were obtained from the central region of the cubes. The absence of harmful defects is a primary observation. Only a few rounded porosities were seen. It was detected certain molten pool boundaries (highlighted in red dashed lines) in the regions of hatch spacing between single beads and layer height between single layers, which is an inherent feature of metallic AM techniques like L-DED and L-PBF [23], [196], [197].

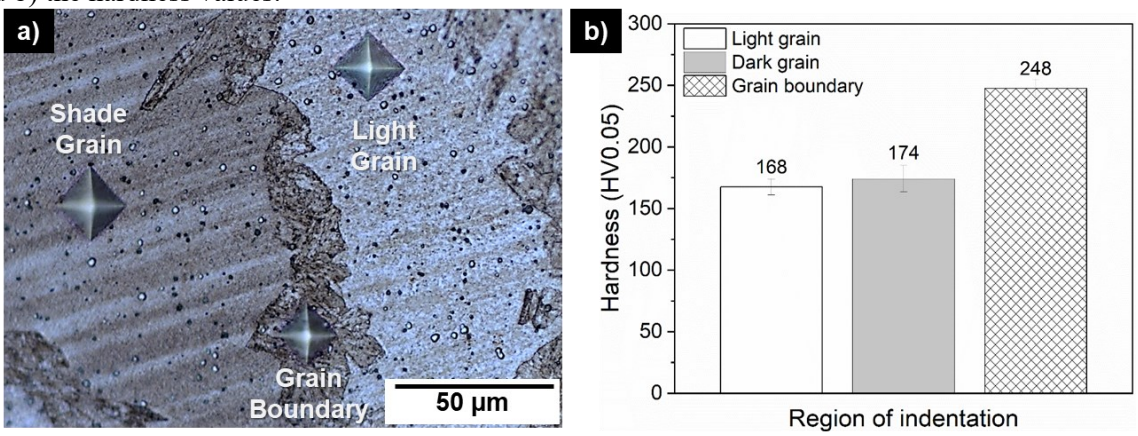
Figure 6.10 - Microstructure aspects of the AISI 410L L-DED AB conditions: a) and b) PRO and RES by OM; c) and d) PRO and RES by SEM.



Source: Author (2025).

Evaluating Figure 6.10a-c, the microstructure of L-DED AB seen in the OM was formed by columnar grains of ferrite with a lighter color, and refined martensite with a darker color, concentrated at the grain boundaries. Another highlight is the multiple grain growth directions related to the process's repeated heating/cooling cycles, which generate new grain nucleation sites and establish a heterogeneous microstructure. Comparing L-DED AB conditions by color contrast quantification analysis using the Image J software, the content of martensitic grain boundaries in RES was 5±0.2% higher (in surface area) regarding PRO condition, which attests to the more refined grains of the first. Figure 6.10b-d captured by SEM confirms the ferritic grains' columnar structure with the refined martensite concentrated at the grain boundaries. Small, rounded dot phases were also observed at higher magnification, as reported by [17], [21]. Observing Figure 6.10a-c, RES showed a higher hardness (239±12 HV0.5) than PRO (228±11 HV0.5), which can be attributed to its refined grains and the consequent higher amount of martensite. Figure 6.11a localized hardness analysis conducted at a lower load (HV0.05, 50 gf) revealed that the hardness of the ferritic light region (174±6 HV0.05) is, on average, 30% lower concerning the martensitic (248±9 HV0.05), as illustrated in Figure 6.11b. A similar performance was described by [6], [53].

Figure 6.11 - Hardness of the different microstructure regions highlighting a) different aspect regions, and b) the hardness values.



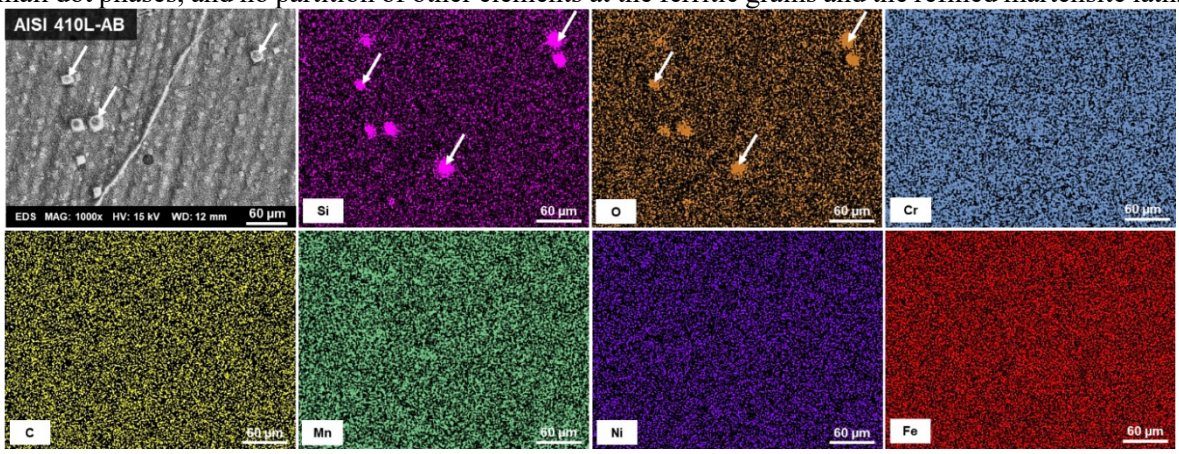
Source: Author (2025).

These microstructure characteristics and hardness can be attributed to the high cooling speed imposed by the laser beam and the low C-content of AISI 410L. The low C-content of the feedstock (0.02 wt.%) is below the solubility limit of body-centered cubic (BCC) structure, which provides a full dissolution of C within ferrite. High cooling speed lowered the martensitic

transformation start temperature (M_s). Besides, in refined microstructures, the higher mechanical resistance imposed by the greater area occupied by grain boundaries provides an additional energy barrier, limiting dislocation mobility and interface motion, which hinders the plastic deformation required for martensitic transformation [161], [162], [197], [198].

To investigate the chemical nature of the phases found, a SEM-EDS map analysis was carried out. Figure 6.12 showed no significant differences concerning the manufacturer-provided values. Since precautions were taken to prevent contamination during manufacturing, this outcome was expected. There were no variations between ferrite grains and refined martensite concentrated at the grain boundaries. The absence of carbides in L-DED conditions indicates that C-content must be interstitially present in the martensite solid-solution [7], [53]. The small, rounded dots in the OM and SEM analysis correspond to Si and O-rich particles, like SiO_2. These chemical composition aspects were analogous in both L-DED parameters [6].

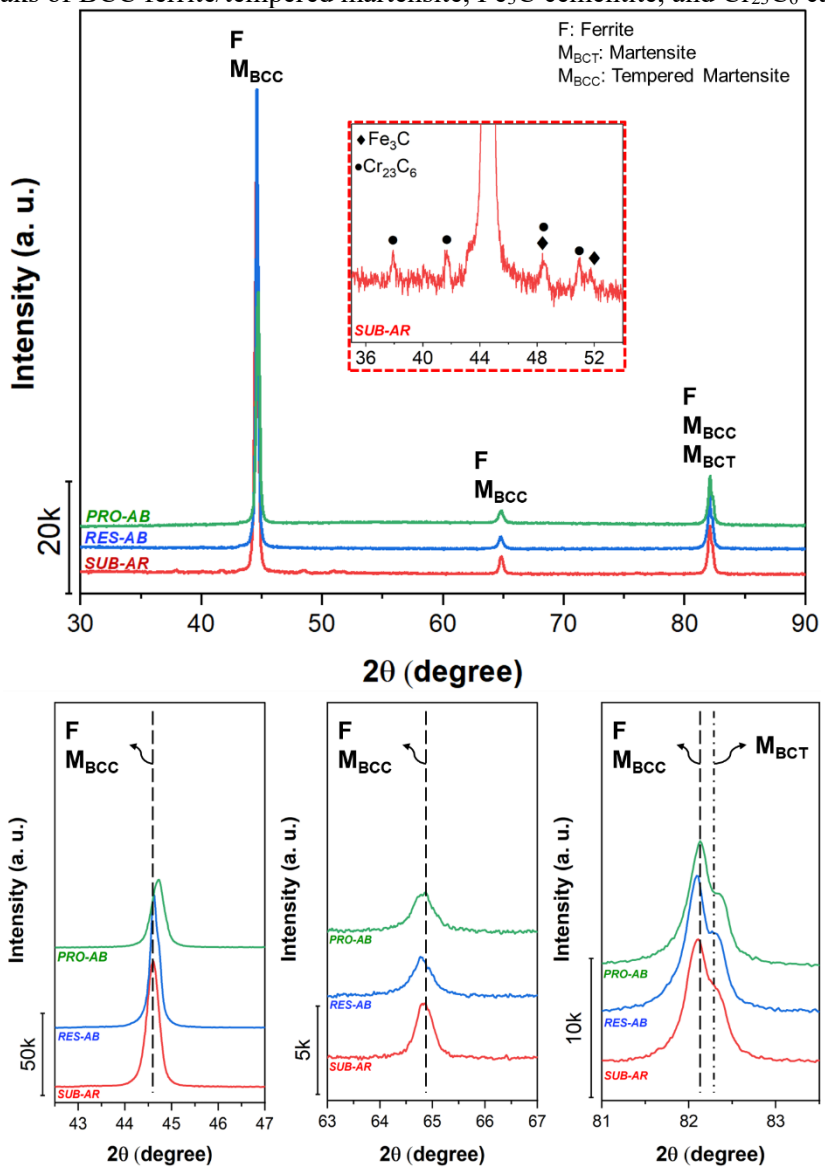
Figure 6.12 - SEM-EDS of the AISI 410L AB condition showing higher contents of Si and O in the small dot phases, and no partition of other elements at the ferritic grains and the refined martensite laths.



Source: Author (2025).

Figure 6.13 XRD diffractograms indicate the predominance of the BCC structure in both L-DED AB conditions, which corresponds to the ferrite and martensite phases. The main peaks were found at 44º, 64º, and 82º. A discrete peak corresponding to the tetragonal body-centered (BCT) martensite was around 82°, partially overlapping with a ferrite/BCC tempered martensite. This suggests the formation of martensite with a more pronounced tetragonal character. This peak was more pronounced in the RES condition, which is consistent with the higher amount of martensite observed in this one. BCT martensite peaks are shifted to higher angles relative to BCC martensite. This, combined with the greater density of grain boundaries in the RES condition, corroborates this observation [46], [155].

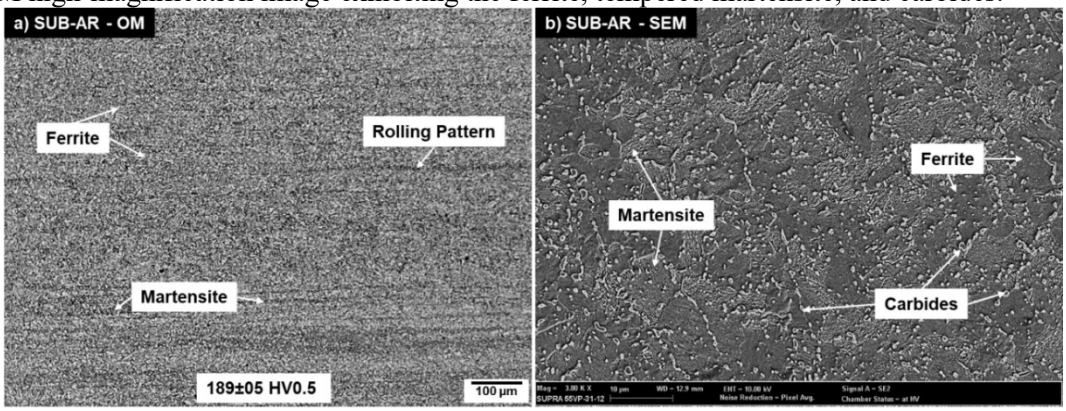
Figure 6.13 - XRD of the L-DED AB showing peaks of BCC ferrite/martensite, and BCT martensite. In the SUB-AR, peaks of BCC ferrite/tempered martensite, Fe_3C cementite, and $Cr_{23}C_6$ carbides.



Source: Author (2025).

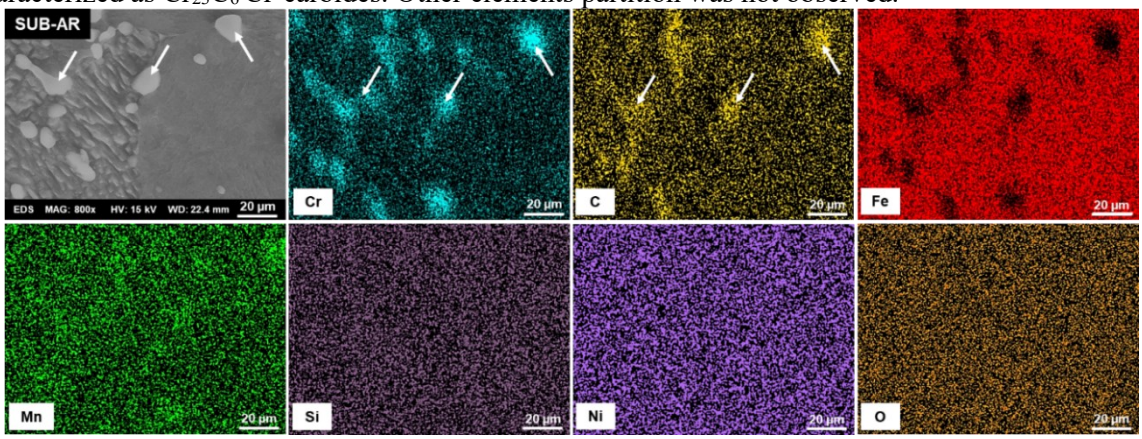
SUB-AR microstructure is depicted in Figure 6.14. OM produced Figure 6.14a, which shows remaining marks from the rolling step. Figure 6.14b SEM enabled for more efficient distinction between ferrite and tempered martensite. Figure 6.13 XRD diffractogram showed peaks of the BCC crystalline structure for SUB-AR, corresponding to ferrite and tempered martensite. During SUB-AR manufacturing, part of the carbon-supersaturated martensite was transformed into BCC tempered martensite, Fe_3C cementite, and $Cr_{23}C_6$-carbides [48], [65], [199]. XRD responses are consistent with the microstructures previously observed in Figure 6.14a-b OM and SEM, and the chemical composition analyzed in Figure 6.15 SEM-EDS.

Figure 6.14 - Microstructure of SUB-AR, highlighting a) OM showing remaining hot-rolling marks, and b) SEM high-magnification image exhibiting the ferrite, tempered martensite, and carbides.



Source: Author (2025).

Figure 6.15 - SEM-EDS of SUB-AR, showing high contents of Cr and C in the small, rounded phases characterized as $Cr_{23}C_6$ Cr-carbides. Other elements partition was not observed.

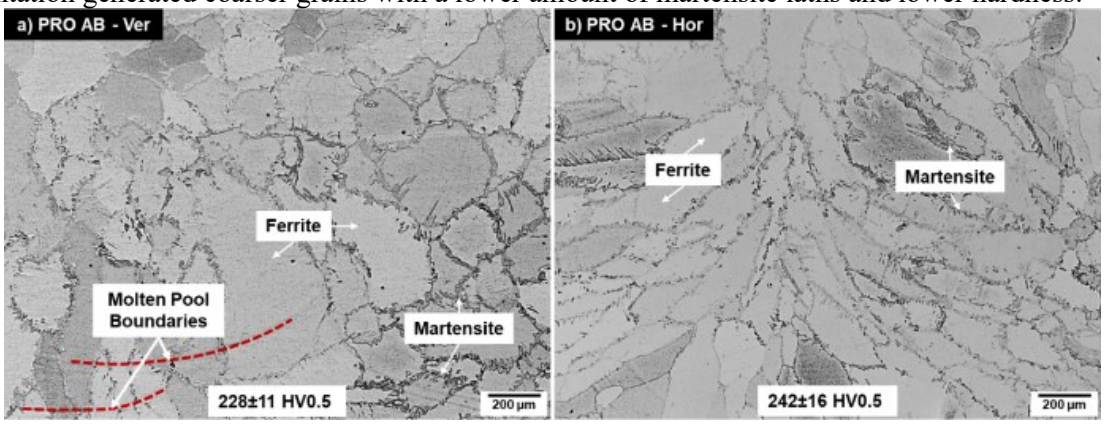


Source: Author (2025).

6.4.2 Effects of the building orientation

Figure 6.16 presents the OM cross-section microstructure of the PRO-AB in different building orientations. In both orientations, columnar ferrite with refined martensite laths concentrated at the grain boundaries was noted. However, the horizontal orientation exhibited more refined grains. Quantitative analysis of grain boundaries indicated a 7±0.3% larger area in the horizontal orientation, correlating with a higher martensite concentration, which slightly increased the hardness. Considering that the samples were built with the same set of L-DED parameters and have the same built volume, the only changes are the orientation and number of layers. In the horizontal orientation, the longer layers have a larger contact area with the substrate, enhancing the heat-sink conduction mechanism. Besides, its smaller number of layers provides fewer reheating cycles. As expected, the combination of these two factors resulted in faster cooling, refined grains, and a higher amount of BCT martensite in the horizontal built samples, a behavior corroborated by several authors [17], [21], [47].

Figure 6.16 - OM of the PRO-AB: the slower cooling of the a) vertical concerning b) horizontal build orientation generated coarser grains with a lower amount of martensite laths and lower hardness.



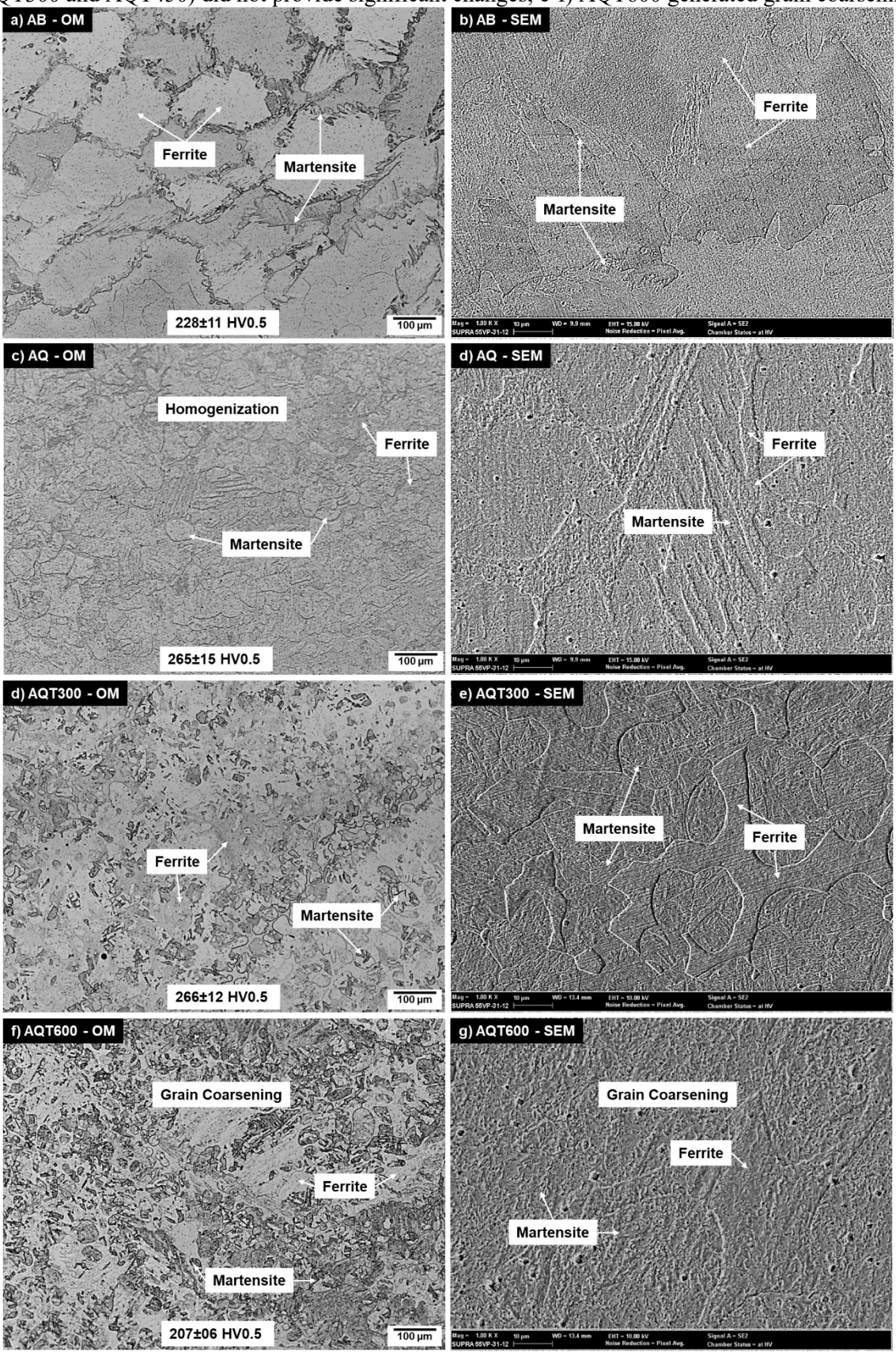
Source: Author (2025).

6.4.3 Effects of the post heat-treatment

The PHT study examined various routes employing MG cube samples manufactured with PRO parameters (Table 4.2). Figure 6.17 presents PRO AB (Figure 6.17a-b) and austenitization plus quenching (Figure 6.17c-d) captured by OM and SEM. The biphasic columnar ferrite with refined martensite laths at grain boundaries in the AB was fully homogenized after AQ. Grain boundary martensite laths were dissolved and dispersed throughout the Fe-matrix. Ferrite was homogeneously distributed, and martensite showed a rounded package morphology. As a result, it is difficult to distinguish between the Fe-matrix and the grain boundaries. Hardness was 13% higher in the AQ regarding the AB condition, which can be attributed to the microstructure homogenization. The austenitization (temperature and time) was sufficient to modify the L-DED thermal history [53], [167], [200].

Figure 6.17 shows the AISI 410L microstructure after tempering. No significant variations regarding the AQ (Figure 6.17c-d) were seen at lower tempering temperatures, AQT300, and AQT450 (Figure 6.17e-f). Grains are maintained at the same refinement level. Hardness supports this observation, remaining nearly constant across the AQ (265±15 HV0.5), AQT300 (266±12 HV0.5), and AQT450 (273±16 HV0.5) conditions. On the other hand, tempering performed at a higher temperature AQT600 (Figure 6.17g-h), generated a significant grain coarsening owing to the slower cooling provided. As a result, hardness decreased (207±6 HV0.5) by 10% and 23% when compared to the AB and lower tempering temperatures (AQT300 and AQT450), respectively. The residual stress relief also provided by AQT600 must have influenced the hardness, as pointed out by some authors in the literature [53], [97], [163].

Figure 6.17 - Effect of austenitization plus quenching (AQ) on the AB microstructure: a-b) ferrite with martensite laths at grain boundaries; c-d) fully homogenization; tempering at a-d) lowest temperatures (AQT300 and AQT450) did not provide significant changes; e-f) AQT600 generated grain coarsening.

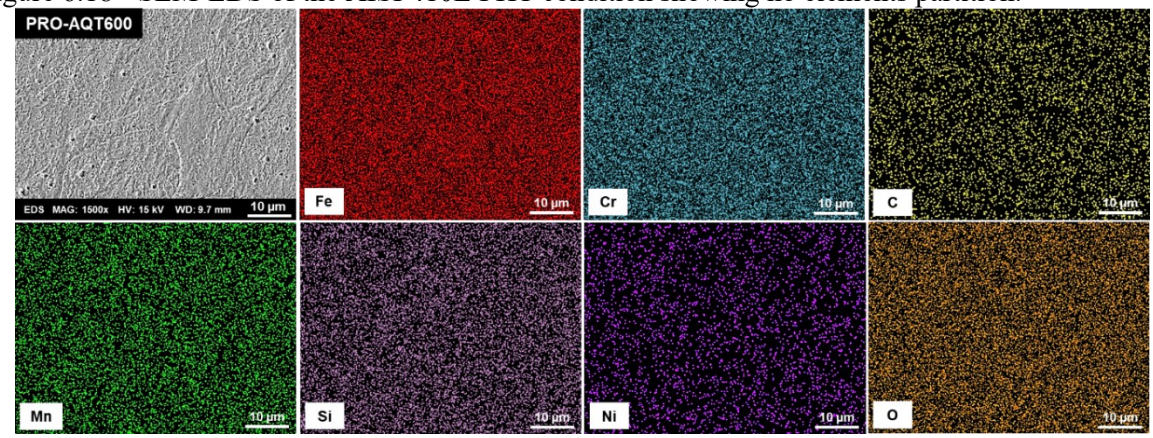


Source: Author (2025).

In Figure 6.18 SEM-EDS, no significant segregation or chemical composition differences were identified between the L-DED AB condition and PHT in other areas of the examined samples. In this sense, only the evaluation of one AQT600 condition was added for behavior illustration. Figure 6.19 presents the XRD analysis, which revealed the same peaks previously described for the AB (Figure 6.13) across all PHT conditions. As expected, notably, there was a reduction in the overlap of the peak shift to the right at 82°. This supports the idea that this peak is associated with the higher tetragonality of BCT martensite found in the AB condition, especially in the RES, which provides faster cooling compared to PRO. The shift of this peak to lower values brings it closer to the BCC structure of ferrite/martensite, which is in accordance with the literature [6], [53], [162], [200].

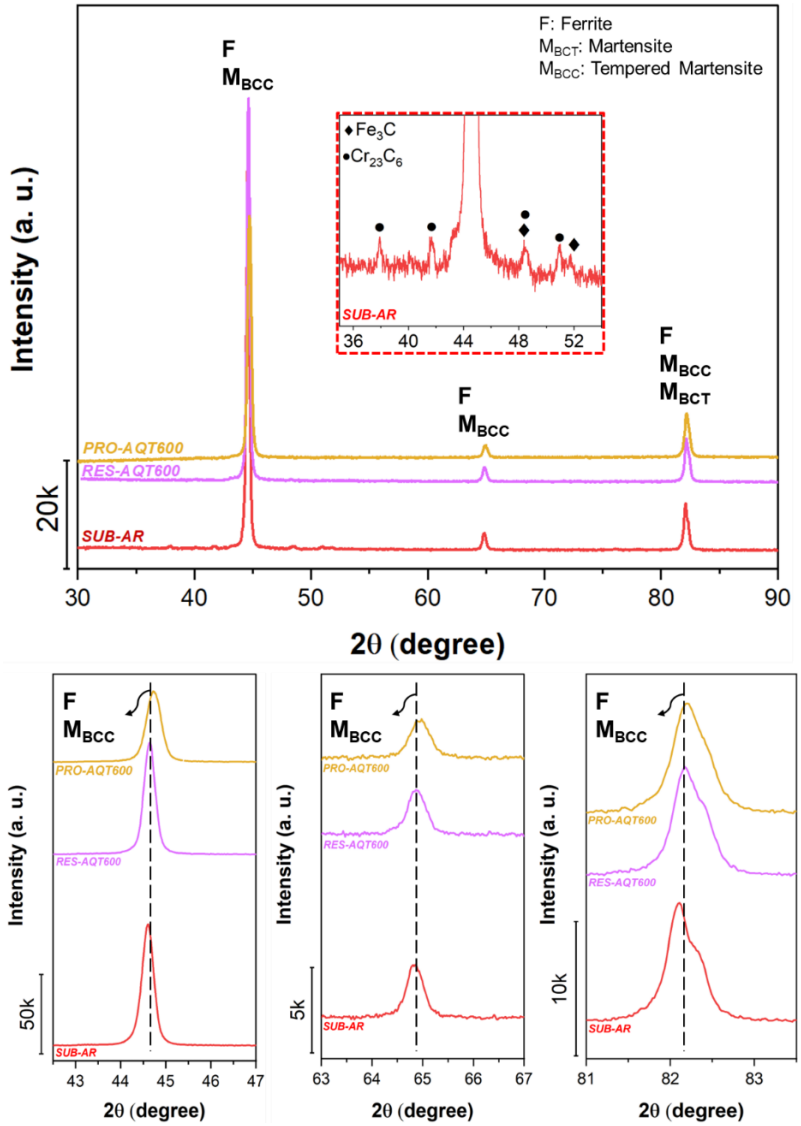
As previously mentioned, all PHT routes were analyzed solely under the PRO condition. Based on the results obtained in this study regarding microstructure and mechanical performance (to be discussed in section 6.5), the AQT600 route was identified as the most suitable option. Accordingly, Figure 6.20 presents a comparison between PRO and RES conditions after undergoing this PHT route. As can be seen, in both parameters, the grain boundaries were homogenized, and the resulting tempered martensite presented a packaged morphology distributed homogeneously throughout the ferritic matrix. However, unlike the PRO-AQT600 condition, in which the martensite was formed preferentially within the rounded recrystallized grains, in the RES-AQT600, it was still possible to detect some martensite laths remaining from the AB structure, as seen in the Figure 6.20 inset, and in 82° shift XRD peaks of Figure 6.19. These observations suggest that the thermal history of the L-DED RES AB is more difficult to eliminate when compared to the PRO AB. In the literature, when dealing with refined microstructures, different authors report similar responses, which are attributed to a more intense thermal gradient and faster cooling, similar to those observed under the RES parameters [8], [85], [162].

Figure 6.18 - SEM-EDS of the AISI 410L PHT condition showing no elements partition.



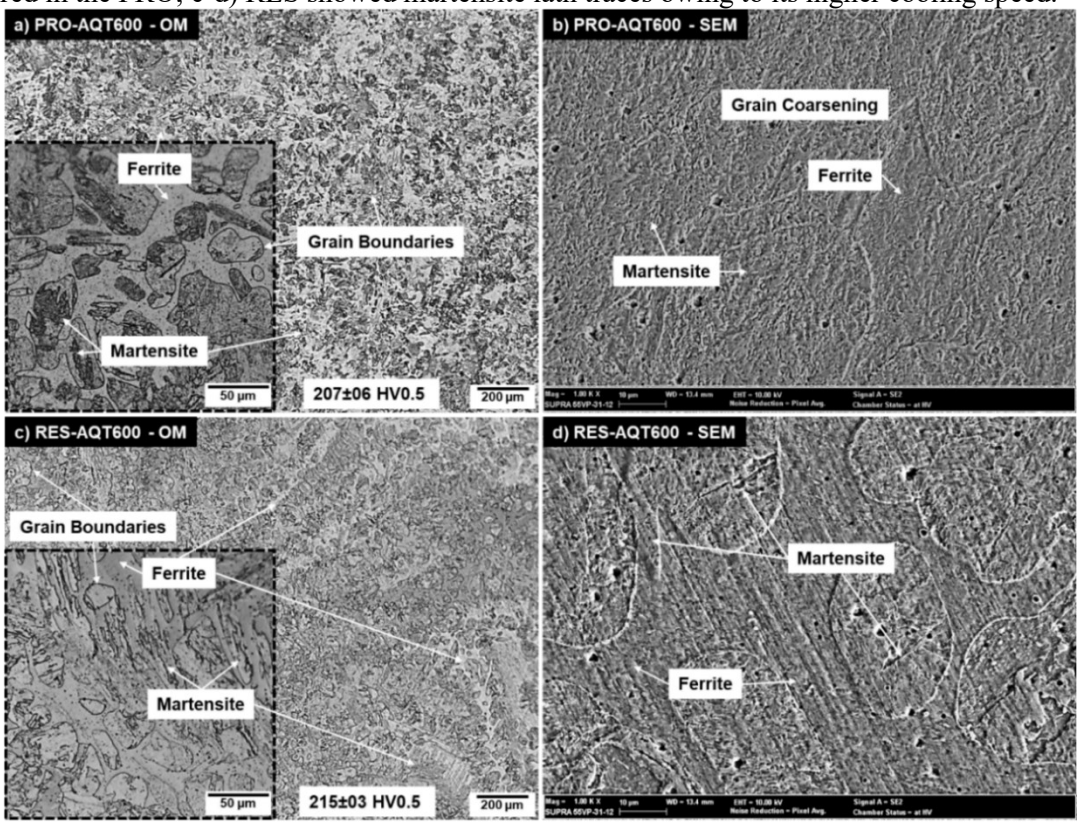
Source: Author (2025).

Figure 6.19 - XRD PHT showed the same AB peaks. Transformation of BCT to BCC martensite was detected.



Source: Author (2025).

Figure 6.20 - Effect of AQT600 on the microstructure: a-b) homogenization and grain coarsening occurred in the PRO; c-d) RES showed martensite lath traces owing to its higher cooling speed.



Source: Author (2025).

6.5 MECHANICAL PROPERTIES

This section presents and discusses the results of tensile and Charpy impact tests on AISI 410L samples in the as-built and post heat-treated states. The effect of build orientation was also evaluated.

6.5.1 Effects of the as-built condition and building orientation on tensile strength and impact toughness

The PHT study was conducted on samples manufactured with PRO parameters. The route with the best response was used to heat-treat the RES samples. Thus, all mechanical tests were conducted only for the PRO in the AB state. Table 6.7 presents the mechanical results of yield strength (YS), ultimate tensile strength (UTS), and elongation (El) from the tensile test and absorbed energy (AE) from the Charpy impact test for the PRO-AB condition in the vertical (Ver) and horizontal (Hor) build orientations. These were benchmarked with the SUB-AR.

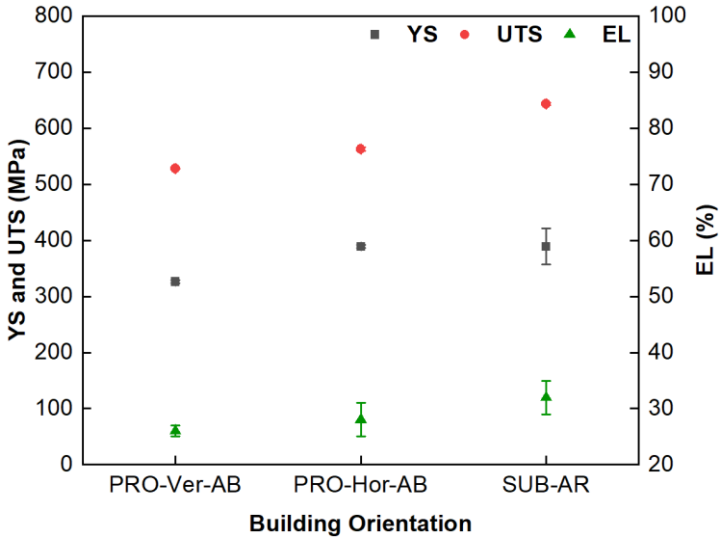
Table 6.7 - Mechanical test results of the different building orientations in the PRO-AB condition.

Mechanical Test Results of the PRO-AB Condition and SUB-AR				
Build Orientation	YS (MPa)	UTS (MPa)	EL (%)	AE (J)
PRO-Ver	326±3	528±1	26±1	6±1
PRO-Hor	389±3	563±3	28±3	7±1
SUB-AR	389±32	643±2	32±3	40±5

Source: Author (2025).

Figure 6.21 graph shows the YS, UTS, and EL for the PRO-AB in the Ver and Hor orientations. The YS and UTS were 6% and 16% higher in the PRO-Hor than in the PRO-Ver, respectively. The EL was comparable in both orientations. When it comes to the PRO-Ver, SUB-AR performed better in terms of YS (~11%). In comparison to PRO-Hor, the performance was similar, with a trend toward enhanced stability in the L-DED process. Regarding PRO-Ver and PRO-Hor, the UTS of SUB-AR was 18% and 13% higher, respectively. The EL of SUB-AR was 19% higher than that of both L-DED building orientations.

Figure 6.21 - YS, UTS, and EL of the PRO-AB in the Ver and Hor building orientations and SUB-AR.



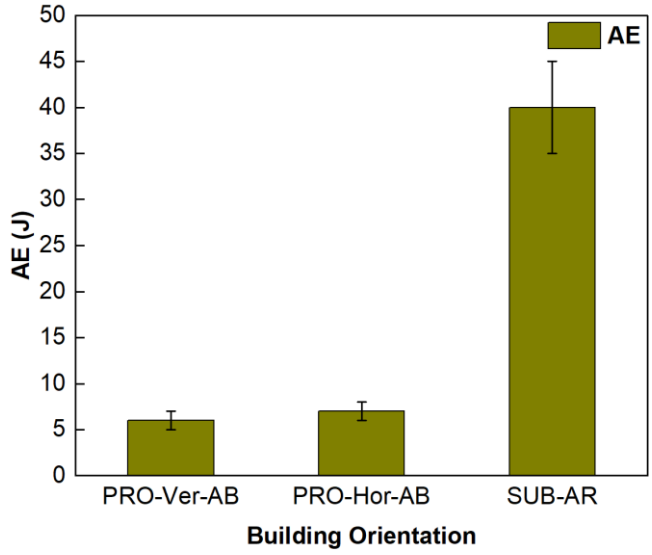
Source: Author (2025).

The YS, UTS, and EL of the two L-DED building orientations are presented in Figure 6.21. Considering that the samples of both orientations were manufactured with the same volume ASTM E8/E8M [181], the differences were the dimensions and number of layers. In the PRO-Ver, the number of layers is 4 times greater, while their area is 4 times lower than that of PRO-Hor. The L-DED travel speed parameter (mm/min) was maintained throughout the process, so the PRO-Ver samples take a shorter time (seconds) to deposit a single layer, but the heat input is more concentrated. As the number of layers increases, heat-sink efficiency is reduced, owing to the longer distance between the top of the part and the substrate, impairing the conduction mechanism, which decreases the cooling speed. In the PRO-Hor, there is a

contrary condition, that is, a smaller number of layers with a larger area and a shorter distance to the substrate. In this sense, the number of thermal cycles is lower, and the cooling is faster, which generates a more refined microstructure in the PRO-Hor, as previously discussed in topic 6.4.2. PRO-Hor resulted in higher hardness, YS, and UTS. No EL reduction was seen when comparing the PRO-Hor with the PRO-Ver [21], [162], [201]. The homogeneous microstructure of the SUB-AR agrees with its slightly higher EL [48], [63].

The Charpy impact test results are exhibited in Figure 6.22 graph. The AE values were comparable in both L-DED building orientations and significantly lower than the SUB-AR, which must be linked to the same justifications as the EL performance. In the Charpy impact test, anisotropy is more severe than in the tensile test. This is because the number of layers is 6 times greater while the area of each layer is 6 times lower in PRO-Ver concerning the PRO-Hor. Thus, the cooling experienced by the horizontal samples is significantly higher than that of the vertical, resulting in a refined microstructure with a greater amount of martensite and, consequently, increased brittleness. Similar interactions are described by [3], [164]. SUB-AR showed an AE superior to both L-DED building orientations, consistent with its homogeneous microstructure, which granted it greater EL, as pointed out by [18], [48].

Figure 6.22 - AE of the PRO-AB in the Ver and Hor building orientations and SUB-AR.

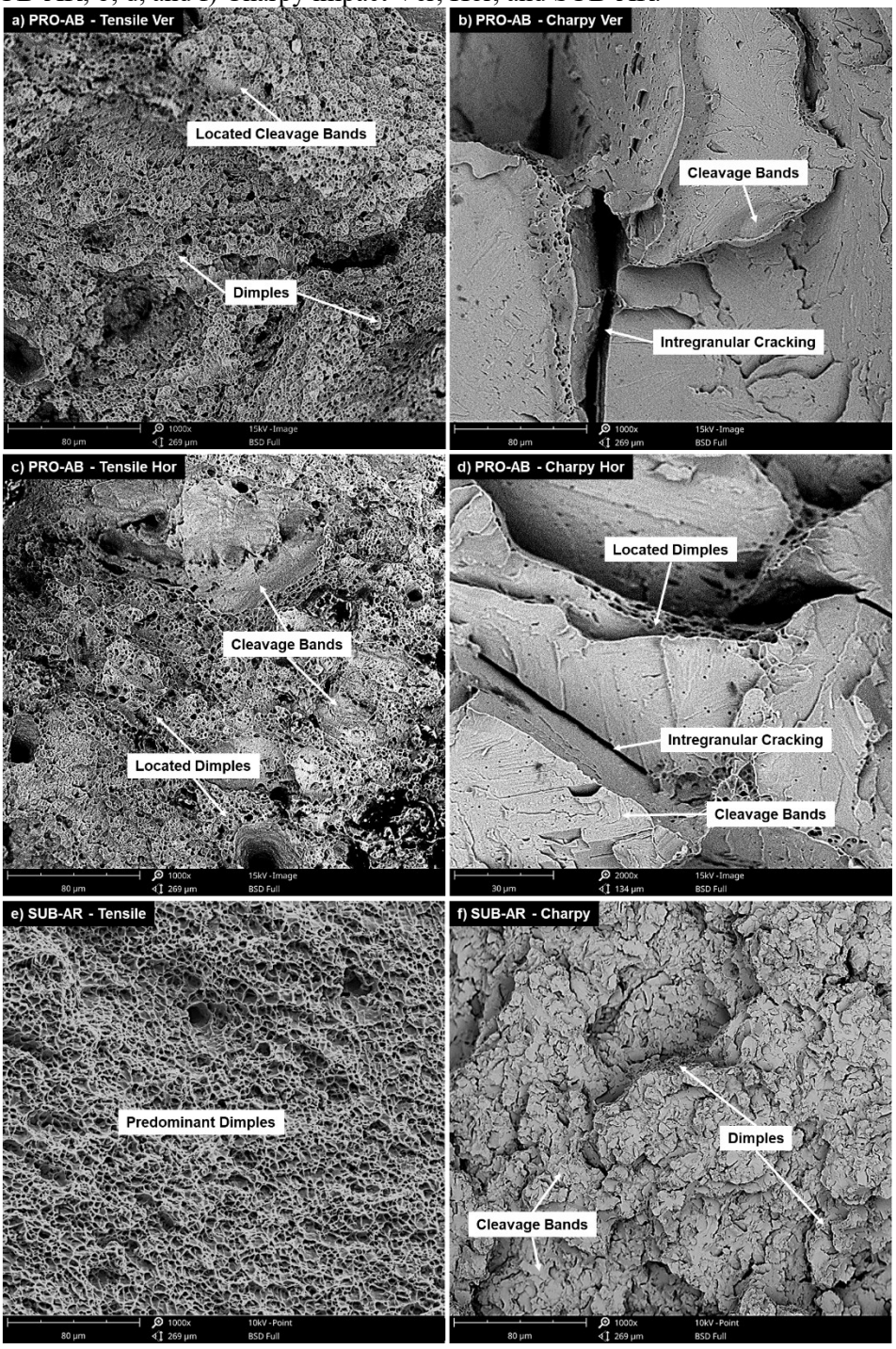


Source: Author (2025).

Tensile fractures showed a quasi-ductile aspect of located dimples with cleavage bands for both L-DED building orientations (Figure 6.26a-c). These mechanisms align with the low ductility at the grain boundaries caused by the hard martensite, in line with the results of [6],

[162]. SUB-AR (Figure 6.23e) showed ductile fracture formed by dimples, as reported by [63], [155]. Figure 6.23b-d Charpy impact fractures showed broad cleavage bands and intergranular cracking in both L-DED building orientations. The shock produced by the fast impact led to quick crack propagation along the grain boundaries. Conversely, the SUB-AR, in turn, exhibited dimples and cleavage bands, as indicated by [3], [21], [164].

Figure 6.23 - SEM fractures of PRO-AB for Ver and Hor building orientations: a, c, and e) tensile Ver, Hor, and SUB-AR; b, d, and f) Charpy impact Ver, Hor, and SUB-AR.



Source: Author (2025).

6.5.2 Effects of the post heat-treatment and building orientation on tensile strength and impact toughness

Table 6.8 and Figure 6.24 show the PHT mechanical test results of the L-DED conditions (PHT routes and building orientations) and SUB-AR. The YS and UTS increased with the austenitization (AQ) and tempering at lower temperatures (AQT300 and AQT450) in a similar level concerning AB condition. As expected, with the tempering carried out at the higher temperature (AQT600), YS and UTS showed a significant reduction compared to the other PHT routes, demonstrating values closer to the AB. Furthermore, the AQ that followed the L-DED process increased hardness. On the other hand, with the tempering temperature increase, the martensite was tempered, which provided a mechanical strength decrease, which is in accordance with the literature [53], [98]. On the other hand, looking for the greater C-content MSS, lower tempering temperatures provided the obtention of higher amounts of martensite and refined Cr-carbides, which enhance YS and UTS regarding the lower C-content MSS. However, with the tempering temperature elevation, these carbides are coarsened, and the mechanical resistance is reduced [47], [202].

Table 6.8 - Mechanical test results of the different PHT conditions and build orientations.

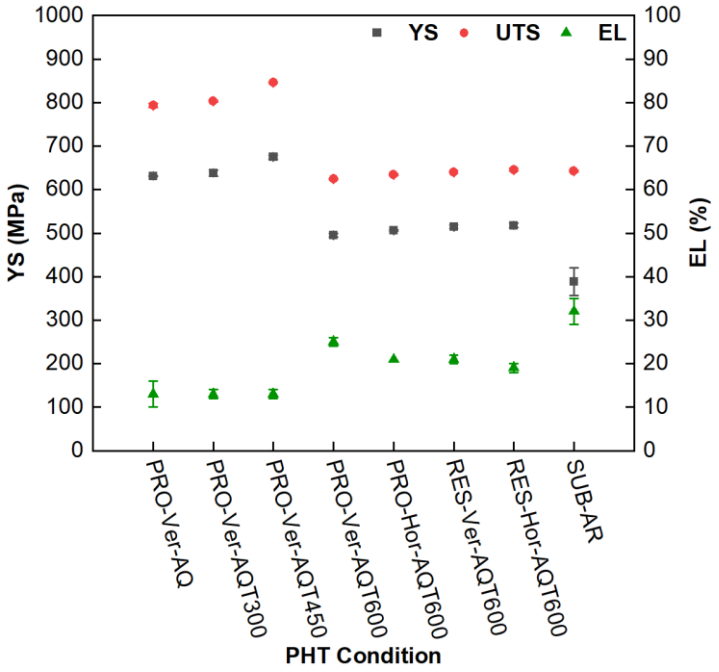
Mechanical Test Results of the PHT Conditions and SUB-AR				
PHT Condition	YS (MPa)	UTS (MPa)	EL (%)	AE (J)
PRO-Ver-AQ	631±1	793±5	15±4	-
PRO-Ver-AQT300	638±7	803±2	13±1	-
PRO-Ver-AQT450	675±5	846±2	15±0	-
PRO-Ver-AQT600	495±4	624±1	21±2	37±10
PRO-Hor-AQT600	506±2	634±2	21±0	14±2
RES-Ver-AQT600	514±4	640±3	23±1	22±9
RES-Hor-AQT600	518±5	641±3	21±1	12±1
SUB-AR	389±32	643±2	32±3	40±5

Source: Author (2025).

When comparing the different L-DED parameters (PRO and RES) and building orientations (Ver and Hor) for the AQT600 in the Figure 6.24 graph, no significant differences were identified in YS and UTS. Regarding the parameters, YS and UTS were, on average, 4±0.4% higher in the RES. This trend may result from the thermal history imposed by the RES parameter, which generated a more refined AB microstructure with a higher amount of BCT martensite, maintaining traces even after the PHT. This justification was corroborated by Figure

6.19 XRD, and some literature highlights [18], [200]. All L-DED PHT conditions outperformed SUB-AR in terms of YS and UTS. UTS exhibited statistically equal values between the AQT600 and SUB-AR. However, YS remained significantly higher. This indicates that AISI 410L processed by L-DED has a greater yield capability regarding SUB-AR. The difference in UTS was reduced in the AQT600, a behavior corroborated by [1], [63].

Figure 6.24 - YS, UTS, EL of the PHT in the Ver and Hor building orientations and SUB-AR.

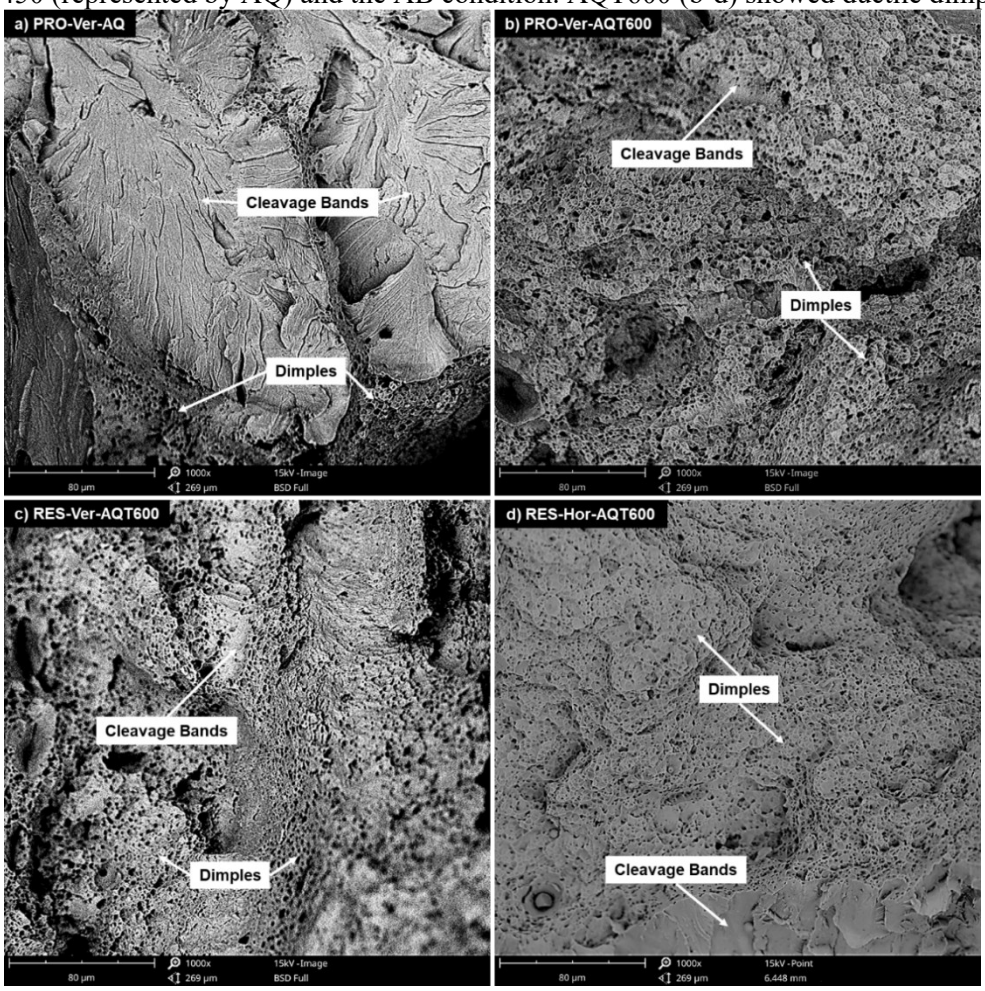


Source: Author (2025).

Figure 6.24 graph also presents an EL performance trend inversely proportional to that observed for hardness, YS, and UTS. The austenitization PHT (AQ) and maintenance at lower tempering temperatures (AQT300 and AQT450) deteriorate this property regarding the AB condition. In the AB microstructure, L-DED samples showed large ferritic bands of high ductility. Only the AQT600 condition with a higher tempering temperature was able to recover this property, given the more intense martensite tempering. Regarding the build orientation, when the PHT AQT600 was performed, the EL values were virtually identical. In literature, for higher C-content MSS, the ductility was compromised with lower tempering temperature performance, both by the formation of a greater amount of refined martensite and by the hard carbides precipitated. Tempering temperature increase helped to recover the EL through the same aspects highlighted for the low C-content MSS, as well as through the carbides coarsening [47], [53], [163]. In the present work, the maximum EL was seen in the SUB-AR. The homogeneous microstructure with ferrite and predominantly tempered martensite supports this performance [40], [56].

Figure 6.25 shows the characteristic PHT tensile fractures. AQ, AQT300, and AQT450 conditions showed similar aspects, with several cleavage bands and a few localized dimples (Figure 6.25a). Conversely, a significantly higher number of dimples were present in the AQT600 (Figure 6.25b), which attests to the tensile results, that is, its lower YS and UTS at the expense of an expressively higher EL regarding the other conditions [53], [162]. No significant differences were observed between L-DED parameters and building orientations (Figure 6.25c-d). SUB-AR exhibited an EL superior to all L-DED conditions, which was reflected in its fractures, predominantly composed of dimples, as previously shown in Figure 6.23e, and also reported by [203].

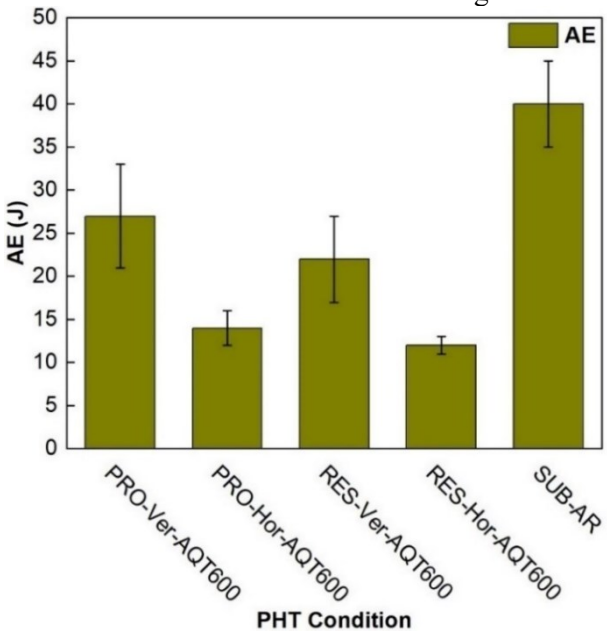
Figure 6.25 - SEM fractures of the PHT tensile conditions: a) no differences were observed between the AQ-AQT450 (represented by AQ) and the AB condition. AQT600 (b-d) showed ductile dimples.



Source: Author (2025).

Figure 6.26 graph shows the Charpy AE of PHT conditions in the different building orientations and SUB-AR. As previously described, in the AQ and tempering at the lower temperatures (AQT300 and AQT450), the maintenance of the refined martensite throughout the ferritic matrix resulted in a lower AE. Martensite tempering provided by the AQT600 improved the AE. In the literature, few studies were found exploring this property in this SS class. Oh *et al.* investigated a 630 MSS, with 0.05 wt.%C, and found a greater AE (138 J) in the AB condition. Nevertheless, a significant AE drop to 27 J was noted after austenitization plus tempering, which is close to the 22 J of the PHT AQT600 condition of the current work. The authors attributed this performance to the transition from an AB microstructure rich in ferrite and retained austenite bands of high ductility to a fully hard and brittle martensitic structure after PHT [163]. Observing other similar materials manufactured by L-PBF, poor performances (5-11 J) attributed to the fully martensitic microstructure and residual stress were also highlighted [164], [166].

Figure 6.26 - AE of the PHT in the vertical and horizontal building orientations and SUB-AR.



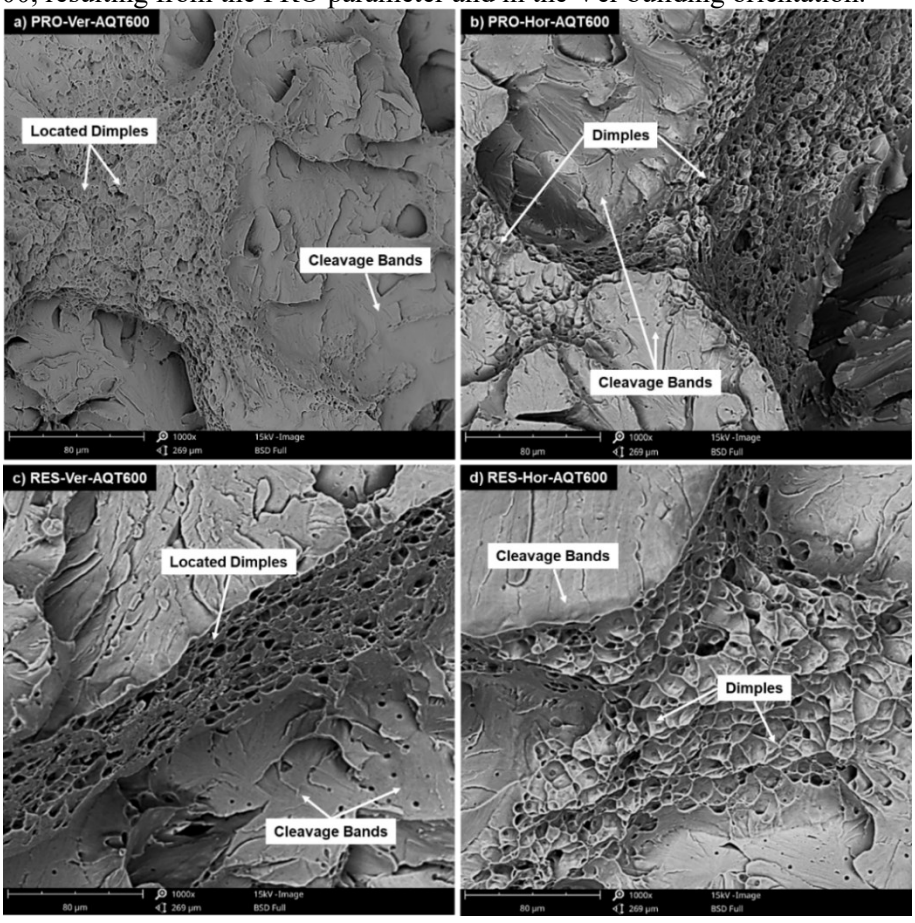
Source: Author (2025).

Observing Figure 6.26, PRO parameter and the Ver orientation showed a higher AE compared to the RES and Hor. The faster cooling of RES, along with the more efficient conduction heat-sink provided by the larger contact area between the layers of samples built in Hor, provided a refined microstructure with a higher amount of martensite laths at grain boundaries. During PHT, these samples presented remaining traces of BCT martensite and a more heterogeneous appearance concerning the PRO-Ver, which increased mechanical strength

but compromised toughness, as highlighted by [21], [164]. The SUB-AR exhibited a higher AE (40 J) than all L-DED conditions. Its annealed microstructure, with coarser homogeneously distributed grains and tempered martensite, corroborated this performance, as described by other authors, who investigated MSS conventionally processed [48], [203].

In the preliminary PHT study, only the AQT600 showed a significant performance improvement concerning the AB condition. AQT600 behavior (Figure 6.27a-d) can be attributed to the homogenization of grain boundaries with refined martensite regarding AB, and the effective residual stress relief concerning the other PHT. The samples built with the PRO parameters and in the Ver orientation exhibited a greater amount of dimples, indicating higher ductility, accordingly with [3], [164]. SUB-AR showed a greater amount of dimples (Figure 6.23f) concerning all L-DED conditions, which is in agreement with its higher ductility, and the literature outcomes [48], [63].

Figure 6.27 - SEM fractures of the PHT Charpy conditions: a higher number of dimples were perceived in the AQT600, resulting from the PRO parameter and in the Ver building orientation.



Source: Author (2025).

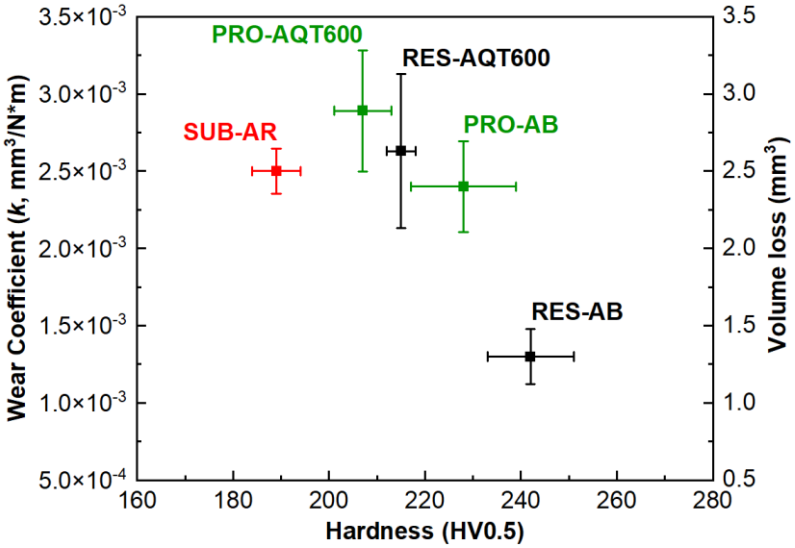
6.6 TRIBOLOGICAL PERFORMANCE

The first section presents and discusses the effects of L-DED parameters (PRO and RES) and post-heat treatment (PHT) on the wear coefficient (k) and friction coefficient (COF). Only the AQT600 PHT was analyzed, as previously discussed in section 6.5. The second section investigates the active wear mechanisms through the wear track analysis.

6.6.1 Effects of L-DED parameters and PHT on tribological performance

Figure 6.28 graph shows the relation between the wear coefficient (k) and volume loss obtained in the dry-sliding linearly reciprocating ball-on-flat tribological test and the hardness of the different conditions. As predicted, except for SUB-AR, an inverse proportion between hardness and wear coefficient was seen. This behavior indicates that the surface hardness of the L-DED processed materials was sufficient to withstand the penetration and sliding of the ball (counterbody) during the test [22]. Conditions with higher hardness, lower wear coefficient, and volume loss were RES-AB, PRO-AB, SUB-AR, RES-AQT600, and PRO-AQT600.

Figure 6.28 - Wear coefficient (k) of different L-DED conditions, and SUB-AR: an inverse link between wear coefficient and hardness was observed.



Source: Author (2025).

The performance variation among conditions can be attributed to distinct microstructural features that influence hardness. As previously discussed, the refined RES-AB microstructure promoted a larger surface area with harder martensite laths. In contrast, the PRO-AB condition exhibited higher ductility due to its coarser microstructure. For the L-DED PHT conditions, the trends were similar. Nevertheless, the superior performance of RES-AQT600 can be ascribed to its initial martensite, which presents a higher amount of BCT

martensite compared to PRO-AQT600, thereby conferring greater hardness to the former. This relationship between higher martensite content, increased hardness, and improved wear resistance is supported in the literature [17], [162]. Even though it was less hard, SUB-AR showed a lower *k* regarding the L-DED PHT conditions. SUB-AR biphasic microstructure formed by ferrite and coarse bands of tempered martensite generated a homogeneous contact interface, while the presence of $Cr_{23}C_6$ at the Fe-matrix and grain boundaries provided anchoring to the tribolayers. The role of carbides for the formation of protective tribolayers is evidenced by [198], [204], [205]. Further discussions will be brought into section 6.6.2.

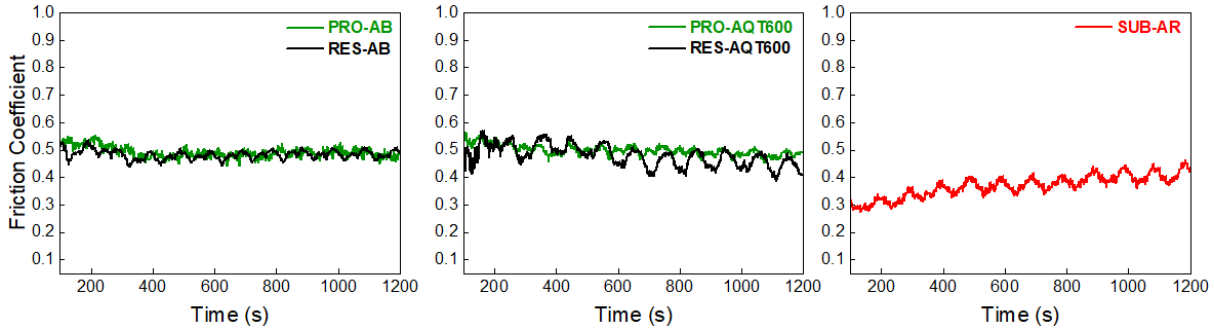
The COF measured during the test is displayed in Figure 6.29 graph. The running-in could be found after 200 s of testing under all evaluated conditions. From this point onwards, the steady state was reached. Considering the values within this regime in Table 6.9, a similar COF average was found when comparing L-DED AB conditions. L-DED PHT conditions also exhibited values that were analogous to each other. Detailed graphs with conditions arranged separately (Figure 6.29) showed a slightly higher COF in the L-DED AB (Figure 6.29a) regarding the PHT (Figure 6.29b). When comparing PRO versus RES, the latter also shows a trend towards a higher COF throughout the test. Conversely, SUB-AR (Figure 6.29c) showed a lower COF than all L-DED conditions [22], [206].

Table 6.9 - COF average of the different AISI 410L L-DED conditions, and 410-REF. The values were taken within the steady regime.

COF Average of the Different L-DED Conditions and SUB-AR					
Condition	PRO-AB	RES-AB	PRO-AQT600	RES-AQT600	SUB-AR
Average	0.48	0.48	0.45	0.46	0.47
Standard Deviation	0.03	0.02	0.05	0.03	0.03

Source: Author (2025).

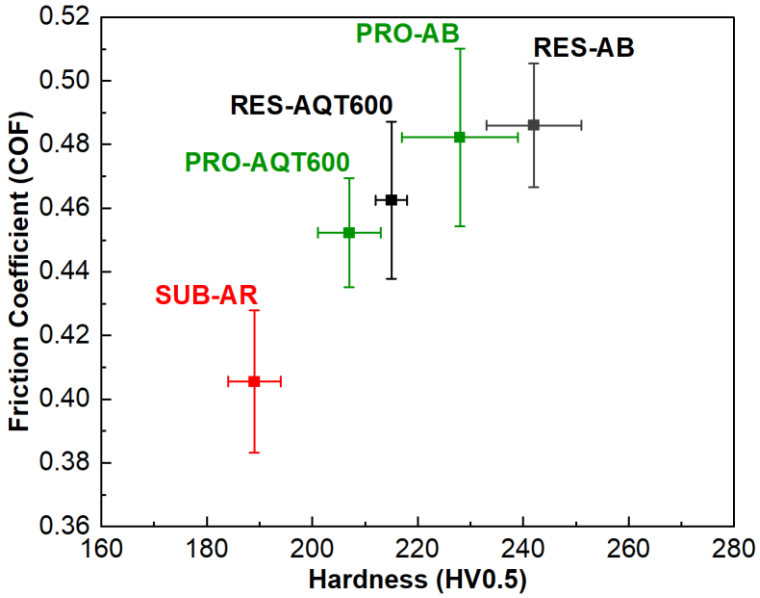
Figure 6.29 - COF of the L-DED conditions, and SUB-AR: the averages of the parameters (a) and state (b) did not differ significantly. SUB-AR (c) showed a lower average than all L-DED conditions.



Source: Author (2025).

Figure 6.30 shows a correlation between COF and hardness. L-DED AB conditions exhibited higher hardness compared to the L-DED PHT and SUB-AR. This suggests that increased surface hardness acts as a barrier against counterbody penetration. Furthermore, as discussed in section 6.4.1, L-DED AB microstructure exhibited a biphasic ferritic matrix with refined martensite laths at the grain boundaries. Therefore, there is a significant hardness difference between these two regions. As a result, deeper penetration occurred over the ductile ferrite during the test, whereas shallower penetration was produced when the ball slid over the hard martensitic grain boundaries. On the other hand, L-DED PHT exhibited a homogenized microstructure, with tempered martensite, and lower hardness. During the tribological test, the penetration and sliding of the ball on the body surface are facilitated. SUB-AR, in turn, showed the lowest hardness and most homogeneous microstructure among the conditions analyzed, which justifies its lowest COF. A similar interaction has been described by [2], [168], [207]. Further discussions will be covered in section 6.6.2.

Figure 6.30 - Relation between COF and hardness. The conditions of higher hardness exhibited a proportionally higher average COF than those of lower hardness.



Source: Author (2025).

To summarize, the COF and *k* were influenced by hardness. In comparison to the L-DED PHT conditions, which displayed a coarser microstructure that offered higher ductility, the more refined microstructure of the L-DED AB conditions produced higher hardness and, as a result, a lower *k*. As tribology science stated, greater hardness does not always translate into improved wear resistance [207]. In this case, SUB-AR showed a lower *k* concerning L-DED PHT conditions. The lower hardness of SUB-AR provided greater debris formation, which became

anchored on the carbides, thereby facilitating the development of a larger amount of tribolayers compared to L-DED PHT. This outcome may be attributed to the aforementioned factors. When compared to SUB-AR, the L-DED RES-AB performed significantly better, and the other L-DED conditions (PRO-AB and both L-DED PHT) were similar. These results suggest that L-DED processing can exert a greater impact on tribological behavior regarding the material's chemical composition. From the perspective of tribological performance, considering the evaluated tribosystem, it is not interesting to heat-treat the material.

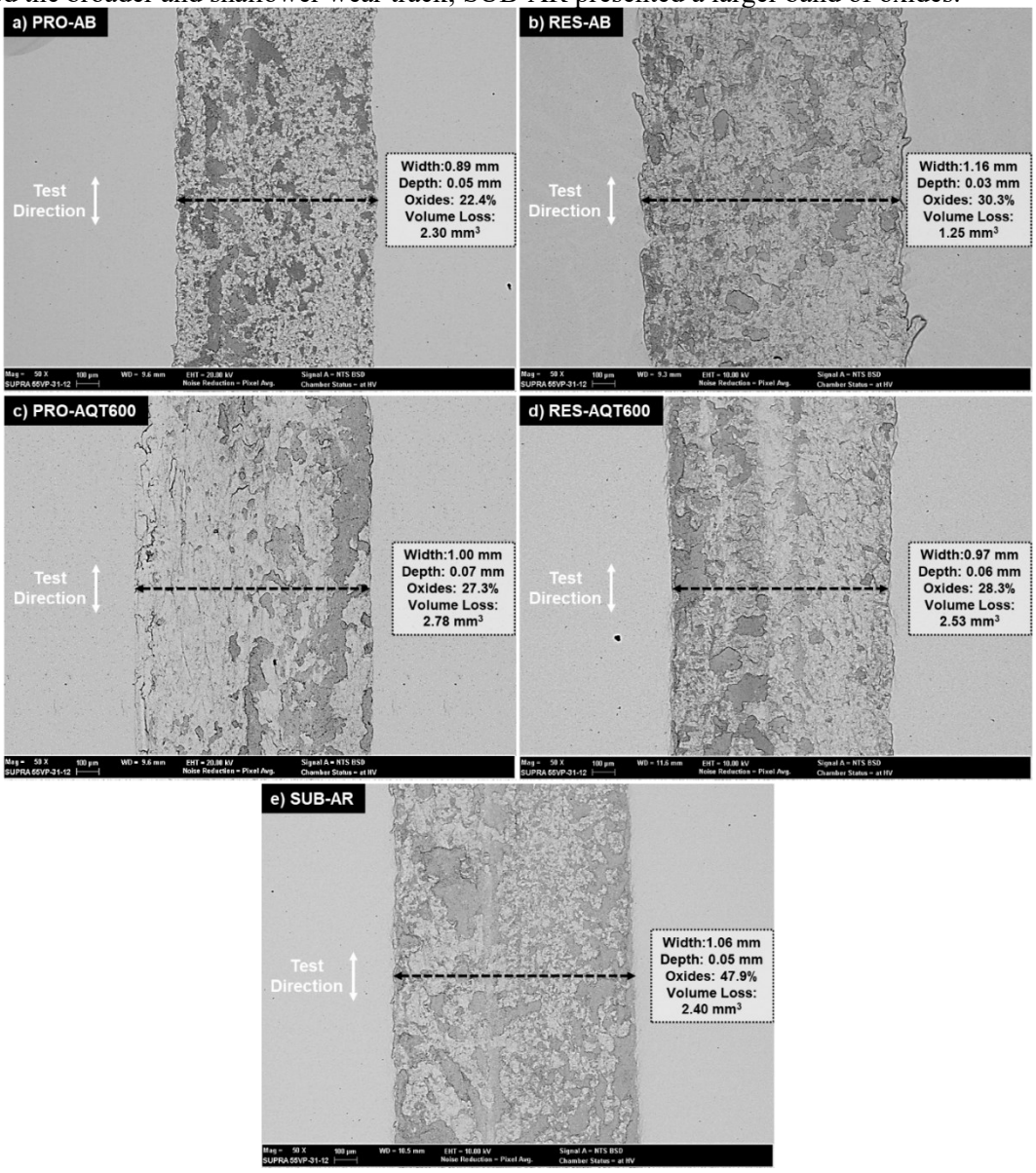
6.6.2 Wear track analysis

Figure 6.31 shows the macroscopic features of the wear tracks. No defects, such as microcracks or voids, were observed on the surface, although they may be present in the subsurface and become apparent during testing [92], [162]. Figure 6.31 also shows the wear tracks' width, depth, and oxide amount. Understanding the dimensions and presence of oxides on the wear tracks is important for assessing the extent of wear and the active wear mechanisms. The widest wear tracks were identified in RES-AB, followed by SUB-AR, PRO-AQT600, and RES-AQT600. PRO-AB was the narrowest. RES-AB showed the shallower wear track, followed by PRO-AB, SUB-AR, RES-AQT600, and PRO-AQT600. Regarding the width and depth, the higher hardness of RES-AB imposed greater resistance against ball penetration, so the body surface was more deformed, evidenced by the material flow towards the wear track edges. Its greater amount of oxides compared to other conditions also suggests that a significant part of the debris remained entrapped in the wear track. The wider area occupied by harder martensite grain boundaries supported the oxides during sliding by acting as a network (to be discussed later). PRO-AB wear track was deeper, narrower, and contained a lower amount of oxides, which points to greater penetration and effective material removal by the ball action.

Figure 6.31 aspects were supported by the PRO-AB lower hardness. In the L-DED PHT conditions, PRO-AQT600 exhibited a slightly wider, deeper wear track with a lower amount of oxides compared to RES-AQT600. As previously discussed, RES-AQT600 retained some refined BCT martensite traces, which may justify the higher hardness and lower k of this condition regarding PRO-AQT600. SUB-AR exhibited wider wear tracks than all L-DED conditions except RES-AB, which can be attributed to its lower hardness regarding all L-DED

conditions. In this context, its *k* exceeded L-DED AB conditions and was lower than PHT ones. SUB-AR's COF was the lowest among all conditions studied. Despite its lower hardness, the extensive formation of oxides on its surface contributed to obtaining these results [6], [18].

Figure 6.31 - Wear tracks macro view of the different L-DED conditions, and SUB-AR: RES-AB showed the broader and shallower wear track; SUB-AR presented a larger band of oxides.

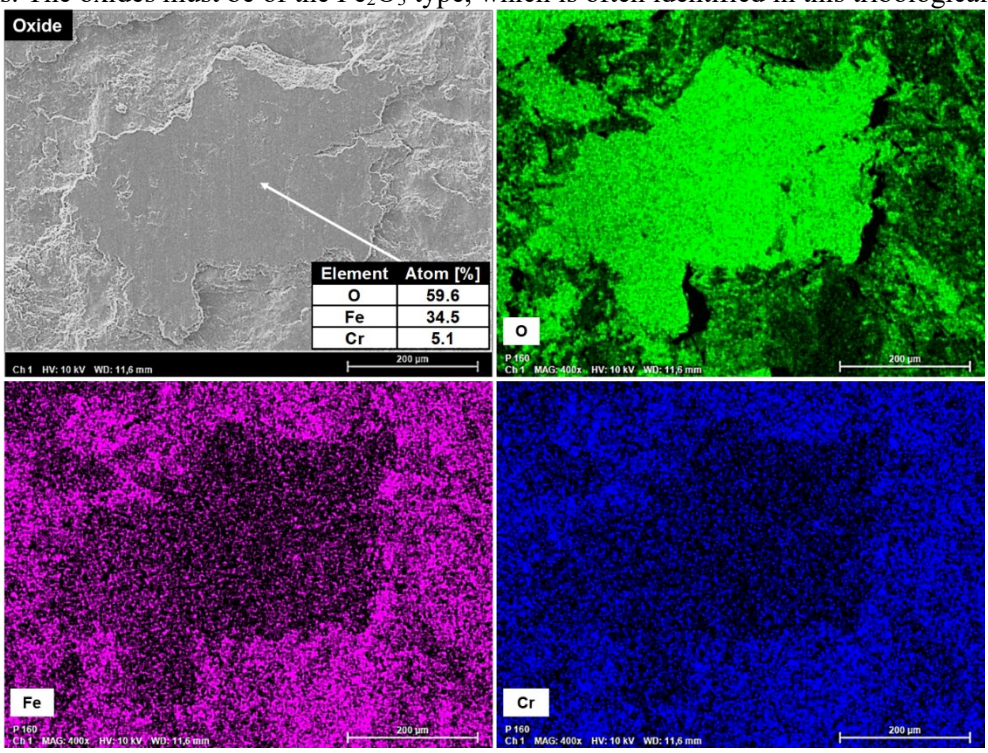


Source: Author (2025).

A common aspect of all wear tracks was the tribolayers. These are formed by sliding between two surfaces, resulting from the accumulation and compaction of debris, which are sintered over surface anchoring areas, undergoing oxidation [115], [116]. In this work, the tribolayers displayed distinct morphology and amount for each condition. However, a common point was the chemical composition, as shown in Figure 6.32 SEM-EDS. In terms of atomic

percentage, the O-content was 60% and the Fe-content was 40%. Based on the data, it must be Fe_2O_3 oxide, commonly reported in the literature for this tribological pair. Cr-content can be justified by its presence in the body and counterbody nominal chemical composition [208].

Figure 6.32 - SEM-EDS chemical composition of the oxide tribolayers formed on the wear tracks of all conditions. The oxides must be of the Fe_2O_3 type, which is often identified in this tribological pair.



Source: Author (2025).

Figure 6.33 shows the wear mechanisms in SEM images at higher magnifications. Firstly, attention is drawn to the tribolayers. These were formed in larger amounts in SUB-AR, followed by RES-AB, PRO-AQT600, RES-AQT600, and PRO-AB, respectively. In both L-DED AB conditions (Figure 6.33a-d), tribolayers were compact with a smooth texture. L-DED PHT (Figure 6.33e-h) and SUB-AR (Figure 6.33i), in turn, exhibited less compact tribolayers, with a rough texture. Under L-DED AB, the higher hardness supported the formation and compaction of tribolayers. The greater amount of compact tribolayers in the RES-AB (Figure 6.33c-d) condition, compared to PRO-AB (Figure 6.33a-b), corroborates this behavior. The more refined RES-AB microstructure provided a higher hardness and a larger area occupied by grain boundaries with BCT martensite of high hardness, which hindered ball penetration and

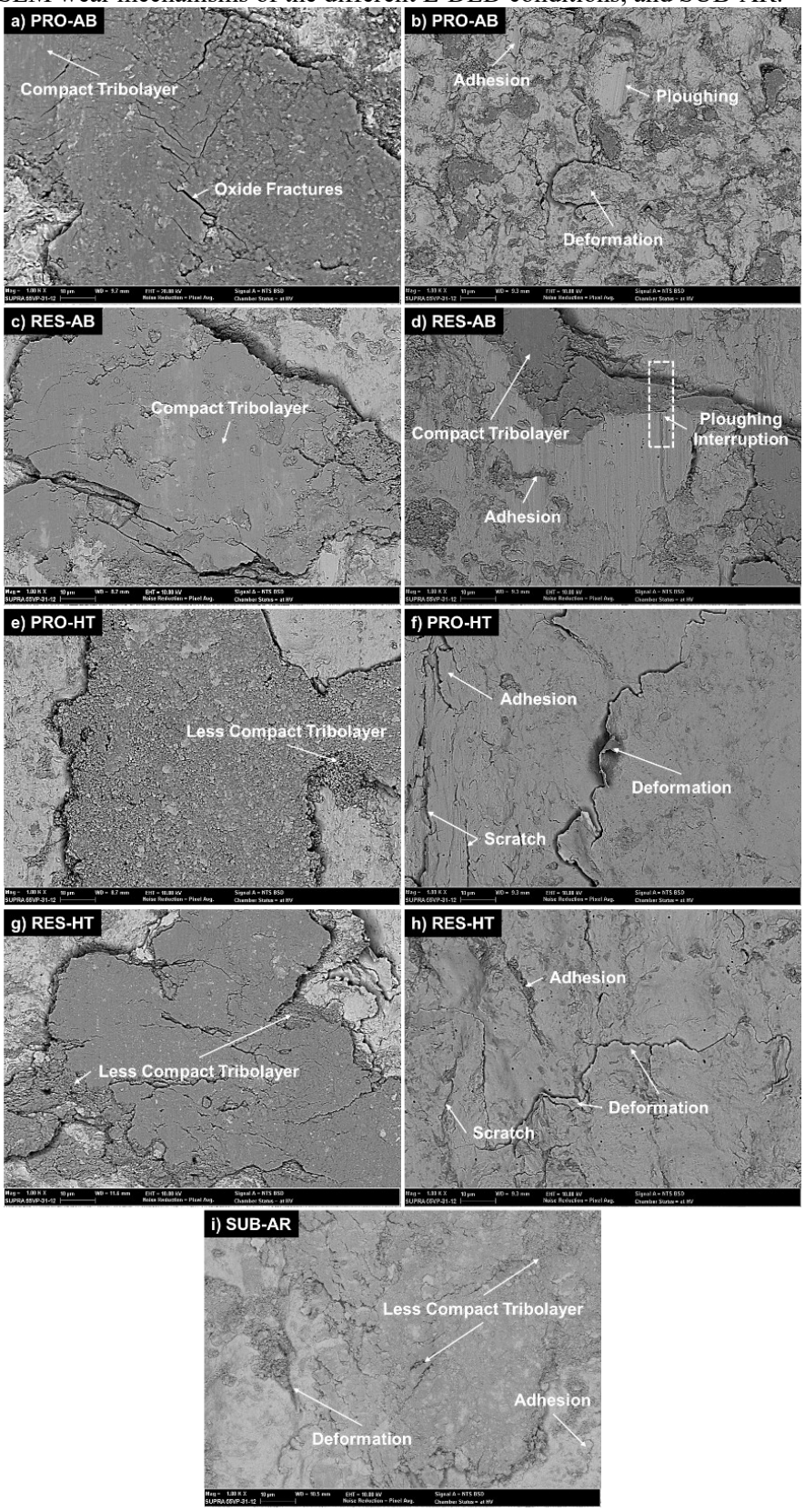
acted as a support network for the oxides during the test. This combination promoted the formation of tribolayers and provided enhanced protection to the tribological pair.

Some fractures observed in the tribolayers of the L-DED AB conditions resulted from their partial or complete breakdown, after which the debris was redeposited in other anchoring areas. In the case of L-DED PHT, the lower hardness hindered the anchoring and compaction of oxides, while the homogenized microstructure produced coarser grains, thereby reducing the support network provided by the grain boundaries. These factors indicate that the generated oxides remained free on wear tracks, and insufficient debris comminution and compression prevented the formation of compact tribolayers. Consequently, throughout the test, contact with the counterbody facilitated the removal of debris from the wear track.

SUB-AR (Figure 6.33i) experienced a phenomenon similar to what occurred in L-DED PHT conditions. The tribolayers formed in the SUB-AR were rough and less compact compared to L-DED AB, which corroborates the lower *k* of the latter. Considering the similar aspects of tribolayers formed in these last two conditions, namely, less compact, it is reasonable to assume that the SUB-AR provided greater support to the oxides formed regarding the L-DED PHT conditions. The SUB-AR's $Cr_{23}C_6$ carbides would have likely aided in the oxides' anchoring. As previously discussed in section 6.6.1, L-DED PHT and SUB-AR exhibited a COF lower than L-DED AB. This suggests that the tribolayers formed under L-DED AB conditions did not generate a lubricating effect to provide a COF decrease. However, they were able to maintain their stability throughout the test. In the literature, tribolayers generated on softer hardness surfaces are reported to be easier to remove than those formed on harder ones, which contributed to increasing the COF and wear coefficient. Wear protection is more effectively provided by compact tribolayers [116], [208].

Regarding the wear mechanisms, in Figure 6.33, adhesion was found in all conditions. Oxides likely covered the exposed Fe-matrix before they were removed in the form of adhesive interfaces. Under the L-DED PHT and SUB-AR conditions, adhesion was more severe concerning the L-DED AB. Contact generated plastic deformation causes the material to flow in front of the ball in the form of wedges. These deformed layers were displaced until they collapsed and were removed from the surface or deposited again on the surface. In this way, new tribolayers can be established. However, the features presented by the L-DED PHT and SUB-AR suggest that adhesion collapses surpassed the amount of tribolayers. This indicates that the wear resulting from the adhesion mechanism was more pronounced than the protective effect provided by the tribolayers formed under these conditions [115].

Figure 6.33 - SEM wear mechanisms of the different L-DED conditions, and SUB-AR.



Source: Author (2025).

In Figure 6.33, scratches were seen in PRO-AQT600. These are created in two or three-bodies by abrasion. In the first, the ball directly scratched the body surface. Free-rolling particles provide a ball/debris/body interface in the three-body interaction, generating the cutting and removal of material. The observed uneven scratches point to the second type. L-DED PHT and SUB-AR conditions' lower hardness facilitates the ball penetration. Besides, the reduced amount of grain boundaries hindered debris anchoring, exposing the ductile Fe-matrix, and making it more prone to material abrasion, deformation, and removal [18], [161].

Figure 6.33 shows plowings on the L-DED AB. These must have been formed through two or three-bodies. During plowing, a portion of the material is deformed and moves in the ball front, generating accumulation and material overflows to the edges, without necessarily removing it from the surface. The plowings observed in both L-DED AB conditions exhibited a straight direction, which is a two-body characteristic. In RES-AB, the plowing had its action interrupted at a tribolayer interface region. Conversely, under L-DED PHT conditions, deformation bands and uneven scratches were seen. These conditions showed a lower hardness tempered martensite and a ductile Fe-matrix more exposed to the counterbody action. SUB-AR also exhibited intense adhesion, with deformation bands. Comparing this to L-DED PHT conditions, however, reveals a broader band of less compact tribolayers, indicating that less material was effectively removed. The better support of the tribolayers in SUB-AR may be related to the $Cr_{23}C_6$ carbides. The literature describes that, besides the refined microstructures having greater hardness, they also form a network, increasing surface irregularity, and reducing the contact interface, decreasing deformation and material removal [168], [176].

The observed wear track features supported the wear performance of the different conditions analyzed. Because the L-DED AB conditions were harder, compact tribolayers were formed and anchored, making it difficult for the ball to penetrate and produce shallower wear tracks and less strong adhesion and abrasion mechanisms. The more refined microstructure of these also seems to have anchored the tribolayers. L-DED PHT loses hardness and the network of grain boundaries. Tribolayers became rough, and poor adhered to the surface, providing adhesion and abrasion. Regarding L-DED PHT, SUB-AR showed a lower k. This is related to the less effective removal of debris, as shown by the larger area of less compact tribolayers supported by the $Cr_{23}C_6$ carbides. The combined action of different wear mechanisms under the studied conditions indicates that it is not sufficient to focus solely on achieving a harder surface. Efforts should be directed toward obtaining defect-free microstructures. Moreover, the microstructure refinement and the characteristics of the tribolayers proved to be critical factors.

6.7 CORROSION RESISTANCE

This section was divided into two topics. The first presents and discusses the effects of L-DED parameters (PRO and RES), while the second is focused on the effects of PHT on the responses of E_{corr}, I_{corr}, and R_p. Corrosion mechanisms were evaluated by OM and SEM.

6.7.1 Effects of L-DED parameters on corrosion resistance

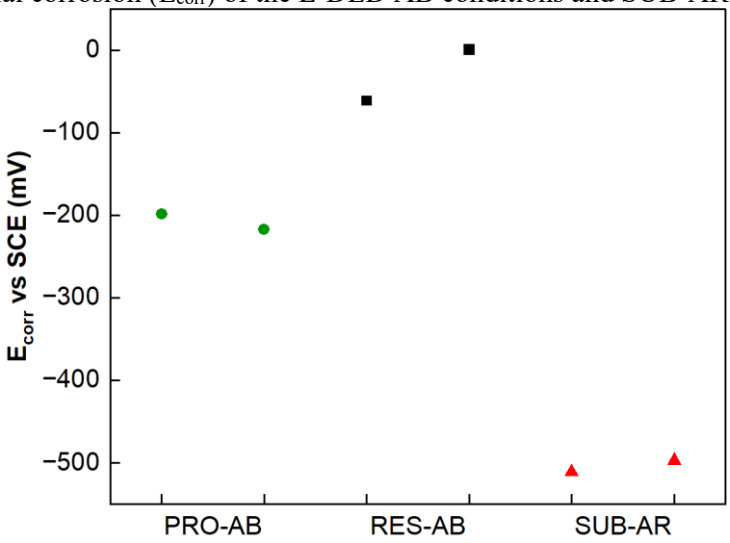
Table 6.10 presents the average data of corrosion potential (E_{corr}), corrosion current (I_{corr}), and polarization resistance (R_p) obtained for the different L-DED conditions and SUB-AR. Figure 6.34 graph shows the E_{corr} of the different L-DED parameters and SUB-AR. As can be seen, the RES-AB exhibited a significantly more positive E_{corr} than the PRO-AB. SUB-AR, on the other hand, showed the most negative value among these three conditions.

Table 6.10 - Tafel parameters of the L-DED conditions and SUB-AR tested in NaCl 3.5% solution.

Tafel Parameters of the Different L-DED Conditions and SUB-AR					
Condition	PRO-AB	RES-AB	PRO-AQT600	RES-AQT600	SUB-AR
E_{corr} (mV)	-258±13	-30±8	-412±12	-383±3	-504±9
I_{corr} ($\mu A/cm^2$)	0.142±0.03	0.004±0.001	0.476±0.03	0.294±0.07	1.185±0.23
R_p (Ωxcm^2)	9.54E+04	2.72±06	2.78±04	3.27±04	1.14±04

Source: Author (2025).

Figure 6.34 - Potential corrosion (E_{corr}) of the L-DED AB conditions and SUB-AR.

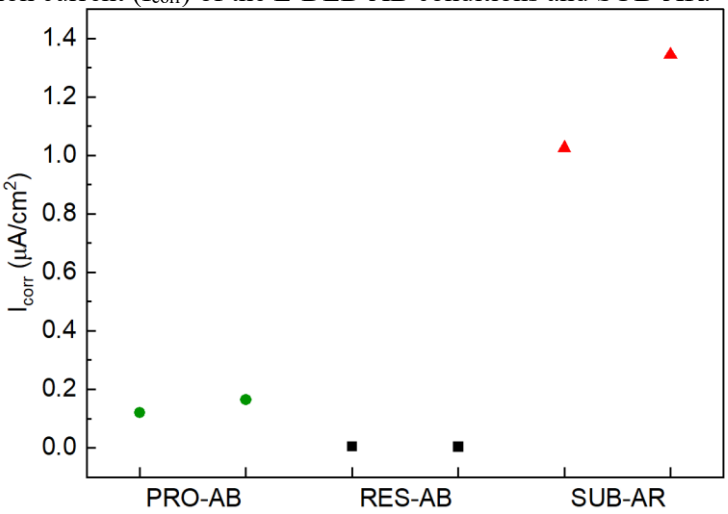


Source: Author (2025).

In the same direction, Figure 6.35 graph illustrates the corrosion current (I_{corr}) behavior. RES-AB exhibited a lower average I_{corr} than PRO-AB. SUB-AR, on the other hand,

showed values much higher than both L-DED parameters. Combining a more positive E_{corr} and a lower I_{corr} for RES-AB supports its greater corrosion resistance when exposed to a medium with chlorides (Cl^-), such as the 3.5% NaCl solution used in this work. Higher E_{corr} indicates that the material resulting from this parametrization is more noble, while the lower I_{corr} suggests it will degrade more slowly. Polarization resistance (R_p) behavior was inversely proportional to I_{corr}. This corrosion parameter showed a significantly higher value in the RES-AB regarding the PRO-AB condition. SUB-AR, on the other hand, exhibited values lower than both L-DED parameters. The combination of more positive R_p and E_{corr} suggests a lower pitting potential, such that the presence of localized corrosion mechanisms tends to be reduced [90], [91], [153].

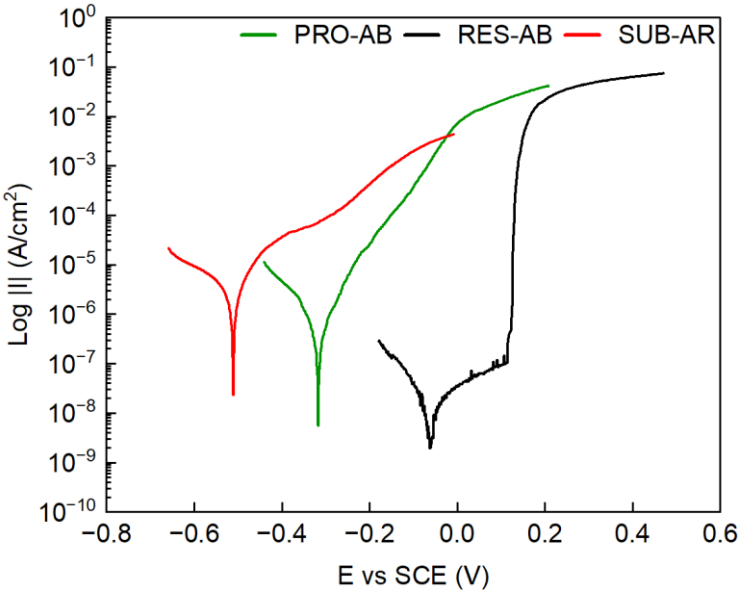
Figure 6.35 - Corrosion current (I_{corr}) of the L-DED AB conditions and SUB-AR.



Source: Author (2025).

Figure 6.36 presents the linear sweep voltammetry curve, highlighting E_{corr} and I_{corr}. Besides observing the anodic passivation and metal dissolution regions, the breakdown potential (E_{break}) was reached. The latter, the inflection point between the cathodic and anodic curves, indicates the stability of the passive layer formed on the sample surface. In this work, the RES-AB condition exhibited a significantly higher E_{break} (0.17 V) compared to PRO-AB (-0.30 V) and SUB-AR (-0.50 V). Besides, RES-AB was the only condition that showed an anodic passivity plateau before passivity breakdown, which is a first indication of its more effective passivation. These observations suggest that the passive layer formed on RES-AB is more continuous, compact, and thicker than those formed under the other studied conditions. With a higher E_{break} and R_p combined with a more positive E_{corr} and a lower I_{corr} value, it can be inferred that the RES-AB condition shows a clear trend for greater corrosion resistance [133], [143], [153], [209].

Figure 6.36 - Linear sweep voltammetry curve of the L-DED AB conditions and SUB-AR.



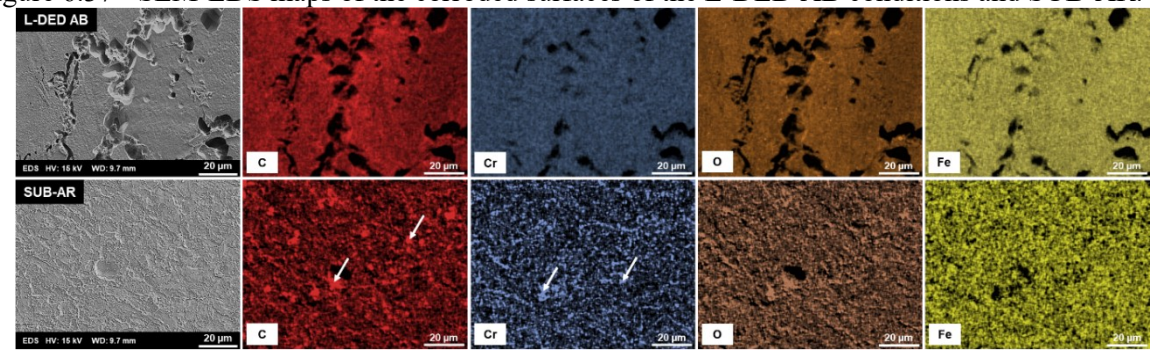
Source: Author (2025).

Several influential sources can be identified to justify the performance difference between the conditions studied. The main discussion points are the starting oxidation level of L-DED samples, microstructure refinement, precipitates, and passive layer characteristics.

Regarding the starting oxidation of the samples, the powder was handled with minimal exposure to the ambient atmosphere, and the multilayer manufacturing steps were performed in a controlled Ar-atmosphere, with an O_2 level below 10 ppm. Before performing the ASTM G3 test [151], all samples underwent the same passivation conditions. Figure 6.37 presents the SEM-EDS conducted on the surface of a representative corroded sample from the PRO-AB, RES-AB, and SUB-AR. In the maps of both L-DED conditions, all elements showed a homogeneous distribution. Cr and O can be attributed to the AISI 410L's chemical composition and the Cr_2O_3 passive layer. Fe_2O_3 oxidation is likely to have formed during the test [91], [176], [210]. In the SUB-AR, C, and Cr were detected in the Cr-carbides [63], [211], [212].

Concerning microstructure refinement, in the context of corrosion, the martensitic phase is less resistant than the ferritic, suggesting a lower corrosion resistance for RES-AB. However, the results described in this section point in the opposite direction. Corrosion responses depend on the combined action of several factors. The larger surface area occupied by grain boundaries provides higher surface energy. Therefore, the more RES-AB refined microstructure offers greater resistance against corrosive agents. These justifications are highlighted in the literature as key factors for ensuring corrosion resistance [91], [138], [173].

Figure 6.37 - SEM-EDS maps of the corroded surfaces of the L-DED AB conditions and SUB-AR.



Source: Author (2025).

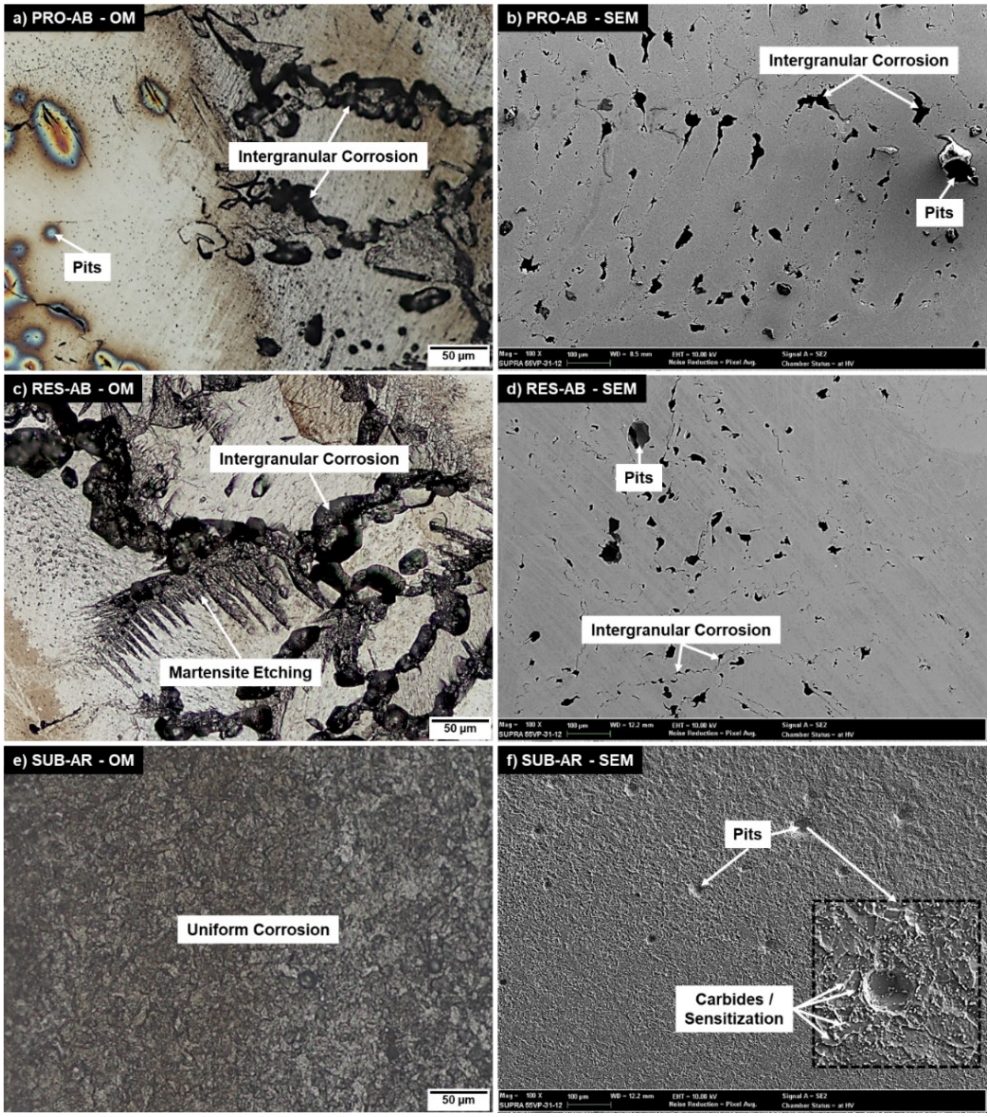
Martensite at the grain boundaries can indicate a higher amount of C in solid-solution. Therefore, the Fe-matrix is depleted in this poor corrosion-resistant element. This was supported by the BCT martensite (Figure 6.13 XRD) of RES-AB. A higher C-content in martensite also points to a lower availability of this element to form precipitates, such as Cr-carbides. PRO-AB allowed greater availability of C and time, due to slower cooling, to form Cr-carbides. These carbides can activate the galvanic corrosion with ferrite and promote sensitization by capturing Cr from Fe-matrix. Regions around these Cr-carbides are depleted in Cr, which is mainly responsible for the formation and maintenance of the passive layer [141], [210], [213]. In the present work, as previously reported in the microstructure (section 6.4), no sufficient evidence was found to confirm the presence of Cr-carbides in AISI 410L processed by L-DED. However, literature indications of their presence can be found elsewhere [53], [200].

Regarding the Cr_2O_3 passive layer, in refined microstructures, this tends to be more continuous, compact, and thicker. Refined grains support the passive layer. The higher volume fraction of grain boundaries also makes it more difficult for pitting corrosion mechanisms. Pits formed on refined grains are also shallower. On the other hand, coarser grains tend to form discontinuous and thinner passive layers, which do not provide corrosion protection. Literature reports that instabilities in the passive layer, regarding continuity and thickness, act as factors that diminish corrosion resistance [138], [141], [153], [173], [177], [214].

An analysis of the corroded surface of a representative sample from each condition was conducted by OM and SEM (Figure 6.38). The main mechanism in both L-DED AB conditions was intergranular corrosion, with the martensite at the grain boundaries being preferentially corroded with respect to the ferritic matrix, as illustrated in OM of Figure 6.38a and Figure 6.38c for PRO-AB and RES-AB, respectively. The martensitic grain boundaries appear dark, while the ferrite remains light. In the SEM, pits were observed. PRO-AB (Figure 6.38b) showed a greater number of pits and larger pit sizes than RES-AB (Figure 6.38d). As

previously stated, the density (section 6.3.1) was similar between L-DED parameters, so the PRO-AB exhibited only a trend for larger porosity dimensions. Therefore, the pits must have formed over porosities. Assuming the presence of Cr-carbides, the larger Cr-depleted Fe-matrix area favored greater pit formation in PRO-AB [133], [136], [142], [214]. In the SUB-AR, Figure 6.38e OM showed uniform corrosion. Figure 6.38f SEM revealed pits and generalized corrosion. These can be attributed to the homogeneous SUB-AR annealed microstructure, with tempered martensite distributed throughout the structure. The Cr-carbides were also identified. Thus, the SUB-AR Fe-matrix is Cr-depleted, providing sensitization. The coarse microstructure also failed to support and maintain the passive layer [63], [169], [211], [212], [215].

Figure 6.38 - Corroded surfaces of the different L-DED AB and SUB-AR.

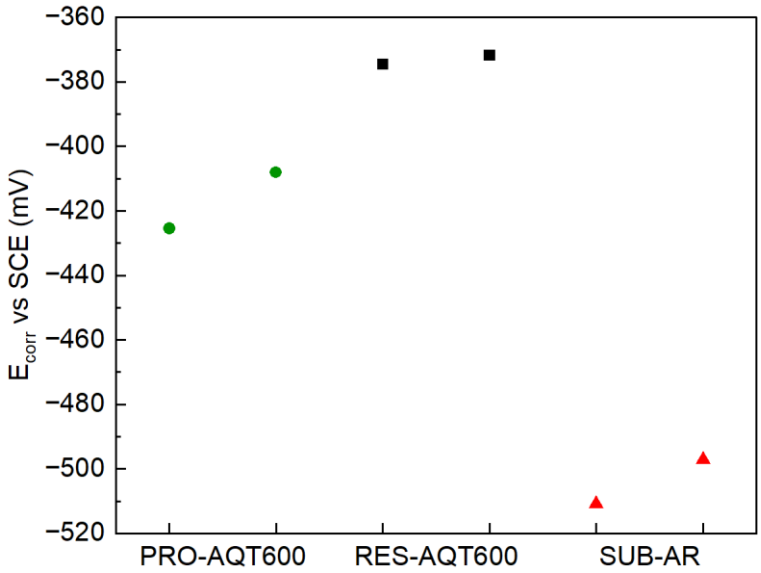


Source: Author (2025).

6.7.2 Effects of PHT on corrosion resistance

The application of the PHT AQT600 was not beneficial in terms of corrosion resistance for the AISI 410L MSS processed by L-DED. Compared to the L-DED AB conditions, the E_{corr}, R_p, and I_{corr} were more negative, lower, and higher, respectively, in both evaluated L-DED PHT. However, these conditions still significantly outperformed the SUB-AR. As seen in Table 6.10, RES-AQT600 showed a trend for higher corrosion resistance than PRO-AQT600. Figure 6.39 graph shows the E_{corr} for both L-DED PHT conditions and SUB-AR, highlighting that the RES-AQT600 generated a more noble potential, indicating higher corrosion resistance.

Figure 6.39 - Potential corrosion (E_{corr}) of the L-DED PHT conditions and SUB-AR.

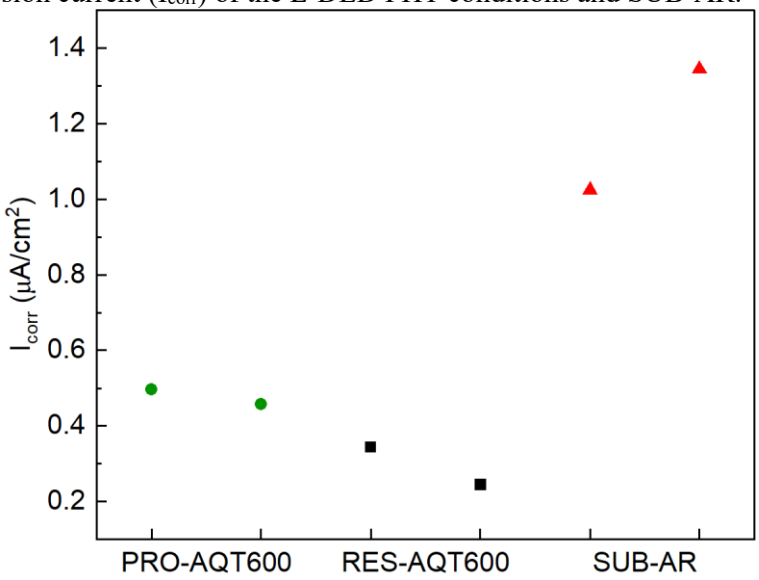


Source: Author (2025).

The largest difference detected for the L-DED PHT was in I_{corr}, as shown in Figure 6.40 graph, which was significantly lower in RES-AQT600 regarding PRO-AQT600. SUB-AR showed a much higher I_{corr} concerning both L-DED conditions. The R_p was slightly higher in RES-AQT600 than PRO-AQT600, while the SUB-AR exhibited a significantly lower R_p than all the other conditions. These results indicate better corrosion resistance for RES-AQT600.

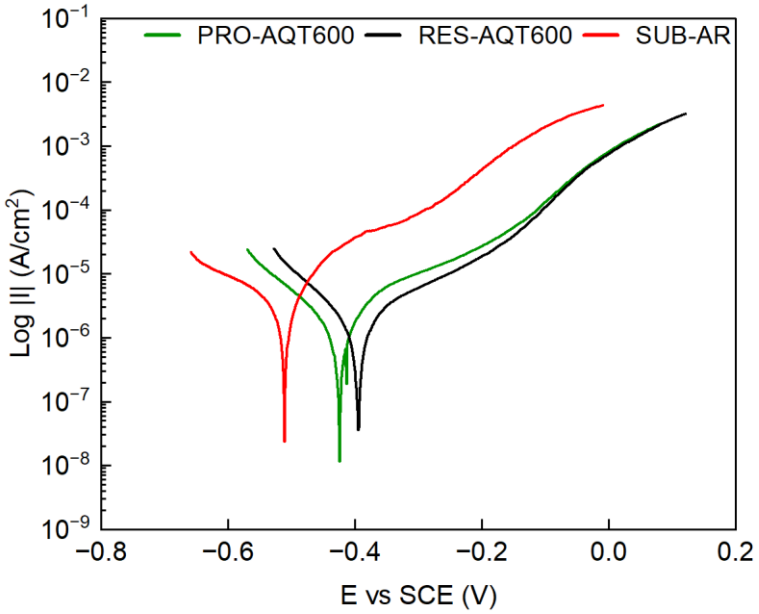
Figure 6.41 shows the linear sweep voltammetry curve. RES-AQT600 exhibited a slightly more positive E_{break} (-0.30 V) than PRO-AQT600 (-0.38 V) and SUB-AR (-0.50 V). This aligns with forming a more suitable passive layer in the former, supporting its greater corrosion resistance. Regarding the L-DED AB conditions, the PRO parameter remained at a similar level of E_{break}, while the RES showed a significant drop.

Figure 6.40 - Corrosion current (I_{corr}) of the L-DED PHT conditions and SUB-AR.



Source: Author (2025).

Figure 6.41 - Linear sweep voltammetry of the L-DED PHT conditions and SUB-AR.



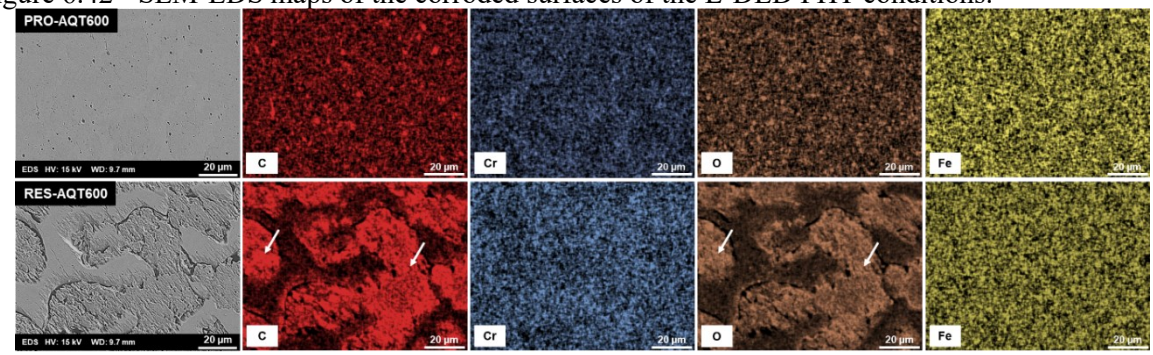
Source: Author (2025).

Some effects explain these differences. As described in section 6.4, with PHT, the AB microstructure underwent homogenization, and the initially refined grains became coarse. Previously concentrated at the grain boundaries, the martensite laths were homogenized into a tempered acicular shape. Martensite tempering was evidenced in the XRD, which revealed only BCC martensite/ferrite peaks, unlike the L-DED AB. Only the RES-AQT600 showed signs of BCT martensite in its microstructure, which gave it higher hardness concerning PRO-AQT600.

As a PHT result, besides the martensite being distributed throughout the structure, the ferrite was C-enriched due to the C-release from the solid-solution at the grain boundaries into the Fe-matrix. Thus, not only was the low corrosion-resistant martensite distributed throughout the material, but the ferrite's corrosion resistance was also depleted. Furthermore, PHT precipitates a greater number of larger Cr-carbides, which triggers sensitization.

Figure 6.42 SEM-EDS maps of the corroded samples did not provide significant chemical composition differences for PRO-AQT600. On the other hand, in the RES-AQT600, higher concentrations of C and O were noted in the martensite regions. Part of the C remained in solid-solution in this phase, which was more affected by corrosion regarding the ferrite, which possesses low C-content. This supports the previously highlighted microstructure and hardness. The other detected elements can be related to the AISI 410L's nominal chemical composition, the Cr_2O_3 passive layer, and the Fe_2O_3 corrosion product [215]–[217].

Figure 6.42 - SEM-EDS maps of the corroded surfaces of the L-DED PHT conditions.



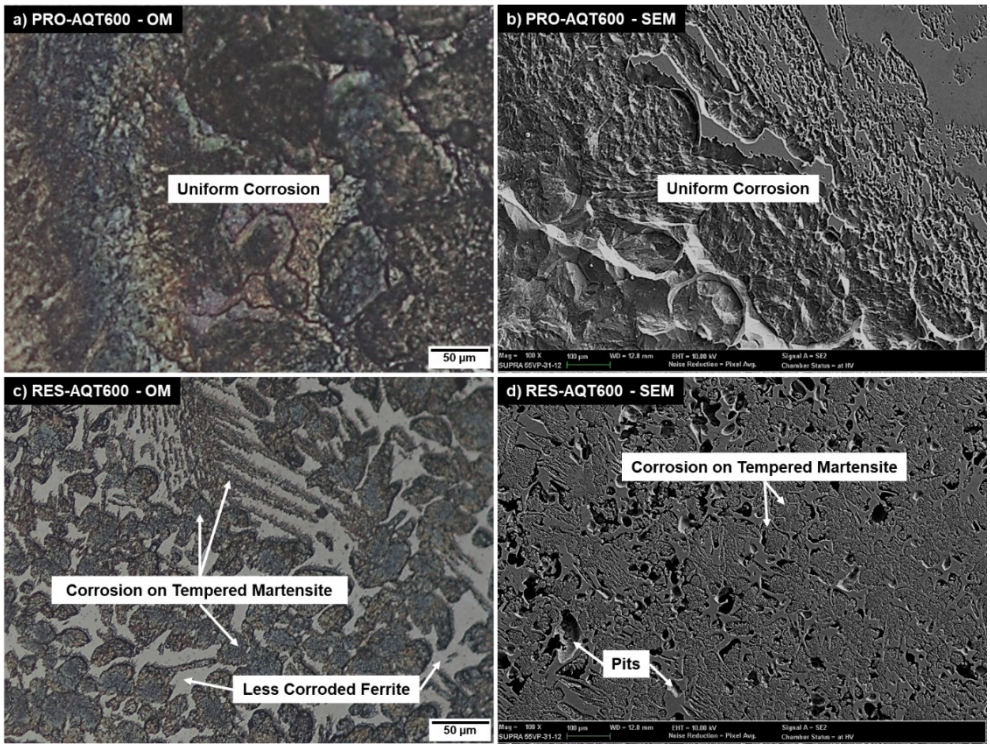
Source: Author (2025).

Another influence is the microstructure refinement. Despite the homogenization of the grains achieved with the PHT, the RES-AQT600 showed traces of L-DED thermal history, with a more refined microstructure. Therefore, its surface energy exceeds PRO-AQT600, which helps in combat against corrosion. A greater amount of martensite also points to a lower availability of C in the Fe-matrix. Furthermore, the entrapment of a larger portion of C in solid-solution decreases the possibility of nucleation of precipitates, such as Cr-carbides, which leads to sensitization, as pointed by [136], [138], [153], [177], [209].

The more refined microstructure of RES-AQT600 also favors the formation and maintenance of the Cr_2O_3, which tends to be more continuous, compact, and thicker. On the other hand, coarser microstructures exhibited thin and discontinuous layers, leaving the material surface exposed to corrosion. In this context, the passive layer formed in PRO-AQT600 was less effective. The SUB-AR experienced a similar effect, but on a more accelerated scale, due to its even coarser and more homogeneous microstructure [176], [199], [212], [213], [216].

The corrosion mechanisms were investigated by OM and SEM and are presented in Figure 6.43. OM allowed the observation of uniform corrosion in the PRO-AQT600 (Figure 6.43a), with no preferential corroded regions. In the RES-AQT600 (Figure 6.43c), preferential corrosion was observed in the regions occupied by tempered martensite (dark color). In contrast, the ferritic regions showed less intense corrosion (light color). This behavior was corroborated by SEM, which showed uniform corrosion across the entire extent of PRO-AQT600 (Figure 6.43b), whereas in RES-AQT600 (Figure 6.43d), pitting and preferential uniform corrosion were observed in concentrated regions corresponding to the tempered martensite bands. In Figure 6.43c, the remaining martensite laths were preferentially corroded. Assuming the presence of Cr-carbides, besides the uniform corrosion of PRO-AQT600, it is likely that this condition also suffered sensitization, leaving the Cr-content below the required limit to maintain the passive layer stability. No evidence of desensitization was found either. In this process, during the tempering stage, Cr is diffused from the carbides, restoring the regions previously depleted of this element due to carbide nucleation. In the SUB-AR, besides the uniform corrosion, the presence of a large number of Cr-carbides resulted in a corrosion performance lower than all the L-DED conditions [138], [171], [176], [199], [211], [217].

Figure 6.43 - Corroded surfaces of the different L-DED PHT conditions.



Source: Author (2025).

7 RESEARCH ACCOMPLISHMENTS

This section presents the main conclusions obtained from this work, some recommendations for future work on this research topic, and the scientific contributions.

7.1 CONCLUSIONS

This Thesis investigated the low carbon-content martensitic stainless steel (MSS) AISI 410L processed by laser directed energy deposition (L-DED) under two as-built (AB) parametrizations, one for production (PRO), with a higher deposition rate, and one for resolution (RES), with a lower deposition rate. The material was also analyzed in the heat-treated (PHT) state, with the PHT route also being a study purpose. The anisotropy was evaluated through different building orientations. The performance was analyzed in terms of microstructure, hardness, tensile and Charpy impact mechanical properties, tribology, and corrosion. A higher C-content commercial MSS AISI 410 was used as reference (SUB-AR):

In terms of L-DED parameters optimization to define an experimental route:

- By applying the design of experiments, it was defined as a set of optimized L-DED parameters. In the first single beads step, minimum and maximum limits of the L-DED hardware used were established, as well as a stable set of parameters.
- In the second single layers step, the influence of the hatch spacing parameter on the geometric properties was investigated. The behavior was modeled through regression functions, and with the acceptance criteria established, the desirability function allowed the identification of a L-DED parameter set that simultaneously met all these criteria.
- In the multilayers (cubes) step, the influence of layer height on the density of L-DED multilayer parts was investigated.
- From these steps, it was concluded that establishing clear acceptance criteria is essential, as even minor changes in L-DED parameters can significantly alter geometry and density responses, leading to shifts in the process windows.

In terms of microstructure features regarding the AB and PHT studied conditions:

- The AB microstructure of AISI 410L processed by L-DED was composed of BCC ferrite and BCT martensite laths concentrated at the grain boundaries. This is a result of the laser fast cooling speed and the low C-content of AISI 410L. The different parameters (PRO and RES) and build orientation (VER and HOR) influenced grain refinement.

- With PHT, the microstructure underwent homogenization during the austenitization plus quenching (AQ). Previously refined grains became coarser, and the martensite exhibited a rounded package shape. Tempering at lower temperatures (AQT300 and AQT450) did not result in significant modifications concerning the AQ condition. AQT600 led to martensite tempering and residual stress relief. In the RES, BCT martensite lath traces were still observed, which was due to its AB more refined microstructure regarding PRO.
- Microstructure analysis showed that laser fast cooling, especially at lower deposition rates and larger substrate contact areas, provides refined microstructures. Due to the low feedstock carbon-content, martensite formed at grain boundaries, enhancing hardness locally. Heat-treatment revealed that only higher tempering temperatures modify the microstructure, achieving homogenization and martensite tempering.

In terms of mechanical properties concerning AB and PHT conditions in the different building orientations:

- PRO-Hor resulted in higher hardness, YS, and UTS concerning Pro-Ver, which indicates that the building orientation that produced a more refined microstructure increased the mechanical strength. The EL was similar between both building orientations. The higher amount of martensite formed in the more refined microstructure of RES-Hor embrittles the material, resulting in lower AE regarding PRO-Ver. Except for this last one, all other properties exceeded the SUB-AR. This performance was evident in the fractures, with large cleavage bands versus the dimple's characteristic of ductile fracture in the SUB-AR.
- With the application of PHT AQ, AQT300, and AQT450, hardness, YS, and UTS increased concerning AB. In these conditions, the microstructure remained refined, with high mechanical strength. With the AQT600, effective homogenization and martensite tempering occur, factors that reduce hardness, YS, and UTS. Ductility was restored, which increased EL and AE concerning the AB conditions and those tempered at lower temperatures. The parameters (PRO and RES) and building orientations (Ver and Hor) did not significantly affect YS, UTS, and EL. However, AE was lower in both the RES parameter and the Hor orientation, owing to the hardness increase.
- The mechanical properties were found to be linked to the microstructure. In the as-built conditions, refined grains and a higher martensite content enhanced hardness and

mechanical strength but also made the material brittle. For applications requiring greater toughness, it is important to apply heat-treatment at higher tempering temperatures to homogenize the martensite within the ferritic matrix and temper the martensite.

In terms of tribological performance regarding the AB and optimized PHT route:

- Besides the higher hardness, the larger martensitic bands of the RES-AB support the compact tribolayers. As a result, a more stable COF and a lower *k* were found in the tribological test. In the L-DED PHT conditions, besides the lower hardness, the thinner area of grain boundaries was not sufficient to provide the formation and support of compact tribolayers. This combined effect resulted in a higher *k*.
- SUB-AR microstructure with coarser grains and tempered martensite generated lower hardness and COF across all conditions. Its higher *k* compared to L-DED AB, and lower when compared to L-DED PHT, is justified by its lower hardness and greater amount of oxides. The Cr_7C_3 carbides support the less compact tribolayers.
- The responses of the analyzed tribosystem indicated that the refined microstructure directly produced by L-DED processing is advantageous due to the greater hardness levels it provides and its facilitation of compact tribolayer formation.
- The results suggest that the L-DED parameters can significantly influence the tribological performance of AM AISI 410L compared to the chemical composition (e.g., C-content) and PHT performed. L-DED RES parameters will provide a longer lifespan for the AM L-DED AISI 410L part when subjected to this tribosystem.

In terms of corrosion resistance regarding the AB and optimized PHT route:

- The RES-AB condition exhibited significantly superior performance concerning PRO-AB and SUB-AR. The former's more refined microstructure provided higher surface energy and support for the Cr_2O_3 passive layer. The martensite laths at the grain boundaries removed C from the Fe-matrix, reducing corrosion activity and sensitization.
- PHT tempered martensite and coarser grains resulted in uniform corrosion and inadequate support for the Cr_2O_3 passive layer, which worsened performance regarding L-DED AB. RES-AQT600 exhibited better performance than PRO-AQT600, due to the more refined RES-AB microstructure, and traces of BCT martensite remained after the PHT, which provides greater C-content catchment from the Fe-matrix, and the lower sensitization concerning PRO-AQT600. SUB-AR suffered from uniform corrosion and sensitization due to its coarser tempered microstructure with many Cr-carbides.

- It was possible to conclude that the corrosion responses are aligned with the tribological performance. The refined microstructure resulting from L-DED processing reduced C-content from the ferritic matrix, provided higher surface energy, and promoted the formation of more stable passive layers.

Regarding the L-DED thermal history and PHT route influence:

- Due to the better combination of mechanical strength, tribological, and corrosion resistance properties, it proved to be more advantageous to use the L-DED RES parameters to additively manufacture AISI 410L multilayer parts. Furthermore, the PHT performance only makes sense if the specific final application requires higher toughness.
- The results highlight the possibility of using L-DED parameter modification between the core and the surface of the part. Thus, the core can be built with a PRO parameter that has a higher deposition rate and productivity, while the layers closer to the surface can be deposited with a RES parameter to provide better geometrical accuracy and properties.

7.2 RECOMMENDATIONS FOR FUTURE WORK

- Parametric evaluation of the L-DED process focuses more on resolution conditions to enhance mechanical, tribological, and corrosion performance properties.
- Investigate tribological performance through other test setups, using different counterbody materials and lubricating media, and investigating the resulting debris, to understand the material's performance when subjected to other tribosystems.
- Studying corrosion resistance by other techniques, such as immersion in aqueous solutions and exposure to salt spray, aiming to understand the action of the corrosion mechanisms.
- Process AISI 410L under similar energy densities using L-DED and L-PBF, to verify the effects of different features intrinsic to each process, such as layer thickness.
- Analyze the level of degradation of AISI 410L powder and the respective effects on the microstructure and properties during controlled cycles of feedstock reuse.
- Investigate AISI 410L mixed with other metallic powders to form functionally graded materials, to enhance specific properties.
- Study the performance of in-situ parts, manufactured and/or cladded with AISI 410L MSS by L-DED, using the parameters and conditions developed throughout this work.

7.3 LIST OF PUBLICATIONS

Table 7.1 presents the full papers published in International Journals and those in the development stage. Table 7.2 presents the papers published in event proceedings (national and international) and those in development for presentation at future events.

Table 7.1 - Full papers published in international journals and papers in the development stage.

No.	Title	Journal	DOI
1	Influence of post-processing heat-treatment on the mechanical performance of AISI 410L stainless steel manufactured by the L-DED process	Journal of Laser Applications	10.2351/7.0001135 | Impact Factor: 1.9 | CAPES: A4
2	Tribological performance of 410L martensitic stainless steel parts manufactured by Laser directed energy deposition	Journal of Engineering Tribology	10.1177/13506501241290383 | Impact Factor: 1.8 | CAPES: A4
3	On the development of an operational map and a robust processing range for laser-directed energy deposition of AISI 410L stainless steel	International Journal of Advanced Manufacturing Technology	10.1007/s00170-025-15362-9 | Impact Factor: 3.2 | CAPES: A2
4	Mechanical properties of AISI 410L stainless steel parts manufactured by laser directed energy deposition in the as-built and heat-treated states	IntechOpen (Book Chapter)	10.5772/intechopen.1007404
5	Effects of L-DED parameters and pos heat-treatments routes on AISI 410L electrochemical corrosion resistance	Planned	In Development
6	AISI 410L processed by L-DED: A review on processability, heat-treatment, microstructure features, mechanical strength, tribological performance, and corrosion resistance	Planned	In Development

Source: Author (2025).

Table 7.2 - Papers published in event proceedings (national and international) and those that are in development for presentation at future events.

No.	Title	Event	DOI
1	Laser directed energy deposition (L-DED) of AISI 410L: Development of an operational map and the effect of processing parameter on the bead geometry	COBEM 2021 (International)	10.26678/ABCM.COBEM 2021.COB2021-1878
2	Laser directed energy deposition process optimization parameters for AISI 410L single layers	COBEM 2023 (International)	10.26678/ABCM.COBEM 2023.COB2023-0684
3	Tribological performance of 410L martensitic stainless steel parts manufactured by laser directed energy deposition	TRIBOBR 2023 (International)	10.13140/RG.2.2.15887.56 484
4	Influence of post-processing heat-treatment on the mechanical performance of AISI 410L stainless steel manufactured by L-DED process	ICALEO 2023 (International)	Paper 0784_1173_000161
5	Mechanical performance of laser directed energy deposition produced AISI 410L martensitic stainless steel parts in different build orientations	CONEM 2024 (National)	10.26678/ABCM.CONEM 2024.CON24-0445
6	Corrosion performance of AISI 410L martensitic stainless steel parts manufactured by laser directed energy deposition in different parametrizations	COBEF 2025 (National)	Presented (Waiting DOI) *Honored with 1st Place Distinction in Oral Presentation Category
7	Corrosion resistance of AISI 410L martensitic stainless steel manufactured by laser directed energy deposition in the as-built and post heat-treated states	COBEM 2025 (International)	Full Paper Submitted (Waiting Response)

Source: Author (2025).

REFERENCES

[1] M. N. Batista, M. C. Marinelli, and I. Alvarez-Armas. **Effect of initial microstructure on surface relief and fatigue crack initiation in AISI 410 ferritic-martensitic steel**. *Fatigue and Fracture of Engineering Materials and Structures*. vol. 42, no. 1. pp. 61–68. 2019. DOI: doi: 10.1111/ffe.12868.

[2] K. A. M. B. Gonçalves, G. L. de Faria, R. H. M. de Siqueira, T. R. de Oliveira, and M. S. F. de Lima. **Heat treatment effects on the hardness and wear behavior of laser-welded AISI40 martensitic steel plates**. *The International Journal of Advanced Manufacturing Technology*. vol. 114, no. 3–4. pp. 1155–1163. 2021. DOI: 10.1007/s00170-021-06942-6.

[3] D. C. Moreira, H. C. Furtado, J. S. Buarque, B. R. Cardoso, B. Merlin, and D. D. C. Moreira. **Failure analysis of AISI 410 stainless-steel piston rod in spillway floodgate**. *Engineering Failure Analysis*. vol. 97, no. Jan. pp. 506–517. 2019. DOI: 10.1016/j.engfailanal.2019.01.035.

[4] S. A. Hosseini, K. Gheisari, H. Moshayedi, F. Warchomicka, and N. Enzinger. **Basic alloy development of low-transformation-temperature fillers for AISI 410 martensitic stainless steel**. *Science and Technology of Welding and Joining*. vol. 25, no. 3. pp. 243–250. 2020. DOI: 10.1080/13621718.2019.1681159.

[5] P. Gradl, D. C. Tinker, A. Park, O. R. Mireles, M. Garcia, R. Wilkerson, and C. Mckinney. **Robust metal additive manufacturing process selection and development for aerospace components**. *Journal of Materials Engineering and Performance*. vol. 31, no. 3. pp. 6013–6044. 2022. DOI: 10.1007/s11665-022-06850-0.

[6] B. Nayebi, H. Najafi, and A. Farnia. **Microstructural, hardening, and wear characteristics of surface re-melted AISI 410S stainless steel via fiber laser process**. *Journal of Mechanical Science and Technology*. vol. 35, no. 10. pp. 4419–4426. 2021. DOI: 10.1007/s12206-021-0912-6.

[7] O. O. Lima, G. S. Prass, and A. S. C. M. D'Oliveira. **Impact of deposition procedures on 410L multilayer plasma transferred arc processing**, in *ABCM Series on Mechanical Sciences and Engineering_12th Brazilian Manufacturing Engineering Congress - COBEF*, D. de Oliveira, M. Ziberov, and A. R. Machado, Eds. Brasília (BR): ABCM, 2024, pp. 126–139. DOI: 10.1007/978-3-031-43555-3.

[8] F. Khodabakhshi, M. H. Farshidianfar, A. P. Gerlich, M. Nosko, V. Trembo, and A. Khajepour. **Microstructure, strain-rate sensitivity, work hardening, and fracture behavior of laser additive manufactured austenitic and martensitic stainless steel structures**. *Materials Science & Engineering A*. vol. 756, no. Apr. pp. 545–561. 2019. DOI: 10.1016/j.msea.2019.04.065.

[9] M. Baumers, P. Dickens, C. Tuck, and R. Hague. **The cost of additive manufacturing: Machine productivity, economies of scale and technology-push**. *Technological Forecasting and Social Change*. vol. 102, no. Jan. pp. 193–201. 2016. DOI: 10.1016/j.techfore.2015.02.015.

[10] T. DebRoy, H. L. Wei, J. S. Zuback, T. Mukherjee, J. W. Elmer, J. O. Milewski, A. M. Beese, A. Wilson-Heid, A. De, and W. Zhang. **Additive manufacturing of metallic components – Process, structure and properties**. *Progress in Materials Science*. vol. 92, no. Mar. pp. 112–224. 2018. DOI: 10.1016/j.pmatsci.2017.10.001.

[11] S. M. Thompson, L. Bian, N. Shamsaei, and A. Yadollahi. **An overview of direct laser deposition for additive manufacturing; Part I: Transport phenomena, modeling and diagnostics**. *Additive Manufacturing*. vol. 8, no. Oct. pp. 36–62. 2015. DOI: 10.1016/j.addma.2015.07.001.

[12] ISO/ASTM 52900. **Standard Terminology for Additive Manufacturing – General Principles – Terminology**. International Organization for Standardization, Pennsylvania, pp. 1–19, 2015. DOI: 10.1520/F3177-21.

[13] ASTM F3187. **Standard Guide for Directed Energy Deposition of Metals**. International Organization for Standardization, Pennsylvania, pp. 1–22, 2016. DOI: 10.1520/F3187-16R23.

[14] B. Bax, R. Rajput, R. Kellet, and M. Reisacher. **Systematic evaluation of process parameter maps for laser cladding and directed energy deposition**. *Additive Manufacturing*. vol. 21, no. Jan. pp. 487–494. 2018. DOI: 10.1016/j.addma.2018.04.002.

[15] N. Shamsaei, A. Yadollahi, L. Bian, and S. M. Thompson. **An overview of direct laser deposition for additive manufacturing; Part II: Mechanical behavior, process parameter optimization and control**. *Additive Manufacturing*. vol. 8, no. Oct. pp. 12–35. 2015. DOI: 10.1016/j.addma.2015.07.002.

[16] A. Dass and A. Moridi. **State of the art in directed energy deposition: From additive manufacturing to materials design**. *Coatings*. vol. 9, no. 7. pp. 1–26. 2019. DOI: 10.3390/coatings9070418.

[17] I. Hemmati, V. Ocelík, and J. T. M. De Hosson. **The effect of cladding speed on phase constitution and properties of AISI 431 stainless steel laser deposited coatings**. *Surface and Coatings Technology*. vol. 205, no. 21–22. pp. 5235–5239. 2011. DOI: 10.1016/j.surfcoat.2011.05.035.

[18] H. Zhu, M. Ouyang, J. Hu, J. Zhang, and C. Qiu. **Design and development of TiC-reinforced 410 martensitic stainless steel coatings fabricated by laser cladding**. *Ceramics International*. vol. 47, no. Jan. pp. 12505–12513. 2021. DOI: 10.1016/j.ceramint.2021.01.108.

[19] A. W. Gebisa and H. G. Lemu. **Additive manufacturing for the manufacture of gas turbine engine components: Literature review and future perspectives**, in *Proceedings of the ASME Turbo Expo-Turbomachinery Technical Conference and Exposition*, 2018, pp. 1–10. DOI: 10.1115/GT2018-76686.

[20] D. Thomas. **Costs, benefits, and adoption of additive manufacturing: a supply chain perspective**. *International Journal of Advanced Manufacturing Technology*. vol. 85, no. 5–8. pp. 1857–1876. 2016. DOI: 10.1007/s00170-015-7973-6.

[21] G. A. Ravi, X. J. Hao, N. Wain, X. Wu, and M. M. Attallah. **Direct laser fabrication of three dimensional components using SC420 stainless steel**. *Materials and Design*. vol. 47, no. May. pp. 731–736. 2013. DOI: 10.1016/j.matdes.2012.12.062.

[22] Q. Fang, Y. Liu, D. Hu, Y. Zhao, J. Li, and H. Chen. **Effect of Ni on the microstructure and properties of laser cladding 316 L + 410 composite stainless steel coatings**. *Surface and Coatings Technology*. vol. 478, no. Sept. p. 130465. 2024. DOI: 10.1016/j.surfcoat.2024.130465.

[23] S. Cooke, K. Ahmadi, S. Willerth, and R. Herring. **Metal additive manufacturing: Technology, metallurgy and modelling**. *Journal of Manufacturing Processes*. vol. 57, no. Jul. pp. 978–1003. 2020. DOI: 10.1016/j.jmapro.2020.07.025.

[24] A. J. Thiesen. **Selection of Processing Parameters for the Laser Directed Energy Deposition Process Applied to Additive Manufacturing: A Methodological Proposal**, *Master Thesis*, no. Federal University of Santa Catarina, Post-Graduation Program in Engineering and Mechanical Sciences. p. 181, 2021. DOI: https://repositorio.ufsc.br/handle/123456789/227036.

[25] A. Alfaify, M. Saleh, F. M. Abdullah, and A. M. Al-Ahmari. **Design for additive manufacturing**. *Sustainability*. vol. 12, no. 7936. pp. 1–22. 2020. DOI: 10.3390/su12197936.

[26] N. Kladovasilakis, P. Charalampous, I. Kostavelis, D. Tzetzis, and D. Tzovaras. **Impact of metal additive manufacturing parameters on the powder bed fusion and direct energy deposition processes: A comprehensive review**. *Progress in Additive Manufacturing*. vol. 6, no. 3. pp. 349–365. 2021. DOI: 10.1007/s40964-021-00180-8.

[27] L. E. dos Santos Paes, H. S. Ferreira, M. Pereira, F. A. Xavier, W. L. Weingaertner, and L. O. Vilarinho. **Modeling layer geometry in directed energy deposition with laser for additive manufacturing**. *Surface and Coatings Technology*. vol. 409, no. Nov. p. 126897. 2021. DOI: 10.1016/j.surfcoat.2021.126897.

[28] L. E. dos Santos Paes, M. Pereira, F. A. Xavier, W. L. Weingaertner, A. S. C. M. D'Oliveira, E. C. Costa, L. O. Vilarinho, and A. Scotti. **Understanding the behavior of laser surface remelting after directed energy deposition additive manufacturing through comparing the use of iron and Inconel powders**. *Journal of Manufacturing Processes*. vol. 70, no. Aug. pp. 494–507. 2021. DOI: 10.1016/j.jmapro.2021.08.061.

[29] L. E. dos Santos Paes, M. Pereira, F. A. Xavier, W. L. Weingaertner, and L. O. Vilarinho. **Lack of fusion mitigation in directed energy deposition with laser (DED-L) additive manufacturing through laser remelting**. *Journal of Manufacturing Processes*. vol. 73, no. Aug. pp. 67–77. 2022. DOI: 10.1016/j.jmapro.2021.10.052.

[30] L. E. dos Santos Paes, J. R. Andrade, M. G. Prates, D. D. B. G. de Souza, S. L. Brião, F. S. Lobato, E. dos Santos Magalhães, B. T. P. Jacob, R. P. Reis, and L. O. Vilarinho. **Path planning strategies for hardness improvement employing surface remelting in AISI 1045 steel**. *Surface and Coatings Technology*. vol. 425, no. Jul. p. 127728. 2021. DOI: 10.1016/j.surfcoat.2021.127728.

[31] R. de M. Castro, E. I. M. Curi, L. F. F. Inacio, A. da S. Rocha, M. Pereira, R. G. N. Silva, and A. de S. P. Pereira. **Laser remelting of WCCoCr coated by HVOF tribological properties and energy efficiency**. *Surface & Coatings Technology*. vol. 427, no. Dec. p. 127841. 2021. DOI: 10.1016/j.surfcoat.2021.127841.

[32] R. M. Pôrto, A. de Souza Pinto Pereira, and M. Pereira. **Parametrization methodology for laser remelting applied over laser metal deposition single tracks**. *Journal of Laser Applications*. vol. 32, no. 2. p. 022069. 2020. DOI: 10.2351/7.0000098.

[33] J. M. S. de Sousa, R. G. N. Silva, A. de S. P. Pereira, C. Amaral, and M. Pereira. **Effect of laser remelting on tribological performance of Ni-Cr-B-Si coatings deposited by laser metal deposition**. *Soldagem & Inspeção*. vol. 25, no. Apr. pp. 1–13. 2020. DOI: 10.1590/0104-9224/si25.15.

[34] F. Cavilha Neto, M. Pereira, L. E. dos Santos Paes, M. C. Fredel, and L. F. Bossa. **Effect**

of power modulation frequency on porosity formation in laser welding of SAE 1020 steels. *International Journal of Advanced Manufacturing Technology*. vol. 112, no. 9–10. pp. 2509–2517. 2021. DOI: 10.1007/s00170-020-06482-5.

[35] F. Cavilha Neto, M. C. Fredel, M. Pereira, and L. E. dos S. Paes. **Laser power modulation to grain refinement of SAE 1045 steel welds**. *Journal of Laser Applications*. vol. 32, no. 2. p. 022027. 2020. DOI: 10.2351/7.0000096.

[36] F. Cavilha Neto, M. Pereira, L. E. dos Santos Paes, M. R. Viotti, and M. C. Fredel. **Reducing processing-induced residual stresses in SAE 4140 steels laser welded using modulated power emission**. *Optics and Laser Technology*. vol. 140, no. Mar. p. 107032. 2021. DOI: 10.1016/j.optlastec.2021.107032.

[37] C. Li, Z. Y. Liu, X. Y. Fang, and Y. B. Guo. **Residual Stress in Metal Additive Additive**. *Procedia CIRP*. vol. 71, no. 2212–8271. pp. 348–353. 2018. DOI: 10.1016/j.procir.2018.05.039.

[38] V. Chiaverini. *Aços e Ferros Fundidos*, 7th ed. São Paulo, São Paulo: Associação Brasileira de Metalurgia e Materiais, 2015.

[39] S. Sam, C. R. Das, V. Ramasubbu, S. K. Albert, A. K. Bhaduri, T. Jayakumar, and E. R. Kumar. **Delta ferrite in the weld metal of reduced activation ferritic martensitic steel**. *Journal of Nuclear Materials*. vol. 455, no. 1–3. pp. 343–348. 2014. DOI: 10.1016/j.jnucmat.2014.07.008.

[40] E. Mabruri, S. Prifiharni, M. S. Anwar, T. B. Romijarso, and B. Adjiantoro. **Mechanical properties optimization of the modified 410 martensitic stainless steel by heat treatment process**. *Materias Today*. vol. 5, no. 2214–7853. pp. 14918–14922. 2018. DOI: 10.1016/j.matpr.2018.04.030.

[41] K. Holmberg and A. Erdemir. **Influence of tribology on global energy consumption, costs and emissions**. *Friction*. vol. 5, no. 3. pp. 263–284. 2017. DOI: 10.1007/s40544-017-0183-5.

[42] S. Papavinasam. *Corrosion Control in the Oil and Gas Industry*. London, United Kingdom: Elsevier, 2014.

[43] B. N. Popov. *Corrosion engineering: Principles and solved problems*. Amsterdan, Nethelands: Elsevier, 2015.

[44] K. S. Hein, Y. qing Wang, Y. Li, Q. feng Liu, K. yu Chen, Y. Chen, J. jing Chen, W. L. Jin, R. jie Wu, and J. Xia. **A holistic approach to evaluating techniques for monitoring coated steel degradation: Integrating techniques and applications**. *Progress in Organic Coatings*. vol. 200, no. Oct. p. 109067. 2025. DOI: 10.1016/j.porgcoat.2025.109067.

[45] A. N. Isfahany, H. Saghafian, and G. Borhani. **The effect of heat treatment on mechanical properties and corrosion behavior of AISI420 martensitic stainless steel**. *Journal of Alloys and Compounds*. vol. 509, no. 9. pp. 3931–3936. 2011. DOI: 10.1016/j.jallcom.2010.12.174.

[46] Q. Lai, R. Abrahams, W. Yan, C. Qiu, P. Mutton, A. Paradowska, M. Soodi, and X. Wu. **Influences of depositing materials, processing parameters and heating conditions**

on material characteristics of laser-cladded hypereutectoid rails. *Journal of Materials Processing Technology*. vol. 263, no. Aug. pp. 1–20, 2019. 2019. DOI: 10.1016/j.jmatprotec.2018.07.035.

[47] M. K. Alam, M. Mehdi, R. J. Urbanic, and A. Edrisy. **Mechanical behavior of additive manufactured AISI 420 martensitic stainless steel**. *Materials Science & Engineering A*. vol. 773, no. Aug. p. 138815. 2020. DOI: 10.1016/j.msea.2019.138815.

[48] G. Chakraborty, C. R. Das, S. K. Albert, A. K. Bhaduri, V. T. Paul, G. Panneerselvam, and A. Dasgupta. **Study on tempering behaviour of AISI 410 stainless steel**. *Materials Characterization*. vol. 100, no. Feb. pp. 81–87. 2015. DOI: 10.1016/j.matchar.2014.12.015.

[49] H. S. Yang and H. K. D. H. Bhadeshia. **Austenite grain size and the martensite-start temperature**. *Scripta Materialia*. vol. 60, no. 7. pp. 493–495. 2009. DOI: 10.1016/j.scriptamat.2008.11.043.

[50] J. C. Lippold and D. J. Kotecji. *Welding Metallurgy and Weldability of Stainless Steel*. Cambridge, United Kingdom: John & Willey Sons, Inc., 2005.

[51] K.-H. Zum Gahr. *Microstructure and Wear of Materials*. New York, United States of America: Elsevier, 1987.

[52] E. Mortazavian, Z. Wang, and H. Teng. **Finite element investigation of residual stresses during laser powder deposition process as an innovative technique to repair worn rails**. *Proceedings of the Institution of Mechanical Engineers, Part F: Journal of Rail and Rapid Transit*. vol. 237, no. 1. pp. 21–32. 2023. DOI: 10.1177/09544097221089410.

[53] W. Zhai, N. Wu, and W. Zhou. **Laser metal deposition of low carbon 410L stainless steel and heat treatment**. *Materials Science and Engineering: A*. vol. 872, no. Apr. pp. 1–10. 2023. DOI: 10.1016/j.msea.2023.144987.

[54] E. Folkhard. *Welding Metallurgy of Stainless Steel*, no. 7. New York, United States of America: Springer-Verlag/Wien, 1988.

[55] E. Sadeghi, N. Markocsan, and S. Joshi. **Advances in corrosion-resistant thermal spray coatings for renewable energy power lants. Part I: Effect of composition and microstructure**. *Journal of Thermal Spray Technology*. vol. 28, no. 8. pp. 1749–1788. 2019. DOI: 10.1007/s11666-019-00938-1.

[56] S. Zhang, P. Wang, D. Li, and Y. Li. **Investigation of the evolution of retained austenite in Fe-13%Cr-4%Ni martensitic stainless steel during intercritical tempering**. *Materials and Design*. vol. 84, no. 11. pp. 385–394. 2015. DOI: 10.1016/j.matdes.2015.06.143.

[57] P. Wang, S. P. Lu, N. M. Xiao, D. Z. Li, and Y. Y. Li. **Effect of delta ferrite on impact properties of low carbon 13Cr-4Ni martensitic stainless steel**. *Materials Science and Engineering: A*. vol. 527, no. 13–14. pp. 3210–3216. 2010. DOI: 10.1016/j.msea.2010.01.085.

[58] M. Moradi, H. Arabi, S. Jamshidi Nasab, and K. Y. Benyounis. **A comparative study of laser surface hardening of AISI 410 and 420 martensitic stainless steels by using diode laser**. *Optics and Laser Technology*. vol. 111, no. Sep. pp. 347–357. 2019. DOI: 10.1016/j.optlastec.2018.10.013.

[59] D. A. Porter and K. E. Easterling. *Phase Transformations in Metal and Alloys*. Hong

Kong, China: Springer-Science+Business Media, B.V., 1992.

[60] J. Huang and Z. Xu. **Effect of dynamically recrystallized austenite on the martensite start temperature of martensitic transformation**. *Materials Science and Engineering A*. vol. 438–440, no. Sep. pp. 254–257. 2006. DOI: 10.1016/j.msea.2006.02.069.

[61] R. Colaço and R. Vilar. **Stabilisation of retained austenite in laser surface melted tool steels**. *Materials Science and Engineering A*. vol. 385, no. 1–2. pp. 123–127. 2004. DOI: 10.1016/j.msea.2004.06.069.

[62] M. C. Tsai, C. S. Chiou, J. S. Du, and J. R. Yang. **Phase transformation in AISI 410 stainless steel**. *Materials Science and Engineering A*. vol. 332, no. Apr. pp. 1–10. 2002. DOI: 10.1016/S0921-5093(01)01710-5.

[63] S. K. Bonagani, B. Vishwanadh, S. Tenneti, N. Naveen Kumar, and V. Kain. **Influence of tempering treatments on mechanical properties and hydrogen embrittlement of 13 wt% Cr martensitic stainless steel**. *International Journal of Pressure Vessels and Piping*. vol. 176, no. Aug. p. 103969. 2019. DOI: 10.1016/j.ijpvp.2019.103969.

[64] T. Angeliu, E. L. Hall, M. Larsen, A. M. Y. Linsebigler, and C. Mukira. **The long-term aging embrittlement of Fe-12Cr steels below 773 K**. *Metallurgical and Materials Transactions A: Physical Metallurgy and Materials Science*. vol. 34, no. Apr. pp. 927–934. 2003. DOI: 10.1007/s11661-003-0223-9.

[65] E. Mabruri, Z. A. Syahlan, Sahlan, S. Prifiharni, M. S. Anwar, S. A. Chandra, T. B. Romijarso, and B. Adjiantoro. **Influence of austenitizing heat treatment on the properties of the tempered type 410-1Mo stainless steel**. *Materials Science and Engineering*. vol. 202, no. 1. pp. 0–7. 2017. DOI: 10.1088/1757-899X/202/1/012085.

[66] ASTM A276. **Standard Specification for Stainless Steel Bars and Shapes**. International Organization for Standardization, Pennsylvania, pp. 1–8, 2017. DOI: 10.1520/A0276_A0276M-24A.

[67] A. Hakami, S. A. Ojo, D. Victor, A. Florence, D. Uzuh, and R. Ann. **Advancements in metal additive manufacturing: Opportunities, limitations, impact on properties, and potential solutions: A review**. *Progress in Additive Manufacturing*. vol. 9, no. 6. pp. 1–49. 2024. DOI: 10.1007/s40964-024-00885-6.

[68] R. Poprawe. *Tailored Light 2 Laser Application Technology*. Aachen, Germany: Springer, 2011.

[69] X. Song, S. Feih, W. Zhai, C. Sun, F. Li, R. Maiti, J. Wei, Y. Yang, V. Oancea, L. Romano, and A. M. Korsunsky. **Advances in additive manufacturing process simulation: Residual stresses and distortion predictions in complex metallic components**. *Materials & Design*. vol. 193, no. Aug. p. 108779. 2020. DOI: 10.1016/j.matdes.2020.108779.

[70] T. Yu, J. Sun, W. Qu, Y. Zhao, and L. Yang. **Influences of z-axis increment and analyses of defects of AISI 316L stainless steel hollow thin-walled cylinder**. *The International Journal of Advanced Manufacturing Technology*. vol. 97, no. Jul. pp. 2203–2220. 2018. DOI: 10.1007/s00170-018-2083-x.

[71] J. Gutjahr. **Efeitos da Reutilização do Pó Metálico no Processo Laser Directed**

Energy Deposition (L-DED): Uma Análise Sobre a Degradação da Matéria-Prima e Suas Consequências no Processo e no Comportamento de Peças Fabricadas por Manufatura Aditiva, *Tese de Doutorado*, no. Universidade Fedral de Santa Catarina, Programa de Pós-Graduação em Engenharia Mecânica. p. 256, 2022.

[72] G. Zhu, D. Li, A. Zhang, G. Pi, and Y. Tang. **The influence of standoff variations on the forming accuracy in laser direct metal deposition**. *Rapid Prototyping Journal*. vol. 17, no. 2. pp. 98–106. 2011. DOI: 10.1108/13552541111113844.

[73] G. Zhu, D. Li, A. Zhang, G. Pi, and Y. Tang. **The influence of laser and powder defocusing characteristics on the surface quality in laser direct metal deposition**. *Optics and Laser Technology*. vol. 44, no. 2. pp. 349–356. 2012. DOI: 10.1016/j.optlastec.2011.07.013.

[74] O. Nenadl, V. Ocelík, A. Palavra, and J. T. M. De Hosson. **The prediction of coating geometry from main processing parameters in laser cladding**. *Physics Procedia*. vol. 56, no. C. pp. 220–227. 2014. DOI: 10.1016/j.phpro.2014.08.166.

[75] A. Aversa, A. Saboori, E. Librera, M. de Chirico, S. Biamino, M. Lombardi, and P. Fino. **The role of directed energy deposition atmosphere mode on the microstructure and mechanical properties of 316L samples**. *Additive Manufacturing*. vol. 34, no. Feb. p. 101274. 2020. DOI: 10.1016/j.addma.2020.101274.

[76] M. Ansari, R. S. Razavi, and M. Barekat. **An empirical-statistical model for coaxial laser cladding of NiCrAlY powder on Inconel 738 superalloy**. *Optics and Laser Technology*. vol. 86, no. Aug. pp. 136–144. 2016. DOI: 10.1016/j.optlastec.2016.06.014.

[77] F. Lia, J. Park, J. Tresler, and R. Martukanitz. **Partitioning of laser energy during directed energy deposition**. *Additive Manufacturing*. vol. 18, no. Sep. pp. 31–39. 2017. DOI: 0.1016/j.addma.2017.08.012.

[78] X. Lu, M. Cervera, M. Chiumenti, J. Li, X. Ji, G. Zhang, and X. Lin. **Modeling of the effect of the building strategy on the thermomechanical response of Ti-6Al-4V energy deposition**. *Metals*. vol. 10, no. 1643. pp. 1–18. 2020. DOI: 10.3390/met10121643.

[79] B. J. Dawes, R. Bowerman, and R. Trepleton. **Introduction to the additive manufacturing powder metallurgy supply chain_Exploring the production and supply of metal powders for AM processes**. *Johnson Matthey Technology Review*. vol. 59, no. 3. pp. 243–256. 2015. DOI: 10.1595/205651315X688686.

[80] U. de Oliveira, V. Ocelík, and J. T. M. De Hosson. **Analysis of coaxial laser cladding processing conditions**. *Surface and Coatings Technology*. vol. 197, no. 2–3. pp. 127–136. 2005. DOI: 10.1016/j.surfcoat.2004.06.029.

[81] J. Gutjahr. **Desenvolvimento e Implementação de um Sistema CNC, Modular e Reconfigurável, para Processos Laser**, *Dissertação de Mestrado*, no. Universidade Federal de Santa Catarina, Programa de Pós-Graduação em Engenharia Mecânica. p. 196, 2016.

[82] A. A. Siddiqui and A. K. Dubey. **Recent trends in laser cladding and surface alloying**. *Optics and Laser Technology*. vol. 134, no. Aug. p. 106619. 2021. DOI: 10.1016/j.optlastec.2020.106619.

[83] V. Ocelík, U. de Oliveira, M. de Boer, and J. T. M. de Hosson. **Thick Co-based coating on cast iron by side laser cladding: Analysis of processing conditions and coating**

properties. *Surface and Coatings Technology*. vol. 201, no. 12. pp. 5875–5883. 2007. DOI: 10.1016/j.surfcoat.2006.10.044.

[84] I. Garmendia, J. Pujana, A. Lamikiz, M. Madarieta, and J. Leunda. **Structured light-based height control for laser metal deposition**. *Journal of Manufacturing Processes*. vol. 42, no. Mar. pp. 20–27. 2019. DOI: 10.1016/j.jmapro.2019.04.018.

[85] M. H. Farshidianfar, F. Khodabakhshi, A. Khajepour, and A. P. Gerlich. **Closed-loop deposition of martensitic stainless steel during laser additive manufacturing to control microstructure and mechanical properties**. *Optics and Lasers in Engineering*. vol. 145, no. Feb. p. 106680. 2021. DOI: 10.1016/j.optlaseng.2021.106680.

[86] S. Roy, B. Silwal, A. Nycz, M. Noakes, E. Cakmak, P. Nandwana, and Y. Yamamoto. **Investigating the effect of different shielding gas mixtures on microstructure and mechanical properties of 410 stainless steel fabricated via large scale additive manufacturing**. *Additive Manufacturing*. vol. 38, no. Sept. p. 101821. 2021. DOI: 10.1016/j.addma.2020.101821.

[87] ASTM F3413. **Guide for Additive Manufacturing - Design - Directed Energy Deposition**. International Organization for Standardization, Pennsylvania, pp. 1–24, 2019. DOI: 10.1520/F3413-19E01.

[88] S. Kou. *Welding metallurgy*, 2nd ed. Hoboken, United States of America: John Wiley & Sons, Inc., 2003.

[89] Z. Wang, T. A. Palmer, and A. M. Beese. **Effect of processing parameters on microstructure and tensile properties of austenitic stainless steel 304L made by directed energy deposition additive manufacturing**. *Acta Materialia*. vol. 110, no. May. pp. 226–235. 2016. DOI: 10.1016/j.actamat.2016.03.019.

[90] M. Ziętala, T. Durejko, M. Polański, I. Kunce, T. Płociński, W. Zieliński, M. Łazińska, W. Stępniowski, T. Czujko, K. J. Kurzydłowski, and Z. Bojar. **The microstructure, mechanical properties and corrosion resistance of 316 L stainless steel fabricated using laser engineered net shaping**. *Materials Science and Engineering A*. vol. 677, no. Nov. pp. 1–10. 2016. DOI: 10.1016/j.msea.2016.09.028.

[91] J. X. Fang, S. Y. Dong, S. B. Li, Y. J. Wang, B. S. Xu, J. Li, B. Liu, and Y. L. Jiang. **Direct laser deposition as repair technology for a low transformation temperature alloy: Microstructure, residual stress, and properties**. *Materials Science and Engineering A*. vol. 748, no. Dec. pp. 119–127. 2019. DOI: 10.1016/j.msea.2019.01.072.

[92] L. Reddy, S. P. Preston, P. H. Shipway, C. Davis, and T. Hussain. **Process parameter optimisation of laser clad iron based alloy: Predictive models of deposition efficiency, porosity and dilution**. *Surface & Coatings Technology*. vol. 349, no. May. pp. 198–207. 2018. DOI: 10.1016/j.surfcoat.2018.05.054.

[93] F. Mazzucato, A. Aversa, R. Doglione, S. Biamino, A. Valente, and M. Lombardi. **Influence of process parameters and deposition strategy on laser metal deposition of 316L powder**. *Metals*. vol. 9, no. 1160. pp. 1–11. 2019. DOI: 10.3390/met9111160.

[94] P. Nie, O. A. Ojo, and Z. Li. **Numerical modeling of microstructure evolution during laser additive manufacturing of a nickel-based superalloy**. *Acta Materialia*. vol. 77, no. May. pp. 85–95, 2014. Doi: 10.1016/j.actamat.2014.05.039. 2014. DOI:

10.1016/j.actamat.2014.05.039.

[95] X. Zhao, X. Lin, J. Chen, L. Xue, and W. Huang. **The effect of hot isostatic pressing on crack healing, microstructure, mechanical properties of Rene88DT superalloy prepared by laser solid forming**. *Materials Science and Engineering A*. vol. 504, no. 1–2. pp. 129–134. 2009. DOI: 10.1016/j.msea.2008.12.024.

[96] Q. Lai, R. Abrahams, W. Yan, C. Qiu, P. Mutton, A. Paradowska, and M. Soodi. **Investigation of a novel functionally graded material for the repair of premium hypereutectoid rails using laser cladding technology**. *Composites Part B: Engineering*. vol. 130, no. Aug. pp. 174–191. 2017. DOI: 10.1016/j.compositesb.2017.07.089.

[97] M. Fenech, B. Mallia, M. Grech, and J. C. Betts. **Post-deposition heat treatment of Co-deposited Cr3C2 and aisi 410 stainless steel using the coaxial laser deposition technique**. *Journal of Materials Science*. vol. 48, no. 5. pp. 2224–2235. 2013. DOI: 10.1007/s10853-012-6998-6.

[98] T. Roy, R. Abrahams, A. Paradowska, Q. Lai, P. Mutton, M. Soodi, P. Fasihi, and W. Yan. **Evaluation of the mechanical properties of laser cladded hypereutectoid steel rails**. *Wear*. vol. 432–433, no. Jan. p. 202930. 2019. DOI: 10.1016/j.wear.2019.202930.

[99] F. Khodabakhshi, M. H. Farshidianfar, S. Bakhshivash, A. P. Gerlich, and A. Khajepour. **Dissimilar metals deposition by directed energy based on powder-fed laser additive manufacturing**. *Journal of Manufacturing Processes*. vol. 43, no. Oct. pp. 83–97. 2019. DOI: 10.1016/j.jmapro.2019.05.018.

[100] M. Gao, Z. Wang, X. Li, and X. Zeng. **The effect of deposition patterns on the deformation of substrates during direct laser fabrication**. *Journal of Engineering Materials and Technology, Transactions of the ASME*. vol. 135, no. 3. pp. 1–6. 2013. DOI: 10.1115/1.4024195.

[101] S. Gruber, C. Grunert, M. Riede, E. López, A. Marquardt, F. Brueckner, and C. Leyens. **Comparison of dimensional accuracy and tolerances of powder bed based and nozzle based additive manufacturing processes**. *Journal of Laser Applications*. vol. 032016, no. Apr. pp. 1–13. 2020. DOI: 10.2351/7.0000115.

[102] C. Greer, A. Nycz, M. Noakes, B. Richardson, B. Post, T. Kurfess, and L. Love. **Introduction to the design rules for metal big area additive manufacturing**. *Additive Manufacturing*. vol. 27, no. Nov. pp. 159–166. 2019. DOI: 10.1016/j.addma.2019.02.016.

[103] H. Mazaheri Tehrani, R. Shoja-Razavi, M. Erfanmanesh, S. H. Hashemi, and M. Barekat. **Evaluation of the mechanical properties of WC-Ni composite coating on an AISI 321 steel substrate**. *Optics and Laser Technology*. vol. 127, no. Feb. p. 106138. 2020. DOI: 10.1016/j.optlastec.2020.106138.

[104] L. E. dos S. Paes. **Refusão a Laser Aplicada à Manufatura Aditiva por Soldagem de Deposição**, no. Universidade Fedral de Santa Catarina, Programa de Pós-Graduação em Engenharia Mecânica. p. 188, 2019.

[105] M. Barekat, R. Shoja Razavi, and A. Ghasemi. **Nd:YAG laser cladding of Co-Cr-Mo alloy on γ-TiAl substrate**. *Optics and Laser Technology*. vol. 80, no. Jan. pp. 145–152. 2016. DOI: 10.1016/j.optlastec.2016.01.003.

[106] S. E. Aghili and M. Shamanian. **Investigation of powder fed laser cladding of NiCr-**

chromium carbides single-tracks on titanium aluminide substrate. *Optics and Laser Technology*. vol. 119, no. May. pp. 105652, 2019. Doi: 10.1016/j.optlastec.2019.105652. 2019. DOI: 10.1016/j.optlastec.2019.105652.

[107] M. Song, X. Lin, F. Liu, H. Yang, and W. Huang. **Effect of environmental oxygen content on the oxide inclusion in laser solid formed AISI 420 stainless steel**. *Materials and Design*. vol. 90, no. Jan. pp. 459–467. 2016. DOI: 10.1016/j.matdes.2015.11.003.

[108] M. Manjaiah, J. Y. Hascoët, and M. Rauch. **Effect of process parameters on track geometry, microstructural evolution on 316L stainless steel multi-layer clads**. *Materials Science and Engineering B: Solid-State Materials for Advanced Technology*. vol. 259, no. May. p. 114583. 2020. DOI: 10.1016/j.mseb.2020.114583.

[109] J. Zeng, G. Lian, M. Feng, and Z. Lin. **Inclined shaping quality and optimization of laser cladding**. *Optik*. vol. 266, no. Jun. p. 169598. 2022. DOI: 10.1016/j.ijleo.2022.169598.

[110] S. Donadello, M. Motta, A. G. Demir, and B. Previtali. **Monitoring of laser metal deposition height by means of coaxial laser triangulation**. *Optics and Lasers in Engineering*. vol. 112, no. Sept. pp. 136–144. 2019. DOI: 10.1016/j.optlaseng.2018.09.012.

[111] I. M. Hutchings and P. Shipway. *Tribology: friction and wear of engineering materials*, 2nd ed. Oxford (UK): Butterworth-Heinemann, 2017. DOI: 10.1016/0261-3069(92)90241-9.

[112] R. Shah, M. Woydt, N. Huq, and A. Rosenkranz. **Tribology meets sustainability**. *Industrial Lubrication and Tribology*. vol. 73, no. 3. pp. 430–435. 2021. DOI: 10.1108/ILT-09-2020-0356.

[113] M. Woydt. **The importance of tribology for reducing CO2 emissions and for sustainability**. *Wear*. vol. 474–475, no. 6. p. 203768. 2021. DOI: 10.1016/j.wear.2021.203768.

[114] E. A. dos S. Almeida, J. C. G. Milan, H. L. Costa, A. P. Krelling, and C. E. Costa. **Sliding wear of borided sintered AISI M2 steel coated with AlTiN/CrN multilayer**. *Wear*. vol. 410–411, no. May. pp. 11–24. 2018. DOI: 10.1016/j.wear.2018.05.025.

[115] D. B. Salvaro, M. Silvério, C. Binder, R. O. Giacomelli, A. N. Klein, and J. D. B. De Mello. **Genesis and stability of tribolayers in solid lubrication: Case of pair DLC-stainless steel**. *Journal of Materials Research and Technology*. vol. 5, no. 2. pp. 136–143. 2016. DOI: 10.1016/j.jmrt.2015.10.008.

[116] A. Pauschitz, M. Roy, and F. Franek. **Mechanisms of sliding wear of metals and alloys at elevated temperatures**. *Tribology International*. vol. 41, no. 7. pp. 584–602. 2008. DOI: 10.1016/j.triboint.2007.10.003.

[117] Y. Yang, B. Liu, B. Lin, J. Jin, H. Ren, Y. Chen, M. Pan, and Y. Liang. **Influencing mechanisms of niobium and nitrogen implantation on tribological properties of 8Cr4Mo4V steel under starved lubrication**. *Tribology International*. vol. 204, no. Nov. p. 110490. 2025. DOI: 10.1016/j.triboint.2024.110490.

[118] C. J. Scheuer and R. P. Cardoso. **An overview on plasma-assisted thermochemical treatments of martensitic stainless steels**. *Surface Topography: Metrology and Properties*. vol. 11, no. Jan. p. 013001. 2023. DOI: 10.1088/2051-672X/acb372.

[119] C. Micallef, Y. N. Zhuk, and R. J. K. Wood. **Galling resistance of nanostructured CVD tungsten/tungsten carbide coatings**. *Surface Topography: Metrology and Properties*. vol. 7, no. May. p. 025004. 2019. DOI: 10.1088/2051-672X/ab1535.

[120] Z. Afshar, M. Nouri, H. Elmkhah, N. Lin, and A. Fattah-. **Evaluating the corrosion and tribological performance of nanostructured CrN/TiN and TiN/CrN configurations applied on 410 stainless steel**. *Philosophical Magazine*. vol. 104, no. 13–14. pp. 590–613. 2024. DOI: 10.1080/14786435.2024.2341322.

[121] E. M. do Nascimento, L. M. do Amaral, and A. S. C. M. D'Oliveira. **Characterization and wear of oxides formed on CoCrMoSi alloy coatings**. *Surface and Coatings Technology*. vol. 332, no. May. pp. 408–413. 2017. DOI: 10.1016/j.surfcoat.2017.07.081.

[122] R. G. N. Silva, A. de S. P. Pereira, J. M. S. Sousa, M. Pereira, and R. H. G. Silva. **Tribological comparison of Inconel 625 coatings deposited via laser metal deposition and tungsten inert gas welding process**. *Journal of Laser Applications*. vol. 32, no. 2. pp. 1–8. 2020. DOI: 10.2351/7.0000090.

[123] Y. Xiang, D. Yu, X. Cao, Y. Liu, and J. Yao. **Effects of thermal plasma surface hardening on wear and damage properties of rail steel**. *Proceedings of the Institution of Mechanical Engineers, Part J: Journal of Engineering Tribology*. vol. 232, no. 7. pp. 787–796. 2018. DOI: 10.1177/1350650117729073.

[124] A. Wei, Y. Tang, T. Tong, F. Wan, S. Yang, and K. Wang. **Effect of WC on Microstructure and Wear Resistance of Fe-Based Coating Fabricated by Laser Cladding**. *Coatings*. vol. 12, no. 8. pp. 1–15. 2022. DOI: 10.3390/coatings12081209.

[125] C. Sánchez de Rojas Candela, A. Riquelme, P. Rodrigo, B. Torres, and J. Rams. **Wear behavior of additively manufactured 316L/SiCp composites with up to 60 wt% SiCp**. *Ceramics International*. vol. 48, no. 22. pp. 33736–33750. 2022. DOI: 10.1016/j.ceramint.2022.07.319.

[126] ASTM D2714-94. **Standard Test Method for Calibration and Operation of the Falex Block-on-Ring Friction and Wear Testing Machine**. International Organization for Standardization, Pennsylvania, pp. 1–4, 2019. DOI: 10.1520/D2714-94R19.

[127] ASTM G99. **Standard Test Method for Wear and Friction Testing With a Pin-on-Disk or Ball-on-Disk Apparatus**. International Organization for Standardization, Pennsylvania, pp. 1–6, 2023. DOI: 10.1520/G0099-23.

[128] ASTM G133. **Standard Test Method for Linearly Reciprocating Ball-on-Flat Sliding Wear**. International Organization for Standardization, Pennsylvania, pp. 1–10, 2022. DOI: 10.1520/G0133-22.

[129] ASTM G65. **Standard Test Method for Measuring Abrasion Using the Dry Sand/Rubber Wheel Apparatus**. International Organization for Standardization, Pennsylvania, pp. 1–14, 2021.

[130] M. M. De Oliveira, H. L. Costa, W. M. Silva, and J. D. B. De Mello. **Effect of iron oxide debris on the reciprocating sliding wear of tool steels**. *Wear*. vol. 426–427, no. July. pp. 1065–1075. 2019. DOI: 10.1016/j.wear.2018.12.047.

[131] N. A. Shapagina and V. V. Dushik. **Coatings based on refractory materials for corrosion and wear applications**. *Materials*. vol. 17, no. 23. pp. 1–48. 2024. DOI: 10.3390/ma17235936.

[132] Y. Cai, Y. Zhao, X. Ma, K. Zhou, and Y. Chen. **Influence of environmental factors on atmospheric corrosion in dynamic environment**. *Corrosion Science*. vol. 137, no. Jul. pp. 163–175. 2018. DOI: 10.1016/j.corsci.2018.03.042.

[133] J. Hufenbach, J. Sander, F. Kochta, S. Pilz, A. Voss, U. Kühn, and A. Gebert. **Effect of selective laser melting on microstructure, mechanical, and corrosion properties of biodegradable FeMnCS for implant applications**. *Advanced Engineering Materials*. vol. 22, no. 10. pp. 1–8. 2020. DOI: 10.1002/adem.202000182.

[134] S. Kiremit, J. Cremer, Y. Stallmeier, A. Sonntag, M. Klöcker, D. Anselmetti, A. Hütten, and T. Kordisch. **Development of an in situ micro-corrosion cell for the investigation of pitting corrosion on austenitic and ferritic stainless steels**. *Corrosion and Materials Degradation*. vol. 4, no. 1. pp. 104–119. 2023. DOI: 10.3390/cmd4010007.

[135] H. B. M. Ali. **Atmospheric Pitting Corrosion of Stainless Steel**, *Doctoral Thesis,* no. University of Birmingham, College of Engineering and Physical Sciences. p. 250, 2016.

[136] M. Alizadeh and S. Bordbar. **The influence of microstructure on the protective properties of the corrosion product layer generated on the welded API X70 steel in chloride solution**. *Corrosion Science*. vol. 70, no. May. pp. 170–179. 2013. DOI: 10.1016/j.corsci.2013.01.026.

[137] L. Chang, M. G. Burke, and F. Scenini. **Understanding the effect of surface finish on stress corrosion crack initiation in warm-forged stainless steel 304L in high-temperature water**. *Scripta Materialia*. vol. 164, no. Apr. pp. 1–5. 2019. DOI: 10.1016/j.scriptamat.2019.01.032.

[138] D. K. Jangir, A. Verma, K. M. Sankar, A. S. Khanna, and A. Singla. **Influence of grain size on corrosion resistance and electrochemical behaviour of mild steel**. *International Journal for Research in Applied Science and Engineering Technology*. vol. 6, no. 4. pp. 2875–2881. 2018. DOI: 10.22214/ijraset.2018.4479.

[139] R. A. M. Anaee and M. H. Abdulmajeed. **Tribocorrosion**, in *Advances in Tribology*, 1st ed., London, United Kingdom: Intech Open Science | Open Minds, 2016, pp. 89–110. DOI: 10.5772/63657.

[140] R. F. Schaller, A. Mishra, J. M. Rodelas, J. M. Taylor, and E. J. Schindelholz. **The role of microstructure and surface finish on the corrosion of selective laser melted 304L**. *Journal of The Electrochemical Society*. vol. 165, no. 5. pp. 234–242. 2018. DOI: 10.1149/2.0431805jes.

[141] J. R. Cruz, C. E. B. Marino, and A. S. C. M. D'Oliveira. **Corrosion resistance of FeCrMnSiB austenitic stainless steels processed by plasma transferred arc**. *Journal of Materials Engineering and Performance*. vol. 33, no. 12. pp. 1–11. 2024. DOI: 10.1007/s11665-024-09893-7.

[142] J. Suryawanshi, T. Baskaran, O. Prakash, S. B. Arya, and U. Ramamurty. **On the corrosion resistance of some selective laser melted alloys**. *Materialia*. vol. 3, no. Mar. pp. 153–161. 2018. DOI: 10.1016/j.mtla.2018.08.022.

[143] G. Ko, W. Kim, K. Kwon, and T. K. Lee. **The corrosion of stainless steel made by additive manufacturing: A review**. *Metals*. vol. 11, no. 3. pp. 1–21. 2021. DOI: 10.3390/met11030516.

[144] A. Vahedi Nemani, M. Ghaffari, S. Salahi, J. Lunde, and A. Nasiri. **Effect of interpass temperature on the formation of retained austenite in a wire arc additive manufactured ER420 martensitic stainless steel**. *Materials Chemistry and Physics*. vol. 266, no. Jan. pp. 1–5. 2021. DOI: 10.1016/j.matchemphys.2021.124555.

[145] I. Taji, M. H. Moayed, and M. Mirjalili. **Correlation between sensitisation and pitting corrosion of AISI 403 martensitic stainless steel**. *Corrosion Science*. vol. 92, no. Mar. pp. 301–308. 2015. DOI: 10.1016/j.corsci.2014.12.009.

[146] A. Vahedi Nemani, M. Ghaffari, S. Salahi, and A. Nasiri. **Effects of post-printing heat treatment on the microstructure and mechanical properties of a wire arc additive manufactured 420 martensitic stainless steel part**. *Materials Science and Engineering A*. vol. 813, no. Dec. p. 141167. 2021. DOI: 10.1016/j.msea.2021.141167.

[147] T. Müller, A. Heyn, M. Babutzka, and P. Rosemann. **Examination of the influence of heat treatment on the corrosion resistance of martensitic stainless steels**. *Materials and Corrosion*. vol. 66, no. 7. pp. 656–662. 2015. DOI: 10.1002/maco.201407861.

[148] C. Örnek. **Additive manufacturing–A general corrosion perspective**. *Corrosion Engineering Science and Technology*. vol. 53, no. 7. pp. 531–535. 2018. DOI: 10.1080/1478422X.2018.1511327.

[149] ASTM G48. **Standard Test Methods for Pitting and Crevice Corrosion Resistance of Stainless Steels and Related Alloys by Use of Ferric Chloride Solution**. International Organization for Standardization, Pennsylvania, pp. 1–11, 2020. DOI: 10.1520/G0048-11R20E01.

[150] ASTM G85. **Standard Practice for Modified Salt Spray (Fog) Testing**. International Organization for Standardization, Pennsylvania, pp. 1–14, 2019. DOI: 10.1520/G0085-19.

[151] ASTM G3. **Standard Practice for Conventions Applicable to Electrochemical Measurements in Corrosion Testing**. International Organization for Standardization, Pennsylvania, pp. 1–9, 2019. DOI: 10.1520/G0003-14R24.

[152] G. P. V. Dalmora, E. P. Borges Filho, A. A. Maraschin Conterato, W. S. Roso, C. E. Pereira, and A. Dettmer. **Methods of corrosion prevention for steel in marine environments: A review**. *Results in Surfaces and Interfaces*. vol. 18, no. Oct. p. 100430. 2025. DOI: 10.1016/j.rsurfi.2025.100430.

[153] S. D. Nath, H. Irrinki, G. Gupta, M. Kearns, O. Gulsoy, and S. Atre. **Microstructure-property relationships of 420 stainless steel fabricated by laser-powder bed fusion**. *Powder Technology*. vol. 343, no. 1. pp. 738–746. 2019. DOI: 10.1016/j.powtec.2018.11.075.

[154] G. R. Ebrahimi, H. Keshmiri, M. Mazinani, A. Maldar, and M. Haghshenas. **Multi-stage thermomechanical behavior of AISI 410 martensitic steel**. *Materials Science & Engineering A*. vol. 559, no. Sept. pp. 520–527. 2013. DOI: 10.1016/j.msea.2012.08.136.

[155] F. Khodabakhshi, M. H. Farshidianfar, A. P. Gerlich, M. Nosko, V. Trembo, and A. Khajepour. **Effects of laser additive manufacturing on microstructure and**

crystallographic texture of austenitic and martensitic stainless steels. *Additive Manufacturing*. vol. 31, no. Jun. p. 100915. 2020. DOI: 10.1016/j.addma.2019.100915.

[156] M. Fenech, M. Grech, and J. C. Betts. **The in-flight temperature variation and dissolution of WC powder particles producing an Fe-Cr-W-C system by direct laser deposition**. *Surface and Coatings Technology*. vol. 207, no. Jun. pp. 211–217. 2012. DOI: 10.1016/j.surfcoat.2012.06.063.

[157] J. Chen, L. Xue, and S. H. Wang. **Experimental studies on process-induced morphological characteristics of macro- and microstructures in laser consolidated alloys**. *Journal of Materials Science*. vol. 46, no. 17. pp. 5859–5875. 2011. DOI: 10.1007/s10853-011-5543-3.

[158] B. Vamsi Krishna and A. Bandyopadhyay. **Surface modification of AISI 410 stainless steel using laser engineered net shaping (LENSTM)**. *Materials and Design*. vol. 30, no. 5. pp. 1490–1496. 2009. DOI: 10.1016/j.matdes.2008.08.003.

[159] Y. Uematsu, R. Sasaki, T. Kakiuchi, S. Yamamoto, A. Zensho, and R. Sano. **Fatigue design curves for laser-metal-deposited type 420 stainless steel and effect of an interval during deposition process**. *The International Journal of Advanced Manufacturing Technology*. vol. 116, no. Jul. pp. 2917–2927. 2021. DOI: 10.1007/s00170-021-07605-2.

[160] Q. Lai, R. Abrahams, W. Yan, C. Qiu, P. Mutton, A. Paradowska, X. Fang, M. Soodi, and X. Wu. **Effects of preheating and carbon dilution on material characteristics of laser-cladded hypereutectoid rail steels**. *Materials Science & Engineering A*. vol. 712, no. Dec. pp. 548–563. 2018. DOI: 10.1016/j.msea.2017.12.003.

[161] T. Roy, Q. Lai, R. Abrahams, P. Mutton, A. Paradowska, M. Soodi, and W. Yan. **Effect of deposition material and heat treatment on wear and rolling contact fatigue of laser cladded rails**. *Wear*. vol. 412–413, no. Jul. pp. 69–81. 2018. DOI: 10.1016/j.wear.2018.07.001.

[162] S. Huang, D. Li, L. Zhang, X. Zhang, and W. Zhu. **Tailoring the mechanical properties of laser cladding-deposited ferrous alloys with a mixture of 410L alloy and Fe–Cr–B–Si–Mo alloy powders**. *Materials*. vol. 12, no. 3. pp. 1–12. 2019. DOI: 10.3390/ma12030410.

[163] W. J. Oh, Y. Son, S. Y. Cho, S. W. Yang, G. Y. Shin, and D. S. Shin. **Solution austenitization and precipitation hardening effect on the mechanical properties of 630 stainless steel fabricated via laser melting deposition**. *Materials Science & Engineering A*. vol. 794, no. Jul. p. 139999. 2020. DOI: 10.1016/j.msea.2020.139999.

[164] A. Deev, P. Kuznetsov, A. Zhukov, and V. Bobyr. **The structure and properties of the samples produced by selective laser melting of 410L steel-based metal powder**. *Physical Procedia*. vol. 89, no. Dec. pp. 31–38. 2017. DOI: 10.1016/j.phpro.2017.08.013.

[165] R. Seede, B. Zhang, A. Whitt, S. Picak, S. Gibbons, P. Flater, A. Elwany, R. Arroyave, and I. Karaman. **Effect of heat treatments on the microstructure and mechanical properties of an ultra-high strength martensitic steel fabricated via laser powder bed fusion additive manufacturing**. *Additive Manufacturing*. vol. 47, no. May. p.

102255. 2021. DOI: 10.1016/j.addma.2021.102255.

[166] Y. Tian, K. Chadha, and C. Aranas. **Laser powder bed fusion of ultra-high-strength 420 stainless steel: Microstructure characterization, texture evolution and mechanical properties**. *Materials Science & Engineering A*. vol. 805, no. Oct. p. 140790. 2021. DOI: 10.1016/j.msea.2021.140790.

[167] V. H. Meura, J. T. Pacheco, M. T. Veiga, A. Rabelo, L. J. da Silva, J. C. Milan, and C. E. da Costa. **Effect of post-heat treatment on microstructure and tribological performance of AISI 410L coatings processed by laser-directed energy deposition (L-DED)**. *Progress in Additive Manufacturing*. vol. 8. pp. 1–11. 2023. DOI: 10.1007/s40964-023-00404-z.

[168] N. Jeyaprakash, C. hua Yang, K. R. Ramkumar, and G. zhou Sui. **Comparison of microstructure, mechanical and wear behaviour of laser cladded stainless steel 410 substrate using stainless steel 420 and Colmonoy 5 particles**. *Journal of Iron and Steel Research International*. vol. 27, no. 12. pp. 1446–1455. 2020. DOI: 10.1007/s42243-020-00447-4.

[169] A. Shahriari, M. Ghaffari, L. Khaksar, A. Nasiri, A. Hadadzadeh, B. S. Amirkhiz, and M. Mohammadi. **Corrosion resistance of 13wt.% Cr martensitic stainless steels: Additively manufactured CX versus wrought Ni-containing AISI 420**. *Corrosion Science*. vol. 184, no. Sept. p. 109362. 2021. DOI: 10.1016/j.corsci.2021.109362.

[170] L. Wang, A. Seyeux, and P. Marcus. **Thermal stability of the passive film formed on 316L stainless steel surface studied by ToF-SIMS**. *Corrosion Science*. vol. 165, no. Nov. p. 108395. 2020. DOI: 10.1016/j.corsci.2019.108395.

[171] K. Morshed-Behbahani, N. Zakerin, P. Najafisayar, and M. Pakshir. **A survey on the passivity of tempered AISI 420 martensitic stainless steel**. *Corrosion Science*. vol. 183, no. Feb. p. 109340. 2021. DOI: 10.1016/j.corsci.2021.109340.

[172] Q. Wang, J. Huang, L. Guan, Y. Zhang, P. Jiang, J. Chen, X. Yuan, and W. Wu. **Electrochemical corrosion behavior of 18Ni 300 maraging steel obtained by laser cladding deposition and selective laser melting in corrosive mediums: A comparative study**. *Journal of Materials Engineering and Performance*. vol. 31, no. Oct. pp. 8389–8404. 2022. DOI: 10.1007/s11665-022-06849-7.

[173] F. Kochta, A. Gebert, U. Kühn, S. Oswald, T. Gemming, C. Leyens, and J. Kristin. **Improved corrosion behavior of a novel Fe85Cr4Mo8V2C1 tool steel processed by laser powder bed fusion**. *Journal of Alloys and Compounds*. vol. 867, no. Jun. p. 158887. 2021. DOI: 10.1016/j.jallcom.2021.158887.

[174] A. Yazdanpanah, M. Franceschi, P. Rebesan, and M. Dabalà. **Correlation of lack of fusion pores with stress corrosion cracking susceptibility of L-PBF 316L: Effect of surface residual stresses**. *Materials*. vol. 15, no. 20. pp. 1–16. 2022. DOI: 10.3390/ma15207151.

[175] A. F. Candelária and C. E. Pinedo. **Influence of the heat treatment on the corrosion resistance of the martensitic stainless steel type AISI 420**. *Journal of Materials Science Letters*. vol. 22, no. Aug. pp. 1151–1153. 2003. DOI: 10.1023/A:1025179128333.

[176] J. X. Fang, S. Y. Dong, Y. J. Wang, B. S. Xu, Z. H. Zhang, D. Xia, W. B. Ren, and P. He. **Microstructure and properties of an as-deposited and heat treated martensitic stainless steel fabricated by direct laser deposition**. *Journal of Manufacturing*

Processes. vol. 25, no. Jan. pp. 402–410. 2017. DOI: 10.1016/j.jmapro.2016.12.014.

[177] S. D. Nath, G. Gupta, M. Kearns, O. Gulsoy, and S. V. Atre. **Effects of layer thickness in laser-powder bed fusion of 420 stainless steel**. *Rapid Prototyping Journal*. vol. 26, no. 7. pp. 1197–1208. 2020. DOI: 10.1108/RPJ-10-2019-0279.

[178] K. B. Small, D. A. Englehart, and T. A. Christman. **Etching specialty alloys**. *Advanced Materials & Processes*. vol. 32. pp. 32–37. 2008.

[179] H. S. Ferreira. **Modelagem Matemática de Revestimentos Fabricados pelo Processo de Manufatura Aditiva de Laser Metal Deposition (LMD) e Posteriormente Fundidos**, *Trabalho de Conclusão de Curso*, no. Universidade Federal de Santa Catarina, Programa de Graduação em Engenharia Mecânica. p. 102, 2019.

[180] ASTM E384. **Standard Test Method for Microindentation Hardness of Materials**. International Organization for Standardization, Pennsylvania, pp. 1–40, 2017. DOI: 10.1520/E0384-22.

[181] ASTM E8/E8M. **Standard Test Methods for Tension Testing of Metallic Materials**. International Organization for Standardization, Pennsylvania, pp. 1–35, 2022. DOI: 10.1520/E0008_E0008M-24.

[182] ASTM E23. **Standard Test Methods for Notched Bar Impact Testing of Metallic Materials**. International Organization for Standardization, Pennsylvania, pp. 1–27, 2018. DOI: 10.1520/E0023-24.

[183] J. W. Hur, S. Y. Baek, and K. Kim. **Effect of displacement on kinetic frictional behaviour between electro-deposited coating and AISI 52100 steel under fretting conditions**. *Proceedings of the Institution of Mechanical Engineers, Part J: Journal of Engineering Tribology*. vol. 230, no. 9. pp. 1172–1179. 2016. DOI: 10.1177/1350650116628826.

[184] F. A. Vicente. **Efeito da Dopagem e da Topografia na Tribologia e Resistência à Corrosão de Filmes de DLC**, *Dissertação de Mestrado,* no. Universidade Federal de Santa Catarina, Programa de Pós-Graduação em Ciência e Engenharia de Materiais. p. 91, 2022. DOI: 10.13140/RG.2.2.15066.93123.

[185] G. BRASIL. **GMS, Quality Certificate (AISI 410 Stainless Steel)**. GMS BRASIL, pp. 1, São Paulo, São Paulo, p. 1, 2020.

[186] Höganäs S/A. **HÖGANÄSCertifIcate of analysis - powder 410L Stainless Steel (53-150 µm)**. HÖGANÄS S/A, pp. 1, Mogi das Cruzes, São Paulo, p. 1, 2019.

[187] ASTM B215. **Standard Practices for Sampling Metal Powders**. International Organization for Standardization, Pennsylvania, pp. 1–7, 2020. DOI: 10.1520/B0215-20R25.

[188] I. RPM Innovations. **RPM INNOVATIONS Inc, RPMI 535 Opeartions Manual - Safety Procedures**. pp. 1-143, Rapid City, Virginia (USA), p. 143, 2017.

[189] J. Powell, D. Koti, and X. Garmendia. **Assessing the quality and productivity of laser cladding and direct energy deposition: Guidelines for researchers**. *Journal of Laser Applications*. vol. 35, no. Feb. p. 012024. 2023. DOI: 10.2351/7.0000897.

[190] S. E. Aghili and M. Shamanian. **Investigation of powder fed laser cladding of NiCr-chromium carbides single-tracks on titanium aluminide substrate**. *Optics and Laser Technology*. vol. 119, no. May. p. 105652. 2019. DOI: 10.1016/j.optlastec.2019.105652.

[191] T. E. Abioye, J. Folkes, and A. T. Clare. **A parametric study of Inconel 625 wire laser deposition**. *Journal of Materials Processing Technology*. vol. 213, no. 12. pp. 2145–2151. 2013. DOI: 10.1016/j.jmatprotec.2013.06.007.

[192] H. El Cheikh, B. Courant, J. Y. Hascoët, and R. Guillén. **Prediction and analytical description of the single laser track geometry in direct laser fabrication from process parameters and energy balance reasoning**. *Journal of Materials Processing Technology*. vol. 212, no. 9. pp. 1832–1839. 2012. DOI: 10.1016/j.jmatprotec.2012.03.016.

[193] S. Donadello, V. Furlan, A. G. Demir, and B. Previtali. **Interplay between powder catchment efficiency and layer height in self-stabilized laser metal deposition**. *Optics and Lasers in Engineering*. vol. 149, no. Aug. p. 106817. 2022. DOI: 10.1016/j.optlaseng.2021.106817.

[194] J. Gutjahr, M. Pereira, J. M. S. de Sousa, H. S. Ferreira, and A. Thiesen Júnior. **Powder degradation as a consequence of laser interaction: A study of SS 316L powder reuse on the laser directed energy deposition process**. *Journal of Laser Applications*. vol. 36, no. 1. p. 012022. 2024. DOI: 10.2351/7.0001093.

[195] A. T. Sutton, C. S. Kriewall, and J. W. Newkirk. **Scholars ' Mine Powders for Additive Manufacturing Processes : Characterization Techniques and Effects on Part Properties**, in *27th Annual International Solid Freeform Fabrication Symposium*, 2016, pp. 1004–1030. [Online]. Available: https://scholarsmine.mst.edu/mec_aereng_facwork Part

[196] Â. Cunha, A. Marques, M. R. Silva, F. Bartolomeu, F. S. Silva, M. Gasik, B. Trindade, and Ó. Carvalho. **Laser powder bed fusion of the steels used in the plastic injection mould industry: a review of the influence of processing parameters on the final properties**. *International Journal of Advanced Manufacturing Technology*. vol. 121, no. 7–8. pp. 4255–4287. 2022. DOI: 10.1007/s00170-022-09588-0.

[197] A. Toenjes, J. Schmidt, and M. Hesselmann. **Processability of water atomized 410L steel with laser powder bed fusion**. *Progress in Additive Manufacturing*. vol. 1, no. Jan. pp. 1–9. 2025. DOI: 10.1007/s40964-025-00979-9.

[198] A. N. de Moura, C. M. de Alcântara, E. A. Vieira, W. da S. Labiapari, M. A. da Cunha, T. R. de Oliveira, and M. T. D. A. Orlando. **Microstructure, crystallographic aspects and mechanical properties of AISI 420 martensitic stainless steel after different thermomechanical process routes**. *Materials Chemistry and Physics*. vol. 305, no. Sept. p. 127723. 2023. DOI: 10.1016/j.matchemphys.2023.127723.

[199] S. Y. Lu, K. F. Yao, Y. B. Chen, M. H. Wang, X. Liu, and X. Ge. **The effect of tempering temperature on the microstructure and electrochemical properties of a 13 wt.% Cr-type martensitic stainless steel**. *Electrochimica Acta*. vol. 165, no. 2. pp. 45–55. 2015. DOI: 10.1016/j.electacta.2015.02.038.

[200] S. A. Evlashin, A. A. Volkova, R. V. Mendagaliev, K. D. Babkin, J. V. Bondareva, A. P. Simonov, Y. O. Kuzminova, O. N. Dubinin, D. A. Chernodubov, A. A. Shibalova, I. A. Kobykhno, and O. G. Klimova-Korsmik. **Magnetic and mechanical properties of 316L/410L/316L sandwich structure produced by direct energy deposition**.

Materials Today Communications. vol. 37, no. Oct. pp. 17–20. 2023. DOI: 10.1016/j.mtcomm.2023.107230.

[201] L. C. Shen, X. H. Yang, J. R. Ho, P. C. Tung, and C. K. Lin. **Effects of build direction on the mechanical properties of a martensitic stainless steel fabricated by selective laser melting**. *Materials*. vol. 13, no. 22. pp. 1–18. 2020. DOI: 10.3390/ma13225142.

[202] H. K. Kang, H. Lee, C. S. Oh, and J. Yoon. **Microstructure and Mechanical Properties of Laser Direct Energy Deposited Martensitic Stainless Steel 410**. *Micromachines*. vol. 15, no. 7. pp. 1–14. 2024. DOI: 10.3390/mi15070837.

[203] M. Mirzaee, A. Momeni, N. Aieni, and H. Keshmiri. **Effect of quenching and tempering on microstructure and mechanical properties of 410 and 410 Ni martensitic stainless steels**. *Journal of Materials Research*. vol. 32, no. 3. pp. 687–696. 2017. DOI: 10.1557/jmr.2016.485.

[204] G. Sun, R. Zhou, J. Lu, and J. Mazumder. **Evaluation of defect density, microstructure, residual stress, elastic modulus, hardness and strength of laser-deposited AISI 4340 steel**. *Acta Materialia*. vol. 84, no. 1. pp. 172–189. 2015. DOI: 10.1016/j.actamat.2014.09.028.

[205] E. O. Correa, N. G. Alcântara, L. C. Valeriano, N. D. Barbedo, and R. R. Chaves. **The effect of microstructure on abrasive wear of a Fe-Cr-C-Nb hardfacing alloy deposited by the open arc welding process**. *Surface and Coatings Technology*. vol. 276, no. Aug. pp. 479–484. 2015. DOI: 10.1016/j.surfcoat.2015.06.026.

[206] S. Ghatrehsamani, S. Akbarzadeh, and M. Khonsari. **Experimental and numerical study of the running-in wear coefficient during dry sliding contact**. *Surface Topography: Metrology and Properties*. vol. 9, no. 1. p. 015009. 2021. DOI: 10.1088/2051-672X/abbd7a.

[207] W. Qi, L. Chen, H. Li, L. Tang, and Z. Xu. **Solid–Liquid Composite Lubrication (SLCL) Based on Diamond-Like Carbon (DLC) Coatings and Lubricating Oils: Properties and Challenges**. *Coatings*. vol. 14, no. 12. pp. 1–27. 2024. DOI: 10.3390/coatings14121475.

[208] M. Varga, H. Rojacz, H. Winkelmann, H. Mayer, and E. Badisch. **Wear reducing effects and temperature dependence of tribolayer formation in harsh environment**. *Tribology International*. vol. 65, no. Sept. pp. 190–199. 2013. DOI: 10.1016/j.triboint.2013.03.003.

[209] S. Gollapudi. **Grain size distribution effects on the corrosion behaviour of materials**. *Corrosion Science*. vol. 62, no. May. pp. 90–94. 2012. DOI: 10.1016/j.corsci.2012.04.040.

[210] J. R. Cruz and R. Bertazzoli. **Characterization of corrosion within friction stir weld zones of an API X-70 steel using a novel microcell setup**. *Journal of Materials Engineering and Performance*. vol. 29, no. 1. pp. 98–108. 2020. DOI: 10.1007/s11665-019-04531-z.

[211] T. Guo, D. Zhang, Z. Hui, C. Han, and L. Zhao. **The effect of trace boron element on local corrosion resistance of casted 0.04C-16Cr ferritic stainless steel**. *Advanced Materials Research*. vol. 415–417, no. Dec. pp. 800–806. 2012. DOI:

10.4028/www.scientific.net/AMR.415-417.800.

[212] P. D. Krell, S. Li, and H. Cong. **Synergistic effect of temperature and HCl concentration on the degradation of AISI 410 stainless steel**. *Corrosion Science*. vol. 122, no. Mar. pp. 41–52. 2017. DOI: 10.1016/j.corsci.2017.03.027.

[213] M. Ferhat, A. Benchettara, S. E. Amara, and D. Najjar. **Corrosion behaviour of Fe-C alloys in a sulfuric medium**. *Journal of Materials and Environmental Science*. vol. 5, no. 4. pp. 1059–1068. 2014.

[214] J. R. Cruz, J. M. S. Sousa, H. S. Ferreira, A. T. Junior, and C. E. B. Marino. **Impact of feedstock recycling on the corrosion resistance of Inconel 625 processed by L-DED**. *Materials Research*. vol. 27, no. May. pp. 1–16. 2024. DOI: 10.1590/1980-5373-MR-2023-0578.

[215] Y. Yu, S. Shironita, K. Souma, and M. Umeda. **Effect of chromium content on the corrosion resistance of ferritic stainless steels in sulfuric acid solution**. *Heliyon*. vol. 4, no. 11. pp. 1–13. 2018. DOI: 10.1016/j.heliyon.2018.e00958.

[216] C. Örnek, B. Payam, A. Gloskovskii, K. Kazmanlı, N. Mohamed, B. Derin, M. Ürgen, C. E. Chou, H. W. Yen, B. Avcı, and S. Ooi. **Understanding the passive behaviour of low-chromium high-strength hybrid steel in corrosive environments**. *Materials Degradation*. vol. 7, no. 1. pp. 1–15. 2023. DOI: 10.1038/s41529-023-00392-z.

[217] B. S. Kumar, V. Kain, and B. Vishwanadh. **Effect of tempering treatments on microstructure and intergranular corrosion of 13 wt% Cr martensitic stainless steel**. *Corrosion The Journal of Science and Engineering*. vol. 73, no. 4. pp. 362–378. 2017. DOI: 10.5006/2141.